X-ray and Optical Properties of X-ray Luminous Active Galactic Nuclei

Mirko Krumpe

Universität
Potsdam

Potsdam 2007

Astrophysikalisches Institut Potsdam
Arbeitsgruppe "Galaxien und Quasare"

X-ray and Optical Properties of X-ray Luminous Active Galactic Nuclei

von
Mirko Krumpe

Potsdam, den 03. Dezember 2007

Erstgutachter: Prof. Dr. Matthias Steinmetz
Zweitgutachter: Prof. Dr. Rüdiger Staubert
Drittgutachter: Prof. Dr. Ian McHardy
Viertgutachter: Prof. Dr. Günther Hasinger

Contents

List of Figures

List of Tables

Allgemeinverständliche Zusammenfassung

Giacconi et al. (1962) entdeckten mit Hilfe von Raketenexperimenten auf der Suche nach Röntgenstrahlung vom Mond eine scheinbar diffuse extragalaktische Röntgenhintergrundstrahlung. Spätere Satellitenmissionen detektierten ein Maximum dieser Strahlung bei ∼30 keV. Abbildenden Röntgensatelliten wie *ROSAT* (1990-1999) gelang es, bis zu 80% des diffusen Hintergrundes unter 2 keV in einzelne Punktquellen aufzulösen, von denen die überwiegende Mehrheit aktive Galaxienkerne waren. Der Röntgenhintergrund ist somit wahrscheinlich als die Emission der Gesamtheit aller akkretierenden superschweren (mehrere Millionen Sonnenmassen) schwarzen Löcher in den Zentren von Galaxien in der kosmischen Geschichte zu verstehen. Zur Erklärung des Maximums der spektralen Energieverteilung der Röntgenhintergrundstrahlung bei ∼30 keV benötigen theoretische Modelle jedoch zusätzliche Populationen von röntgenabsorbierenden aktiven Galaxienkernen (AGN). Derzeitige Röntgenmissionen wie *XMM-Newton* und *Chandra* ermöglichen die Untersuchung dieser Quellklassen.

Die vorliegende Arbeit untersucht die Quellpopulationen, die den Röntgenhimmel dominieren. Dazu wird die 120 ksec *XMM-Newton* Beobachtung im Marano Feld, Ziel einer früheren optischen AGN-Durchmusterung am Südhimmel, ausgewertet. Die optischen und Röntgeneigenschaften der unterschiedlichen Quellpopulationen werden untersucht und Unterschiede erarbeitet. Für die röntgenabsorbierende Objektklasse der Typ II AGN, die man als möglichen Erzeuger der Röntgenstrahlung um 30 keV betrachtet, wird aus den Röntgenspektren das Ausmaß der Absorption ermittelt. Um die Anzahl dieser selten gefundenen Objekte zu erhöhen, werden in dieser Arbeit zusätzliche Objekte aus der Röntgendurchmusterung des "*XMM-Newton* Serendipitous Medium Sample" einbezogen. Die Abhängigkeit der Absorption von der Rotverschiebung und der Röntgenleuchtkraft wird untersucht.

Von 328 Röntgenquellen im Marano Feld konnten 140 spektroskopisch klassifiziert werden. Es wurden 89 Typ I AGN, 36 Typ II AGN, 6 Galaxien und 9 Sterne gefunden. Nur basierend auf den optischen und Röntgeneigenschaften können AGN, Galaxien und Sterne unterschieden werden. Typ I und II AGN lassen sich nicht klar trennen und zeigen große Gemeinsamkeiten in den untersuchten Eigenschaften. Mit Hilfe von zusätzlichen Aufnahmen im nahen Infraroten (K-Band) konnten erfolgreich mehrere seltene Typ II AGN identifiziert werden.

Die Röntgenspektren von Typ II AGN aus dem *XMM-Newton* Marano Feld und dem "*XMM-Newton* Serendipitous Medium Sample" wurden ausgewertet. Die Objekte weisen nur eine mäßige Absorption auf und scheinen somit nicht einen Hauptbestandteil des Röntgenstrahlungshintergrundes um 30 keV zu erzeugen. Obwohl Selektionseffekte nicht vollständig verstanden sind, zeigen Typ II AGN keine erkennbare Abhängigkeit der Absorption von der Rotverschiebung oder der Röntgenleuchtkraft.

Abstract

Giacconi et al. (1962) discovered a diffuse cosmic X-ray background with rocket experiments when they searched for lunar X-ray emission. Later satellite missions found a spectral peak in the cosmic X-ray background at $\sim$30 keV. Imaging X-ray satellites such as *ROSAT* (1990-1999) were able to resolve up to 80% of the background below 2 keV into single point sources, mainly active galaxies. The cosmic X-ray background is the integration of all accreting super-massive (several million solar masses) black holes in the centre of active galaxies over cosmic time. Synthesis models need further populations of X-ray absorbed active galaxy nuclei (AGN) in order to explain the cosmic X-ray background peak at $\sim$30 keV. Current X-ray missions such as *XMM-Newton* and *Chandra* offer the possibility of studying these additional populations.

This Ph.D. thesis studies the populations that dominate the X-ray sky. For this purpose the 120 ksec *XMM-Newton* Marano field survey, named for an earlier optical quasar survey in the southern hemisphere, is analysed. Based on the optical follow-up observations the X-ray sources are spectroscopically classified. Optical and X-ray properties of the different X-ray source populations are studied and differences are derived. The amount of absorption in the X-ray spectra of type II AGN, which are considered as a main contributor to the X-ray background at $\sim$30 keV, is determined. In order to extend the sample size of the rare type II AGN, this study also includes objects from another survey, the *XMM-Newton* Serendipitous Medium Sample. In addition, the dependence of the absorption in type II AGN with redshift and X-ray luminosity is analysed.

We detected 328 X-ray sources in the Marano field. 140 sources were spectroscopically classified. We found 89 type I AGN, 36 type II AGN, 6 galaxies, and 9 stars. AGN, galaxies, and stars are clearly distinguishable by their optical and X-ray properties. Type I and II AGN do not separate clearly. They have a significant overlap in all studied properties. In a few cases the X-ray properties are in contradiction to the observed optical properties for type I and type II AGN. For example we find type II AGN that show evidence for optical absorption but are not absorbed in X-rays. Based on the additional use of near infra-red imaging (K-band), we were able to identify several of the rare type II AGN.

The X-ray spectra of type II AGN from the *XMM-Newton* Marano field survey and the *XMM-Newton* Serendipitous Medium Sample were analysed. Since most of the sources have only $\sim$40 X-ray counts in the *XMM-Newton* PN-detector, I carefully studied the fit results of simulated X-ray spectra as a function of fit statistic and binning method. The objects revealed only moderate absorption. In particular, I do not find any Compton-thick sources (absorbed by column densities of $N_{\mathrm{H}} > 1.5 \times 10^{24}\,\mathrm{cm}^{-2}$). This gives evidence that type II AGN are not the main contributor of the X-ray background around 30 keV. Although bias effects may occur, type II AGN show no noticeable trend of the amount of absorption with redshift or X-ray luminosity.

Chapter 1

Introduction

At the end of the 19th century, the study of electric current in extremely evacuated glass tubes was one of the most fascinating research fields in physics. These experiments became possible after the development of an advanced mercury evacuation pump around 1890 by Heinrich Geißler.

Wilhelm Conrad Röntgen, who was a physics professor at Würzburg University, Germany at this time, investigated the properties of cathode rays (electron beam) by using a fluorescent screen inside an extremely evacuated glass tube.

On November 8, 1895 he likely used higher voltages than usual and investigated if a fluorescent screen glows in the immediate vicinity of his specially constructed Hittorf glass tube. Surprisingly, the fluorescent screen did not only glow in the proximity of the glass tube, but also in considerable distances and even when opaque black paper was wrapped around the tube. Since it was known that electron beams can only penetrate up to a few centimetre in air, Röntgen realised the discovery of a new kind of radiation which he named by its unknown properties "X-rays". He kept the discovery of X-rays as a secret for weeks and conducted further experiments. He found that X-rays expose photographic plates and thus he took plates of his laboratory door, sporting gun, a set of weights, and his wife's hand (December 22, 1895). These experiments showed the unique properties of X-ray to radiate through different materials with different thicknesses. On December 28, 1895 he released the first publication on X-rays. The possibility to visualise the human skeleton made him so famous that the German Emperor Wilhelm II invited him for a private demonstration in Berlin on January 14, 1896.

For his discovery, W. C. Röntgen received the first Nobel Prize in physics in 1901. He refused to apply for a patent. On May 3, 1897 after his third publication on X-rays he finished his research on X-rays and returned towards his old passion – the research of crystals.

After the discovery of X-rays was announced in the United Kingdom, Silvanus Phillips Thompson repeated Röntgen's experiments and later complained that Röntgen left "little for others to do beyond elaboration his work".

1.1   X-rays – A physical characterisation

From the physical point of view, X-rays are electromagnetic wave radiation, analogous to optical light. X-rays overlap in their long wavelengths with the ultraviolet radiation and are also not well defined at short wavelengths. Lenk & Gellert (1989) define X-rays as radiation of 80 nm up to 10^{-5} nm wavelength which corresponds to 15 eV – 120 MeV. This wavelength range covers also γ-rays which belong to X-rays in the broader sense. These radiations differ in their physical origins, but exhibit identical properties.

X-rays propagate straight-lined and exhibit wave-particle dualism. The wavelength of X-rays is comparable to atomic dimensions. Hence, a reflection or refraction of X-rays is in general not feasible due to the large size of atomic structure (Lenk & Gellert 1989). Only at very small incident angles refraction and reflection are achievable. The incident angle for reflection further decreases as the energy of the X-rays increases.

Similar to optical radiation, X-rays can be affected by diffraction. Since the corresponding wavelengths are much shorter than in the optical regime, diffraction is again only possible by diffractive objects comparable in size to atomic dimensions like space lattice of crystals. Furthermore, partial polarisation of X-rays is observed.

A considerably different property of X-rays compared to optical light is the penetration of matter. This unique feature of X-rays has been the main reason for practical application. When X-rays penetrate matter, the intensity of the radiation decreases by scatter processes and absorption (μ_{sca}, μ_{abs} in Eq. 1.1, Lenk & Gellert 1989).

$$I = I_0 \, e^{-\mu_{\mathrm{total}}\, d} = I_0 \, e^{-(\mu_{\mathrm{abs}}+\mu_{\mathrm{sca}})\, d} \ , \quad \mu_{\mathrm{abs}} = C \cdot Z^4 \cdot \lambda^3 \qquad (1.1)$$

The absorption characteristics is only determined by the properties of the material's atoms, while optical light absorption is mostly affected by the properties of the chemical bonds. The absorption of X-rays of a given wavelength λ increases significantly with the atomic number Z of the absorbing material. The absorption coefficient increases with ascending wavelength λ. Therefore, high energy X-ray photons can penetrate much deeper into matter than low energy X-ray photons. X-rays with long wavelength can only be detected in vacuum since they are easily absorbed by air.

1.1.1   Interaction of X-rays and matter

The X-rays and matter interact through different physical processes: (1) – classical Rayleigh-Thomson scattering, (2) – Compton-effect, (3) – photo-electric effect, and (4) – electron-positron pair production.

(1) *the incident radiation is emitted as coherent radiation with the same wavelength*
The interaction between photons and free electrons (Thomson scattering) or bound electrons, as well as atoms (Rayleigh scattering) happens without a transfer of energy. The photon only changes its direction. The conservation of the photon's energy (elastic scattering) is accomplished when $\alpha \sim 0$ where α is defined as $\alpha = h\,\nu/m_{\text{particle}}\,c^2$.

(2) *emission of incoherent X-ray radiation with increased wavelength*
The inelastic scattering of photons on free or weakly bound electrons (Compton-effect) transfers energy from the photon to the electron. The increase in the photon's wavelength is given by

$$\lambda_{\text{scattered}} - \lambda_{\text{incident}} = \Delta\lambda = \frac{h}{m_{0_{\text{e}}}\,c}(1 - \cos\theta),\qquad(1.2)$$

where θ corresponds to the photon's scattering angle, i.e. the angle between the propagation of the incident and scattered photon. Energy and momentum conservation apply, since the photon gives part of its energy to the interaction electron, in the form of kinetic energy. The energy shift depends on the angle of scattering and is maximal when the photon is scattered backwards ($\theta = 180°$). In this case the increase in wavelength of $0.0485\,\text{Å}$ is independent of the incident wavelength. The Klein-Nishina-Equation, which gives the differential cross section for the photon scattering on electrons at rest, can
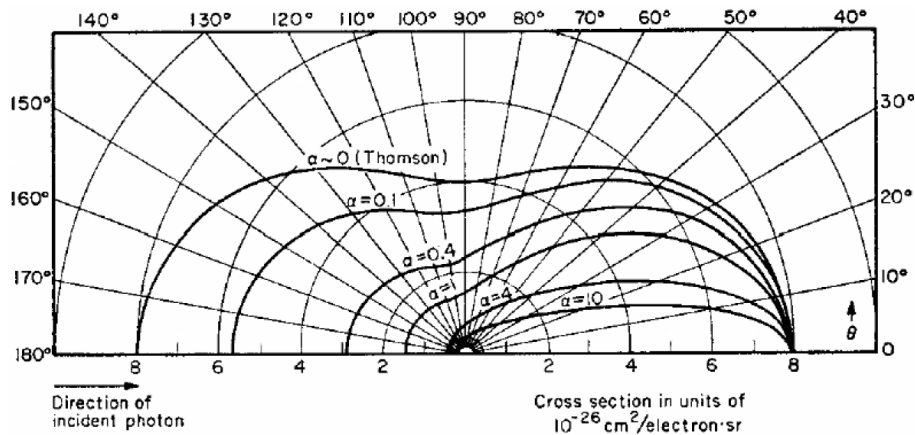
Figure 1.1: Cross section for photon scattering in dependence of incident angle θ and energy of the photon (taken from Siegbahn 1968). The diagram is based on the Klein-Nishina-Equation. The parameter α represents the photon's energy by $\alpha = h\,\nu/m_{0_{\text{e}}}\,c^2$, ($\alpha = 0.1 \rightarrow 51\,\text{keV}$, $\alpha = 0.4 \rightarrow 205\,\text{keV}$, $\alpha = 1 \rightarrow 511\,\text{keV}$, $\alpha = 4 \rightarrow 2\,\text{MeV}$, $\alpha = 10 \rightarrow 5,1\,\text{MeV}$). For the case of $\alpha \sim 0$ the derived cross section equals the cross section of Thomson scattering.

be used to derive the Compton-scattering cross section (see Fig. 1.1). The cross section is only dependent on the energy and the angle of the incident photon. Higher photon energies results in smaller scattering angles (for $-90° < \theta < 90°$). The cross section scales linearly with the atomic number of the absorbing material:

$$\sigma_{\text{compton}} \propto \frac{Z}{E_{\text{photon}}}. \tag{1.3}$$

(3)   *the energy of the X-ray photon is assigned to an electron which gets ejected by the interacting atom*
A photon transfers its total energy onto a shell electron. The photon gets absorbed and an electron is ejected from the atom's shell. If the photon's energy is larger than the required characteristic ionisation energy, the energy difference is transferred into kinetic energy of the ejected electron. The vacancy is filled by another electron from an upper shell. The released energy is emitted as characteristic radiation or radiation less as an emission of an Auger electron[1]. The cross section of the photo-electric effect is:

$$\sigma_{\text{photo}} \propto \frac{Z^5}{E_{\text{photon}}^{7/2}}. \tag{1.4}$$

Therefore, the photo-electric effect is the dominating interaction of low energy radiation and between photons and atoms with increasing atomic number.

(4)   *the photon is converted into an electron-positron pair*
When a photon has an energy higher than twice the electron's rest mass energy ($E_{\text{photon}} > 1.022\,\text{MeV}$), one of the ways that such a photon interacts with matter is by producing an electron-positron pair in the vicinity of the coulomb field of an atom or electron. The studied phenomena in this thesis do not reach such high energies. However, for the sake of completeness this interaction process is briefly described. The cross section is:

$$\sigma_{\text{pair}} \propto Z^2 \times ln\frac{E_{\text{photon}}}{2\,m_{0\text{e}}\,c^2}. \tag{1.5}$$

Therefore, the pair production increases with higher photon's energy and atomic numbers.

---

[1]The emission of an electron from an atom causes the emission of a second electron (Auger effect). The energy of a photon removes an electron from the core level of an atom. An electron from a higher energy level falls into the vacancy. The released energy is transferred to another electron from an upper shell which get ejected too. Auger electrons are mainly emitted by light elements. With increasing atomic number, the atom more frequently emits a recombination photon.
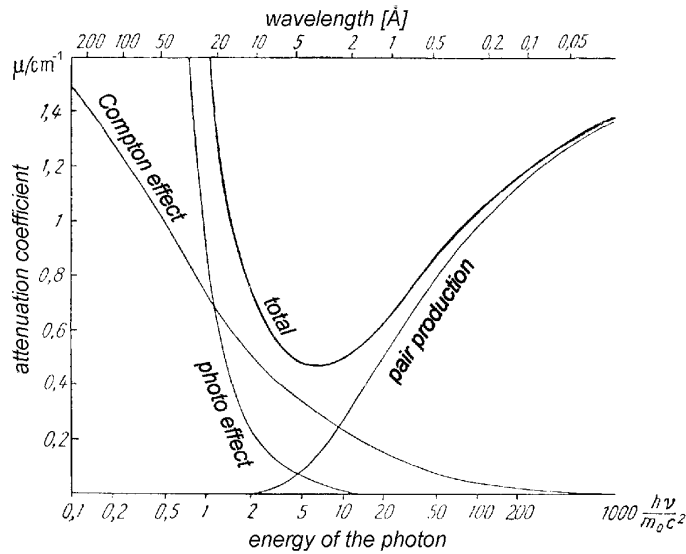
Figure 1.2: Pb attenuation coefficient vs. photon energy diagram for the Compton-effect, photo-electric effect, and pair production (based on a plot shown in Gerthsen et al. 1986). The resulting superposition of all effects is shown in the total line.
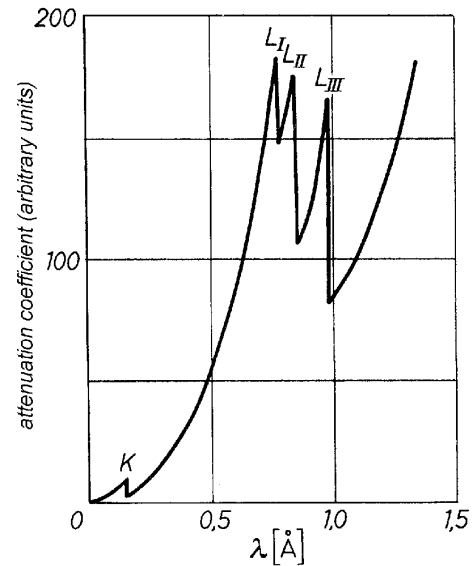
Figure 1.3: Resulting attenuation coefficient for Pb with consideration of electron shell effects (taken from Gerthsen et al. 1986).

The different cross sections are summed up to derive the X-ray attenuation coefficient

$$\mu_{\text{total}} = \mu_{\text{abs}} + \mu_{\text{sca}} = n \times Z \times (\sigma_{\text{compton}} + \sigma_{\text{photo}} + \sigma_{\text{pair}}), \tag{1.6}$$

where n is the particle density and Z the atomic number of the absorbing material. The cross section decreases with shorter wavelength of the X-rays for the photo-electric and Compton-effect. However, the X-ray attenuation coefficient does not decrease indefinitely (Fig. 1.2), since the cross section for electron-positron pair production increases at shorter wavelength.

1.1.2 Continuum and characteristic X-ray radiation

As a result of classical electrodynamics an accelerated electric charge radiates perpendicular to the direction of its motion (in the charge's rest frame). An electron, which interacts with the coulomb potential of the atomic core, changes its direction of motion and radiates a photon. Dependent on the primary kinetic energy of the electron the photon is emitted in the X-ray wavelength range. This process is called bremsstrahlung radiation and produces a continuous spectrum. The continuum radiation abruptly stops at λ_{min}. The corresponding photon energy is equal to the total kinetic energy of the electron. In the case of electrons which were accelerated by an electric field, the following equation applies

$$\lambda_{\text{min}} = \frac{h\,c}{e\,U} = \frac{123.4\,\text{nm}}{U\,\text{in V}}\ . \tag{1.7}$$

The intensity of the bremsstrahlung radiation is given by

$$I(\lambda) = C \, Z \frac{1}{\lambda^2}(\frac{1}{\lambda_{\mathrm{min}}} - \frac{1}{\lambda}) + B \, Z^2 \frac{1}{\lambda^2}, \quad \text{with } C >> B, \tag{1.8}$$

where C and B are specific constants for the target material. The first derivative of Eq. 1.8 determines the maximum of the bremsstrahlung radiation intensity with $\lambda_{\mathrm{max.\,Int.}} \simeq 1.5 \, \lambda_{\mathrm{min}}$.

At higher electron energies, bremstahlung radiation is superposed with a line spectrum, the so-called characteristic line spectrum. It is caused by the discrete electron shells in an atom. A fast moving electron ejects an inner shell electron. Electrons from upper shells fill the vacancies and emit an X-ray photon with a material-specific energy. In 1913 Moseley discovered the correlation between the wavelength of the emitted X-ray photon and the atomic number Z (Gerthsen et al. 1986)

$$\frac{1}{\lambda} = R_\infty \times (Z - K)^2 \times (\frac{1}{n_1^2} - \frac{1}{n_2^2}). \tag{1.9}$$

The parameter n_1 describes the inner shell that is filled by an electron from the n_2 (outer) shell. The Rydberg constant R_∞ is $1.097373 \times 10^7 \, \mathrm{m}^{-1}$ and K the shielding constant; $K \sim 1$ for the innermost electron shell (K-shell), $K \sim 7.4$ for the second (L) shell. Consequently, the characteristic X-ray lines are divided in series (K-series, L-series, M-series etc., corresponding to the filled electron shell).

The excitation of the characteristic X-ray lines cannot only be accomplished by fast moving electrons or protons which eject an electron from the inner shell. Apart from excitation due to different radioactive processes, an X-ray photon can eject an inner shell electron too. The wavelength of the incident photon has to be greater than the wavelength given in Eq. 1.9, since the inner shell electron cannot be moved into already occupied upper shell levels. Hence, the incident photon has to provide at least the ionisation energy of the corresponding electron to stimulate characteristic X-ray emission of an atom. The comparatively smooth gradient of the attenuation coefficient with respect to the energy of the photon (see Sect. 1.1.1) is violated at the absorption edges of the material where the absorption coefficient increases substantially (Fig. 1.3). Absorption edges occur in a line series as well, since the energy of the incident photon is most effectively absorbed at the transition energy from an inner shell to the continuum.

1.2   X-ray astronomy

As discussed in Sect. 1.1 X-rays are not well defined in terms of wavelength range. From a historical point of view, X-rays were subdivided on the basis of their "hardness", i.e. the capability of penetrating matter. Therefore, the term "soft X-rays" is used for long wavelength (low energy) regime, while "hard X-rays" refer to high energy photons. The separation in soft and hard X-ray is arbitrary again.

X-ray astronomy generally implies the study of physical phenomena in an energy range of approximately 0.1-100 keV. Throughout the history of X-ray astronomy different physical units have been used, and are still used. Figure 1.4 shows the correlation of the most common units in the energy range of 0.1-100 keV. Assuming that X-rays are mainly due
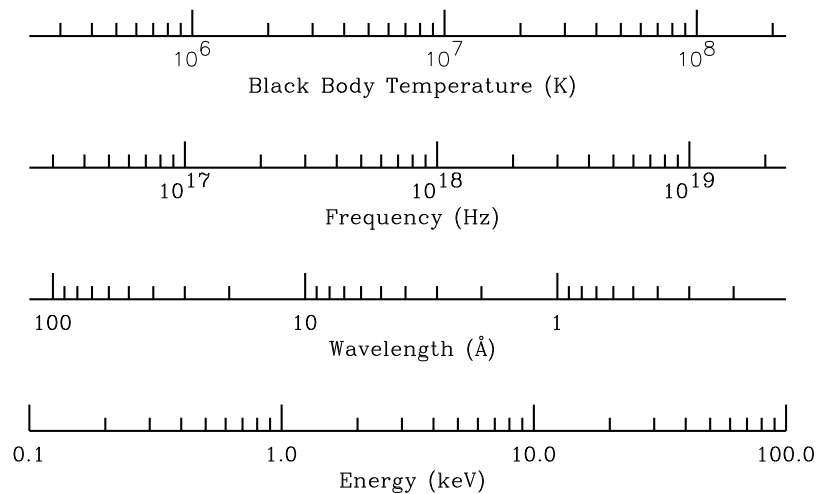
Figure 1.4: Correlation of the most common units in X-ray astronomy. The classical energy range in X-ray astronomy (lower panel), corresponding wavelength range (in Angstrom) and frequency range, as well as the associated black body temperature (top panel, assuming Wien's displacement law and the photon's energy represents the peak of the emission of a black body) are given in this plot.

to black body radiation, X-ray observations map the high temperature universe.

1.2.1 History of X-ray astronomy

Almost 70 years went by from Wilhelm Conrad Röntgen's discovery of X-rays to the first detection of an extrasolar X-ray source. X-rays cannot penetrate the Earth's atmosphere. For example, 10 cm air at sea level pressure will stop 90% of 3 keV photons (Charles & Seward 1995). Thus, X-rays from astronomical sources are not observable from the ground. However, the higher the energy, the more easily air is penetrated by X-rays; a 30 keV photon will penetrate to 35 km altitude. To observe X-rays from celestial sources it is necessary to reach high altitudes.

Balloon experiments by Hess (1912) went up to 5300 m and detected an increase of the γ-radiation with higher altitudes. Further experiments during night and day time, as well as during solar eclipses confirmed that the radiation must be of cosmic origin.

After the Second World War the Naval Research laboratory conducted experiments

onboard captured V2 rockets and detected an unexpected intensity level which was interpreted as due to X-ray emission from the Sun (Burnight 1949, Friedman et al. 1951). The detectors consisted of a photographic plate behind a beryllium filter that only allowed X-ray radiation to pass through. The discovery actually caused many scientists to lose interest in the search of X-ray sources other than the Sun. The Sun could only be detected as a bright X-ray source since it is close to Earth. Assuming a similar X-ray luminosity, the expected X-ray fluxes from nearby stars required 1960's instrumentation to be about 100,000 times more sensitive. Therefore, scientists devoted to more detailed studies of the Sun in the 1950s. The first satellite X-ray observatories were launched in 1959. Both experiments, which were designed to study the solar X-ray and UV emission, were swamped by the Van Allen Belt radiation and no useful data were obtained (Friedman 1960). The restricted payload capacity and the exceptional high G-forces during the rocket launches prevented the significant improvement of X-ray detector technologies.

Around 1960 a group at American Science and Engineering, led by Riccardo Giacconi, developed a new detector that was 100 times more sensitive than the detector used by Friedman. The experiment was intended to study X-ray fluorescence produced on the lunar surface by X-ray from the Sun and to explore the sky for other possible sources. The first launch in October 1961 was successful, but the doors, designed to protect the X-ray detectors during the launch, failed to open. In anticipation of a manned Moon landing the experiment received further support. On June 18, 1962 the second launch took place and this time two of the three X-ray Geiger counters worked well. Although the experiment failed to detect any X-ray emission from the Moon's surface, the first extrasolar X-ray source was discovered. Because of its location and intensity, Giacconi et al. (1962) excluded a scattering body belonging to our solar system. This source became known as Sco X-1 (see Figures 1.5, 1.6). In addition, in other regions of the sky explored by the detectors, the count rate did not go to zero (Fig. 1.5). Giacconi et al. (1962) concluded that a diffuse X-ray background, which increases close to the Galactic equator, is present.

After the discovery of Sco X-1 two weaker sources were found by Gursky et al. (1963). One of these was identified as the Crab Nebula by using its lunar occultation in July 1964 (Bowyer et al. 1964a). All detected sources had $f_X \sim 10^{-7} \, \mathrm{erg \, cm^{-2} \, s^{-1}}$.

Astronomers were thus forced to interpret the observations. Some of the known X-ray sources radiate ten thousand times as much energy as the Sun does. The optical identification of Sco X-1 (Sandage et al. 1966) with a 13th magnitude star suggested that unusual physical processes must occur in these objects. Among the production processes possible candidates were bremsstrahlung radiation, inverse Compton-effect with photons of star light, synchrotron radiation, thermal emission, and characteristic X-ray excitation (Giacconi & Gursky 1965, see Sect. 1.2.4).

Rocket and balloon-borne experiments were only able to observe parts of the sky. In December 1970 the first all-sky satellite survey was prepared by a group led by R. Giacconi. The satellite *Uhuru*, which orbited in a low equatorial Earth orbit to minimize the background due to particles in the Van Allen Belt radiation, had a $1° \times 10°$ field of view with proportional counters sensitive to 2-20 keV (Bradt et al. 1992). The *Uhuru* data showed that variability is a common characteristic of most bright X-ray sources. In total *Uhuru*
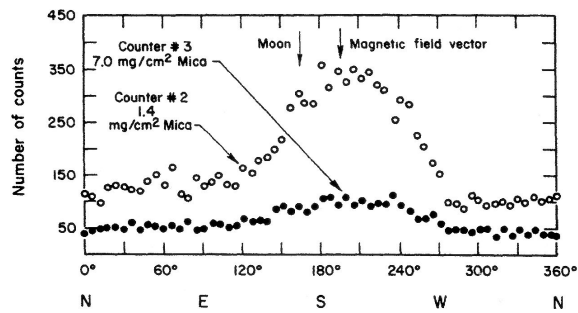
Figure 1.5: Azimuthal distribution of X-rays from the Geiger counters with two different window thicknesses (taken from Giacconi et al. 1962). The data show the existence of the discrete celestial X-ray source Sco X-1 at an azimuth $\sim 195°$ and the diffuse X-ray background. No X-ray emission from the Moon was found (the peak at the Moon's location is not significant if considering the error in the count number).
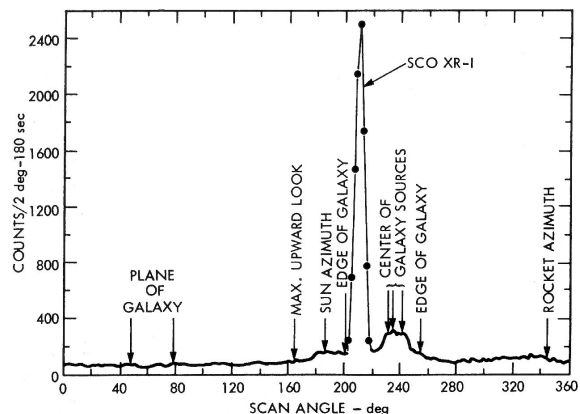
Figure 1.6: Data from a rocket-borne X-ray detector flown in October 1967 (taken from Charles & Seward 1995). The count rate of the detector is shown while it scanned a great circle containing the X-ray source Sco X-1 and a cluster of sources in the direction of the Galactic centre.

discovered 339 X-ray sources which could be partially classified as binary stellar systems, supernova remnants, Seyfert galaxies, and clusters of galaxies. The map of sources showed a significant clustering in the Galactic plane. The high degree of isotropy in the cosmic X-ray background led to the conclusion that the cosmic X-ray background must be mainly extragalactic.

Beginning in 1977 NASA launched the first series of very large scientific payloads called High Energy Astronomy Observatories (*HEAO*). Instead of using small satellites with up to 150 kg such as *Uhuru*, the launch of payloads 2.5×5.8 m in size and $\sim$3000 kg in mass offered the possibility for experiments to use large and very sensitive detectors. *HEAO-1* yielded a catalogue of 842 X-ray sources (1-20 keV) in a systematic all-sky survey which reached $f_X \sim 10^{-11}$ erg cm^{-2} s^{-1}. The measurements of the spectrum of the cosmic X-ray background between 3-50 keV could be remarkably well fitted with a thermal bremsstrahlung radiation model with a temperature of 40 keV (Marshall et al. 1980). Since no other spectral features were evident and the spectrum was not typical of previously resolved extragalactic sources, a truly diffuse emission from a hot plasma was considered. Later Gruber et al. (1999) showed a corrected spectral energy distribution ($E^2 f_{\text{Phot.}}(E)$) of the cosmic X-ray background (Fig. 1.7) with a significant peak around 30 keV.

The *HEAO-2* spacecraft *Einstein*, the first imaging X-ray telescope to orbit the Earth on a satellite, was launched in November 1978. It made use of grazing-incidence focusing optics for celestial X-ray sources, a technology that had already been used to take the first X-ray image of the Sun on October 15, 1963.

An index of refraction around unity for all materials in the X-ray regime (Greulich 1998) prevents the construction of imaging systems as in the optical wavelength range. In 1951
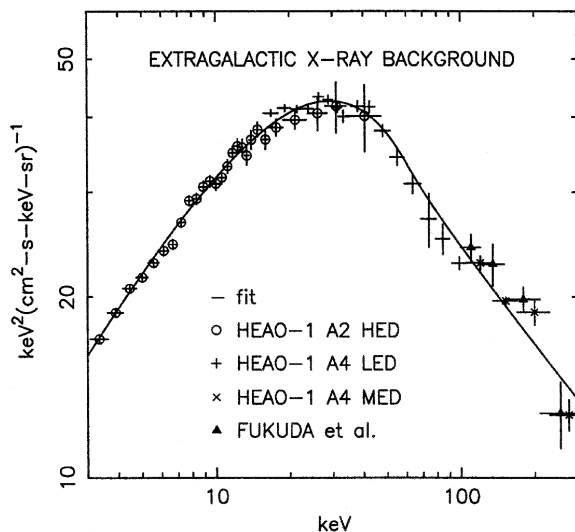
Figure 1.7: Spectral energy distribution ($E^2 f_{\mathrm{Phot.}}(E)$) of the diffuse cosmic X-ray background measured with *HEAO* by several different detectors (taken from Gruber et al. 1999).
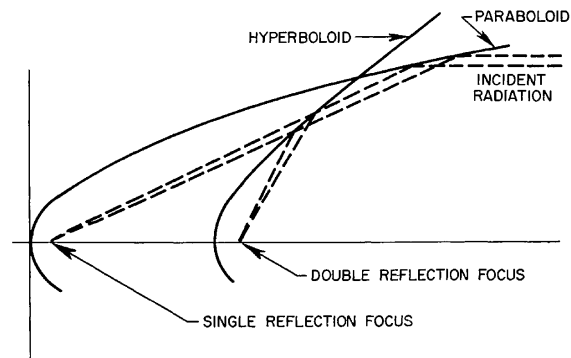
Figure 1.8: Ray path through focusing X-ray telescopes for both single reflection and double reflection systems (taken from Giacconi & Gursky 1965). For off axis radiation the single reflection system produces a circle in the focal plane, while the double reflection system still produces a point focus.

Hans Wolter analysed mirrors which had concentric figures of revolution, i.e. paraboloids, hyperboloids and ellipsoids in the context of X-ray microscopes. His primary goal was to design a system that had higher resolution than was possible in the optical wavelength regime. He showed that for a true image over an extended field of view X-rays have to undergo two reflections (Fig. 1.8) from either a paraboloid/hyperboloid or paraboloid/ellipsoid combination mounted in a coaxial and confocal arrangement (Aschenbach 1985).

The nested mirror system on *Einstein* resulted in a true in-focus image of objects and an enormous gain in sensitivity ($f_{\mathrm{X}} \sim 3 \times 10^{-14}\,\mathrm{erg\,cm^{-2}\,s^{-1}}$ in the 1-3 keV band, Giacconi et al. 1979). *Einstein's* imaging capability and high sensitivity yielded significant gain in knowledge and understanding of the X-ray universe. The high-angular resolution of a few tens of arcseconds enabled a significant improvement in X-ray counterpart determination.

A European milestone in X-ray astronomy was the first European Space Agency (ESA) launch of the three-axis pointed satellite *EXOSAT* in May 1983. With its small field of view and high sensitivity it was perfectly suited for the study of individual sources.

On June 1, 1990 *ROSAT* a German-American-British X-ray satellite was launched. It consisted of a 4-fold nested grazing incidence Wolter telescope and a smaller extreme ultraviolet telescope. The primary objective of *ROSAT*, which reached a flux limit of $f_{\mathrm{X}} \sim 10^{-15}\,\mathrm{erg\,cm^{-2}\,s^{-1}}$ in the 0.5-2 keV band, was to obtain a deep all-sky survey. At the end of its operation in 1999 it detected a total of $\sim$145.000 discrete sources (Voges et al. 2001).

1.2.2 The cosmic X-ray background

The cosmic X-ray background (CXRB) was already discovered during the first successful rocked flight by Giacconi et al. (1962). As already described in Sect. 1.2.1 the CXRB with a spectral energy distribution peak at ∼30 keV in a spectral energy distribution plot was thought to be diffuse radiation from a hot plasma (thermal bremsstrahlung radiation Marshall et al. 1980). Giacconi et al. (1979) resolved ∼25% of the 1-3 keV cosmic X-ray background observed with *Einstein* into discrete sources and concluded that a large fraction of the background indeed is due to unresolved discrete sources. The majority of their identifications were active galactic nuclei (AGN) at cosmological distances. Since the discovery of the CXRB scientists have intensely debated if its origin is really diffuse. They considered the superposition of previously unresolved X-ray sources, as well as a combination of a diffuse and discrete component.

Diffuse background radiation is a common phenomenon in all wavelength ranges (Fig. 1.9, Henry 1999). The cosmic γ-ray background radiation was already discovered by Hess (1912). By using a 20-foot horn-reflector antenna, Penzias & Wilson (1965) discovered a 3.5 K background radiation, which was isotropic, unpolarised, and free from seasonal variations within the limits of their observations. Therefore, the X-ray background seemed to be yet another diffuse cosmic background in the universe.

Uhuru revealed a high degree of isotropy in the hard 3-50 keV CXRB and demonstrated this component to be mainly extragalactic. Observational constraints and theoretical models for a discrete origin of the CXRB required a very large number of sources ($N > 10^6$ sr^{-1}, Schwartz 1980). An isothermal bremsstrahlung radiation model corresponding to an optically thin, hot plasma, and the suggested mechanism of inverse Compton-scattering by Felten & Morrison (1966) (see Sect. 1.2.4) was ruled out since it predicts a Compton-distortion in the spectrum of the microwave background, which was not observed in the spectrum obtained from the *COBE* satellite (Mather et al. 1990).

However, a discrete origin of the CXRB was also difficult to accept, since the resolved X-ray sources showed X-ray spectra that did not fit the spectrum of the CXRB. In the 3-20 keV energy range the CXRB spectrum is well approximated by a flat power law with a spectral index $\alpha \simeq 0.4$ (photon index $\Gamma \simeq 1.4$). Among the extragalactic sources found by *Einstein*, AGN were known to be the strongest X-ray emitters (Tananbaum et al. 1979) and were considered to be the prime candidates able to satisfy the energy requirements of the CXRB. However, the fact that their X-ray spectra in the 2-10 keV energy range were characterised by slopes of $\alpha \simeq 0.7$ (Turner & Pounds 1989) was the main problem for models in which most of the CXRB is due to AGN.

The breakthrough for the discrete nature of the CXRB was accomplished by deep 0.5-2 keV surveys with *ROSAT*. For the first time the vast majority (up to 80%) of the soft CXRB was resolved into discrete sources (Hasinger et al. 1998). In order to understand the populations contributing to the X-ray background complete optical identifications of sources detected in the X-ray surveys were performed. The bulk of these sources were classified as AGN (e.g. McHardy et al. 1998, Lehmann et al. 2001). It became evident that the dominating celestial emission of the 0.5-2 keV CXRB is the integrated emission
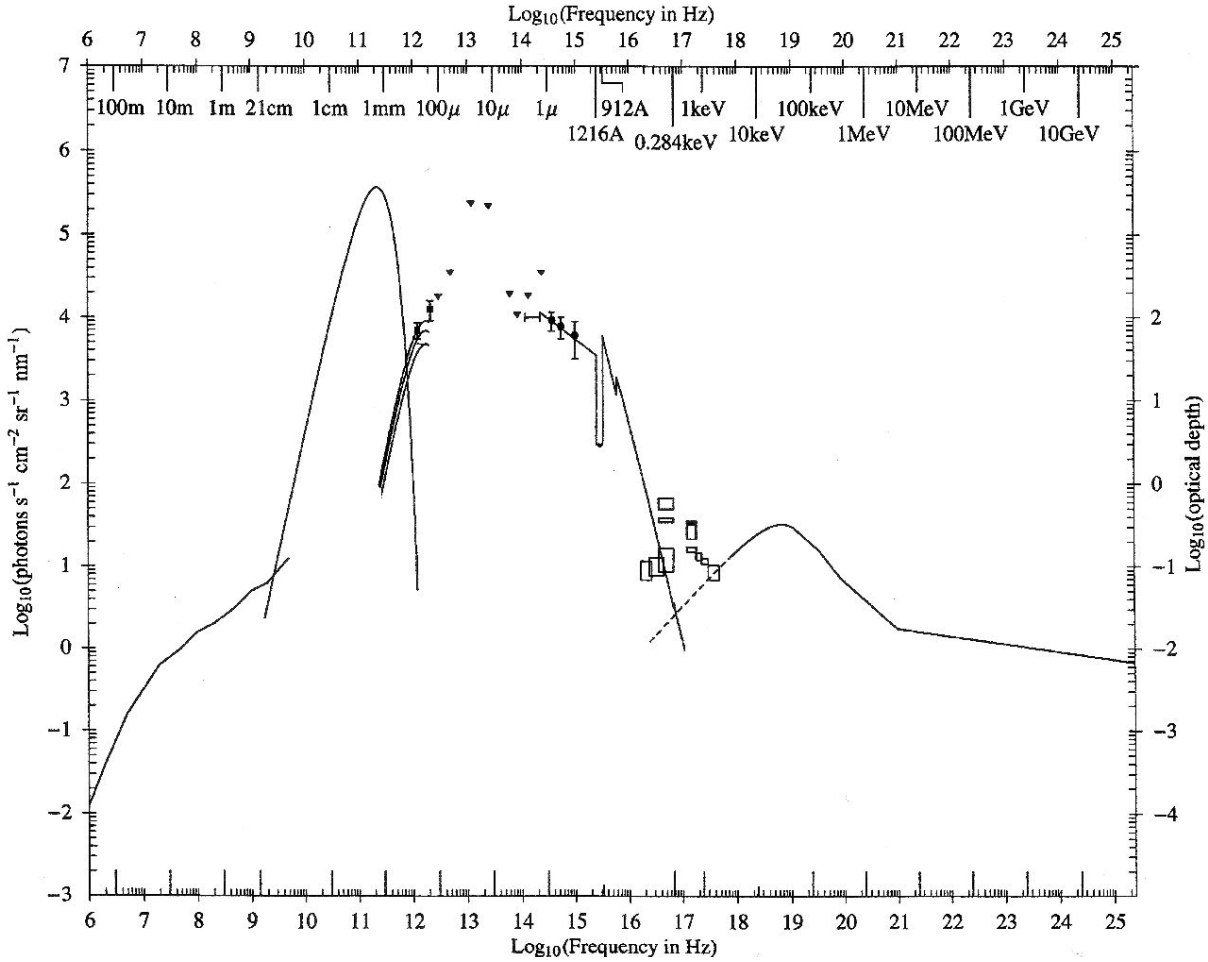
Figure 1.9: Background radiation spectrum of the universe over a wide wavelength range (from the radio to the γ-ray regime). At an energy of $\sim$30 keV the spectral peak of the cosmic X-ray background is visible. The figure is based on a plot shown in Henry (1999). Ray path through focusing X-ray telescopes for both single reflection and double reflection systems (taken from Giacconi & Gursky 1965). For off axis radiation the single reflection system produces a circle in the focal plane, while the double reflection system still produces a point focus.

of discrete sources, summed over all cosmic epochs. The deep *ROSAT* observations with limiting fluxes of $f_X = 10^{-15}\,\mathrm{erg\,cm^{-2}\,s^{-1}}$ detected an AGN sky density of $\sim$780-870 deg^{-2} (Brandt & Hasinger 2005) larger than at any other wavelength range. McHardy et al. (1998) reported a new population, galaxies with narrow emission lines (NELGs), which dominate at the faintest *ROSAT* X-ray fluxes and eventually could contribute to the CXRB. The pioneer satellite missions *ASCA* and *BeppoSAX* performed imaging X-ray surveys up to 10 keV but were both heavily source-confused due to their limited angular resolution. They resolved $\sim$30% of the 2-10 keV CXRB (limiting flux $f_X \sim 5 \times 10^{-14}\,\mathrm{erg\,cm^{-2}\,s^{-1}}$) and reached AGN sky densities of $\sim$100 deg^{-2}. The observations suggested the presence of a large fraction of absorbed and luminous AGN (Comastri et al. 2001). The absolute level
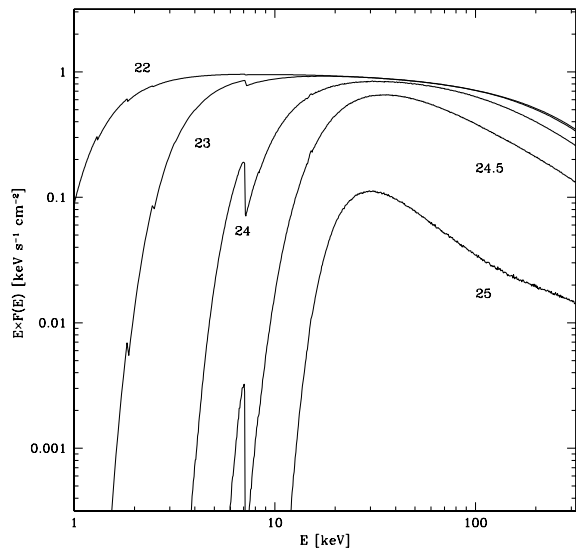
Figure 1.10: Effect of photo-electric absorption and Compton-down-scattering on the typical AGN X-ray spectrum, assuming a power law with photon index $\Gamma = 2$, plus an exponential cut-off at 300 keV (taken from Comastri 2004). The labels correspond to the logarithm of the absorbing hydrogen column density $N_{\rm H}$.
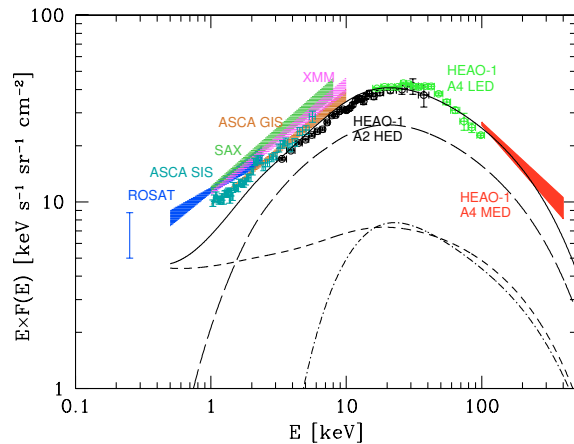
Figure 1.11: AGN contribution to the spectral energy density of the CXRB, as measured by different instruments as labelled (taken from Comastri 2004). The contributions of unabsorbed (dashed line), Compton-thin (long-dashed line), Compton-thick (dot-dashed line), and the summed emission of the different AGN populations (solid line) are shown.

of the CXRB was still a matter of debate, because different X-ray missions determined different normalisations (see Hasinger et al. 1998).

The newly obtained results also improved the theoretical understanding of the CXRB. Synthesis models based on the unification model of AGN (Setti & Woltjer 1989 and see Sect. 1.3.2) tried to explain the CXRB by a mixture of unabsorbed and absorbed AGN (Fig. 1.10), modelling with the corresponding luminosity function and its cosmological evolution (Comastri et al. 1995). The models predicted that about 85% of the radiation produced by the accretion onto super-massive black holes have to be absorbed (Fabian & Iwasawa 1999) and a substantial contribution to the CXRB comes from high-luminosity, absorbed X-ray sources, such as type II QSOs (quasi-stellar objects). However, these models encountered a number of challenges. Type II QSOs had only scarcely been detected. The evolution of absorption over cosmic time, as well as the dependence of absorption on the intrinsic luminosity were free parameters.

The current X-ray satellite missions *XMM-Newton* and *Chandra* improved the sensitivity and angular resolution in the 0.2-12 keV energy range. They enabled the study of absorbed X-ray source populations that were predicted by the CXRB synthesis models. Instead of finding a large number of absorbed, high-luminosity QSO, a large population of absorbed, low-luminosity X-ray sources at low redshifts were found (Hasinger et al. 2001). The missing CXRB radiation turned out to be foreground radiation from narrow emission line galaxies which harbour obscured AGN. Further deep X-ray surveys, e.g. Barger et al.
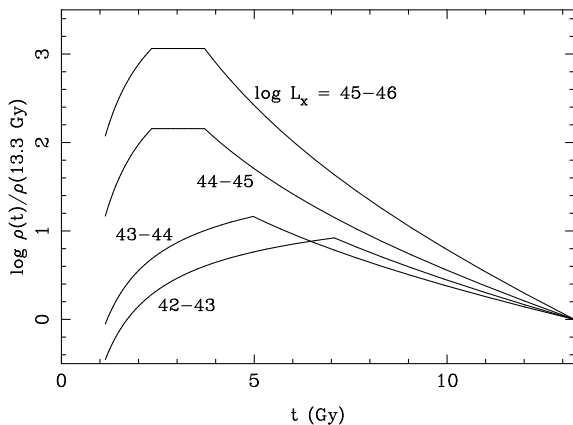
Figure 1.12: Co-moving density of type I AGN (selected from soft X-ray) versus cosmic time. The x-axis represents the age of the universe. The plot is taken from Hasinger et al. (2005).
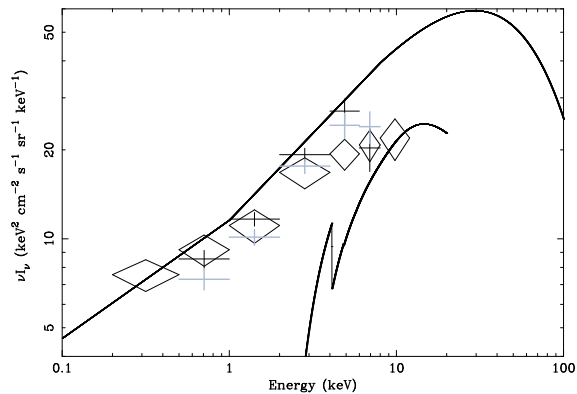
Figure 1.13: Current status of the resolved fractions of the CXRB (taken from Worsley et al. 2005). The upper curve shows the total CXRB. The intensity resolved into sources in the CDF-N, CDF-S and XMM-Lockman Hole are shown as black crosses, grey crosses, and black diamonds, respectively. The lower curve shows the spectrum of the best-fitting model for the missing AGN. In reality the missing population will be a mixture of sources at different redshifts and with different levels of absorption which will smear out the sharp feature at 4 keV.

(2003), increased the sample size of this X-ray population and confirmed the result. The absorption ranges from $10^{21} < N_H/\,cm^{-2} < 10^{24}$ (Compton-thin absorption). However, to explain the spectral peak of the CXRB synthesis models require a large number of even more heavily absorbed sources, so-called Compton-thick objects which are absorbed by column densities of $N_H > 1.5 \times 10^{24}\,cm^{-2}$ (Fig. 1.11). *XMM-Newton* and *Chandra* detected these sources in the local universe (Comastri 2004). Although there is evidence of a large fraction of Compton-thick AGN at high redshift (Martínez-Sansigre et al. 2007), no securely confirmed Compton-thick object has been found so far at high redshifts.

The current understanding of the CXRB is the following. The CXRB is the summed emission from point sources, principally AGN, over cosmic time. Source populations with different amounts of absorption are needed to explain the peak of the CXRB at ∼30 keV (Fig. 1.11). Recent observations constrain the parameter space of the different X-ray source populations in the synthesis models. Evolution effects, such as the luminosity-dependent evolution of soft X-ray selected AGN (Fig. 1.12, Hasinger et al. 2005), are reliably derived and help to improve the theoretical understanding of the CXRB.

While the CXRB is resolved to ∼85% and ∼80% in the 0.5-2 keV and the 2-10 keV energy bands respectively, it is only resolved by ∼50% above 6 keV (Worsley et al. 2005). The decrease in resolved fraction at energies ≳4 keV is present in *Chandra* and *XMM-*

Newton data (Fig. 1.13). The missing fraction has a spectral shape that is consistent with a population of faint, heavily absorbed AGN. Deep *Chandra* and *XMM-Newton* data, as well as stacking analysis have failed so far to detect this source population. Future X-ray missions will be able to map the energy range of the CXRB's peak and hopefully reveal the origin of the radiation.

1.2.3   Current and future X-ray missions

The most important current X-ray missions are the European X-ray satellite *XMM-Newton* and the American X-ray satellite *Chandra*.

Chandra was launched with the Space Shuttle Columbia on July 23, 1999. It consists of four pairs of nested iridium-coated mirrors with an aperture diameter of 1.2 m and is equipped with four science instruments, an advanced CCD imaging spectrometer (ACIS), a high resolution camera (HRC), high resolution grating spectrometers (HETGS) and low energy transmission grating spectrometer (LETGS). *Chandra* operates in an energy range of 0.1-10 keV and has an effective area of $\sim$800 cm^2 at 1.5 keV. It's huge advantage is a spatial resolution of less than 1 arcsec.

XMM-Newton was launched on December 10, 1999 with an Ariane 5. It consists of three X-ray mirror modules. Each has 58 nested gold-coated mirrors with an outer diameter of 0.7 m. Two telescope modules have reflection grating arrays as well as a CCD camera (EPIC MOS camera). The third telescope module is only equipped with a CCD detector (EPIC PN detector). In addition, *XMM-Newton* has an 0.3 m optical-ultraviolet telescope aligned with the X-ray telescopes onboard. The operational energy range of the X-ray instruments is 0.1-12 keV. *XMM-Newton* has a spatial resolution of $\sim$5 arcsec, but a much larger effective area compared to *Chandra* ($\sim$4300 cm^2 at 1.5 keV). Therefore, *XMM-Newton* is perfectly suited for X-ray spectroscopy and time-resolved observations. *Chandra* and *XMM-Newton* utilize different designs and complement one another well.

In the near future *Spectrum-X-Gamma* will be launched. It consists of various instruments, and is an international collaboration. One instrument will be *eRosita*, a telescope array of seven Wolter-I systems each with 54 nested mirror modules. The instrumental sensitivity is similar to *XMM-Newton*. *eRosita* will perform an all-sky survey up to 10 keV. It is expected to discover $\sim$10^6 new AGN and $\sim$10^5 galaxy clusters. Further instruments planned on *Spectrum-X-Gamma* will be the all-sky-monitor *LOBSTER* and the high energy X-ray telescope *ART*.

With respect to the remaining issues of the CXRB, the most interesting energy range in the X-ray regime is $\sim$30 keV where the spectral energy distribution peak of the CXRB occurs. As technologies improve, future missions will be able to observe this energy regime.

NASA is currently considering to launch a single X-ray observatory with four identical coaligned X-ray telescopes named *Constellation X*. Each telescope will have a focal length of 10 m and a diameter of 1.3 m. It will be able to operate in an energy range of 0.3-40 keV. ESA plans to launch the X-ray evolving universe spectrometer (*XEUS*) which will consist of two separate spacecraft, a mirror spacecraft and a detector spacecraft, that will orbit at

Earth's 2nd Lagrange point. *XEUS* will be 100 times more sensitive than *XMM-Newton*. It is expected to have an energy range of 0.1-40 and an effective area of $3\,\mathrm{m}^2$ at $7\,\mathrm{keV}$ and $0.1\,\mathrm{m}^2$ at $40\,\mathrm{keV}$. The spatial resolution will be comparable to *XMM-Newton* or better.

1.2.4 The origin of X-rays in astrophysics

In this section I briefly summarise the five dominant physical processes that produce X-ray radiation in astrophysical objects. Since the spectral signature of each is unique, a measurement with sufficiently high spectral resolution over a broad energy range allows one to deduce the X-ray emission process (see the spectra of three processes in Fig. 1.14). However, more than one production mechanism is usually involved for the same source.

black body radiation A body which lacks both transmission and reflection will absorb all electromagnetic radiation incident upon it. At thermal equilibrium, the emissivity of a surface equals its absorptivity (Kirchhoff's law). The spectrum radiated is a well-defined continuum with a spectral peak emission dependent only on the temperature of the body. The form of the spectrum is given by

$$B_\nu\left(T\right) \;=\; \frac{2\,h\,\nu^3}{c^2}\,\frac{1}{e^{\frac{h\nu}{kT}}-1} \tag{1.10}$$

$$B_\lambda\left(T\right) \;=\; \frac{2\,h\,c^2}{\lambda^5}\,\frac{1}{e^{\frac{hc}{\lambda kT}}-1} \tag{1.11}$$

where h is Planck's constant, c the speed of light, and k Boltzmann's constant. The relationship between the temperature T of the black body, and the wavelength λ_{max} at which the maximum of the intensity of the radiation occurs is given by Wien's displacement law

$$\lambda_{max}\,T = const. = 2.898 \times 10^7 \;\text{Å K} . \tag{1.12}$$

If an astrophysical object has a surface temperature of one million degrees or higher, it will emit black body radiation with photons in the X-ray range (see Fig. 1.4). Isolated neutron stars for example, are expected to have a surface temperature of the order of $10^7\,\mathrm{K}$ (Cameron 1959). Therefore, Bowyer et al. (1964b) proposed thermal emission as the source of X-ray emission from neutron stars.

bremsstrahlung radiation A hot, optically thin gas will emit bremsstrahlung radiation. The atoms of the gas are ionised. Due to collisions, positive ions and negative electrons have the same averaged energy (thermal equilibrium) which is only determined by the temperature. Bremsstrahlung radiation occurs as a result of the deflection of moving electrons by the positive ion. The strong electric force causes a change in the electron's trajectory. Every acceleration of a charged particle such as electrons causes the emission
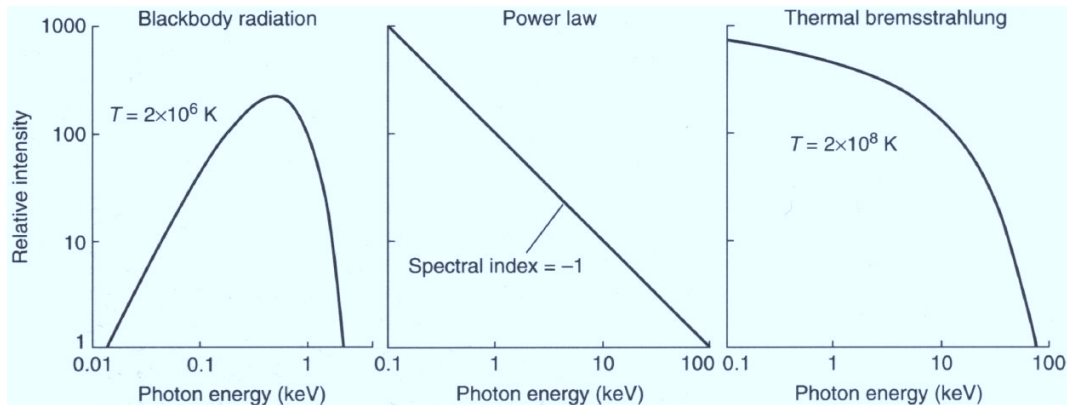
Figure 1.14: Three basic spectral forms expected from astrophysical processes (taken from Charles & Seward 1995). At the left is the blackbody spectrum expected from a dense object at a temperature of 2×10^6 K. At the centre is a power law spectrum expected from synchrotron radiation produced in a region containing a magnetic field and high energy electrons. At the right a thermal bremsstrahlung radiation spectrum from a thin, very hot gas is shown (without characteristic X-ray emission).

of electromagnetic radiation. In the case of thermal equilibrium the electrons have a well-determined distribution which is characterised by the Maxwell-Boltzmann distribution.

The spectral energy distribution of the 'thermal bremsstrahlung radiation' is determined by the temperature of the plasma. The higher the temperature, the faster the motion of the electron and the higher the energy of the photon that is radiated. The form of the spectrum is given by

$$B_\nu (T) = a\, G\, Z^2\, n_{\text{elec}}\, n_{\text{ion}}\, \frac{e^{-\frac{h\nu}{kT}}}{(kT)^{1/2}} \tag{1.13}$$

where a is a constant, G the Gaunt factor (to correct the classical treatment for quantum-mechanical effect), Z the charge of the positive ions, and $n_{\text{elec}}\, n_{\text{ion}}$ the product of the electron and positive ion density. Above a plasma temperature of 10^6 K the majority of the radiation is emitted as an X-ray continuum due to the process of bremsstrahlung radiation.

The intracluster medium of clusters of galaxies reaches temperatures of $10^7 - 10^8$ K caused by gravitational heating. Therefore, it becomes fully ionised and emits via thermal bremsstrahlung radiation in the X-ray band.

inverse Compton-scattering In Sect. 1.1.1 the Compton-effect as a physical interaction process between X-rays and matter was described. Instead of transferring energy from the photon to the electron ('normal' Compton-effect), the inverse Compton-effect describes the transfer of energy from an electron to the photon. The fast electron (a few MeV) collides with a photon of a few eV and gives part of its energy to the photon which is scattered

to a shorter wavelength.

The process of inverse Compton-scattering can produce the high energy X-ray and γ-ray radiation from AGN (Dermer et al. 1992). The accretion disk surrounding the super-massive black hole is believed to produce a thermal spectrum peaking in the UV and is enclosed by a corona of relativistic electrons. The inverse Compton-scattering of these electrons with photons in the optical and UV-range causes the X-ray emission (for details see Sect. 1.3.3).

The same effect is observed when photons from the cosmic microwave background inter-act with the high-energy electrons of the hot gas of a galaxy cluster. The cosmic microwave background photons are scattered to higher energies, resulting in the Sunyaev-Zeldovich effect.

synchrotron radiation   Synchrotron radiation is produced by relativistic electrons that move in a magnetic field. The magnetic field exerts a force perpendicular to the direction of motion. Hence the electron is accelerated and emits radiation. The frequency of the emitted photon depends on the energy of the electron, the magnetic field strength, and the direction of motion to the magnetic field B.

For non-relativistic velocities the radiation is called cyclotron radiation and the fre-quency of emission is simply the frequency of gyration in the magnetic field (Rybicki & Lightman 2004). The spectrum consists of a single line. When the electron speed v/c increases, higher harmonics of the fundamental frequency are observable. More and more harmonics with increasing contributions to the total spectrum occur. For a relativistic particle ($v \sim c$) the superposition of all these harmonics gives a continuous frequency spectrum which is called synchrotron radiation.

In astrophysical objects the particle velocities are expected to be isotropic and the magnetic field somewhat aligned. The usual spectral form assumed for electrons is a power law, and so the spectrum of the resulting synchrotron radiation is a power law as well (Charles & Seward 1995). Synchrotron radiation is always polarised. The observation of a power law spectrum with polarisation is usually a proof of synchrotron emission. Aschenbach & Brinkmann (1975) showed that the Crab Nebula is one example of X-ray emission due to synchrotron radiation. Synchrotron X-rays indicate the existence of very energetic electrons.

There are two special cases that can occur with the process of synchrotron radia-tion: synchrotron self-Compton-scattering and synchrotron self-absorption. In the case of synchrotron self-Compton-scattering the low energy photons, produced by a relativistic electrons moving in a magnetic field, interacting again with relativistic electron plasma, are inverse Compton-scattered toward shorter wavelength. The effect of synchrotron self-absorption is observed at a certain frequency where the absorption coefficient is significantly increasing. The electron plasma absorbs the synchrotron radiation that was produced by it below a critical frequency (turnover frequency). For synchrotron photons with frequen-cies higher than the critical frequency the plasma stays optically thin and synchrotron self-absorption does not occur.

characteristic X-ray excitation Monochromatic X-ray radiation is produced by the K-series transition following a K-shell ionisation (see Sect. 1.1.2). This process occurs in collisions of a substantial flux of high energy with elements heavier than hydrogen (except at very high temperatures when the atoms are completely ionised). Since the conditions for this process are similar to bremsstrahlung radiation, the characteristic X-ray radiation is superimposed on the continuous X-ray spectrum of bremsstrahlung radiation from a hot gas.

Acton (1965) mentioned already in the beginning of X-ray astronomy that characteristic X-ray excitation may make an important contribution to the X-ray emission of solar flares. Another process causing line emission is X-ray fluorescence (see Sect. 1.3.3).

1.3 Active Galactic Nuclei

After World War II scientists and engineers engaged in wartime radar projects used their knowledge and followed up the pioneering works of Karl Jansky in the 1930s. Thus, radio dishes and interferometers appeared in many astrophysical institutes and revealed the existence of cosmic radio sources. The optical identification of the radio source Cygnus A was the key observation to support the extragalactic origin of radio sources. One of the early catalogues of radio sources is the Third Cambridge Catalogue which was published in 1959 by members of the Radio Astronomy Group of the University of Cambridge. The sources were listed in increasing order of right ascension and with the prefix 3C.

During the study of the angular sizes of radio galaxies, astronomers found most sources in a range of several tens arcseconds to a few arcminutes. However, a few sources had a diameter of only a few arcseconds. The optical identification of 3C 48, which was one of the sources with less than one arcsecond angular size, led Smith & Hoffleit (1961) to the assumption that this object may be, apart from the Sun, the first known radio star. They interpreted the non-thermal radio emission, optical variability, and the optical spectrum of these star-like objects as remnants of a nova, as well as supernova explosions. Lunar occultations helped to fix the positions of the radio sources very accurately in the sky. More star-like objects were found. Schmidt (1963) discovered that the spectrum of the 13th magnitude bright optical counterpart of 3C 273 was redshifted by about 16%. At the same time, Greenstein & Matthews (1963) derived from a newly obtained spectrum of 3C 48 a redshift of $z = 0.367$ which was the highest redshift at the time. These observations clearly revealed the extragalactic origin of these quasi-stellar radio sources, so-called quasars.

Burbidge & Burbidge (1967) specified the following quasar criteria: star-like object identified with a radio source, variable light, large ultraviolet flux, broad emission lines in the spectra, and high redshift. Later surveys of objects, that had a UV excess, found a large number of objects which had no radio couterparts, so-called quasi-stellar objects (QSOs). Only 15%-20% (Urry & Padovani 1995) of the sources were found to be radio-loud. In these objects powerful jets and the induced lobes are contributing to the AGN's

luminosity. Radio-quiet objects do not show jet-related emissions.

The most mysterious aspect of all these sources is the very high luminosity which must be produced in a very small volume. Quasars and QSOs are the most luminous systems known in the universe which exist for a significant period of time. Gamma-ray bursts might be more luminous but they are rapidly fading. Besides other considered physical processes, Salpeter (1964) and Lynden-Bell (1969) suggested accreting super-massive (several million solar masses) black holes as central engine of quasars and QSOs. Accretion of matter into a relativistically deep gravitational potential is one of the few processes in nature efficient enough to produce such luminosities without having to process unreasonably large amounts of mass.

1.3.1 The Zoo of Active Galactic Nuclei

The term active galactic nuclei (AGN) is a genus for the huge diversity of objects that are considered to be powered by accretion onto super-massive black holes - hence their compact region at the centre of a galaxy has usually a much higher luminosity than the host galaxy. From a historical point of view, the objects were discovered in different frequency ranges. Studies and initial classification schemes in the optical, radio, and X-ray regime led to a large number of different, very confusing terminologies for AGN. In the beginning of AGN research, scientists did not realise the possible connections between differently classified subgroups of AGN. A short overview of the properties of the most important types of AGN will be given here. For more details see Blandford et al. (1990) and Kembhavi & Narlikar (2000). I will follow the convention to divide AGN into two classes, radio-quiet and radio-loud objects. Kellermann et al. (1989) found that AGN from the Palomar Bright Quasar Survey, spanning a range over nearly 10^4 in optical luminosity, separate into radio-quiet and radio-loud objects. He suggested radio-quiet objects to have a radio-to-optical flux ratio of $R_{\rm R/Opt} < 1$, where

$$R_{\rm R/Opt} = \frac{f_\nu(5\,{\rm GHz})}{f_\nu(4000\mathring{A})}. \tag{1.14}$$

The different object classes are given in order of increasing optical luminosity.

radio-quiet AGN

Low-ionisation nuclear emission line regions (LINERs) These objects appear in their optical spectra as normal galaxies with strong and narrow emission lines of elements with low ionisation state (O I, N II). They were first identified by Heckman (1980). LINERs are commonly found in almost half of all spiral galaxies (Ho et al. 1993). The driving mechanisms are disputed (Véron-Cetty & Véron 2000) and include stellar effects and very low accretion of super-massive black holes.

Seyfert galaxies This group of AGN was discovered by Carl Seyfert (1943). A Seyfert galaxy in the optical is usually a normal spiral galaxy with respect to its morphol-

ogy, but with an additional point source in its core (McLeod & Rieke 1995, Sarajedini et al. 1999), which corresponds to the active core region.

Based on accurate observations of the emission lines Khachikian & Weedman (1974) divide this object class in two sub-classes - Seyfert I and Seyfert II. The optical spectrum of a Seyfert I galaxy shows strong broad permitted emission lines (10^3 km/s $< v < 10^4$ km/s) and narrow (a few 10^2 km/s) forbidden lines. In the case of a Seyfert II galaxy no broad emission lines are found in the spectrum. Only narrow emission lines (a few 10^2 km/s) for permitted and forbidden transitions are present. The division in line width between Seyfert I and II is not well determined in the literature. Different line width criteria have been applied to distinguish between the two classes. The specific FWHM criteria range from 1000 (e.g., Weedman 1977) up to 2000 km/s (e.g., Steidel et al. 2002). Hao et al. (2005) provided a formal separation criterion by showing the width distribution of the Hα line is strongly bimodal among AGN, with a significant dip at FWHM(Hα)=1200 km/s. Véron-Cetty & Véron (2000) state that the number of known Seyfert II galaxies is larger than the known population of Seyfert I galaxies. Osterbrock (1981) found objects with spectral properties intermediate between Seyfert I and Seyfert II and established a new group of Seyfert 1.5, 1.8, and 1.9 based on the line widths of Hα and Hβ.

Quasi-stellar objects (QSOs) These are essentially more luminous versions of Seyfert I and Seyfert II galaxies. They are also divided in type I and type II QSOs based on the emission line properties in their optical spectra (see Seyfert galaxies). Despite their high intrinsic luminosities type II QSOs are difficult to identify. A significant fraction of the emitted power gets absorbed. Furthermore, their lack of emission lines in a wide optical wavelength range hampers their identification. Kleinmann et al. (1988) discovered the first type II QSOs. About 150 optically selected type II QSOs from the Sloan Digital Sky Survey were studied in Zakamska et al. (2003).

To separate Seyferts from QSOs, Schmidt & Green (1983) somewhat arbitrarily define a QSO as an object with an absolute B-band magnitude of $M_B < -23$. QSOs are found most frequently in elliptical host galaxies, but spirals as well can host QSOs (McLure et al. 1999, Bahcall et al. 1997).

radio-loud AGN

radio galaxies These object show nuclear (jet) and extended radio emission (lobes). With respect to their optical spectra radio galaxies exist in two types, broad line radio galaxies (BLRGs) and narrow line radio galaxies (NLRGs). They are the radio-loud counterparts to Seyfert I and Seyfert II galaxies. Their luminosities are comparable to Seyfert galaxies as well. However, radio galaxies differ in some aspects from radio-quiet Seyfert galaxies. For example the hosts of radio galaxies are primarily elliptical galaxies.

BL Lac objects This object class is distinguished by rapidly variable, polarised optical, radio and X-ray emission. The first object in the class of BL Lac objects was the "variable star" BL Lacertae which was identified as a radio source. Oke & Gunn (1974)
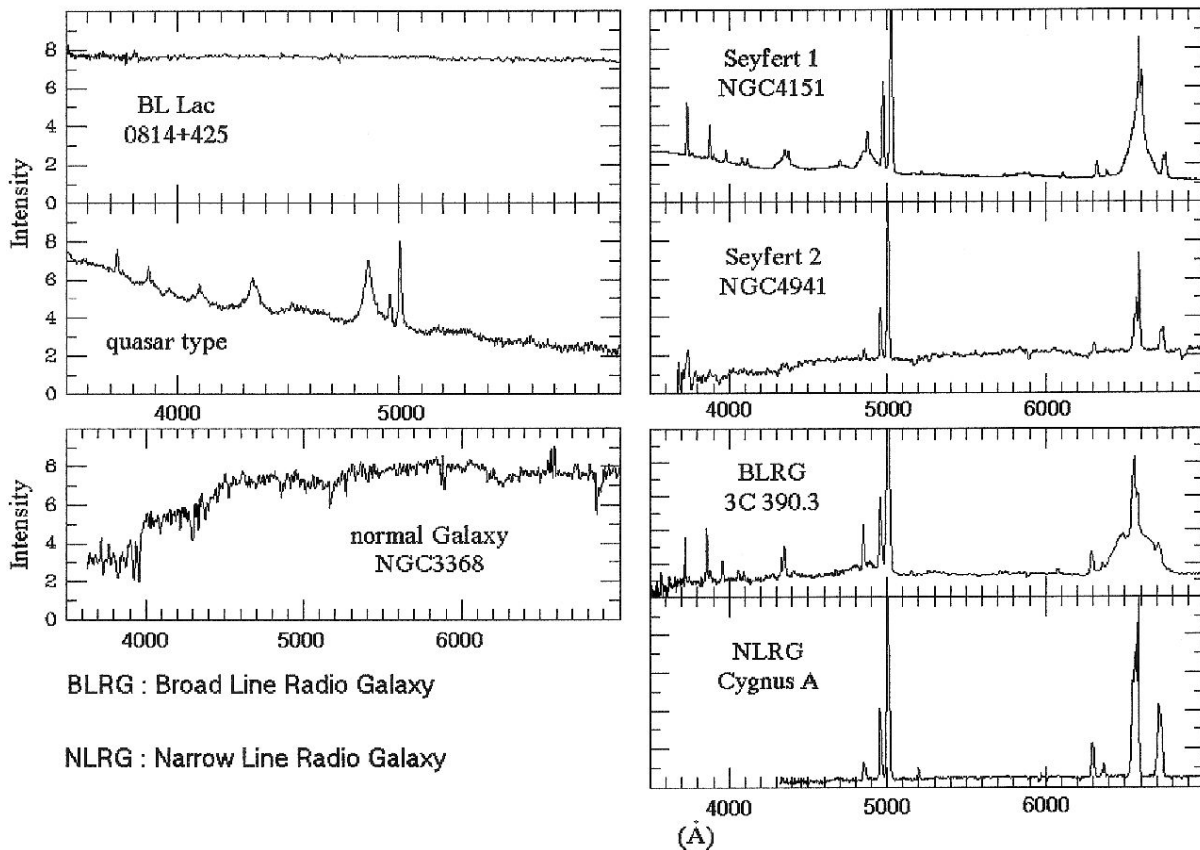
Figure 1.15: Optical spectra for different AGN types. The x-axes are in units of Å. For illustration purposes an optical spectrum of a normal galaxy, which harbours usually no AGN, is shown. However, the X-ray source population class of X-ray bright optically normal galaxies (XBONGs, see Sect. 3.5.3) may be an exception, where the AGN does not reveal itself in the spectrum of the host galaxy. The figure is based on a plot from http://nrumiano.free.fr/Images_gx/spectra_agn_E.gif.

determined it to be of extragalactic origin. The optical spectrum of a BL Lac object has no or only weak emission or absorption lines. BL Lacs show variability on timescales of only a few days, and a high degree of polarised light that can also vary.

Quasars This are the radio-loud counterparts to quasi-stellar objects (QSOs) with the addition of emission from a jet. Thus they show strong optical continuum emission, as well as broad and narrow emission lines (see QSOs).

1.3.2 Unification Model of Active Galactic Nuclei

The current understanding of the collective properties of AGN is summarised by the so-called unification models. Antonucci (1993) and Urry & Padovani (1995) explain the variety in observed properties of AGN primarily by orientation and intrinsic luminosity.
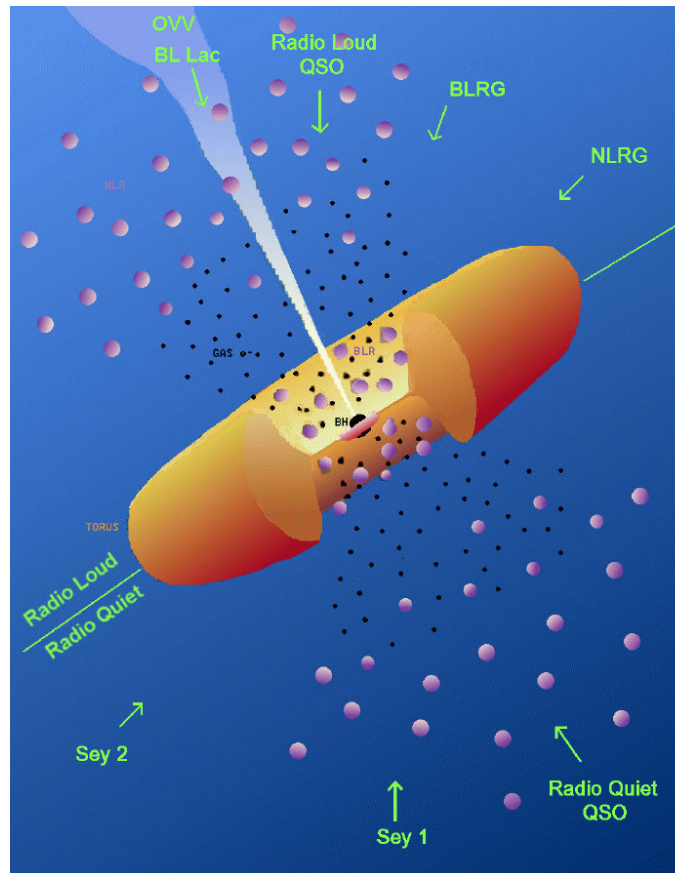
Figure 1.16: Schematic diagram of the unification model for AGN. The central super-massive ($\sim 10^6 - 10^9 \, M_\odot$) black hole is surrounded by a luminous accretion disk. Depending on the viewing angle a thick dusty torus may obscure the clouds in the broad emission lines, which are orbiting in the immediate vicinity of the black hole, as well as the accretion disk itself. Narrow emission lines are produced in clouds much farther from the central source. A jet may originate in the immediate vicinity of the super-massive black hole (upper left side) and the AGN will be observable as a radio-loud AGN (BL Lac or OVV - optically violent variable AGN). The absence of a jet will result in a radio-quiet AGN (lower right side). The figure is taken from the *BeppoSAX* calendar and is based on a plot by Urry & Padovani (1995) and modified by M. Polletta.

In the unification scheme every AGN type is intrinsically the same object. It is powered by a super-massive ($\sim 10^6$-$10^9 \, M_\odot$) black hole in the centre and a surrounding accretion disk which extends up to a few parsec. Due to different Kepler velocities and viscosity the accretion disk is heated. The disk emits most of its energy in the UV and soft X-ray regime.

Broad emission lines are produced in clouds orbiting the accretion disk and likely by the disk itself (Urry & Padovani 1995, see Fig. 1.16). The clouds in the so-called broad line region (BLR) are photo-ionised by the UV/soft X-ray radiation of the accretion disk and move with velocities of a few 10^4 km/s. Through reverberation mapping

(Netzer & Peterson 1997, Peterson & Wandel 2000) it is possible to determine the dimension of the BLR, which varies between few light-days ($R \sim 10^{13}$ m) and several light-weeks ($R \sim 10^{14}$ m, Kaspi et al. 2000).

A thick dusty torus extending to ≥ 100 pc (Elitzur et al. 2004) with temperatures of $T \sim 1000$ K encloses the central engine. It obscures the broad line region from transverse lines of sight and re-emits in the infrared wavelength range. At distances of $\sim$10-1000 pc slow-moving ($v \leq 1000$ km/s) clouds are orbiting the central source. This region is called narrow line region (NLR).

In the case of a radio-loud AGN a jet emanates from the region near the black hole and extends out to several 10^6 pc as an additional component (see upper-left corner of Fig. 1.16). A jet consists of an outflow of high energy particles. The particles form a collimated plasma, which moves with relativistic speed and emits synchrotron radiation. If the jet is almost parallel to the line of sight, the jet becomes a significant contribution in the observed spectrum and an the object will be classified as BL Lac object or flat spectrum radio quasar.

If the viewing angle on this axis-symmetric geometry is such that the innermost region is directly observable, the optical spectrum is characterised by a strong blue continuum and broad emission lines (Seyfert I type). These high ionisation emission lines are produced in the BLR. The motion of a large number of clouds with a few 10^4 km/s causes Doppler-broadening of the emission lines.

If the line of sight to the nucleus and the BLR passes through a sufficient amount of obscuring material in the torus, the observed spectrum is dominated only by narrow emission lines. The slow-moving, low density clouds in the NLR produce the narrow forbidden emission lines.

The luminosity of the AGN is dependent on its mass accretion rate $\dot{M}$. This implies that AGN of both Seyfert types exist in a wide range of observable luminosities. The unification model therefore predicts the existence of a large number of high-luminosity obscured AGN (type II QSOs). Based on available SDSS spectra, Zakamska et al. (2003) proved their common existence.

In the present work, I will refer to type I and type II AGN. These terms correspond to the Seyfert type which is based on the optical spectrum. An object with broad permitted and narrow forbidden emission lines is classified as type I AGN, while a type II AGN is an objects that shows only narrow forbidden emission lines in its optical spectrum.

The terminology QSO will be used in the present thesis for an AGN with a high intrinsic luminosity. In the optical the conventional dividing line between Seyfert galaxies and QSOs is $M_{\mathrm{B}} = -23$. However type II QSOs are more efficiently found in follow-up observations of X-ray surveys (Szokoly et al. 2004; Mainieri et al. 2002; Krumpe et al. 2007c; Barcons et al. 2007; Tedds et al. 2007). The definition of type II QSOs is therefore somewhat arbitrary. Zakamska et al. (2003) define a type II QSO only based on its optical properties, while Mainieri et al. (2002) use the term "type II QSO" for an object with an intrinsic X-ray luminosity of $L_{\mathrm{X_{INT}}} > 10^{44}$ erg/s (0.5-10 keV) and an absorbing hydrogen column density of $N_{\mathrm{H}} > 10^{22}$ cm^{-2}.

Throughout this thesis I use the definition of a type II QSO to be an object with narrow forbidden and narrow permitted emission lines in the optical spectrum, as well as a de-absorbed intrinsic X-ray luminosity $L_{X_{INT}} > 10^{44}$ erg/s (0.5-10 keV band). Hence, the type II classification is strictly based on the optical spectrum.

Recent Observations and Outlook on the Unification Model

Part of the great diversity of AGN classes is explained by the unification model. As described in Section 1.3.2, the central source is an accreting super-massive black hole that is surrounded by a dusty torus.

However, puzzling results have emerged from recent IR observations. The obscuring dust in AGN must re-radiate the absorbed radiation at longer wavelengths. The $10\,\mu$m torus emission in NGC 1068 was observed with VLTI interferometry by Jaffe et al. (2004). Their analysis reveal a central hot component (dust temperature $T > 800$ K) and a cooler dust component ($T = 320$ K) which extends up to $r \simeq 1.7$ pc. The presence of a dust temperature of only $\sim$300 K so close to the AGN is a fundamental problem. NGC 1068's intrinsic luminosity of $L_{AGN} \sim 2 \cdot 10^{45}$ erg/s (Mason et al. 2006) leads to a dust temperature of 960 K at $r = 2$ pc. A temperature of 320 K is expected only at $r = 26$ pc and not at $r \simeq 1.7$ pc as Jaffe et al. (2004) report.

Another puzzle is the observed similarity between the IR emission from type I and type II AGN. The main conclusion of the unification model assumes that the torus obscuration is highly anisotropic. However, Lutz et al. (2004) surprisingly showed that the IR emission seems to be nearly isotropic. On the basis of the $6\,\mu$m emission normalized to the intrinsic 2-10 keV X-ray emission, type I and type II AGN are identical within the errors. Horst et al. (2006) reached the same conclusions when they used $12\,\mu$m emission.

Furthermore, as widely reported in literature, 5-20% of all AGN have different obscuration indicators in the X-rays and in the optical, such as X-ray absorbed type I AGN (e.g. Comastri et al. 2001; Brusa et al. 2003; Akiyama et al. 2003) or X-ray unabsorbed type I AGN (e.g. Panessa & Bassani 2002; Caccianiga et al. 2004; Wolter et al. 2005; Tozzi et al. 2006). The spectroscopic analysis of 117 serendipitous sources in the HELLAS2XMM 1dF survey by Perola et al. (2004) found about 10% of the identified broad line AGN have an X-ray absorption of $N_H > 10^{22}$ cm^{-2}. X-ray and optical transitions between type I and type II AGN are observed as well. Cohen et al. (1986) and Tran et al. (1992) report on extreme spectral variations in Seyfert galaxies Markarian 1018 and Markarian 993 and even the transition of a classical type II AGN toward a type I AGN is observed in NGC 7582 (Aretxaga et al. 1999). Variability of the X-ray absorbing gas was also found to be common in AGN on timescales from months to years (Risaliti et al. 2002). Recent observations by Lamer et al. (2003) (NGC 3227) and Risaliti et al. (2007) (NGC 1365) derive N_H variability on the timescale of days.

These discrepancies must be resolved by adapting the unification model, which successfully explains the majority of the observations. A promising approach substitutes the
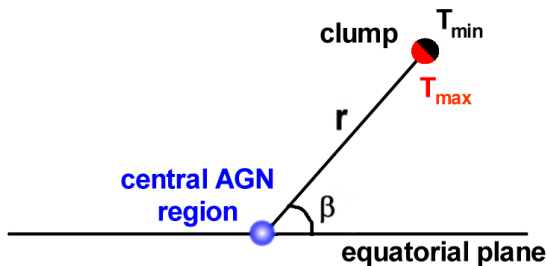
Figure 1.17: Simplified geometric view of an AGN with a single clump. Depending on the observer's viewing angle different fractions of the illuminated cloud will be visible.
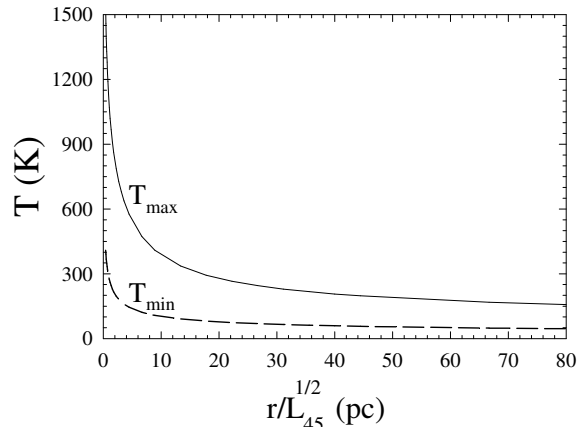
Figure 1.18: Maximal and minimal surface dust temperatures of an optically thick cloud at a distance r with L in units of $10^{45}\,\mathrm{erg/s}$ (taken from Elitzur 2006).

"doughnut"-like torus by dusty clouds, which are individually optically thick. The idea was already raised by Krolik & Begelman (1988). In recent years the model has been improved. The temperature of an optically thick dusty cloud is much higher on the side illuminated by the AGN than on the opposite, dark side (Fig. 1.17). As the result of the low temperatures on the dark side of the clouds, clumpiness provides a natural explanation for the compactness of the IR emission from AGN tori since the cloud's dust temperature at a distance of $r \sim 2\,\mathrm{pc}$ will range from $950\,\mathrm{K}$ (illuminated side) to $250\,\mathrm{K}$ for the dark side in the case of NGC 1068 (Fig. 1.18). Not only can clumpiness explain the VLTI data, it can be expanded to account for the other observed discrepancies in the unification model. The physical properties by replacing the sharp torus by a simple smooth Gaussian distribution of clumpy, optically thick clouds was studied in Elitzur et al. (2004). The cloud distribution starts at the dust sublimation radius, and the number of clouds encountered on average along a radial equatorial line is N_0. Their simple cloud distribution is

$$N_{\mathrm{CLOUD}} \sim N_0\, e^{(-\beta/\sigma)^2}\, r^{-q} \tag{1.15}$$

and depends only on the angular width parameter σ, the radial power law distribution with index q, the radial distance from the centre r, and the viewing angle β (with respect to the equatorial plane, see Fig. 1.19 c). At the same viewing angle, the AGN obscuration is identical for all sides. The obscuration depends only on the total number of clouds along the line of sight. Because of the Gaussian angular distribution for a smooth-density torus, the obscuration is highly anisotropic and decreases significantly with increasing viewing angle β. Elitzur et al. (2004) show that the variation of SED with viewing angle is moderate and becomes isotropic for $q \sim 2$. A clumpy torus can produce extremely anisotropic obscuration of an AGN, while the IR emission is nearly isotropic. In this new picture the difference between type I and II AGN is not an issue of orientation but of probability for

Figure 1.19: Different torus models for the unification scheme. left: a) sharp edge torus with smooth distribution of matter – classical pict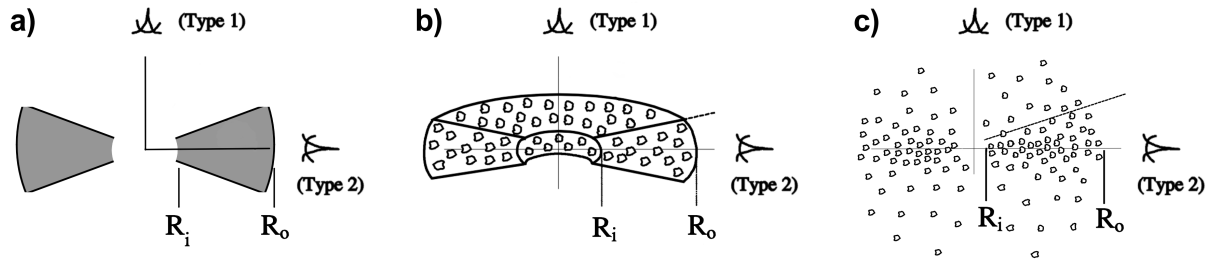ure of an AGN torus, middle: b) sharp edge torus with clumpy matter distribution – torus model that can explain the recent IR observations, right: c) soft edge torus with clumpy matter distribution – torus model that can explain the recent IR observation and transient/discrepant objects. In a and b type I AGN is recognized if the central region is observed from the top or the bottom, while a type II AGN is seen if viewed from the side. An AGN with the clumpy cloud distribution as shown in c can be seen from any direction as a type I or type II depending if the central engine can be seen directly or a cloud is blocking the path of light. The plots are based on Fig. 3 in Elitzur (2006) and Fig. 2 in Elitzur et al. (2004).

a direct view on the AGN's central engine. Transient objects can be easily explained by a moving cloud which obscures or uncovers the central region of the AGN.

The advanced unification model also addresses the question of the nature of the torus and BLR. Suganuma et al. (2006) show via IR reverberation mapping that the dust sublimation radius and the size of the BLR scales with luminosity as $L^{1/2}$ over a range of 10^6 in luminosity. Netzer & Laor (1993) proposed already that the BLR size is bound by the dust sublimation. X-ray observations confirm the existence of dust free clouds in proximity to the AGN and dusty clouds at a few pc (Risaliti et al. 2002). Therefore, Elitzur (2006) suggests that the torus is a smooth continuation of the broad line region. The different radiative signatures represent the change in cloud composition across the dust sublimation radius R_d. The inner clouds are dust-free since they are directly exposed to the AGN ionising continuum radiation. The outer clouds are dusty because they are shielded from the radiation. Thus, the BLR (occupying $r \leq R_d$) and the torus ($r > R_d$) are the inner and outer segments of the same clumpy structure.

Further developments of the unification model are continuously debated. These model are essential to expand our knowledge in AGN research since they make prediction which can be tested by observations. For example, Elitzur & Shlosman (2006) mentioned that the torus disappears at bolometric luminosities of $L_{BOL} \lesssim 10^{42}$ erg/s because mass accretion can no longer sustain the required cold outflow rate. The verification of such hypotheses will improve our understanding of AGN from the observational and theoretical point of view.

Table 1.1: X-ray luminosities of different types of AGN. The table is based on Charles & Seward (1995). The values of Seyfert galaxies and QSOs/quasars have been adopted to be consistent with the present Ph.D. thesis. The X-ray luminosity for X-ray bright optically normal galaxies (XBONGs) is taken from Brandt & Hasinger (2005), the example from Comastri et al. (2002).

Type	$L_{\mathrm{X_{OBS}}}$[erg/s]	Example
Normal galaxies	$10^{37} - 10^{39}$	M31
Narrow emission line galaxies	$10^{40} - 10^{43}$	Mkn 176
X-ray bright optically normal galaxies	$10^{41} - 10^{43}$	CXOU J031238.9-765134
Seyfert galaxies	$10^{43} - 10^{44}$	NGC 4151
BL Lac objects	$10^{44} - 10^{46}$	OJ 287
QSOs/quasars	$10^{44} - 10^{47}$	3C273

1.3.3 The X-ray View of Active Galactic Nuclei

Besides a number of important features that were revealed in the X-ray spectra of AGN, the most surprising is the uniformity of the observed slopes over decades in X-ray luminosity (Table 1.1). The X-ray spectra of AGN have photon indices of $\Gamma \sim 1.6$ (radio-loud AGN) and $\Gamma \sim 1.9$ (radio-quiet AGN, Reeves & Turner 2000).

Walter & Fink (1993) suggested that the X-ray spectra of all AGN consist of two basic universal components. The first is an IR to X-ray power law with the energy index of order of 1. The second component represents the Big Blue Bump which is expected to be the blackbody radiation of the accretion disk itself (UV - soft X-ray energy range). Walter & Fink (1993) argued that all AGN X-ray spectra can be explained by different normalisations of the two components. This simple picture of AGN X-ray spectra is not expected from accretion disk models, but is nevertheless observed. The bolometric luminosity, including X-ray emission, should scale with the accretion rate $\dot{M}$ (Czerny et al. 2003). Furthermore, the optical flux, coming from the outer parts of the disk, should be related to the black hole mass (Tripp et al. 1994).

The observed X-ray power law up to several tens of keV cannot be explained by the thermal emission of the accretion disk that only produces a blackbody spectrum with most of the photons in an energy range of a few eV. A promising mechanism for the production is inverse Compton-scattering (Haardt & Maraschi 1993). For relativistic and non-relativistic electrons, a power law photon distribution can be produced from repeated inverse Compton-scatterings of a non-power law electron distribution (Rybicki & Lightman 2004). The mechanism is not well understood because of many unknown parameters. The first question is the origin of the photons that are scattered to higher energies. The accretion disk is expected to harbour a strong magnetic field. Therefore, synchrotron emission of the hot plasma itself which is surrounding the accretion disk could be inverse Compton-scattered. Wardziński & Zdziarski (2000) analysed this scenario and found the process to be only marginally important in luminous X-ray sources containing accreting black holes. In addition, bremsstrahlung radiation would contribute significantly in the case that the
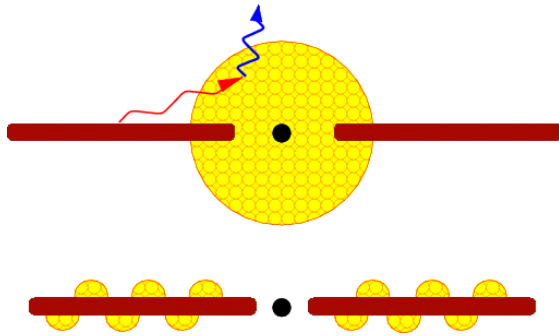
Figure 1.20: Different geometries for an accretion disk and the comptonising corona (taken from Reynolds & Nowak 2003). In the centre is the super-massive black hole (black) which is surrounded by an accretion disk (brown). The comptonising corona (hot plasma, yellow) is up-scattering the photons from the accretion disk to higher energies. The top figure refers to a sphere geometry which cools too effectively in order to explain the observed power law in hard X-rays. The bottom geometry is a patchy corona. This set-up is not very effectively Compton-cooled since it is attached to the accretion disk through small regions.
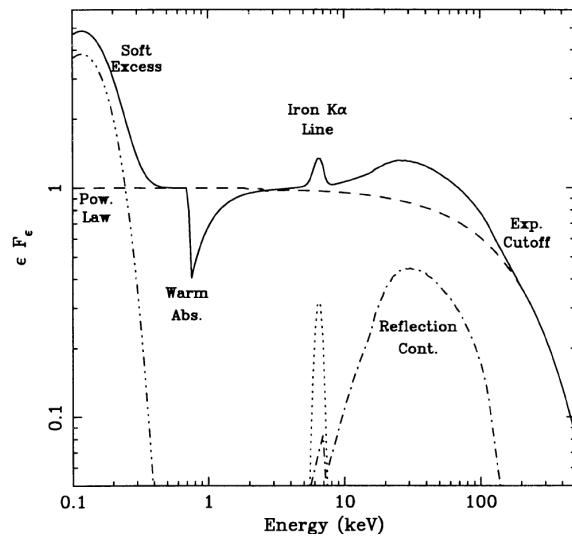
Figure 1.21: Schematic representation of the νF_ν X-ray spectrum of a Seyfert I galaxy (taken from Fabian 1999). The dashed line represents the universally observed power law in the X-ray spectrum. The main spectral components that frequently occur in X-ray spectra of AGN are illustrated and modify the simple power law X-ray spectra.

hot plasma extends to regions far away from the accretion disk. Thus, the corona (hot plasma) is easily cooled and it is difficult to obtain the required high temperature. The dominant radiative process in these sources appears to be Comptonization of blackbody radiation emitted by cold matter in the vicinity of the hot plasma.

The second issue is the unknown geometry of the coronal system. In order to achieve higher coronal temperatures and thus to explain the extent of the observed power law up to several tens of keV, various small coronal regions attached to the accretion disk - a so-called patchy corona or pill box geometry (Fig. 1.20) - are required (Stern et al. 1995).

Besides the universal property of a power law, X-ray spectra contain additional frequently observed features (Fig. 1.21) such as:

- soft excess

  The soft excess in AGN X-ray spectra below 1 keV is suggested as primary emission from the accretion disk (Pounds & Reeves 2002). This causes the observation of much steeper ($\Gamma = 2$) AGN X-ray spectra above 1 keV. A self-consistent ionised reflection model by Ross & Fabian (2005) explains the soft excess by proper treatment of fluorescence lines, absorption edge, and atomic features.

- photo-electric absorption
  At soft X-ray energies absorbers can modify the shape of the X-ray spectrum significantly. The absorption is strongest at low energies for cold materials and only in the hard X-rays is the incident power law observable. For a warm absorber the lighter elements are fully ionised, therefore, they become transparent for soft X-rays. This produces absorption features which can mimic a soft excess.

  – cold absorber
    A neutral gas will reduce the observed flux in soft X-rays via photo-electric absorption. Eq. 1.4 illustrates that the effect decreases with higher photon energy. Consequently, the soft X-ray photons get absorbed first. An increasing column density of absorbing material in the line of sight towards the central engine of the AGN will also effect higher photon energies. The amount of absorption can therefore be derived from the X-ray spectra (see Fig. 1.10).

  – warm absorber
    A warm absorber is a significantly ionised medium present in the line of sight towards the black hole. Observationally it is seen through the presence of narrow absorption lines and edges. The grating spectrometers on *XMM-Newton* and *Chandra* are able to resolve most of the lines which originate from highly ionised atoms such as C IV, O VII, and O VIII. The presence of these ionisation states suggests a temperature of the medium of the order $10^5 - 10^6$ K. Warm absorbers show column densities of the order $N_{\rm H} \sim 10^{23}\,{\rm cm}^{-2}$ and are likely to be clumpy (Czerny et al. 2003). Although the presence of a warm absorber is observed due to absorption features superimposed onto the transmitted spectrum from the central region, this medium predominantly scatters the incoming photons.

- iron Kα fluorescence line
  The most prominent emission line found in AGN X-ray spectra is the iron Kα line at 6.4 keV (see Figures 1.21, 1.22). This is due to the combination of high fluorescent yield (the probability that an excited ion will de-excite via fluorescence rather than Auger effect) and the large cosmic abundance of iron. The fluorescent line is excited when the surface layer of the accretion disk responses to the external incident hard X-ray illumination from the corona. The incident photons can be either Compton-scattered by free electrons or outer electrons of elements in the disk, or photo-electrically absorbed by atom. To do so, the photon must possess an energy higher than the required photo-ionisation energy. The K-shell photo-ionisation will be followed by a transition of an L-shell electron to fill the K-shell by the emission of a photon (Kα fluorescence). The same process that produces the Kα fluorescence causes an iron K-absorption edge. The cross section for the photo-ionisation of the incident photon energy is the highest, if the energy fits exactly the photo-ionisation energy of 7.1 keV. The effectiveness of reprocessing incident X-rays into iron Kα photons drops rapidly with increasing energy causing an iron edge at 7.1 keV.
  A weak 'shoulder' on the low-energy side of the iron Kα line is observable, because

some photons get Compton-scattered before they escape from the disk and thus lose energy. The relative strengths of astrophysical emission lines are measured via the use of equivalent widths (EW). The equivalent width of an emission line is the energy range over which the continuum radiation contains a flux equal to that contained in the emission line (Reynolds & Nowak 2003).

The iron Kα line, which has an intrinsically small energy width, will be dramatically broadened if the radiation originates from the immediate vicinity of the black hole where strong relativistic effects occur (see Laor 1991 for the characteristic double hump structure with a very prominent blue wing and a red tail).

- Compton-reflection hump
  X-rays reprocessed in cold matter produce not only fluorescent emission lines, they also cause the so-called Compton-reflection hump (see Fig. 1.22) in the 20-100 keV band (George & Fabian 1991). The main argument is the following. At higher photon energy ($E \geq 30$ keV) the cross section for the photo-electric effect is significantly decreasing. Thus, an incident photon reaches a larger penetration depth into the cold material. The photon suffers several Compton-scattering events before it escapes from the disk. For very high energies ($E \geq 100$ keV) the probability of photo-electric absorption is negligible, the photons penetrate deep into the material and undergo many scattering in order to escape. Therefore, high energy photons lose more energy in order to escape from the disk than low energy photons. The deposited energy is dominated by absorption processes in the uppermost layers of the material for low-energy photons, while electron scattering increases in deeper layers for high energy photons. Therefore, low-energy photons ($E \leq 20$ keV) have in comparison with high-energy photons a higher probability to escape from the disk, since they are interacting on its surface. Both processes result in a Compton-reflection hump at intermediate energies.

- exponential cut-off
  A high energy cut-off at 100-300 keV is observed in the AGN X-ray spectra. This finding is explained by the process that generates the power-law in AGN - inverse Compton-scattering. The scattering electrons of the corona have a certain energy distribution. Therefore, the scattered photons can only be shifted up to certain energies. The cut-off is determined by the high energy tail of the corona's electron distribution.

Iron lines play a key role in studying the environment near accreting black holes and test our basic understanding of physics under extreme conditions. X-ray observations showed that the equivalent width of the iron Kα emission line is anti-correlated with X-ray luminosity of the AGN (X-ray Baldwin effect, Iwasawa & Taniguchi 1993).

Recently, self-consistent models of reflection by an ionised disk became available (Ross & Fabian 2005) and include a range of relevant fluorescence lines, absorption edges, Compton-reflections, and Compton-broadening of atomic features. These models gave a
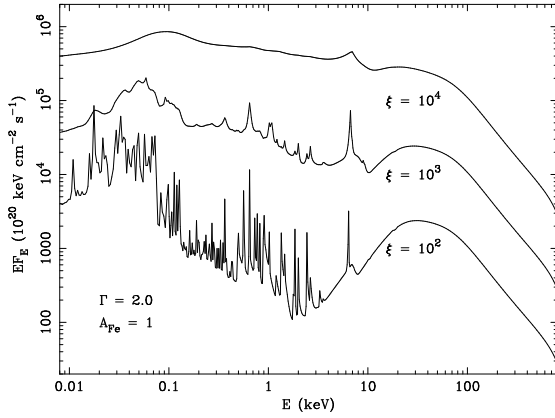
Figure 1.22: Reflected spectra for three different values of the ionisation parameter ξ from Ross & Fabian (2005). The spectra are shown without relativistic blurring. The incident spectrum has $\Gamma = 2$, and iron has solar abundance.

Figure 1.23: XMM-Newton PN (black) and MOS (green, red) spectra of RBS 1423 (observer frame). A single power law has been fitted to the 0.2-12 keV data. The relativistically broadened hydrogen-like iron line is seen as positive residuals between ∼4-7 keV. In the soft energies (0.2-0.5 keV) a discrepancy between the XMM-Newton camera types and a possible soft excess is noticed. The plot is taken from Krumpe et al. (2007b).

theoretical explanation for the X-ray Baldwin effect. As the X-ray luminosity increases, the upper layers of the disk become progressively more ionised until any reprocessing feature is suppressed. The ionisation parameter ξ determines the equivalent width of the observed iron Kα line (Fig. 1.22).

The prediction of ionised reflection in luminous objects was recently confirmed in an *XMM-Newton* observation of RBS 1423 (Fig. 1.23, Krumpe et al. 2007b). This object is one of the first QSOs with a significantly broadened ionised iron Kα line. The disk models require hydrogen-like iron and an inner radius of only a few Schwarzschild radii.
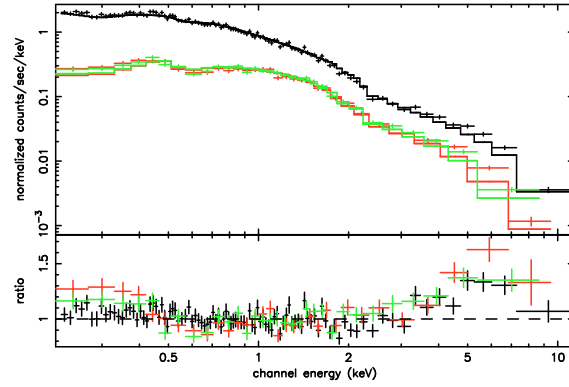
Chapter 2

Aims & Approach

Motivation

X-ray surveys are essential to characterise the source population of the X-ray sky and are the only means to understand the nature of the cosmic X-ray background radiation. Deep X-ray surveys have been carried out during the last decades (Hasinger et al. 1998; Lehmann et al. 2001; Alexander et al. 2003) and showed that up to 80% of the soft X-ray background is due to active galactic nuclei (AGN). X-ray emission has been found to be a universal characteristic of all AGN. The X-ray luminosity of these objects is in the range of $\sim 10^{42} - 10^{48}$ erg/s and accounts for a considerable fraction of their bolometric luminosity. Moreover, the emission we observe in the X-ray is only a fraction of the total energy produced in X-rays, since the bulk of the energy (up to 90% for absorbed sources) has been absorbed and re-emitted at longer wavelengths.

XMM-Newton and *Chandra*, thanks to their high sensitivity in the hard X-ray regime, opened the absorbed X-ray universe for further studies and revealed a large population of obscured, low-luminosity, low-redshift X-ray sources (Hasinger et al. 2001). To characterise the X-ray sky properly and understand the peak of the spectral energy distribution of the X-ray background at ~ 30 keV (Worsley et al. 2005), numerous surveys with varying limiting flux and survey area are needed. These surveys will reveal the different X-ray source populations, their contribution to the cosmic X-ray background, the abundance of source population over cosmic time, and can attempt to answer if there is any evolution.

Aim

The thesis will focus on the following questions:

- What are the X-ray source populations in medium deep X-ray surveys?

- What are the X-ray and optical properties of these populations?

- What distinguishes type II AGN from other X-ray source populations such as type I AGN?

- Are the physical processes different for type I and II AGN, or are the same physical processes acting as predicted by the unification model?

- Does the absorption in type II AGN evolve with redshift or X-ray luminosity?

Approach

This thesis will study and analyse the medium deep *XMM-Newton* Marano field survey. The X-ray and optical follow up observations will be analysed to determine the fraction of different X-ray source populations among the X-ray counterpart in the *XMM-Newton* Marano field survey.

Based on the X-ray data a well-defined sample will be selected. The different X-ray source populations in this sample will be studied with respect to their X-ray and optical properties.

The analysis will focus on AGN. The results will be compared to the findings of other surveys. The success of the additional use of K-band data which should increase the counterpart identification of obscured objects, will be evaluated.

The integration of other X-ray surveys, in which the Astrophysical Institute of Potsdam is involved in, will be used to study the evolution of an absorbed X-ray source population (type II AGN) which is expected to be a main contributor of the still insufficiently resolved hard cosmic X-ray background.

Chapter 3

The XMM-Newton X-ray survey in the Marano field

In this chapter, I present new *XMM-Newton* data and spectroscopic classifications of X-ray sources in the Marano field. Different X-ray source classes are identified and their properties are studied.

During the first two years of operation, *XMM-Newton* performed various "guaranteed time program" observations. These observations were given to different groups, which contributed significantly to the development, construction, and operation of *XMM-Newton*. The Institute of Astronomy and Astrophysics in Tuebingen, which is a partner in the *XMM-Newton*-EPIC-PN consortium, as well as the Astrophysical Institute of Potsdam, which participates in the *XMM-Newton* Survey Science Center (SSC), joined parts of their guaranteed time programs. In 1997 both institutes (Tuebingen-PI: G. Lamer, Potsdam-PI: G. Hasinger) proposed a deep *XMM-Newton* observation of the Marano field.

The Marano field was named by an early optical quasar survey up to a limiting magnitude of $B_J = 22.0$ by Marano et al. (1988). Based on different optical selection techniques (colour-colour diagrams, optical spectra, variability analysis) they discovered 23 broad emission line quasars and defined an extensive list of quasar candidates. Zitelli et al. (1992) completed this work by presenting a spectroscopically complete sample of quasars with $B_J \leq 22.0$ using this list of quasar candidates. They confirmed 54 quasars including the already known 23 quasars.

The Marano field has been extensively studied in various wavelength ranges (see overview in Table 3). Between December 1992 and July 1993, *ROSAT* observed the central Marano field ($\sim 0.2\,\mathrm{deg}^2$) for 56 ksec (Zamorani et al. 1999). The data revealed 50 X-ray sources with a limiting flux of $f_X \geq 4 \times 10^{-15}\,\mathrm{erg\,cm^{-2}\,s^{-1}}$ in the *ROSAT* band (0.5-2.0 keV). Multi-colour CCD and spectroscopic data were used to classify 42 X-ray sources (33 quasars, 2 galaxies, 3 clusters, and 4 stars). 66% of the optically selected quasars within the *ROSAT* field of view were detected as *ROSAT* X-ray sources. Gruppioni et al. (1997) carried out a deep radio survey at 1.4 and 2.4 GHz and detected 68 radio sources ($f_R > 0.2$ mJy).

Table 3.1: Observational data obtained in the Marano field. Explanation of the abbreviations: ESO - European Southern Observatory, AAT - Anglo Australian Telescope, NTT - New Technology Telescope, ATCA - Australian Telescope Compact Array, IR - Infrared, VLT - Very Large Telescope.

Data	Facility	Date	Reduced/Analysed by	Reference
optical imaging, spectroscopy	ESO 3.6 m	1981-84	Marano	Marano et al. (1988)
optical spectroscopy	ESO 3.6 m AAT	1984-89 Jan. 1988	Zitelli	Zitelli et al. (1992)
56 ksec X-ray survey	ROSAT	1992-93	Zamorani	Zamorani et al. (1999)
optical imaging	ESO 3.5 m NTT	1992-94	Zamorani	Zamorani et al. (1999)
1.4 GHz & 2.4 GHz radio survey	ATCA	Jan. 1994	Gruppioni	Gruppioni et al. (1997)
optical imaging	ESO 3.5 m NTT	1992-95	Mignoli	Mignoli & Zamorani (1998)
120 ksec X-ray survey	XMM-Newton	2000	Lamer/Krumpe	Krumpe et al. (2007c)
optical imaging	ESO 2.2 m	Nov. 2000	Mignoli/Krumpe	Krumpe et al. (2007c)
near-IR imaging	ESO 3.5 m NTT	Nov. 2001	Lamer/Krumpe	Krumpe et al. (2007c)
optical spectroscopy	ESO VLT	2000-02	Krumpe	Krumpe et al. (2007c)

Follow-up observation provided redshifts for 30 objects.

The new *XMM-Newton* data comprise an area three times larger, compared to the *ROSAT* survey, and are thus almost comparable in size to the optical quasar survey. We reach a survey sensitivity of $f_X \sim 1.5 \times 10^{-15}\,\mathrm{erg\,cm^{-2}\,s^{-1}}$ (turnover flux in the 0.5-2 keV band) over a contiguous area of $0.6\,\mathrm{deg}^2$. In terms of sensitivity the *XMM-Newton* survey of the Marano field is thus comparable with deep *ROSAT* surveys (e.g., the UDS, Hasinger et al. 1998, see Fig. 3.1) or with medium deep *Chandra* surveys (e.g., ChaMP, Green et al. 2004).

An Italian group (G. Zamorani, M. Mignoli) contributed with their deep ESO Wide-Field-Imager observation of the Marano field to the optical follow-up program. At the ESO Very Large Telescopes, FORS1 guaranteed time was used by S. Wagner (Heidelberg) to
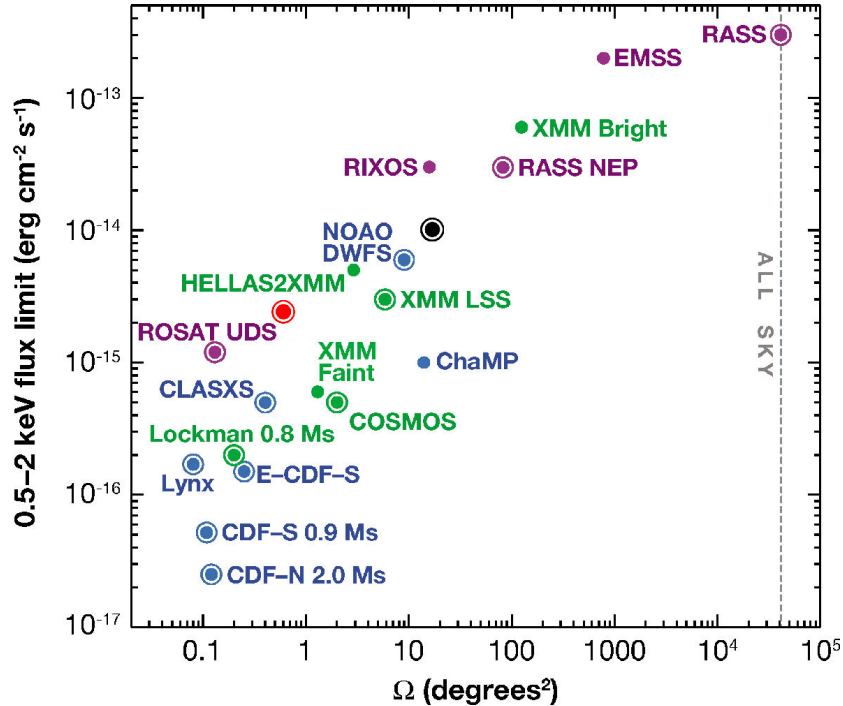
Figure 3.1: Distribution of some well-known extragalactic X-ray surveys by Chandra (blue), XMM-Newton (green), and earlier missions (purple) in the 0.5-2 keV flux limit versus solid angle Ω. Circled dots denote surveys that are contiguous (by 2005). The most sensitive flux limit is shown. The vertical dotted line shows the solid angle of the whole sky. The red circle represents the XMM-Newton Marano field survey, the black circle the XMM-Newton Serendipitous Medium Sample which are studied in this thesis. The figure is based on a plot shown in Brandt & Hasinger (2005).

provide the first set of optical follow-up spectra in the Marano field.

In 2002, I became involved in the preparation and the reduction of the FORS2 follow-up run during my master thesis. The analysis of the *XMM-Newton* Marano field survey is published in Krumpe et al. (2007c).

The chapter is organised as follows. In Sect. 3.1 I list the X-ray and optical data and the reduction of the data. Section 3.2 describes and summarises the spectroscopic classification of the X-ray sources. In Sect. 3.3 I make use of the spectroscopic classification and redshift determination to analyse the properties of different object classes. I concentrate on a 'core sample' of objects in the central part of the field, where I reached the highest degree of completeness in the spectroscopic classification. Section 3.4 addresses additional objects in the Marano field that are not X-ray detected. These objects were obtained as a control sample. Section 3.5 discusses the results of the different object classes.

3.1 Observations and data reduction

3.1.1 XMM-Newton X-ray observations

Since the area of the optical quasar survey in the Marano field is larger than the *XMM-Newton* field of view, the X-ray observations have been performed as a grid of 4×4 overlapping pointings with a spacing of ~ 5 arcmin in right ascension and declination. The pointing in the north-western corner of the grid was shifted to cover the position of a deep far-infrared survey with the ISO satellite (Table 3.2 and Fig. 3.2). The ISO data are not addressed in this Ph.D. thesis.

Due to the overlapping pointings some deviations from the standard *XMM-Newton* data analysis procedures were necessary, and are described here. The photon event tables from the 16 grid pointings were merged into a single event table with a common sky coordinate frame using the *XMM-Newton* SAS (Gabriel et al. 2004) task `merge`. In this coordinate frame we created 240 images (one for each pointing, energy range, and instrument). The 5 bands used are 0.2-0.5 keV, 0.5-2.0 keV, 2.0-4.5 keV, 4.5-7.5 keV, and 7.5-12.0 keV. Each image has 963×963 pixels with four arcseconds binning. For each of these images separate exposure maps and background maps were created using the SAS tasks `eexpmap` and `esplinemap`. One of the pointings (ObsID 0129320801) had accidentally been scheduled with 'medium' thickness filters, while all other pointings had been observed with 'thin' filters. To correct for the somewhat lower throughput of the medium filters at soft energies, we multiplied all exposure maps of this pointing with a correction factor derived from the energy conversion factors for the 'thin' and 'medium' filters. These ECFs were taken from the SSC document SSC-LUX-TN-0059 v.3 (Osborne 2001). The correction is largest in the softest band (0.2-0.5 keV), where the effective exposure in the affected pointing is reduced by 11%.

We then added the images, exposure maps, and background maps of the individual pointings, resulting in 15 images for 5 energy bands and 3 detectors. These images were used simultaneously as input for a detection run with `eboxdetect` and `emldetect`. The task `emldetect` applies a PSF-fit to each source found by `eboxdetect` to determine the source parameters. Since we use merged mosaic images of the field, each source image results from the superposition of several pointings. In each pointing the source is detected at a different position on the detector. Therefore, the standard configuration of `emldetect`, which uses the off-axis angle and position-angle of each source to extract the appropriate PSF from calibration files, could not be used here. Instead `emldetect` was modified to use the calibration PSF corresponding to an off-axis angle $\theta = 5$ arcmin throughout the entire field. This PSF is circularly symmetric and is a good representation of the point sources in the merged images.

For this work no extent models were fitted to the sources, therefore the source list produced by `emldetect` does not contain any information about whether a source is extended or point-like. Generally, the X-ray data reduction and analysis was performed with *XMM-Newton* SAS version 5.1 (from 18/06/2001) with the abovementioned exception of an

Table 3.2: XMM-Newton observations of the Marano field. Filter: T.-thin, M.-medium

XMM-orbit/ ObsID	Date (2000)	RA (3h:min:ss)	DEC (-55:min:ss)	Time (ks)	Filter
106/0112940201	7/7	15:27	06:13	10.3	T.
107/0112940201	10/7	16:03	21:41	10.4	T.
107/0112940301	10/7	15:27	11:22	10.6	T.
107/0112940401	10/7	15:27	16:32	10.5	T.
107/0112940501	10/7	15:27	21:41	7.8	T.
129/0129321001	22/8	16:03	11:22	6.1	T.
129/0129320801	22/8	16:03	16:32	10.6	M.
129/0129320901	22/8	16:03	06:13	10.6	T.
130/0110970101	24/8	13:09	03:54	10.9	T.
130/0110970201	24/8	14:15	11:22	9.1	T.
130/0110970301	24/8	14:15	16:32	9.1	T.
130/0110970401	24/8	14:15	21:41	9.1	T.
131/0110970501	26/8	14:51	06:13	9.1	T.
131/0110970601	26/8	14:51	11:22	9.9	T.
133/0110970701	30/8	14:51	16:32	9.9	T.
133/0110970801	30/8	14:51	21:41	8.8	T.

adapted version of `emldetect`. The version of `emldetect` used here suffered from an error, which resulted in the overestimation of detection likelihood values (*XMM-Newton*-NEWS #29, 11-Mar-2003). All likelihood values quoted here have been corrected to adhere to the relation $ML = -\ln(P)$, where ML is the detection likelihood and P is the probability that the detection is caused by a random fluctuation of the background.

All count rates and derived quantities are taken from the PSF fitting of `emldetect`. Using the combined exposure maps, `emldetect` corrects the source count rates for all spatial variations of telescope and detector efficiency, i.e., the count rates relate to the optical axis of each EPIC camera. Following Cash (1979), the 68% confidence intervals for the source positions and source fluxes were calculated using `emldetect` as follows: Each parameter is varied until the statistic

$$C = 2 \sum_{i=1}^{N} (e_i - n_i \ln e_i) \tag{3.1}$$

exceeds the best-fit value of C by 1, where e_i is the source model at the position of pixel i and n_i is the number of counts in pixel i. We used energy conversion factors (ECFs) to calculate source fluxes in the band 0.2-10 keV (from the total EPIC count rate in the band 0.2-12 keV) and in the band 0.5-2.0 keV (from the EPIC count rate in the band 0.5-2.0 keV). The ECFs were derived by using `XSPEC` and the *XMM-Newton* SAS calibration files to simulate power law spectra with photon index $\Gamma = 1.8$ and the Galactic column density of the field $N_{\rm H} = 2.7 \times 10^{20}\,{\rm cm}^{-2}$.

For all sources 3 hardness ratios of the form
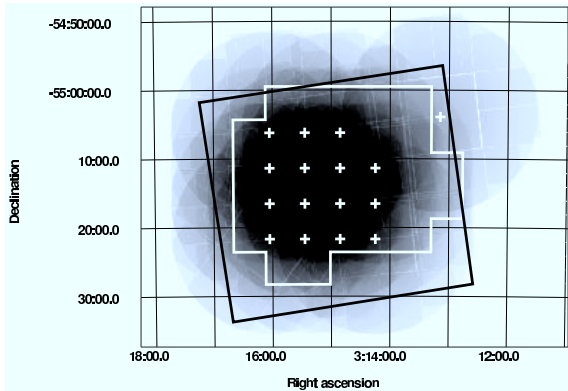
$$HR = \frac{CR_2 - CR_1}{CR_1 + CR_2} \tag{3.2}$$

Figure 3.2: Averaged MOS1 and MOS2 exposure map (0.5-2.0 keV) of the 4×4 pointing pattern (small white crosses). The exposure time in the central region reaches 78 ksec. The black rectangle shows the area covered by the WFI R-band images. The white polygon marks the area covered by the SOFI K-band images (see Sect. 3.1.2).
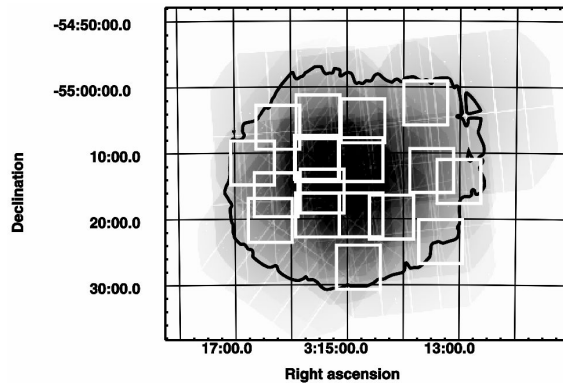

Figure 3.3: PN exposure map (0.5-2.0 keV) of the 4×4 pointing pattern. The exposure time in the central region reaches 35.5 ksec. The area inside the black contour marks the 'core sample' region where the PN-detector exposure time exceeds six ksec. White rectangles show the position of the spectroscopic masks for the optical follow-up observations (see Sect. 3.1.4).

were calculated between the adjacent PN-detector energy bands 0.2-0.5 keV, 0.5-2.0 keV, 2.0-4.5 keV, and 4.5-7.5 keV. For example, $HR2$ was calculated between the bands 0.5-2.0 keV and 2.0-4.5 keV. The different energy responses of the MOS- and PN-detectors result in different hardness ratios for the same source. If not noted otherwise the PN-values are used throughout the paper. Unless mentioned otherwise, all errors refer to a 68% confidence interval.

In total we detected 328 X-ray sources with detection likelihoods $ML \geq 5.0$. The X-ray fluxes are in the range $f_{\mathrm{X}} = (0.16 - 54) \times 10^{-14} \, \mathrm{erg \, cm^{-2} \, s^{-1}}$ (0.2-10 keV). The X-ray flux histogram (Fig. 3.4) shows the X-ray detection limit of our survey. Below $f_{\mathrm{X}} \sim 5 \times 10^{-15} \, \mathrm{erg \, cm^{-2} \, s^{-1}}$ we are unable to detect the majority of the X-ray sources. In the central region (Fig. 3.3) we found 252 X-ray sources. The complete X-ray source list can be found in the Appendix A.

Since the PSF-modelling task `emldetect` was only used with point-source models here, the detection procedure was not very sensitive to diffuse emission from clusters of galaxies. However, visual inspection of the X-ray images revealed no obviously extended sources. We estimate that extended cluster emission down to 0.5-2.0 keV fluxes of $2 \times 10^{-14} \, \mathrm{erg \, cm^{-2} \, s^{-1}}$ should be detectable in this survey. The cluster $\log N(\log S)$ of Rosati et al. (1998) gives a surface density of ~ 6 clusters per square degree at this flux. We would therefore expect about four clusters in the total area of the *XMM-Newton* observations and about two clusters in the $0.28 \, \mathrm{deg}^2$ core region of the survey. Given the considerable cosmic variance of the cluster surface density the non-detection of clusters in the survey is consistent with the $\log N(\log S)$. In any case the small number of expected clusters does not suggest a significant contribution of clusters of galaxies to our source sample.
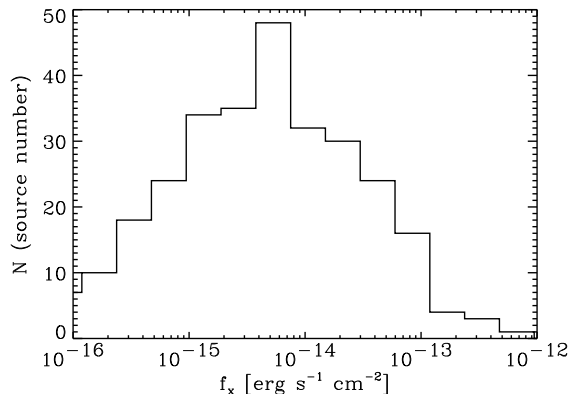
Figure 3.4: 0.2-10 keV X-ray flux histogram of the 328 XMM-Newton detected X-ray sources in the Marano field. Up to an X-ray flux of $f_X \sim 5 \times 10^{-15}\, \mathrm{erg\, cm^{-2}\, s^{-1}}$ (turnover flux) we detected more and more sources. Below that X-ray flux the detection rate decreases dramatically.
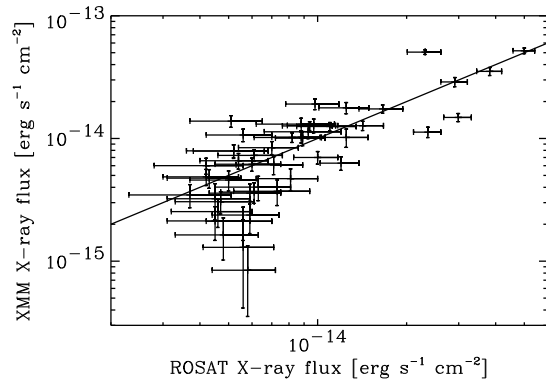
Figure 3.5: Comparison between the 0.5-2 keV X-ray fluxes measured by ROSAT and XMM-Newton of all 50 ROSAT X-ray sources in the Marano field. XMM-Newton fluxes are averages of the three individual EPIC camera fluxes. The black solid line represents equal ROSAT and XMM-Newton fluxes.

XMM-Newton redetected all 50 *ROSAT* X-ray sources (Zamorani et al. 1999). However, two *ROSAT* X-ray sources have low detection likelihoods and were thus not included in the final *XMM-Newton* X-ray source list (Appendix A). Figure 3.5 compares *ROSAT* and *XMM-Newton* EPIC X-ray fluxes in the 0.5-2.0 keV band.

The X-ray fluxes of both missions are comparable down to *ROSAT* fluxes of $f_X \sim 6 \times 10^{-15}\, \mathrm{erg\, cm^{-2}\, s^{-1}}$. Among the 13 objects (broad emission line objects) with $f_X \geq 10^{-14}\, \mathrm{erg\, cm^{-2}\, s^{-1}}$ (*ROSAT*), five show variability of about a factor of two in both directions. Throughout this chapter, I refer to the X-ray sources by mentioning the X-ray source number without any letter as suffix (e.g. 452). These numbers refer to the sequence numbers in the original emldetect source list and are non-contiguous due to the removal of sources below $ML = 5.0$ after correction of the detection likelihoods.

3.1.2 The optical data

WFI R-band observations

The central region of the Marano field has been observed in the $UBVRI$ bands with the ESO Wide-field-Imager (WFI). Here I make use of the deep (4000 sec) R-band image with a limiting magnitude $R \simeq 22.5$ (defined as turnover magnitude minus 0.5 mag, see Fig. 3.6). The WFI-image covers an area of 35×32 arcmin well aligned with the region of the deepest XMM-Newton coverage (Fig. 3.2).
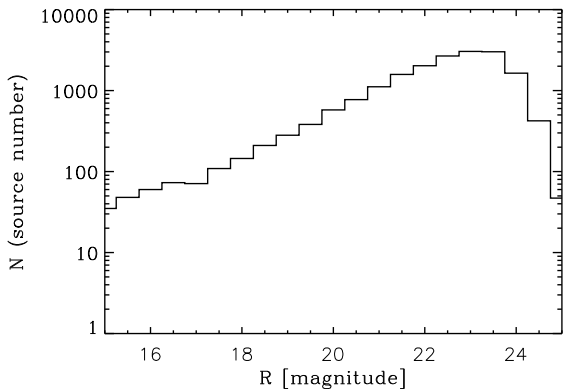
Figure 3.6: Magnitude histogram of the sources detected in the WFI R-band image. Completeness in detecting objects is lost for $R > 23$.
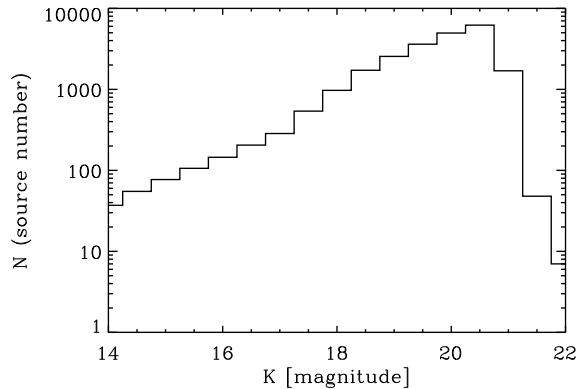
Figure 3.7: Histogram of the K-band magnitudes in the NTT-SOFI images. Completeness in detecting objects is lost for $K > 20.5$.

SOFI K-band observations

The K-band data $(2.0 - 2.3\,\mu\text{m})$ were obtained at the ESO New Technology Telescope (NTT) with the SOFI instrument. With an area of 754 arcmin^2 the K-band mosaic covers a slightly smaller area than the WFI R-band observation and is well aligned with the deepest XMM-Newton exposure (Fig. 3.2). The SOFI observations consist of a mosaic of 33 jittered pointings, each covering 5×5 arcmin with an exposure time of 29 minutes each. The limiting magnitude is $K \simeq 20$ (turnover magnitude minus 0.5 mag, see Fig. 3.7).

VLT R-band pre-images

R-band pre-images for the spectroscopic follow-up observation were obtained with the Focal Reducer and Spectrograph FORS1 and FORS2 at the ESO Very Large Telescope (VLT). The first run (FORS1) contained six and the second run (FORS2) 12 optical images. The summed pre-imaging area is $\sim$530 arcmin^2 in the central region of the Marano field (Fig. 3.3). Since the field was not contiguously covered by FORS spectroscopy, the pre-images also cover only $\sim$50% of the central area of the X-ray survey.

3.1.3 Target selection for optical spectroscopy

Our target selection for the optical spectroscopy was primarily based on FORS1/FORS2 R-band pre-images. WFI R-band and SOFI K-band data were used in addition to support the target selection on the pre-images in case of faint counterparts. The chosen fields represent a compromise in terms of maximum survey area and source density because of limited telescope time. First priority for spectroscopic follow up was given to candidates

Table 3.3: Details of FORS2 spectroscopic mask mode observation (see Fig. 3.3)

Mask	Observation (each 1800s)	Filter	Seeing (in arcsec)
mask1	3	none	0.63
mask2	4	none	1.36
mask3	3	none	1.05
mask4	3	none	0.78
mask5	3	none	0.93
mask6	3	GC375	0.75
mask7	3	none	0.80
mask8	3	none	0.81
mask9	2	none	0.66
mask10	3	none	0.76
mask11	1	none	0.96
mask12	2	none	0.64

with a likelihood of existence $ML > 10$ within a $2\sigma_X$ error radius. The total position error is $\sigma_X = \sqrt{\sigma_{\text{stat.}}^2 + \sigma_{\text{syst.}}^2}$. The statistical errors $\sigma_{\text{stat.}}$ of the positions were calculated as described in Sect. 3.1.1. The systematic errors are caused by uncertainties in the spacecraft attitude, errors in the linearisation of the detector coordinates, and undersampling of the PSF (in particular for the PN camera). At this stage, we allowed a systematic position error of 2.0 arcsec, see Sect. 3.2.1 for a more accurate estimation of the systematic position errors.

The multi-object spectroscopy masks were designed with the software `fims 2` provided by ESO. For all spectroscopic targets we used straight slitlets with a nominal length of ten arcseconds and a width of one arcsecond. For extended sources or closely spaced candidate counterparts, a different slit length of 6 - 14 arcseconds was used. Remaining available mask positions were filled with candidate objects not fulfilling the main selection criteria and with additional random non-X-ray emitting galaxies.

3.1.4   Spectroscopic observations

The FORS1 multi-object spectroscopy (MOS) run with six masks was obtained on November 20th, 2000 by using grism *GRIS_150I+17*. No order separation filter was used. The exposure time for every mask was 2400 seconds. The seeing was 0.7±0.1 arcsec.

The second run was performed with FORS2 in spectroscopic mask mode (MXU) from November 27th-30th, 2002. We aimed for an exposure time of 3×1800 seconds per mask, but weather and time constraints required some deviations from this general scheme (Table 3.3). Grism *GRIS_150I+27* was used for all masks.

To prevent second order contamination, the first mask (mask6) in the observing sequence was observed through filter GC375, which limited the wavelength range from

Table 3.4: Setups for the optical spectroscopy

	FORS1	FORS2
Grism	GRIS_150I+17	GRIS_150I+27
Dispersion [Å/mm]	230	225
Pixel size [μm]	24 x 24	15 x 15
Step width [Å/Pixel]	5	3

3850 to 7500 Å. A comparison with the second mask without an order separating filter showed that the contamination effect is negligible. Hence, for all following masks the filter was removed from the light path resulting in a wavelength range for central targets of the final spectra from 3500 to 10000 Å.

3.1.5 Spectroscopic data reduction

The reduction of the data was accomplished by a semiautomatic pipeline coded in `MIDAS`. It was specially designed to reduce FORS2-MXU data with as little interaction with the user as possible. After modifications this code was also used to reduce the FORS1-MOS data. The bias correction was done in the standard manner with careful attention to possible time dependence on the bias level and dark current. An ordinary flat field correction was used to rectify the pixel-to-pixel variation.

Wavelength calibration

We established a 2-d wavelength calibration in the pipeline. This allowed us to correct the distortion perpendicular to the dispersion direction and significantly improved the signal-to-noise ratio of the extracted spectra. The calibrated wavelength range is 3500-10000 Å. However, many spectra were located close to the edge of the CCD. Hence, there are substantial variations in the wavelength range of the spectra. The average uncertainty of the wavelength calibration is 0.2 Å but reaches a maximum of $\Delta\lambda \pm 1.5$ Å at long and short wavelength ends. Further details on the optical setups can be found in Table 3.4. We estimate the spectral resolution by measuring the width of the arc lines in the lamp spectra, and find $\Delta\lambda \sim 21$ Å (FWHM).

Object and sky definition

The acquisition slit-through images were used to roughly define the position and width of every single slit in an image. For an optimal definition of the object and sky region in the spectrum, the pipeline then displays intensity profiles in graphic windows and an image

of the corresponding spectrum. After a careful inspection of these pipeline outputs, the object and the sky region were defined manually for every single spectrum. Consequently, bad pixel/lines/columns in the raw data can be excluded for the extraction and scientific misinterpretation of artefacts in the final spectra can be avoided. Whenever possible, two sky regions, on both sides of the target spectrum, were defined.

Extraction of spectra

The extraction is based on an optimal extraction algorithm (Horne 1986) including cosmic ray rejection. Extensive tests determined the optimal extraction parameters. Standard flux calibration was applied. Since FORS2-mask6 was observed with an additional filter, a different standard star was used. All spectra were corrected for atmospheric absorption using the standard ESO extinction correction function scaled to the given air mass.

The n individual spectra of a given counterpart object were combined to form one single final spectrum. The individual spectra were firstly normalised to the same mean intensity. The normalisation factor was determined from an analysis of all spectra in a given mask. The final spectrum is the uncertainty-weighted mean spectrum.

3.2 Spectroscopic classification of the X-ray counterparts

The spectroscopic classification of the individual X-ray sources was primarily based on the FORS1 and FORS2 spectra. In addition, we used optical and X-ray images for a reliable identification (see Appendix E). Broad emission line objects were immediately accepted as X-ray counterparts. Narrow emission line galaxies and normal galaxies were accepted as X-ray counterparts if no other optical candidate was found within the position error range. Stars were regarded as likely counterparts if the X-ray colours indicated a soft X-ray spectrum compatible with coronal emission of ≤ 1 keV. Every X-ray identification was confirmed by at least two individuals.

For the large majority of our spectra the signal-to-noise ratio (SNR) is sufficient to give reliable classifications and redshifts. Like other X-ray identification surveys, we encounter the problem that classification of the optical spectra below a certain SNR is difficult. For spectra with a SNR=3-5, the identification of narrow emission lines was still possible. However, at this SNR faint broad emission lines and normal galaxy spectra are very difficult to identify. For example, the optical spectrum of 480A (in Appendix E) shows a narrow emission line galaxy with a SNR=2.4 (continuum near the O II emission line), which is close to the classification limit. Only one significant narrow emission line at $\sim$7100 Å is found. The spectral shape makes it reasonable to identify this line as O II emission line. Even though this classification is likely, an unambiguous redshift determination and classification of the type cannot be given. Spectra with a SNR less then $\sim$2.5 are not

identifiable. The reliability of the redshift determination and classification of the optical spectra is given by flags in Col. *(9) Flags* of Table B.1.

The complete list of X-ray classifications is given in Table B.1. The description of the columns follows the table in the Appendix B.

3.2.1 Discussion of spurious matches

Since type I AGN are a well-established class of X-ray emitters with relatively low surface density, false matches should not play any role for this object class. However, when investigating the classes of optically normal and narrow emission line galaxies, this problem has to be taken into account due to the high surface densities of these objects. To check the quality of our optical X-ray counterpart identification, we applied various tests.

First, the derived false match rate will depend on the assumed position errors, which take into account the statistical and the systematic position error (see Sect. 3.1.3). The difference in X-ray and optical position scaled to a $1\sigma_X$ position error is shown in Fig. 3.8 a. When we assume systematic errors of 2 arcsec, the theoretical Gaussian distribution (Eq. 3.3)

$$f(r_n) = N_{tot}\, r_n e^{-\frac{1}{2}r_n^2} \ , \ r_n = \frac{r_X - r_O}{\sigma_X} \tag{3.3}$$

peaks significantly later than the observed distribution of the X-ray counterparts. This is not due to the fact that we systematically accepted spurious counterparts as sources, since the type I AGN distribution (shown with dotted lines in Fig. 3.8) is consistent with the total X-ray identification distribution. The fact that we have a large number of type I AGN allows us to estimate the actual systematic position error for our X-ray observation. The observed distribution of the type I AGN position errors can be well reproduced with a systematic error of $\sigma_{syst.} = 0.7$ arcsec (Fig. 3.8 b). Moreover, the distribution of normalised position differences for the total sample agrees well with the theoretical distribution and with the type I AGN distribution when we apply $\sigma_{syst.} = 0.7$ arcsec.

Considering $\sigma_{syst.} = 0.7$ arcsec, we calculate the false match rate by following Sutherland & Saunders (1992) and Ciliegi et al. (2003). For every spectroscopically classified counterpart we determine the likelihood ratio L by

$$L = \frac{Q\, exp(-dist_{OX}^2/2)}{2\pi\sigma_X^2 N(< m_R)} \ , \tag{3.4}$$

where L is the probability of finding the true optical counterpart in this position with this magnitude, relative to that of finding a similar chance background object. Hence, the reliability of a counterpart is given by $P_{true} = L/(1 + L)$. The parameter Q is the probability that the counterpart of the X-ray source is brighter than the limit of the optical survey and has been set here to $Q = 0.5$. $N(< m_R)$ is the number density of catalogue objects
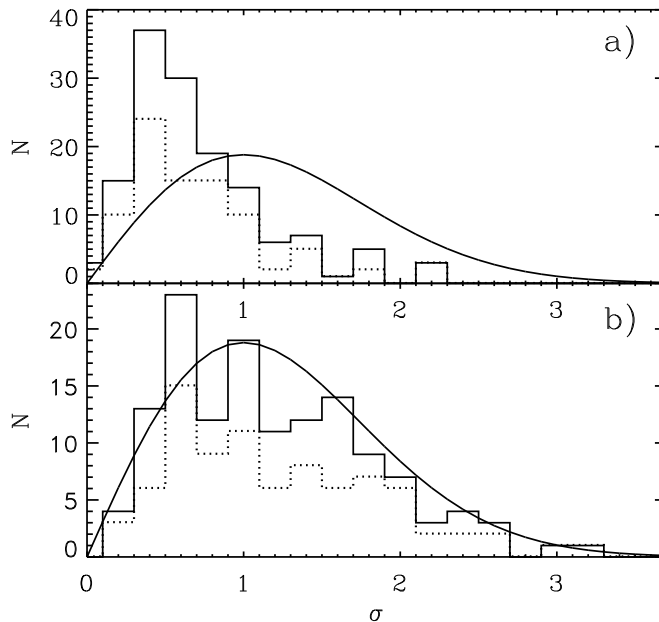
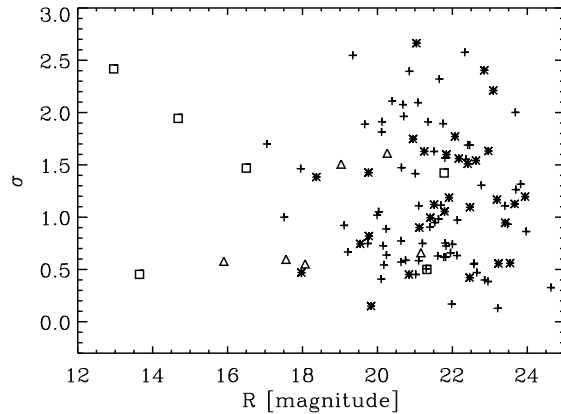Figure 3.8: *a)* Number of objects identified as X-ray counterparts vs. difference in X-ray and optical position scaled to a $1\sigma_X$ position error with a systematic X-ray position error of 2 arcsec. The smooth line represents the theoretical distribution. The distribution of type I AGN, which are a class of well-accepted X-ray emitters, is plotted as a dotted line. The solid line characterises the complete sample including type I AGN, type II AGN, galaxies, and stars. *b)* The $1\sigma_X$ position error was adjusted to the observed distribution by reducing the systematic X-ray position error from 2 arcsec to 0.7 arcsec. The complete sample agrees well with the type I AGN distribution, which gives evidence for a marginally false match rate.

of the relevant class brighter than the counterpart. For narrow emission line counterparts we assumed that about one-third of the field galaxies show line emission detectable in our spectra (Kennicutt 1992). We therefore derive the density of background objects $N(< m_R)$ by multiplying the total number of objects $< m_R$ in the optical catalogue by a factor 0.33. For normal galaxies a factor of 0.67 was applied accordingly.

The total number of false matches can then be calculated by adding up all probabilities $P_{sp} = 1/(1 + L)$ that the counterpart is spurious. Statistically, $\sim 25\%$ of our narrow emission line galaxies are spurious counterparts. However, after visually examining objects with low probabilities P_{true}, we find that in at least two cases (422A, 485A) the X-ray position given by the source detection software is influenced by blending with another X-ray source and the counterparts are consistent with the peak of the brighter X-ray source (see Appendix E, finding chart). Taking this into account, we estimate that the false match rate is $\sim 20\%$ for the sample of type II AGN. For the optically normal galaxies the false match rate calculated with the likelihood method is $\sim 2\%$.

As a further quality check we plot the position error vs. WFI R-band magnitude. False matches would be recognisable due to different distributions of the type I and type II counterparts in this diagram. However, Fig. 3.9 shows that all object classes occupy the same

Figure 3.9: WFI R-band magnitude vs. difference in X-ray and optical position scaled to a $1\sigma_X$ position error with a systematic X-ray position error of 0.7 arcsec. Crosses mark type I AGN, asterisks type II AGN, triangle galaxies, and rectangles stars.

Table 3.5: Origin of optical counterparts to XMM-Newton sources in the Marano field

Obtained optical spectra for X-ray sources	207
Positive literature classifications by Marano et al. (1988) and Zitelli et al. (1992) (partly reobserved)	30
New optical counterparts of ROSAT sources Zamorani et al. (1999) (partly reobserved)	14
New positive spectroscopic classifications of XMM sources	96
Total positive spectroscopic classifications of XMM sources	140

regions in the diagram. Hence, the diagram does not indicate any serious contamination by false matches even for faint counterparts.

3.2.2   Classification summary

In total, we spectroscopically classified 140 of the optically identified X-ray sources. Details are shown in Table 3.5. Like in other deep surveys, e.g., Hasinger et al. (2001), the majority of the X-ray counterparts ($\sim$90%) are related to the accretion on super-massive black holes (type I and type II AGN). Furthermore, we classified a few galaxies and stars as optical counterparts (see Table 3.6).

Table 3.6: X-ray counterpart distribution in the Marano field

Object class	Total number	Percentage
Broad emission line objects (B)	89	63%
Narrow emission line objects (N)	36	26%
Galaxies (G)	6	4%
Stars (S)	9	7%

Table 3.7: Properties of the core sample in the Marano field.

X-ray sources ($t_{\mathrm{PN}} > 6\,\mathrm{ksec}$, $ML > 10$)	170
Optically identified X-ray counterparts	158
Spectroscopically classified optical counterparts	110

3.3 Properties of a core sample of the XMM-Newton Marano survey

Our survey suffers somewhat from incomplete optical coverage of the X-ray survey area and, hence, a low classification rate over the whole area. To reach conclusions for the survey of a certain statistical significance we constrain our survey area and sample size to the central 0.28 deg^2 with a PN-exposure >6 ksec and significance of detection of individual sources with $ML > 10$. We refer to this as the 'core sample'. See Fig. 3.3 for the definition of the core region. Note that the maximum exposure is 35.5 ksec for the PN camera and 78 ksec for each of the MOS cameras.

The core sample contains 170 X-ray sources ($ML > 10$). No optical data are available for six out of the 170 X-ray sources which fall outside the WFI R-band image and are also not covered by VLT pre-images. A further six X-ray sources from the core sample have no optical detection in the WFI R-band image in a $3\sigma_{\mathrm{X}}$ position error circle ($\sigma_{\mathrm{syst.}} = 0.7$ arcsec). 122 X-ray sources are new detections, while 35 are spectroscopically classified ROSAT X-ray sources, and 13 are optically unidentified ROSAT sources. Out of the 140 spectroscopically classified objects in the Marano field, 110 are associated with X-ray sources of the core sample. A summary of the properties of the core sample is given in Table 3.7.

Figure 3.10 shows R-band magnitude histograms of the core sample X-ray sources that were spectroscopically classified and only optically identified, respectively. The (f_{X}, ML)- distribution of X-ray sources in the core region is given in Fig. 3.11. The classification ratio of the core sample is 65%. In the following subsections we refer to this sample.
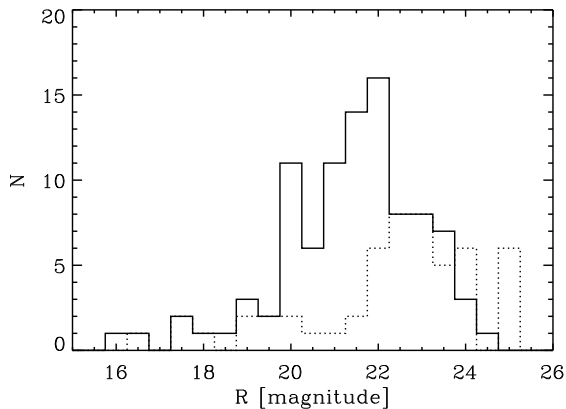
Figure 3.10: WFI R-band magnitude histogram for the core sample in the XMM-Newton Marano field survey. The solid line represents the R-magnitude distribution of the spectroscopically classified X-ray counterparts. The dashed line shows the distribution of the optically identified but not spectroscopically classified X-ray counterparts. Six X-ray sources, which have no counterpart within a $3\sigma_X$ error circle, are assigned to the bin at $R=25$.
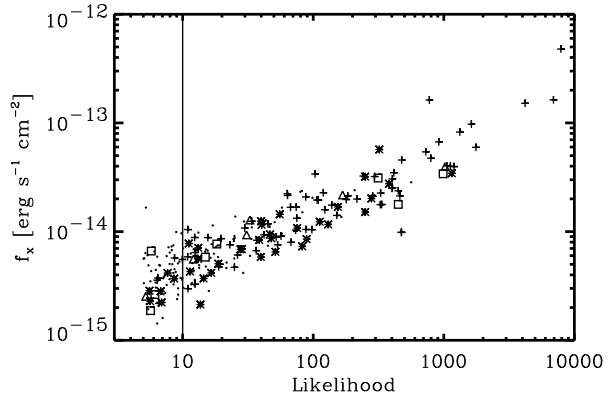
Figure 3.11: Likelihood vs. 0.2-10 keV X-ray flux of the 252 central X-ray sources (core sample, PN-detector exposure time ≥ 6 ksec). Crosses mark type I AGN, asterisks type II AGN, triangle galaxies, and rectangles stars. Dots indicate X-ray sources with no spectroscopic classification. The vertical line indicates $ML = 10$.

3.3.1 X-ray properties

By characterising X-ray sources using only their X-ray properties, we can reveal and study the existence of different X-ray populations and their features. Hardness ratios (see Sect. 3.1.1) are one of the simplest tools we can use to determine the spectral energy distribution in the X-ray regime.

In Fig. 3.12 ($HR2$ vs. $HR3$) we only plot those X-ray sources in an X-ray colour-colour diagram that have the $HR2$ error $\sigma_{\mathrm{HR2}} \leq 0.3$. Different spectroscopic classes occupy different regions in this X-ray colour-colour diagram. A notable separation in type I and type II AGN can be recognised. This result is in agreement with Mainieri et al. (2002) and Caccianiga et al. (2004). Type II AGN are spread over a much broader $HR2$ ($0.9 > HR2 > -0.6$). The lowest $HR2$ values for type II AGN overlap with the highest $HR2$ values for type I AGN. However, we do not see a large fraction of type II AGN occupying the $HR2$ range typical for type I AGN, as was reported by Della Ceca et al. (2004) for the XMM-Newton bright serendipitous survey. Figure 3.12 shows that $HR2$ is a good indicator for intrinsic absorption. The X-ray sources with $HR3 = -1.0$ correspond to non-detections in the 4.5-7.5 keV band. The objects with $HR3 > 0.4$ and soft $HR2$ values have $HR3$ errors ≥ 0.3 (small plot symbols). Therefore, it is likely that their deviation from the typical location of sources in the $HR2 - HR3$ diagram is caused by statistical fluctuations.
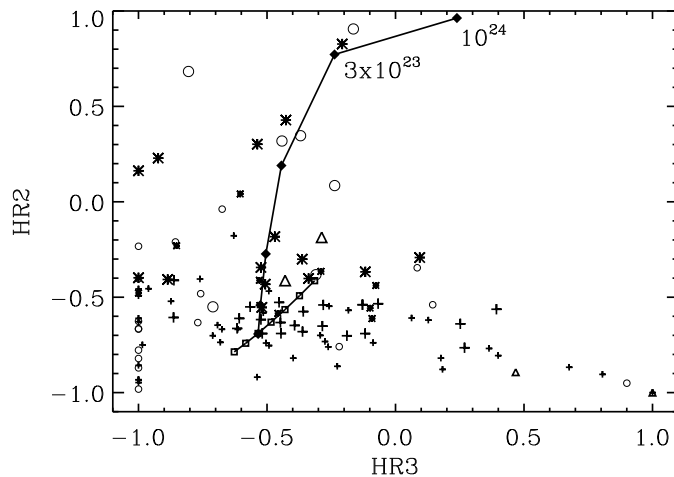
Figure 3.12: X-ray diagnostic diagram based on hardness ratios. $HR2$ is calculated by using the 0.5-2.0 keV & 2.0-4.5 keV band, $HR3$ 2.0-4.5 keV & 4.5-7.5 keV. Only core sample X-ray sources that have $\sigma_{HR2} < 0.3$ are plotted. Labels: crosses - 63 type I AGN, asterisks - 24 type II AGN, triangles - 4 galaxies, and open circles - 24 unidentified X-ray sources with $ML > 10$. Large symbols represent objects with $\sigma_{HR3} < 0.3$, small symbols $\sigma_{HR3} \geq 0.3$. The solid line with box symbols (at $HR2 \sim HR3 \sim -0.5$) represents an unabsorbed power-law X-ray spectrum (corrected for Galactic absorption) with different photon index $\Gamma = 2.4 - 1.2$ in steps of 0.2 (squares). Different hydrogen column densities ($N_H/\text{cm}^{-2} = 10^{20}, 10^{22}, 3 \times 10^{22}, 10^{23}, 3 \times 10^{23}, 10^{24}$; see Sect. 3.3.4) are plotted as a solid line with diamonds for $\Gamma = 2$ and $z = 1$.

The small number of optically normal galaxies spans a large range in $HR2$. Two have $HR2$ values that belong to the softest in the whole core sample. The other two have X-ray spectra similar to those of soft type II AGN or very hard type I AGN.

In addition to the spectroscopically classified objects, we also plot unidentified objects from the core region. Out of the 60 total unidentified X-ray sources, only 24 meet the selection criterion of $\sigma_{HR2} \leq 0.3$. Based on the rather clear separation between type I and II AGN, one may assign a likely classification to the yet unidentified sources. Among the 24 unidentified sources with reliable X-ray colours, the numbers of type I and type II AGN candidates appear to be similar.

3.3.2 Redshift distribution

Previous extensive studies of AGN in the Marano field enable us to compare these samples with our *XMM-Newton* detections. The optical survey by Zitelli et al. (1992) covers $\sim$0.7 deg^2. The selected quasars, which are all of type I, show an almost flat distribution in redshift (Fig. 3.13 a) up to $z = 2.8$. The *ROSAT* 0.2 deg^2 survey in the field (Zamorani et al. 1999) recovered most of the optically selected quasars at redshifts up to $z \sim 1.4$ (Fig. 3.13 b). The newly detected *ROSAT* AGN, with few exceptions, are type I AGN, which is expected due to the limited capability of *ROSAT* to detect absorbed
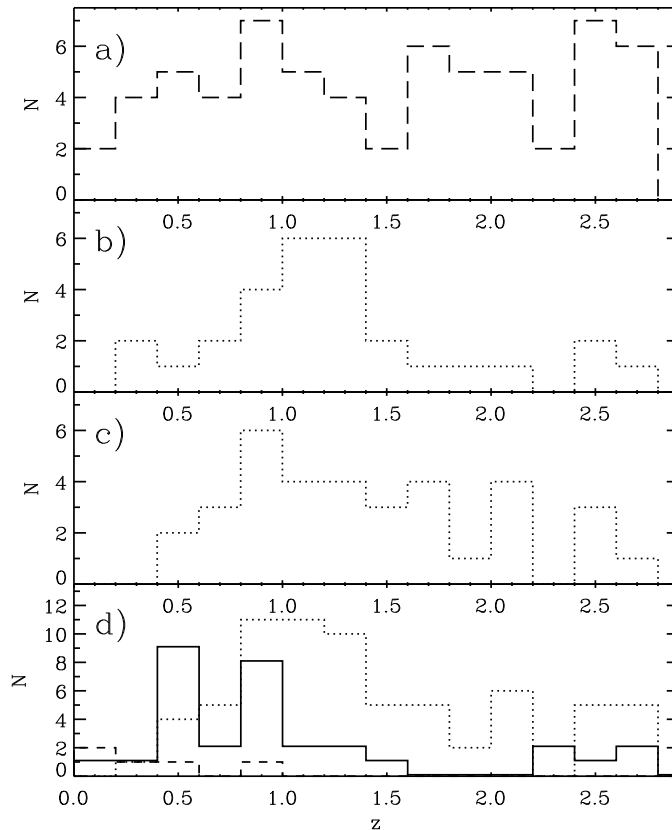
Figure 3.13: Redshift distribution of AGN in the Marano field. *a)* complete sample of 64 optically selected quasars ($B_{\rm J} \leq 22.0$) by Zitelli et al. (1992); *b)* ROSAT X-ray sources (29 type I AGN by Zamorani et al. (1999)); *c)* 35 type I AGN newly detected by XMM-Newton (core region); *d)* redshift distribution of the core sample: dotted line: all 70 XMM-Newton detected type I AGN, solid line: 31 XMM-Newton detected type II AGN, and dashed line: 5 XMM-Newton detected optically normal galaxies.

sources.

In the 0.28 deg^2 core region of the *XMM-Newton* survey we have detected 23 of the 29 broad emission line quasars of the optically selected sample of Zitelli et al. (1992). The detection rate of optically selected quasars remains constantly high over all redshifts. However, looking at the type I AGN newly discovered with *XMM-Newton* (Fig. 3.13 c), it is apparent that the X-ray selection tends to detect quasars at lower redshifts than the optical surveys. This is particularly obvious from the redshift distribution of the *ROSAT* detected quasars, representing the brightest X-ray sources in the field. But the mean redshift $z \sim 1.3$ of the *XMM-Newton* detected type I AGN is also lower than that of the optically selected sample $z \sim 1.5$, despite the fact that the *XMM-Newton* observations are deeper in terms of the surface density of quasars than the optical survey. Possible reasons for these differences are discussed in Sect. 3.5.

The redshift distribution according to the object class of the *XMM-Newton* detected
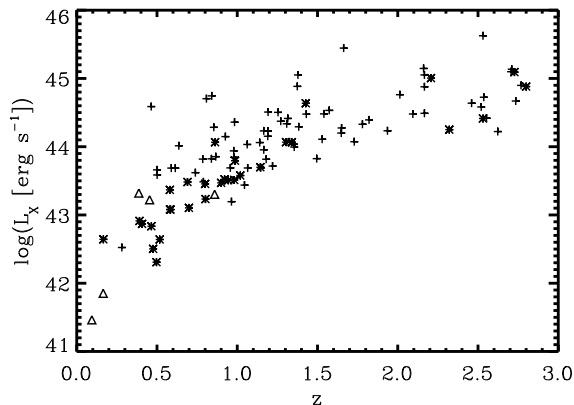
Figure 3.14: Observed rest-frame X-ray luminosity (0.2-10 keV) vs. redshift diagram of the Marano core sample. Labels: crosses - 70 type I AGN, asterisks - 30 type II AGN, and triangles - 5 galaxies.
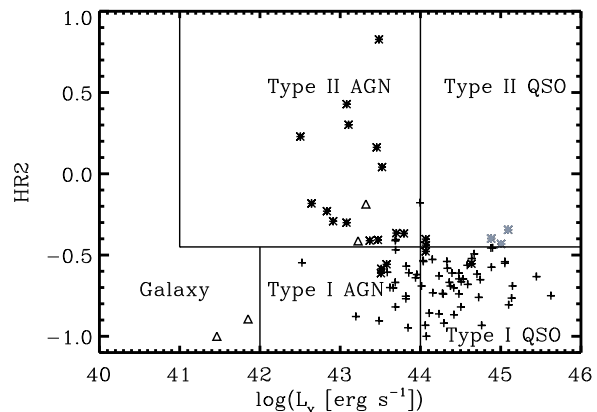
Figure 3.15: Observed rest-frame X-ray luminosity (0.2-1 keV) vs. hardness ratio. $HR2$ is calculated by using 0.5-2.0 keV & 2.0-4.5 keV bands. Only X-ray sources that have $\sigma_{HR2} < 0.3$ are plotted. Labels: crosses - 63 type I AGN, asterisks - 24 type II AGN (grey marked have $z \geq 2.0$), and triangles - 4 galaxies. The diagram separation into different regions is based on Szokoly et al. (2004) with an adjusted threshold in the $HR2$-value.

core sample is given in Fig. 3.13 d. We find that almost half of the new *XMM-Newton* sources are classified as type II AGN with redshifts mostly below 1.0. Type I AGN extend over a wide range of redshifts with a maximum at $z \sim 0.8 - 1.4$. Type II AGN are comparable to type I AGN in number density at low redshifts, but are mostly found below $z = 1$. Five type II QSOs at $z > 2.2$ have been classified. Optically normal galaxies without emission lines are found at $z < 0.9$.

High-redshift type II QSOs with intrinsic absorption are found to be indistinguishable from non-absorbed type I AGN on the basis of their X-ray spectral hardness ratios, since

3.3.3   Observed rest-frame X-ray luminosity

For the X-ray sources with measured redshifts the observed rest-frame X-ray luminosities can be computed. The coverage of the survey in redshift – observed X-ray luminosity space is plotted in Fig. 3.14. Szokoly et al. (2004) showed that the different object classes identified in X-ray surveys occupy different regions in a diagram of hardness ratios versus observed X-ray luminosities. In Fig. 3.15 we follow a scheme similar to that adopted by Szokoly et al. (2004) and consider objects with an X-ray luminosity $\log(L_X \, [\mathrm{erg/s}]) \geq 44.0$ as QSOs. The majority of type I AGN ($\sim 70\%$) are actually type I QSOs. Most of type II AGN ($\sim 71\%$) are low X-ray luminosity objects. Only type II objects with redshifts $z \geq 2.0$ (marked in grey in Fig. 3.15) have X-ray luminosities of type II QSOs.

the absorbed part of the spectrum is shifted out of the observable spectral window towards lower energies. This explains the emptiness of the upper right corner of Fig. 3.15 labelled 'Type II QSO', a classification that applies to low redshift objects only.

Optically normal galaxies show differences in their X-ray luminosity. The $HR2$-soft objects have very low X-ray luminosities. The two $HR2$-hard normal galaxies are found in the same region as the softest type II AGN, but are harder than type I AGN.

Szokoly et al. (2004) use $HR2 = -0.2$ as a threshold for the separation of type I and type II objects. Assuming a $\Gamma = 2$, this value corresponds to a hydrogen column density $N_{\mathrm{H}}/\mathrm{cm}^{-2} = 10^{22}, 10^{23}$ for $z = 0.25$ and 2.1, respectively. For their *Chandra* observation they computed L_{X} in the 0.5-10 keV band and their hardness ratio was based on the 0.5-2 keV & 2-10 keV bands. Because their definition of the X-ray bands differs from our study, the majority of their objects have higher hardness ratios (compared to our $HR2$). Furthermore, the *XMM-Newton* PN-detector, which was used for calculating the hardness ratios, has a higher efficiency in the 0.5-2 keV band compared to the *Chandra* detector. Therefore, we lowered the $HR2$ threshold from $HR2 = -0.2$ in Szokoly et al. (2004) to $HR2 = -0.45$. Our threshold corresponds to $N_{\mathrm{H}}/\mathrm{cm}^{-2} = 0.54 \times 10^{22}, 1.7 \times 10^{22}$, and 5.4×10^{22} for $\Gamma = 2$ and $z = 0.25, 1$, and 2.1. This is about two times lower than the N_{H} cut-off Szokoly et al. (2004) were using.

3.3.4 N$_{\mathrm{H}}$ column densities and de-absorbed intrinsic X-ray luminosities

The hardness ratio diagram (Fig. 3.12) supports the view that the majority of type II AGN and a small fraction of type I AGN are obscured sources. Hence, the observed X-ray luminosity does not represent the intrinsic object X-ray luminosity. The significant deficit of soft photons as compared to a power-law spectrum reflects the existence of an absorbing component that is expressed by the hydrogen column density N_{H}. For most of the sources the number of detected counts is not sufficient to extract a spectrum and fit a power-law model with N_{H} and the photon index Γ as free parameters. We therefore applied a technique that uses the measured hardness ratios to calculate the N_{H} value for each source with a set of fixed power-law indices.

Mainieri et al. (2002) found a mean value of $< \Gamma > \simeq 2$ for 61 type I and type II AGN in the Lockman Hole. The majority of type I and II AGN are found in the range of $\Gamma \simeq 1.7 - 2.3$. The finding is confirmed by Mateos et al. (2005). They find $< \Gamma > = 1.92$ with a $\sigma = 0.28$. Therefore, we used the observed PN-, MOS1-, and MOS2-hardness-ratios (0.2-0.5 keV, 0.5-2.0 keV, 2.0-4.5 keV, and 4.5-7.5 keV) and performed three runs to determine N_{H} with the values $\Gamma = 1.7, 2.0$, and 2.3 for all objects.

First of all, we computed a grid of model hardness ratios for all EPIC instruments with `Xspec` (Arnaud 1996; using the models `wabs`, `zwabs`, and `powerlaw`). As input we use the Galactic absorption along the line of sight in the field with $N_{\mathrm{H}} = 2.7 \times 10^{20}$ cm^{-2}, the redshift of the object and a grid of hydrogen column densities ($N_{\mathrm{H}} = 0$,

$N_{\mathrm{H}} = 10^{20+0.04\,a}$ cm^{-2}, $a \in N_0$, $a = 0..100$). We then computed the χ^2 values for the deviations of the measured hardness ratios and their model values, summed over the three instruments and the three hardness ratios $HR1$, $HR2$, and $HR3$. The procedure was applied only to those sources that had at least five out of nine hardness ratios with $\sigma HR_{\mathrm{obs,i}} < 0.7$.

The N_{H} of a source is determined by finding the minimum of

$$\chi^2(N_{\mathrm{H}}) = \sum_i \frac{(HR_{\mathrm{obs,i}} - HR_{\mathrm{model,i}}(N_{\mathrm{H}}))^2}{\sigma HR^2_{\mathrm{obs,i}}} \quad . \tag{3.5}$$

The models are based on the photon index $\Gamma = 2$. The statistical 1σ errors were derived from the range in N_{H}, where $\chi^2 < \chi^2_{\mathrm{min}} + 1$ (Lampton et al. 1976). For the error calculation we also took into account an intrinsic scatter in the photon indices. Its contribution to the N_{H} error was measured by finding the minimum χ^2 for each source in the grids calculated using $\Gamma = 1.7$ and $\Gamma = 2.3$. The resulting systematic errors were quadratically added to the statistical errors. The N_{H} values and the total errors are given in Table B.1. Due to the uncertainties in the N_{H} determination we regard all values with $N_{\mathrm{H}} \leq 10^{21}$ cm^{-2} as consistent with unabsorbed spectra.

We tested our procedure by performing an individual `Xspec` N_{H}-fit for the brightest type II AGN, which have sufficient X-ray data quality. The hardness ratios of 32A (z=2.727) indicate the highest absorption among the brightest type II AGN. A spectral fit with `wabs`, `zwabs`, `powerlaw`, and Γ as a free parameter determined $N_{\mathrm{H_{32A}}} = (10.0 \pm 3.5) \times 10^{22}$ cm^{-2} and $\Gamma_{32A} = (1.7 \pm 0.3)$. The best fit N_{H}, for a fixed value of $\Gamma = 1.7$, with the hardness-ratio χ^2-minimum fit is $N_{\mathrm{H_{32A}}} = (7.5\,^{+3.4}_{-2.8}) \times 10^{22}$ cm^{-2}. A spectral fit with a fixed $\Gamma_{32A} = 2.0$ results in $N_{\mathrm{H_{32A}}} = (13.4 \pm 2.5) \times 10^{22}$ cm^{-2}. The given N_{H} in Table B.1 was performed with the hardness-ratio χ^2-minimum fit and finds $N_{\mathrm{H_{32A}}} = (14.5\,^{+7.9}_{-8.2}) \times 10^{22}$ cm^{-2}. Hence, both fit methods give comparable results, at least for high SNR sources.

Figure 3.16 shows the computed hydrogen column densities for type I and type II AGN, as well as optically normal galaxies. As expected, the majority of type II AGN show absorption. However, 13% of the type II objects (51A, 132A, 133A, and 607A) have absorbing column densities $N_{\mathrm{H}} < 10^{21}$ cm^{-2}. All of the type II AGN discovered by Mainieri et al. (2002) in the Lockman Hole have absorbed X-ray spectra. The values for optically normal galaxies range from unabsorbed to moderately absorbed. Two of the unabsorbed galaxies have low X-ray luminosities ($L_{\mathrm{X}} < 10^{42}$ erg s^{-1}).

The computed hydrogen column density of type II AGN object 145A is the highest in our sample ($N_{\mathrm{H}} = 10^{24}$ cm^{-2}). Since this corresponds to the highest value in the model grid, no reliable error estimate can be given for this object. However, the extremely high column density for this object is confirmed by the fact that it is one of the few sources detected in the $4.5 - 7.5$ keV EPIC images, but it is not visible in the softer bands.

Based on the hydrogen column densities, we calculated the de-absorbed (intrinsic) X-ray luminosities by computing a correction factor for the observed X-ray flux. Figure 3.17 shows the comparison of the absorbed (a) and de-absorbed (b) X-ray luminosity distributions. Even after correcting the rest-frame X-ray luminosity, type II AGN have
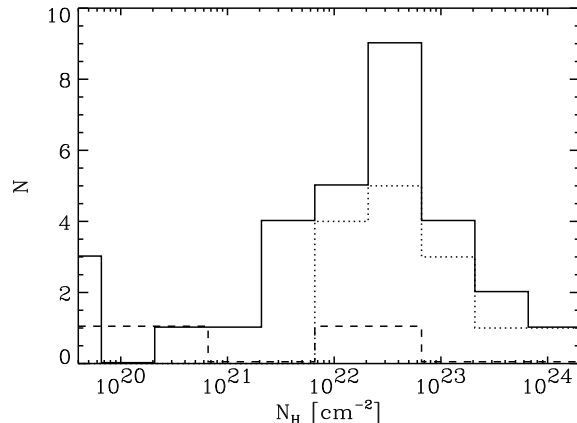
Figure 3.16: Calculated intrinsic hydrogen column density histogram for the Marano field core sample. The solid line shows the distribution of type II AGN that have reasonable fits in hydrogen column density. Objects with $N_H = 0$ are set to $N_H = 5 \times 10^{19}$ cm^{-2}. The dotted line represents only type II AGN that show intrinsic absorption with a significance higher than 2σ in hydrogen column density. Optically normal galaxies are plotted as a dashed line. Dotted line - 14 type I AGN; solid line - 30 type II AGN; dashed line - 5 galaxies.

Table 3.8: Fractions of absorbed sources in different X-ray luminosity bins based on Fig. 3.17 c. Only objects with $N_H > 2 \times \Delta N_H$ are selected.

	$43 \leq \log(L_X \,[\mathrm{erg/s}]) < 44$	$44 \leq \log(L_X \,[\mathrm{erg/s}]) < 45$	$\log(L_X \,[\mathrm{erg/s}]) \geq 45$
Type I	0% (0/19)	10% (4/42)	0% (0/8)
Type II	43% (6/14)	58% (7/12)	33% (1/3)

lower median X-ray luminosities than type I AGN, although type I and II AGN cover the same X-ray luminosity range. Contrary to the almost flat distribution of type II AGN with a median of $L_X \sim 10^{44}$ erg s^{-1}, type I AGN show a significant peak at $L_X \sim 10^{44.4}$ erg s^{-1} in observed (absorbed) and de-absorbed intrinsic X-ray luminosity. Type I AGN 5A exhibits the highest X-ray luminosity in our sample.

The hydrogen column density as a function of the intrinsic X-ray luminosity is shown in Fig. 3.17 c. Mainieri et al. (2002) suggest labelling the region defined by $N_H > 10^{22}$ cm^{-2} and $L_X > 10^{44}$erg s^{-1} as the "type II QSO region". They proposed this classification based on 61 AGN identified from XMM-Newton sources in the Lockman Hole. Following this classification our sample includes 10 type II QSOs.

In our case this region of the plot is also populated by nine type I QSOs, which formally have intrinsic hydrogen column densities $N_H > 10^{22}$ cm^{-2}. However, most of these detections of intrinsic N_H have low significance; only four of all type I QSOs show absorption at the 2σ level (see Table 3.8). For about half of the type II AGN, significant intrinsic absorption ($N_H > 2 \times \Delta N_H$) was measured, and no dependence of the absorbed fraction on luminosity is evident (Table 3.8).
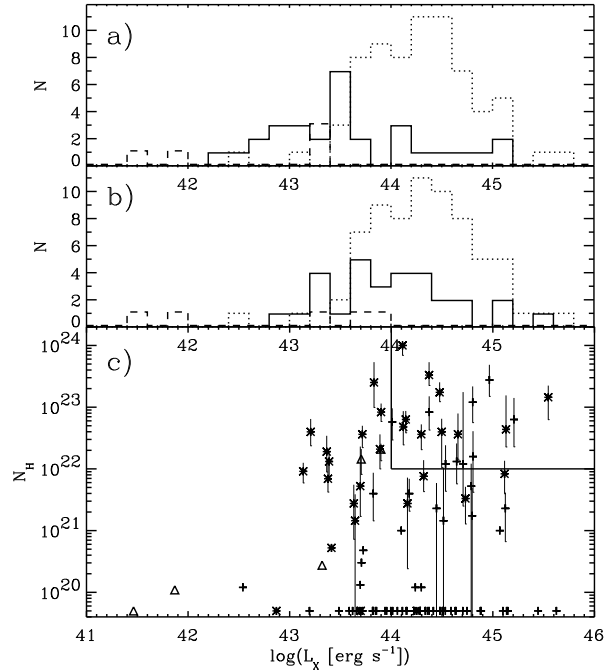
Figure 3.17: *a)* Histogram of the absorbed (observed) rest-frame X-ray luminosity (0.2-10 keV) for the core sample. Dotted line - 70 type I AGN, solid line - 30 type II AGN, and dashed line - 5 galaxies. *b)* Histogram of the rest-frame X-ray luminosity (0.2-10 keV) corrected for intrinsic absorption (core sample). Same notation as in a). *c)* De-absorbed intrinsic rest-frame X-ray luminosity (0.2-10 keV) vs. hydrogen column density (core sample). Crosses - type I AGN, asterisks - type II AGN, and triangles - galaxies. The upper right corner is suggested as being defined as the "Type II QSO region" by Mainieri et al. (2002). Objects with $N_{\mathrm{H}} = 0$ are set to $N_{\mathrm{H}} = 5 \times 10^{19}$ cm^{-2}.

3.3.5   X-ray-to-optical flux ratios

The ratio between X-ray flux and optical flux ($f_{\mathrm{X}}/f_{\mathrm{opt}}$) has been used in previous deep X-ray surveys to characterise the various X-ray emitting classes (Szokoly et al. 2004; Mainieri et al. 2002). To calculate $f_{\mathrm{X}}/f_{\mathrm{opt}}$ values we derived optical fluxes in a band centred at 7000 Å and with a width of 1000 Å using the equation $f_{\mathrm{opt}} = 10^{-0.4R-5.759}$ (Zombeck 1990). For the X-ray fluxes we used the 0.2-10 keV values (see Sect. 3.1.1).

The distribution of our core sample in the ($R - f_{\mathrm{X}}/f_{\mathrm{opt}}$)-plane is illustrated in Fig. 3.18. In general, type I AGN show higher X-ray fluxes and are brighter in the R-band. Type II AGN are found at lower X-ray fluxes and have fainter R-band counterparts. Two of the optically normal galaxies have X-ray-to-optical flux ratios similar to type I and type II AGN. Another two are among the objects with lowest X-ray-to-optical flux ratios in the sample.

Our type I and II AGN show a large variety in X-ray flux and R-band magnitude. They are detected at X-ray fluxes from $f_{\mathrm{X}} \sim 2 \times 10^{-15}$ to 5×10^{-13} erg cm^{-2} s^{-1} and in
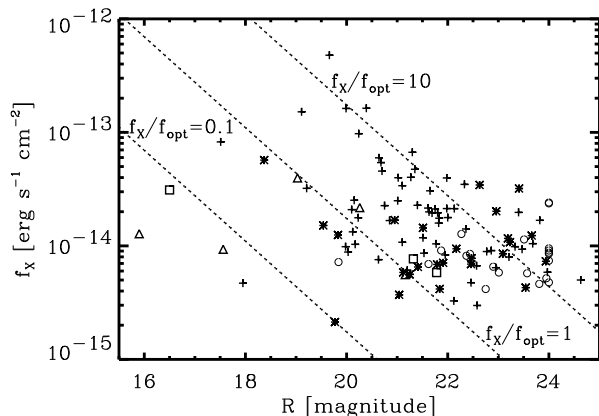
Figure 3.18: Observed rest-frame X-ray flux (0.2-10 keV) vs. R-band magnitude. Dashed lines indicate the f_X/f_{opt} values 0.1, 1.0, and 10. Labels: crosses - 63 type I AGN, asterisks - 25 type II AGN, triangles - 5 galaxies, rectangles - 3 stars, and circles - 21 spectroscopically unidentified sources (R-band lower limits are plotted as circles at $R=24$). Note that for a few objects of the core sample no WFI R-magnitudes were available and therefore these are not plotted here.
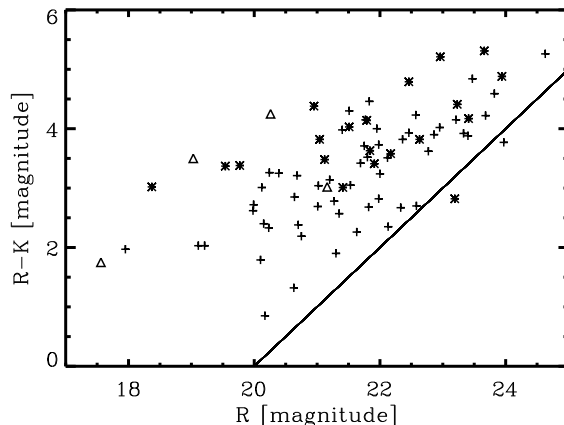
Figure 3.19: Colour magnitude diagram of spectroscopically classified X-ray sources. Labels: crosses - 56 type I AGN, asterisks - 20 type II AGN, and triangles - 4 galaxies. Only objects with detections in both R and K are included. The absence of blue, faint objects (below the solid line) is due only to the K-magnitude limit.

R-band magnitudes from $R \sim 18$ down to the detection limit of $R \sim 24$. There is one type I AGN (191A) at an unusually low value $f_X/f_{opt} = 0.04$, a factor of 100 below the mean value of type I AGN. The highest ratio in X-ray-to-optical flux is found for the type II AGN object 39A with $f_X/f_{opt} = 42.5$.

Most of the stars are found at star-typical $f_X/f_{opt} < 0.05$ with $R < 17$. Nevertheless, we also detected two M stars with $f_X/f_{opt} \sim 1$ and $R \sim 21.5$. Unidentified sources with WFI R-band data are added to Fig. 3.18. We plotted unidentified objects that have no detection in the R-band catalogue at $R = 24$.

3.3.6 Optical-to-near-IR colours

Figure 3.19 shows that type II AGN tend to be fainter and redder in the optical window than type I AGN. This figure shows a general trend for both type I and type II AGN to become redder for fainter R-magnitudes. The lack of faint blue objects can be explained by the K-band detection limit of K=20, beyond which our sample is not complete (see Fig. 3.7). However, the lack of bright red objects cannot be caused by any detection bias. The type II AGN have redder $R-K$ colours, although there is some overlap with the reddest type I AGN in the sample. These trends can be explained by an increasing contribution of the host galaxies for fainter type I AGN and type II AGN. The faint R-magnitudes
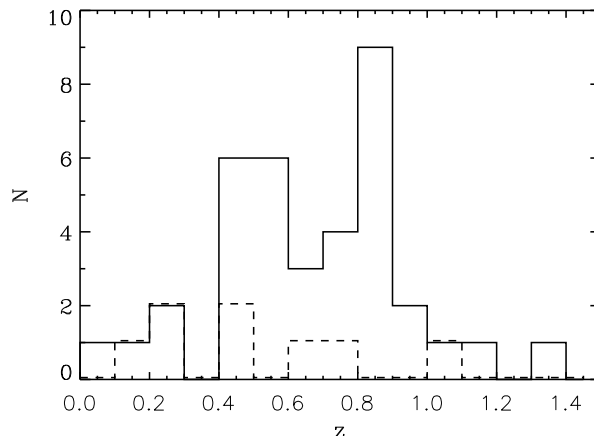
Figure 3.20: Redshift distribution of the additional objects. Labels: solid line - 37 NELGs, and dotted line - 8 optically normal galaxies.

and high $R - K$ values indicate higher optical obscurations in type II AGN. This is in agreement with previous X-ray studies of these objects that revealed a significantly higher ratio of absorbed to unabsorbed objects compared to type I AGN.

In our survey type I and type II objects do not separate as clearly as seen in a similar plot in Mainieri et al. (2002). Therefore, we checked whether the reddest and faintest type I objects are reliably classified. The most extreme type I objects are 69A, 84A, and 585A. Their optical spectra clearly show broad emission lines, but their continua are redder than typical type I spectra. In addition, object 585A shows only weak emission lines.

The optically normal galaxies are brighter in R-magnitudes than the typical type II AGN, but show similar $R - K$. All classified galaxies have $R < 21.5$. The majority of type II AGN and galaxies have $R - K > 3\,\text{mag}$, consistent with the spectrum of the host galaxy being the dominating component. A considerable fraction of type I AGN also have red $R - K$ colours. These are mostly low luminosity objects, where the host galaxy may also dominate the optical continuum.

3.4   Additional objects

In Table F.1 (Appendix F) we list objects in the Marano field that are not related to X-ray sources. These objects were spectroscopically investigated since slit positions on the multi-object spectroscopy masks were still available. The random selection of these additional objects, which follow a similar R-magnitude distribution as the sample of X-ray selected type II objects, is useful to investigate the redshift distribution of the field galaxies in the Marano field.

Figure 3.20 illustrates the redshift distribution of the additional non-X-ray emitting objects in the Marano field. Narrow emission line galaxies (NELGs) outnumber normal galaxies substantially. This is due to the fact that a large fraction of the spectra without

emission lines did not have sufficient SNR to determine a redshift. There is a non-X-ray emitting NELG peak at $z = 0.5 - 0.9$. At $z > 1.0$ the detection of NELGs and normal galaxies drops dramatically.

Despite the low number of objects, from Fig. 3.20 and Fig. 3.13 d we can compare the redshift distributions between X-ray emitting type II AGN and non-X-ray emitting NELGs. Both populations show more or less the same distribution up to $z = 1.2$. The two groups peak at $z = 0.5 - 0.9$.

The similar redshift distributions could mean that the X-ray emitting NELGs are drawn from the same population of galaxies as the control sample. On the other hand, the similar redshift distribution could also be due to a large fraction of false matches of NELGs to our X-ray sources. A detailed discussion of the number of false matches is given in Sect. 3.2.1 and shows that false matches make only a minor contribution to our sample of narrow line AGN.

3.5 Discussion

3.5.1 Type I AGN

In Sect. 3.3.2 we showed that the X-ray selected type I AGN peak at lower redshifts than the optically selected sample. It is interesting to see whether this difference in the redshift distributions is due to a redshift dependence of the QSO spectral energy distributions (SED). As a parameter which characterises the SED, we calculated the optical to X-ray broad band spectral index α_{OX} between the UV luminosity density at 2500 Å and the X-ray luminosity density at 1 keV (see Appendix B, description of the Table B.1).

No significant correlation of α_{OX} with redshift (Fig. 3.21) or X-ray luminosity can be found. However, there is a very significant ($P_{\mathrm{NULL}} < 10^{-6}$) correlation of the optical luminosity and α_{OX} (Fig. 3.22). This correlation has been found in various samples observed with *Einstein* (Avni & Tananbaum 1986), *ROSAT* (e.g., Green et al. 1995; Lamer et al. 1997), and *Chandra* (e.g., Steffen et al. 2006). For a large sample of optically selected AGN, Steffen et al. (2006) computed the bivariate linear regression coefficients of α_{OX} as a function of $\log(L_{\mathrm{opt}})$ and z. They find that α_{OX} is correlated with $\log(L_{\mathrm{opt}})$, but find no significant correlation with z (see also Avni & Tananbaum 1986 for similar results on earlier *Einstein* data).

If α_{OX} and optical luminosity are correlated, a non-linear relation between X-ray luminosity and optical luminosity is expected. Therefore, we plotted the X-ray luminosities versus the optical luminosity densities (Fig. 3.23) and computed the linear regression coefficients between $\log(L_{\mathrm{X}})$ and $\log(l_{2500\mathrm{A}})$. Both variables $\log(L_{\mathrm{X}})$ and $\log(l_{2500\mathrm{A}})$ are measured quantities and neither of them can be regarded as the independent or dependent variable. We used the ordinary least-squares (OLS) bisector algorithm as described by Isobe et al. 1990, which is symmetric regarding the choice of independent and dependent variable.

We find a best-fit regression $\log(L_{\mathrm{X}}) = (0.84 \pm 0.08) \times \log(l_{2500\mathrm{A}}) + (19.37 \pm 2.23)$.
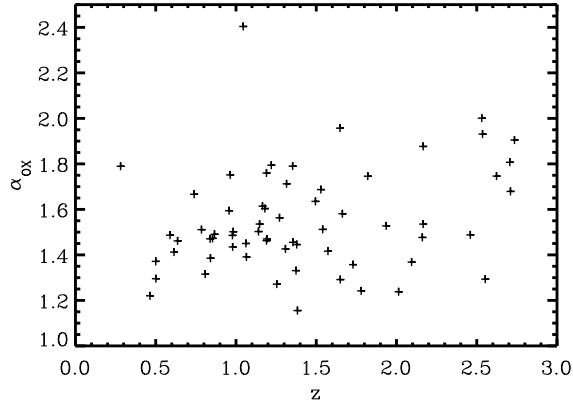
Figure 3.21: UV-to-X-ray spectral index α_{OX} vs. redshift for type I AGN in the core sample.
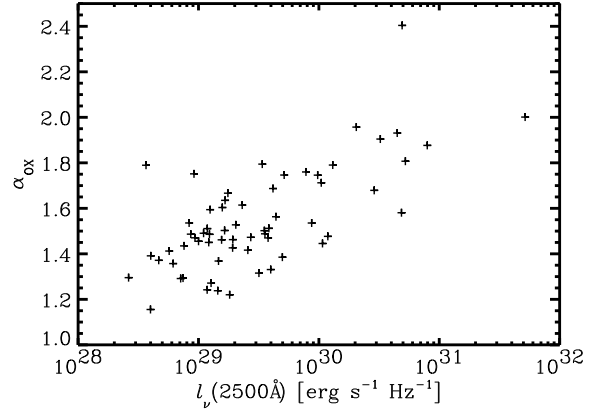
Figure 3.22: UV-to-X-ray spectral index α_{OX} vs. optical luminosity density at $2500\,\text{Å}$ for type I AGN in the core sample.

This slope is marginally (2σ significance) flatter than the $\beta = 1.0$ expected for a linear $L_X - l_{opt}$ relation. With the same method Steffen et al. 2006 find a slightly flatter slope $\beta = 0.721 \pm 0.011$.

A correlation flatter than $\beta = 1$ implies that the optical luminosities in the sample are spread over a wider range of values than the X-ray luminosities. This might explain the above-mentioned discrepancies of the redshift distributions of X-ray and optically selected QSOs. The low luminosity objects are more likely to be detectable in X-rays, while the highest luminosity objects are relatively more luminous in the optical, and therefore detectable at higher redshifts in optical surveys.
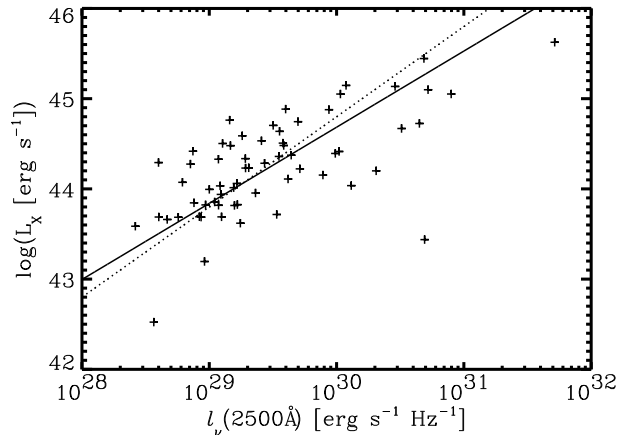
Figure 3.23: Observed 0.2-10 keV rest-frame X-ray luminosity vs. optical luminosity density at 2500 Å for type I AGN in the core sample (crosses). The solid line indicates the best-fit linear regression with a slope $\beta = 0.84$. The dotted line with slope $\beta = 1$ marks a linear $L_X - l_{opt}$ relation.

3.5.2   Type II AGN

Figure 3.13 d shows that most type II AGN are found at redshifts $z \sim 0.5 - 0.9$, with a few objects at $z > 2.2$. No type II objects were identified in the redshift range $z \sim 1.5 - 2.2$. The interesting question is whether this redshift gap reflects the intrinsic distribution or is due to an observational bias.

Type II AGN show only narrow emission lines and the optical continuum radiation is dominated by the host galaxy. The spectroscopic classification of X-ray sources relies on emission lines like Lyα, C IV, C III, Mg II, O II, and others. Analysis of the optical spectra of type II AGN with $z > 0.6$ in our sample, in Szokoly et al. (2004), and in Caccianiga et al. (2004) indicates that almost all objects show no Mg II emission lines. Only in a few cases marginal Mg II emission is identified. Effectively, no strong spectral features are present in the wavelength range between 1909 Å (C III]) and 3727 Å ([O II]).

Since the UV host galaxy continuum is usually very faint, the detection of type II AGN in optical imaging is already hampered by the lack of a strong UV continuum and emission lines, if the imaging band-pass falls into this rest frame range. For R-band imaging (5800-7300 Å) this is the case for the redshift range $z \sim 1.0 - 2.0$. Our multi-object spectroscopy covers a useful range of $\sim$4000 - 9000 Å. This range is reduced if an object is not centred on the mask, but offset from the centre in the dispersion direction. Hence, in many cases only one emission line would be detectable for type II AGN in the redshift range $\sim 1.0 - 2.0$. With a low SNR spectrum this would usually not be sufficient for a clear spectroscopic classification. For a few sources, which were undetected or very faint in the R-band images, we were able to position a MXU slit using the K-band counterparts (e.g., 20A, 63A, and 463A). In all of these cases a high redshift type II AGN could be identified.

Figure 3.12 supports the assumption that a large fraction of the unidentified sources are type II AGN. Above $HR2 = -0.1$ only type II AGN are found as counterparts for classified X-ray sources. In this region 50% of the X-ray sources are not classified and are expected to be type II AGN. Furthermore, Fig. 3.18 gives more evidence that the unidentified sources overlap with the type II AGN region. A ratio $f_X/f_{opt} > 0.5$ is clearly a sign of AGN activity, since normal galaxies and stars usually have $f_X/f_{opt} < 0.05$. Both type II AGN and unidentified objects are found at AGN-typical f_X/f_{opt}, with low X-ray fluxes and faint optical counterparts.

We conclude that the majority of the unidentified X-ray sources are likely to be type II AGN, most of them presumably with redshifts $z > 1$. Therefore, the intrinsic redshift distribution of type II AGN is uncertain. The number of unidentified sources is sufficient to fill the observed gap between $z \sim 1.0 - 2.0$.

3.5.3   X-ray bright optically normal galaxies

Five objects in the core sample have been spectroscopically classified as galaxies without any emission lines. The soft X-ray radiation of the low X-ray luminosity galaxies (objects 120A, 241A) can be explained by a halo of X-ray emitting hot gas around elliptical galaxies

(Sarazin 1997; White & Davis 1998). Three optically normal galaxies have X-ray-to-optical flux ratios and X-ray luminosities typical of AGN. Objects of this type have been named X-ray bright optically normal galaxies (XBONGs; Comastri et al. 2002). The objects 8A, 49A, and 204A have intermediate redshifts ($0.3 < z < 0.9$) and fairly high X-ray luminosities ($\log(L_X \, [\text{erg/s}]) > 43$), rather hard X-ray spectra, and faint optical counterparts ($R > 19$). The high X-ray luminosities and $f_X/f_{\text{opt}} \sim 1$ indicate active nuclei. The computed hydrogen column densities show moderate absorption.

The properties of our XBONGs are in agreement with other studies (Silverman et al. 2005; Severgnini et al. 2003). Even though different scenarios are discussed, the nature of XBONGs still remains unclear (Brandt & Hasinger 2005). Comastri et al. (2002) assume that the non-detection of optical emission lines and the hard X-ray colours are due to a heavily absorbed AGN embedded in a galaxy whose X-ray emission is due to a scattered/reprocessed nuclear component. The three XBONGs do not show harder $HR2$ values than type II AGN and also do not have the highest column densities of the AGN sample. Hence, a heavily absorbed AGN without scattered/reprocessed X-ray radiation is ruled out. Scattered or reprocessed radiation is necessary to explain the X-ray and optical observations. Following Komossa et al. (1998), the observed X-ray luminosity of a scattered emission by a warm reflector is only a hundredth or thousandth of the intrinsic X-ray luminosity. For our objects with observed $\log(L_X \, [\text{erg/s}]) \sim 43 - 44$, this would require intrinsic X-ray luminosities of $\log(L_X \, [\text{erg/s}]) \sim 45 - 47$, which would make them by far the most luminous X-ray emitters in the sample.

Another possible explanation for these objects is given by Severgnini et al. (2003). They studied three low redshift XBONGs with $\log(L_X \, [\text{erg/s}]) \sim 42 - 43$ and find N_H values similar to our sample. In their interpretation the faint emission lines of an obscured or unobscured AGN up to an intrinsic $\log(L_X \, [\text{erg/s}]) \sim 43$ can be overwhelmed by a host galaxy with an absolute magnitude $M_R \geq -22$. However, XBONGs 8A and 49A are not consistent with the scenario mentioned. The AGN of 49A with an intrinsic $\log(L_X \, [\text{erg/s}]) = 43.7$ should be optically too bright to be hidden by a galaxy of $M_R = -21.8$. Moreover, source 8A, which is also detected as a radio source (Gruppioni et al. 1997), has an intrinsic $\log(L_X \, [\text{erg/s}]) = 43.9$. Therefore, it is more X-ray luminous by almost one order of magnitude than the examples in Severgnini et al. (2003). The absolute magnitude of the host galaxy is $M_R = -22.6$, but an optically much brighter galaxy is needed to hide the emission lines of such a powerful AGN. By adding a template type I spectrum to the measured spectra of objects 8A and 49A, we estimated that any hidden type I AGN in these objects would have α_{OX} values of ~ 0.8 or less.

Regarding the X-ray and optical colours, our XBONGs are very similar to type II AGN. Therefore, it is likely that these sources have a narrow line type II spectrum, which is intrinsically weak or dust absorbed and not detected above the continuum of the host galaxy. This result is consistent with Caccianiga et al. (2004), who state that more accurate re-observation (high resolution data and/or better spectral coverage) of hard X-ray emitting galaxies will reveal narrow emission lines and, therefore, their real AGN nature. Severgnini et al. (2003) also claim possible misclassification of type II AGN as XBONGs. However, some of these objects are still classified as XBONGs after a high resolution ob-

servation with better spectral coverage.

As for type II AGN, the observed redshift distribution of XBONGs could be due to an observational bias. XBONGs are found with brighter R-magnitudes than typical type II AGN up to $z = 1$. But missing emission line features make them optically even more difficult to identify than type II AGN. For a reliable classification they have to be optically brighter, thus limiting their maximum redshift.

3.5.4   Stars

In the Marano field survey 7% of the X-ray sources are identified with Galactic stars. As in other deep surveys, these are typically G, K, and M stars, whose X-ray emission is caused by magnetic activity (Brandt & Hasinger 2005). Two sources classified as stars have $f_X/f_{opt} \sim 1$ (Fig. 3.18), which is more typical for AGN. However, we carefully reanalysed the X-ray colours, optical properties, and the optical image. Apart from the unusually high f_X/f_{opt} all existing evidence suggests M stars as reliable counterparts for both X-ray sources.

Chapter 4

X-ray absorption in distant type II QSOs

In Sect. 3.5.2 we demonstrated that we successfully classified a significant number of very rare high redshift type II QSOs by the additional use of the K-band data. This is a notable result for an X-ray survey with only 120 ksec good observation time (exclusion of observation time with high background) and a large fraction (50%) of incomplete optical coverage.

In terms of detected high redshift type II QSOs (five objects with redshift $z > 2.2$), the *XMM-Newton* Marano field survey is comparable to the deepest X-ray surveys performed with *XMM-Newton* and *Chandra*. For example, Szokoly et al. (2004) detected in their 1 Msec observation of the *Chandra* Deep Field South 13 type II QSOs with $z > 2$. Their counterpart selection is based on a limiting magnitude $R \simeq 24.5$ (turnover magnitude minus 0.5 mag). In addition, they have a complete coverage of their $\sim 0.05 \deg^2$ survey. Type II QSOs play an important role in understanding the X-ray universe. Since they show significant absorption, type II QSOs/AGN are considered to be a main contributor to the hard X-ray background and their existence in considerable numbers is needed for the synthesis of the X-ray background (Gilli et al. 2007). The possible evolution of the absorption with intrinsic luminosity and/or redshift is a matter of intensive debate and would essentially influence the X-ray background synthesis models.

Many papers discuss the fraction of absorbed AGN as a function of luminosity and/or redshift, and this is a highly controversial subject (Dwelly & Page 2006; Tozzi et al. 2006; Akylas et al. 2006). However, there are only a few studies (e.g. La Franca et al. 2005) which investigate the evolution of column densities in type II AGN up to high redshift. The majority of these studies focus on the local universe, where the existence of so-called Compton-thick objects is well known (Maiolino et al. 1998; Bassani et al. 1999; Risaliti et al. 2000). A Compton-thick object is absorbed by column densities of $N_H > 1.5 \times 10^{24} \, \mathrm{cm}^{-2}$, so that at this N_H the photo-electric absorption equals the Compton-scattering. Under these conditions only the reflected X-ray component is still observable.

There is evidence for a large fraction of Compton-thick AGN at high redshifts

(Martínez-Sansigre et al. 2007), but only one candidate has been claimed so far at high redshift (Norman et al. 2002), and even in this case the column density is quite uncertain. Most of the X-ray sources from deep *Chandra* and *XMM-Newton* surveys are absorbed by column densities $10^{21} < N_H < 10^{23}$, with hard X-ray luminosities of $10^{42} < L_{X_{INT}} < 10^{44}$ (Comastri 2004; Szokoly et al. 2004; Mainieri et al. 2002; Mateos et al. 2005). These values are typical for Compton-thin ($10^{21} < N_H < 10^{24}$) Seyfert II galaxies at low redshifts.

The *XMM-Newton* Marano field survey in combination with other *XMM-Newton* surveys offers the unique possibility to study the evolution of absorption in distant type II QSOs with redshift, and the dependence with X-ray luminosity. Possible trends are lively debated. The problem can only be addressed with a large number of optically secure classified type II QSOs.

The strategy followed here is to determine the counterparts to X-ray sources and analyse their X-ray spectra in the case of positive classification of type II QSOs. Ptak et al. (2006) followed an inverse approach. They selected type II QSOs from the Sloan Digital Sky Survey and checked the existence of X-ray observations in the public archives of *XMM-Newton* and *Chandra*.

This chapter focuses on properties of type II QSOs found in medium deep surveys performed by us. The study was submitted to A&A (Krumpe et al. 2007a). It is organised as follows. In Sect. 4.1 I describe how I became involved in the different surveys. The selection of the type II QSO candidate sample is given in Sect. 4.2. The study of their X-ray and optical properties is summarised in Sect. 4.3. The X-ray data and the extraction of the X-ray spectra are described in Sect. 4.4. Since X-ray spectra with small numbers of counts have to be fitted, I studied different fitting and binning methods in Sect. 4.5 and then describe the analysis of the X-ray spectra. The results are discussed in Sect. 4.6.

Unless mentioned otherwise, all errors refer to a 68% confidence interval. I assume $H_0 = 70\,\mathrm{km/s/Mpc}$, Ω_M=0.3, and Ω_Λ=0.7.

4.1   The SSC XID programme

A significant part of the data studied in this chapter originates from the involvement of the Astrophysical Institute of Potsdam (AIP) in the XID programme of the *XMM-Newton* Survey Science Center (SSC). Therefore, I will briefly explain AIP's role in the SSC and the XID programme.

The SSC was established to take the responsibility within the *XMM-Newton* project in four main areas:

- development of science analysis software for *XMM-Newton*

- pipeline processing of all *XMM-Newton* observations

Table 4.1: Extragalactic XID programme sample parameters. The table is taken from Watson et al. (2001).

Sample	Flux/$\mathrm{erg\,cm^{-2}\,s^{-1}}$ 0.5-4.5 keV	Sky density $\mathrm{deg^{-2}}$	# EPIC fields	expected R-mag of counterparts
Faint	$> 10^{-15}$	2200	5-10	23-25
Medium	$> 10^{-14}$	340	30-50	21-23
Bright	$> 10^{-13}$	10	1000	17-21

- compilation of the *XMM-Newton* Serendipitous Source Catalogues

- follow-up/identification programme for the *XMM-Newton* serendipitous X-ray sky survey: the XID programme

The SSC consortium was selected by ESA in early 1996 (Watson et al. 2001). It is an international collaboration involving a consortium of ten institutions in the UK, France and Germany. The AIP is one of the institutions. Major contributions of the science analysis software for *XMM-Newton* were coded at the AIP. For example, Dr. Georg Lamer maintains the source detection software. In addition, the AIP is involved in the XID programme.

The high throughput, large field of view, and good imaging capabilities of *XMM-Newton* means that in addition to the primary target of the observation, significant numbers of serendipitous X-ray sources are detected in each pointing. The XID programme aims to ensure that the full potential of the *XMM-Newton* serendipitous source survey is achieved for benefit of the scientific community. The programme is exclusively based on public *XMM-Newton* data. The main components of the XID programme are the optical imaging as well as the spectroscopy of well-defined samples from selected *XMM-Newton* fields, in order to characterise their X-ray source population (e.g. AGN luminosity functions, absorption distribution and evolution, and the relationship between optical emission line and X-ray spectral properties, discovery of new, rare classes of sources). The XID programme aims to provide large enough samples to get 10 objects per sample even for minority objects which present 1% of the *XMM-Newton* source population. Therefore, a sample of 1000 spectroscopically classified objects is aimed for three flux ranges at high Galactic latitudes (Table 4.1). In addition to the extragalactic survey, the SSC is also carrying out a Galactic identification programme down to $f_{\mathrm{X},0.5-4.5\,keV} = 5 \times 10^{-15}\,\mathrm{erg\,cm^{-2}\,s^{-1}}$. The results of the *XMM-Newton* Serendipitous Survey Bright Sample were published in Della Ceca et al. (2004).

The *XMM-Newton* Serendipitous Medium Sample is studying the flux range of the bulk of the objects that contribute to the cosmic X-ray background. The spectroscopic classification is provided by 'An *XMM-Newton* International Survey' (AXIS, Barcons et al. 2002, 2007; Carrera et al. 2007) for the northern hemisphere and the '*XMM-Newton*-2dF wide angle survey' (XWAS, Tedds et al. 2007) for the southern hemisphere.

The AXIS programme includes 1433 serendipitous sources over $4.8\,\mathrm{deg}^2$. The follow-up observation were carried out at the Observatorio del Roque de los Muchachos, Canary Islands, Spain.

XWAS made use of the 2dF multi-fibre spectroscopic facility at the Anglo-Australian Telescope. More than 3000 X-ray sources from 27 *XMM-Newton* pointings with fluxes above $f_{\mathrm{X},0.5-4.5\,\mathrm{keV}} \sim 10^{-14}\,\mathrm{erg\,cm^{-2}\,s^{-1}}$ and optical counterparts brighter than $V \sim 21$ (identified using SuperCosmos, Hambly et al. 2001) were observed. The resulting sky area of the *XMM-Newton* observation was $\sim 11\,\mathrm{deg}^2$. I became involved in the XWAS programme by analysing a significant fraction of the ~ 3000 optical follow-up spectra. 978 serendipitous X-ray sources could be spectroscopically classified. We found 641 (65.5%) broad emission line AGN, 157 (16.1%) narrow emission line galaxies, 57 (5.8%) optically normal galaxies, and 123 (12.6%) stars.

Compared to the *XMM-Newton* Marano field survey the *XMM-Newton* Serendipitous Medium Sample detected a similar fraction of broad emission line AGN and optically normal galaxies. However, it classified many more stars and fewer narrow emission line galaxies. This result can be explained by the fact that the *XMM-Newton* Marano field survey is (compared to *XMM-Newton* Serendipitous Medium Sample) a pencil-beam survey, with much deeper X-ray and optical observations (see Fig. 3.1). Therefore, the wide-angle Medium sample contains more low surface density but optically bright X-ray active stars and fewer faint narrow emission line galaxies. The redshift distributions of the latter peaks at $z = 0.3$ in the *XMM-Newton* Serendipitous Medium Sample data and decreases significantly towards higher redshifts. Nevertheless due to its large area, it is able to detect very rare high redshift type II QSOs that are optically bright. The *XMM-Newton* Marano field survey and the *XMM-Newton* Serendipitous Medium Sample are complementary X-ray surveys, which are both able to detect type II QSOs.

4.2 Definition of the type II QSO sample

The type II QSO candidates discussed here were taken from three different X-ray surveys, the *XMM-Newton* Marano field survey (Krumpe et al. 2007c), the *XMM*-2dF wide angle survey (XWAS, Tedds et al. 2007), and from 'An *XMM-Newton* International Survey' (AXIS, Barcons et al. 2002, 2007; Carrera et al. 2007). To obtain a well-defined sample with secure optical type II classifications and X-ray counterparts I applied a two stage process. I began with a list of 51 spectroscopically classified type II QSO candidates which are associated with X-ray sources. All optical counterparts have $z \geq 0.5$ and observed rest-frame X-ray luminosities (not corrected for intrinsic absorption) of $\log(L_{\mathrm{X_{OBS}}}\,[\mathrm{erg/s}]) > 42.5$.

First, I visually inspected the optical spectra of all type II QSO candidates from all X-ray surveys and determined the FWHM of the emission lines. The type II QSO candidate classification was only based on the optical spectra. Hao et al. (2005) provided a formal separation criterion between type I and II objects by finding a bimodal distribution in the Hα-FWHM with a significant dip at FWHM(Hα)=1200 km/s in the SDSS spec-

tra. The spectral resolution of the optical setup was $\sim$1050 km/s for the Marano field survey, $\sim$700 km/s for XWAS, and $\sim$300-600 km/s for AXIS. Therefore, an intrinsic line of 1200 km/s was observed with $\sim$1250-1600 km/s. We defined emission lines with an instrumental resolution of FWHM $\leq$ 1500 km/s as narrow. Objects with broad emission lines were rejected.

Common AGN high excitation lines such as [O III] or [Ne V] were used to distinguish between type II QSO candidates and normal/starburst galaxies. Objects with no high excitation lines were also rejected.

I introduced two different categories of type II QSO candidates based on the reliability of the type II classification. Objects that have spectra with high excitation lines and at least one permitted AGN emission line that is detected but narrow (e.g. Lyα, C IV, Hβ) are marked with the optical flag 'S' (see Table 4.2) - signifying a secure optical classification. Their optical classification is very robust.

Objects with less secure type II classification belong to the tentative sample (optical flag 'T'). The classification as tentative object can be due to the following reasons:

- The optical spectra show narrow emission lines, common AGN high excitation lines, but no Mg II emission. Only [Ne V] and [O II] are detected in the spectra. The presence of a common AGN high excitation line ([Ne V]) without a broad Mg II suggests the classification as a type II QSO candidate. However, since no other permitted emission line is accessible, a secure type II classification cannot be established.

- Common AGN high excitation lines are narrow but show indications of underlying broad components (optical spectra in Appendix H). These objects are likely to be transition objects between Seyfert type II / type I.

- The signal-to-noise ratio of the Hβ line, or its coincidence with the atmospheric band prevents a robust determination of the FWHM and could hide a weak but broad Hβ component.

For all sources in the tentative sample we give an individual comment below Table 4.2. After inspection of the optical spectra we were left with 14 secure objects and 12 type II objects that belong to the tentative sample.

As a second step to setting up a well-defined type II QSO sample, I verified that the spectroscopically classified counterpart is associated with the X-ray source. For a significant number of objects much deeper imaging data have become available subsequent to the epoch when the spectra were obtained. For example, the XWAS optical counterparts were originally selected from SuperCosmos optical imaging survey data (Hambly et al. 2001). For the majority of the objects we now have additional, deeper imaging data in different bands. These imaging data were obtained with the Wide-Field-Imager (WFI, 2.2 m telescope at La Silla) or the Wide-Field-Camera (WFC, 2.5 m Isaac Newton telescope on La Palma). I visually investigated the best available imaging data (WFI, WFC,
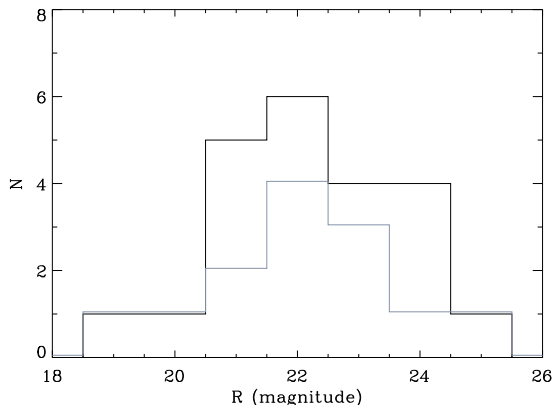
Figure 4.1: *R*-band magnitude histogram of all 22 type II QSO candidates (black) and of the 13 secure type II QSO candidates in grey.
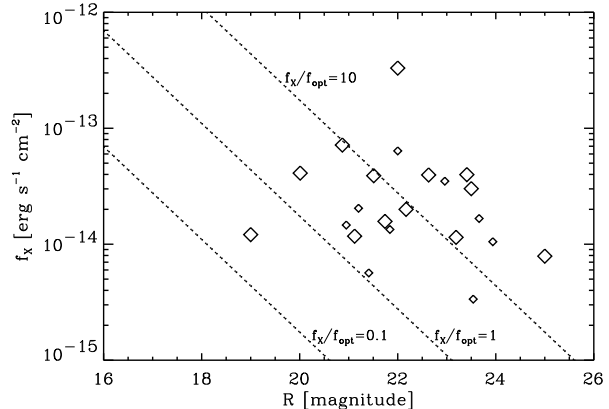
Figure 4.2: Observed 0.5-10 keV X-ray flux vs. *R*-band magnitude. Large symbols represent secure type II QSO candidates while small symbols illustrate tentative type II QSO candidates. Dashed lines indicate $f_{\mathrm{X}}/f_{\mathrm{opt}}$ values of 0.1, 1, and 10.

SuperCosmos) for additional optical counterparts and rejected doubtful counterpart identifications. Furthermore, I computed the probability that the optical object with the *R*-band magnitude m_{R} is associated with the X-ray source. This was based on Eq. 3.4 (see Sect. 3.2.1). Most of our optical counterparts have probabilities of $> 95\%$ that they are associated with the X-ray source. We rejected objects that have probabilities of less than 65%. All objects in the secure sample have probabilities $\geq 83\%$.

After the X-ray counterpart verification our sample consists of 22 sources including 13 secure and 9 tentative objects. The separation between AGN and QSOs was made during the determination of the de-absorbed intrinsic X-ray luminosity (see Sect. 4.5).

4.3 Properties of the type II QSO candidate sample

In Table 4.2 I summarise the observed properties of the objects. I list the name of the spectroscopically classified counterpart, optical coordinates, distance between spectroscopically classified counterpart and X-ray source, the WFI-*R*-band magnitude (unless otherwise mentioned), redshift, optical flag, X-ray counterpart probability, count rate, 0.5-10 keV flux, and the Galactic absorption along the line of sight.

The objects cover a redshift range of $0.5 \leq z \leq 3.278$. Since the lack of emission lines in a wide optical wavelength range hampers the identification of type II objects, I only have one type II QSO candidate in the redshift interval of $z = 1 - 2$. Figure 4.1 shows the *R*-band magnitude histogram of the selected objects. As a simplification we consider the *r*-band (SDSS) magnitude to be equal to the *R*-band magnitude, although we are aware

Table 4.2: Observed properties of the type II QSO sample

(1) No	(2) RA	(3) DEC	(4) $r_{\rm ox}$ [arcsec]	(5) R	(6) z	(7) Opt. flag	(8) XID probab.	(9) CR [ks^{-1}]	(10) Flux 10^{-14} [$\mathrm{erg\,s^{-1}\,cm^{-2}}$]	(11) $N_{\rm H_{GAL}}$ 10^{22} [$\mathrm{cm^{-2}}$]
Marano 9A	3 15 09.9	-55 13 13	1.18	22.63	1.427	secure	0.99	21.3±0.9	3.957	0.027
Marano 20A	3 16 21.5	-55 17 59	0.63	23.5^E	2.207	secure	0.97^K	17.1±1.3	3.014	0.027
Marano 32A	3 15 47.0	-55 17 55	1.44	22.96	2.727	tentative	0.99	12.5±0.9	3.497	0.027
Marano 39A	3 13 39.7	-55 01 51	0.95	23.41	0.862	secure	0.98	19.8±1.5	3.982	0.027
Marano 47A	3 15 38.7	-55 10 44	1.34	23.94	0.900	tentative	0.95	4.5±0.5	1.051	0.027
Marano 50A	3 14 09.9	-55 17 46	1.25	23.66	0.986	tentative	0.96	7.6±0.7	1.667	0.027
Marano 51A	3 16 30.6	-55 15 03	1.83	20.95	0.58	tentative	0.98	10.4±1.0	1.463	0.027
Marano 63A	3 15 16.9	-55 06 02	1.25	23.19	2.800	secure	0.97	7.2±0.7	1.147	0.027
Marano 66A	3 15 00.7	-55 07 18	1.23	21.41	0.981	tentative	0.99	4.0±0.6	0.566	0.027
Marano 116A	3 16 20.7	-55 16 52	1.30	21.2^E	0.581	tentative	0.99^K	5.4±0.9	2.043	0.027
Marano 133A	3 14 26.2	-55 21 13	1.02	23.54	2.321	tentative	0.92	2.7±0.6	0.336	0.027
Marano 171A	3 13 51.4	-55 02 56	2.18	22.17	0.800	secure	0.86	5.8±0.8	1.998	0.027
Marano 224B	3 13 04.8	-55 16 04	1.70	21.51	0.690	secure	0.96	8.9±1.2	3.899	0.027
Marano 253A	3 14 38.0	-55 06 50	2.64	21.84	0.517	tentative	0.65	2.6±0.5	1.341	0.027
Marano 463A	3 16 25.3	-55 08 39	0.55	25.0^E	2.531	secure	0.98^K	3.1±0.8	0.789	0.027
Marano 610A	3 15 51.8	-55 12 22	1.25	21.12	0.699	secure	0.98	3.6±0.6	1.173	0.027
X21516_135	2 26 26.7	-04 36 56	0.90	21.74^r	3.278	secure	0.91	0.9±0.2	1.574	0.025
X00851_154	22 15 41.6	-17 37 54	0.64	19.00	2.976	secure	0.96	1.7±0.2	1.210	0.023
X01135_126	1 52 57.6	-14 08 40	0.91	20.87^{UK}	0.543	secure	0.97^{WFC}	10.5±0.5	7.167	0.015
X03246_092	0 43 46.0	-20 29 56	2.31	20.01^{UK}	0.500	secure	0.83^{WFC}	3.2±0.8	4.104	0.015
phl5200-001	22 28 26.4	-05 18 20	0.63	22.0^r	0.711	secure	0.99^{WFC}	50.0±1.2	33.03	0.053
sds1b-014	2 18 43.0	-05 04 37	0.80	22.0^r	0.962	tentative	0.98^{WFC}	6.1±0.4	6.380	0.026

Comments for Table 4.2:

E – FORS pre-imaging magnitude estimate; cross-calibrated with WFI-R-band magnitude catalogue; magnitude error estimate ±0.5 mag.

K – since no R-band magnitude catalogue entry existed, the X-ray-to-optical counterpart probability calculation (see Eq. 3.4) is based on the K-band magnitude catalogue.

r – SDSS r-band magnitude (AB magnitude).

UK – UK-Schmidt red plate magnitude.

WFC – since no R-band magnitude catalogue entry existed, the X-ray-to-optical counterpart probability calculation (see Eq. 3.4) is based on the WFC-data.

Comments on the optical spectra of tentative objects:

Marano 32A – all narrow emission lines have underlying broad (mainly blue-shifted) components.
Marano 47A – the signal-to-noise ratio of the optical spectrum does not allow the exclusion of the presence of a weak, broad Hβ emission line.
Marano 50A – Hβ and [O III] not covered by the spectrum, however, most likely a type II since no Mg II but [O II] and [Ne V] emission lines.
Marano 51A – Hβ and [O III] covered by the spectrum but Hβ coincides with the edge of the atmospheric A-Band. However, a strong broad Hβ emission line can be ruled out and [O II], [Ne V] emission lines are visible.
Marano 66A – SNR of the optical spectra does not exclude the presence of a weak, broad Hβ emission line ([O II] and [Ne V] emission).
Marano 116A – type II object/X-ray bright optical normal galaxy (XBONG) - galaxy spectrum with prominent [O II] emission line, no Mg II, very weak [O III] emission lines, Hβ coincides with the edge of the A-Band.
Marano 133A – some narrow emission lines have underlying broad, blue-shifted components.
Marano 253A – type II object/XBONG - no Mg II and Hβ emission, weak [O III] emission, the second [O III] line falls into the atmospheric A-band.
sds1b-014 – high SNR spectrum, Hβ and [O III] not covered by the spectrum, however most likely a type II since no Mg II but [O II] and [Ne V] emission lines.

that shifts of 0.5 magnitude between R and r (SDSS) may occur. The majority of our sources have $21 < R < 24$. The 0.5-10 keV flux in the sample ranges from $0.3 - 33 \times 10^{-14}\,\mathrm{erg/s/cm^2}$.

To calculate $f_{\mathrm{X}}/f_{\mathrm{opt}}$ values I derived the optical fluxes in a band centred at 7000 Å with a width of 1000 Å using the equation $f_{\mathrm{opt}} = 10^{-0.4R-5.759}$ (Zombeck 1990). X-ray fluxes were calculated for the 0.5-10 keV energy range. The R-band magnitude vs. X-ray flux plane (Figure 4.2) clearly shows AGN activity in all selected sources, since they have X-ray-to-optical flux ratios of $f_{\mathrm{X}}/f_{\mathrm{opt}} > 0.25$. In accordance with Mainieri et al. (2002) I consider objects with $f_{\mathrm{X}}/f_{\mathrm{opt}} > 0.1$ as AGN. Almost half of the selected type II QSO candidates have noticeable high X-ray-to-optical flux ratios ($f_{\mathrm{X}}/f_{\mathrm{opt}} > 10$). Szokoly et al. (2004) mentioned that type II AGN/QSOs cluster at higher X-ray-to-optical flux ratios than type I AGN. The majority of the spectroscopically classified type II AGN/QSOs in the Lockman Hole also show high $f_{\mathrm{X}}/f_{\mathrm{opt}}$ values (Mainieri et al. 2002). The observed rest-frame 0.5-10 keV X-ray luminosities (not corrected for intrinsic absorption) of our objects range from $L_{\mathrm{X_{OBS}}} \sim 10^{43-45}\,\mathrm{erg/s}$.

4.4 XMM-Newton observations and extraction of X-ray spectra

All data were processed with the `SAS` version 7.0 (Science Analysis Software, Gabriel et al. 2004) package and corresponding calibration files. The `epchain` and `emchain` tasks were used for generating linearised event lists from the raw PN and MOS data. For all sources the effects of photon pile-up was negligible.

The *XMM-Newton* data reduction for the Marano field survey is described in detail in Krumpe et al. (2007c). For the XWAS and AXIS sources I downloaded all available X-ray data from the *XMM-Newton* archive[1] up to and including July 2007. Periods of high background were excluded from the analysis of all relevant datasets in the standard way.

Circular or box-shaped source and background regions were manually determined for all contributing observations. Sources at large off-axis angles in the contributing observations were not considered as follows. The largest off-axis angles were 720 arcsec for the PN and 820 arcsec for the MOS detectors, respectively. The lower PN area was a result of the enhanced background contamination near the edges of the PN detector. Additional X-ray sources in the background regions were masked out. The auxiliary response file (arf) was computed for each source and observation individually. For the Marano field sources, I used appropriately "canned" response matrices from the *XMM-Newton* calibration homepage[2] (*XMM*-revolution 110 and pattern 0-12). The PN y-coordinate of an X-ray source was determined to link the relevant PN response matrix file (rmf for single and double events, version 6.8) to the X-ray spectrum of the source. For the XWAS and AXIS sources the response matrix files were computed on a case-by-case basis. Where multiple X-ray spectra of a given source were added, the mean rmf was computed as a weighted mean. For details of the procedure see Page et al. (2003). The two MOS spectra were always added to form a single MOS spectrum.

The X-ray source of the secure type II object phl5200-001 is surrounded by diffuse X-ray emission. For the reduction of the X-ray spectrum I used a smaller extraction radius for the point source and the diffuse X-ray emission as the background region.

4.5 X-ray spectral analysis

The X-ray spectral analysis was performed with `XSPEC` (Arnaud 1996) version 12.3.0. Although I have found a few objects with several hundreds of net PN source counts in the 0.2-8 keV range, the distribution peaks at ∼40 net PN source counts. An appropriate X-ray spectral analysis for the low count regime has to be found. Although I only refer to the net PN counts in my simulations and in Table 4.5, the fit uses both the PN and MOS data.

---

[1]http://xmm.esac.esa.int/xsa
[2]http://xmm.esac.esa.int/external/xmm_sw_cal/calib

Table 4.3: Set of input parameters for the simulated X-ray spectra.

Parameter	value
0.2-8 keV net counts	10, 40, 100, 130, 200
Redshift	1, 2, 3
Column density [cm^{-2}]	0, 10^{21}, 10^{22}, 10^{23}, 10^{24}
Photon index Γ	2.0

Hence, the total number of counts used by the fit is typically twice that given in Table 4.5.

4.5.1   Defining the appropriate fit statistic and binning method

A problem notorious to X-ray astronomy is proper fitting of spectra with relatively few counts. Tozzi et al. (2006) approached this problem for the X-ray sources in the *Chandra* deep field south by running simulations for two different fitting procedures: Cash statistics (unbinned) and classic χ^2 statistics with a binning of 10 counts per bin (min 10). They concluded that the unbinned Cash-statistic fits (Cash 1979) recovered the input values better for X-ray spectra with less than 50 counts.

I carried out a much more extensive study of the fit results as a function of fit statistic and binning method. This investigation can be used to study the error distribution of the intrinsic column density ($N_{\rm H}$) and to determine how many net PN counts are required to perform free fits of $N_{\rm H}$ and photon index Γ with acceptable errors in both parameters.

I assumed emission from the AGN to be described as a power law with photon index Γ, modulated by Galactic foreground absorption and further intrinsic cold absorption at the redshift of the AGN. Following Mainieri et al. (2002) and Mateos et al. (2005) I simulated X-ray spectra with an input value of $\Gamma = 2$. All simulations included Galactic absorption of $N_{\rm H_{GAL}} = 2 \times 10^{20}$ cm^{-2} and considered all possible parameter combinations of Table 4.3.

The X-ray spectra were normalised to reach the desired 0.2-8 keV PN net counts with a deviation of up to 5%. I added Poisson noise to the X-ray spectra. I used a typical representative background file (Marano 9A). As for the real data I added MOS1 and MOS2 spectra to form a single MOS spectrum. The same source was simulated 1000 times for each set of specific parameters.

The simulated X-ray spectra were grouped by using different binning methods (Table 4.4). Cash and χ^2-statistic were applied to recover the $N_{\rm H}$ input value. The redshift and the Galactic absorption were set to the input value. The nominal initial guess for the intrinsic absorption was $N_{\rm H} = 0$ cm^{-2}, but other initial guesses up to $N_{\rm H} = 10^{24}$ cm^{-2} were tested as well. I studied the recovered $N_{\rm H}$ distribution with different fit statistics and binning methods by analysing the number of mismatches, the peak, the shape and the significance of $N_{\rm H}$ detection. The best fit statistic and binning method was selected by these criteria in the given order. In summary, the most important results of our simulations are

Table 4.4: Fit statistics and binning methods for the simulated X-ray spectra. The data were grouped from a minimum PHA channel (corresponding to $0.2\,\mathrm{keV}$) to the maximum PHA channel (corresponding to $8\,\mathrm{keV}$), with at least n counts per bin (abbreviated as min n) or with a fixed number n of channels (channel n).

Fit statistic	binning methods
Cash-statistic	unbinned, min 1, min 2, min 3,
	min 5, min 10, min 15, channel 60,
	channel 120, channel 180, channel 240
χ^2-statistic	min 10, min 15
Photon index Γ	free fit, 2.0

as follows.

- With only very few exceptions the Cash-statistic with a binning of one count per bin (min 1) recovered the input value best.

    - Even at a level of 40 net PN counts the Cash-statistic with a binning of minimum one count per bin correctly recovers more than 90% of the objects with an intrinsic absorption of $N_\mathrm{H} \sim 10^{22} - 10^{24}\,\mathrm{cm}^{-2}$ up to $z = 3.5$. Figure 4.3 shows the retrieved N_H distribution for an input value of $N_\mathrm{H} = 10^{22}\,\mathrm{cm}^{-2}$ at $z = 2$. The variance of the recovered N_H distribution increases with redshift. However, individual peaks clearly separate in the studied redshift range, when the intrinsic N_H values differ by a factor of approximately 10 in hydrogen column density. The recovered N_H distribution for an intrinsically unabsorbed source at $z = 1$ is shown in Fig. 4.4. Between 50-60% of all objects are correctly recovered independent of redshift. Although not all fits converge at $N_\mathrm{H} = 0\,\mathrm{cm}^{-2}$, none of the resulting N_H values is significantly different from zero. The peak of the misclassified absorbed objects shifts to $N_\mathrm{H} \sim 7 \times 10^{21}\,\mathrm{cm}^{-2}$ for $z = 3$.

    - For 10 net PN counts the fit retrieves a very broad N_H distribution for objects with an intrinsic absorption of $N_\mathrm{H} \sim 10^{22} - 10^{24}\,\mathrm{cm}^{-2}$. Independent of redshift the fit recovers roughly 30% of the intrinsically absorbed X-ray sources as unabsorbed sources ($N_\mathrm{H} = 0\,\mathrm{cm}^{-2}$). However, the fit does not significantly overestimate the N_H values. Although no absorption is recovered with a significance above 2σ due to the large errors, the fitted N_H values can be used as an estimate for the intrinsic N_H values. An unabsorbed X-ray source is correctly recovered by the fit in 50-60% of all cases. In 90% of the cases the fitted N_H values for an intrinsically unabsorbed X-ray source do not exceed $N_\mathrm{H} \sim 10^{22}\,\mathrm{cm}^{-2}$ for $z = 1$ and $N_\mathrm{H} \sim 3 \times 10^{22}\,\mathrm{cm}^{-2}$ for $z = 2$.

- The unbinned Cash-statistic as used in Tozzi et al. (2006) shows the narrowest distribution in N_H for most of the parameter combinations, but the peak of the recovered distribution was found to be strongly dependent on the initial guess of N_H and weakly
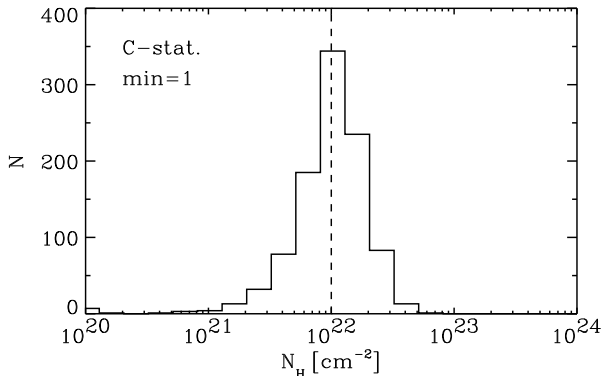
Figure 4.3: Recovered N_{H} distribution for an X-ray source with 40 net PN counts at $z = 2$. The input $N_{\mathrm{H}} = 10^{22}\,\mathrm{cm}^{-2}$ is indicated by the dashed line. Fit method used: fixed $\Gamma = 2$, Cash-statistic, binning: min 1; 1000 simulations.
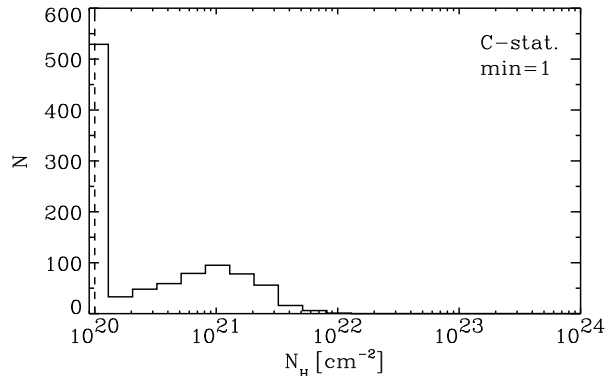
Figure 4.4: Recovered N_{H} distribution of an unabsorbed X-ray source with 40 net PN counts at $z = 1$. The input $N_{\mathrm{H}} = 0\,\mathrm{cm}^{-2}$ is indicated by the dashed line. $N_{\mathrm{H}} = 0\,\mathrm{cm}^{-2}$ is represented by the lowest bin. Fit method used: fixed $\Gamma = 2$, Cash-statistic, binning: min 1; 1000 simulations.

favours $N_{\mathrm{H}} = 10^{22}\,\mathrm{cm}^{-2}$ independent of input parameter for net PN counts less than 100.

- For a binning of min 10 or min 15 I found no difference between the Cash and the χ^2-statistic even at a level of 40 net PN counts. Only the significance of the absorption is marginally higher for the Cash-statistic. There is also no difference between a binning of min 10 and min 15.

- Free fits in N_{H} and Γ are acceptable above 100 PN net counts. The recovered N_{H}-values show a narrow distribution at the input N_{H} value (FWHM$\sim$0.4 dex). For all combinations of fitting and binning methods I retrieved the peak of $\Gamma \simeq 2$. For a binning of minimum one count per bin (min 1) the recovered Γ distribution clearly peaks at Γ=2 with FWHM$\sim$0.8 (FWHM$_{130\mathrm{counts}}$ $\sim$0.4, FWHM$_{200\mathrm{counts}}$ $\sim$0.2).

Simulations as shown in Fig. 4.3 and Fig. 4.4 are used to determine the N_{H} range that belongs to 68% and 90% of all simulations. In Fig. 4.5 I show these distributions for simulations at different redshifts (z=0,1,2,3,3.5) and column densities ($N_{\mathrm{H}} = 0, 10^{22}, 10^{23}\,\mathrm{cm}^{-2}$). The simulations contain 40 net PN counts and so are representative of many of my sources. The Cash-statistic with a binning of at least one count per bin is an appropriate method to determine the column density over a wide range of redshifts. It does not significantly overestimate the input N_{H} values and usually the fit recovers objects of $N_{\mathrm{H}} \lesssim 10^{22}\,\mathrm{cm}^{-2}$ as unabsorbed X-ray sources.
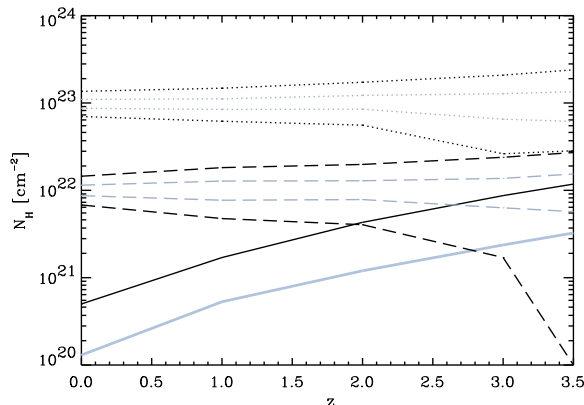
Figure 4.5: Diagnostic N_H vs. redshift plot. The plotted contours contain 68% (grey) and 90% (black) of the simulated X-ray sources with 40 net PN counts in the 0.2-8 keV band (NOTE: The fits used more than twice as many counts since both the PN and MOS data are used). The solid lines are the limits for intrinsically unabsorbed sources. The limits for an intrinsic absorption of $N_H = 10^{22}\,\mathrm{cm}^{-2}$ are shown by dashed lines while dotted lines represent $N_H = 10^{23}\,\mathrm{cm}^{-2}$.

4.5.2 Modelling the X-ray spectra

Following the analysis in Sect. 4.5.1 I grouped the extracted X-ray spectra in bins of at least one count per bin (0.2-8 keV) and used the Cash-statistic to determine N_H. The initial guess was set to $N_H = 0$. I corrected for Galactic absorption and performed free fits in N_H and Γ for spectra with more than 100 net PN counts. For X-ray spectra with less than 100 net PN counts, I fixed $\Gamma = 2$ and only fit N_H. In these cases I give two errors for the value of N_H in Table 4.5. The first is the 1σ error of N_H based on the fit with fixed $\Gamma = 2$, while the second takes into account the systematic shift for different photon indices (deviation in N_H for a fixed $\Gamma = 1.7$ and $\Gamma = 2.3$). The observed 0.5-10 keV X-ray luminosity (not corrected for intrinsic absorption) was computed by a free fit in N_H and Γ for spectra with more than 100 PN counts. I chose again a photon index $\Gamma = 2$ for spectra with less net counts. The same criteria applied for the intrinsic 0.5-10 keV X-ray luminosity after setting $N_H = 0$.

Due to contamination by soft detector background I only used the 0.3-8 keV band for the X-ray spectral analysis of X-ray source X03246_092 (24 net PN counts in 0.3-8 keV band). The X-ray spectrum of Marano 51A was the only X-ray source that could not be well fitted by an absorbed power law (see Appendix H). Positive residuals below 0.5 keV and between 2-4 keV remain in the fit. A fit of an absorbed power law plus a soft excess component reproduce the X-ray data better for this object. No evidence for soft excess was found in the X-ray spectra of the brightest objects.

Table 4.5 shows the computed values. I list the name of the spectroscopically classified counterpart, the XMMU source name of the *XMM-Newton* X-ray source, the observed and intrinsic rest-frame X-ray luminosity, the PN count number in the 0.2-8 keV band, the

column density for a fixed $\Gamma = 2$, the fit quality for a fixed $\Gamma = 2$, the freely fitted photon index of the X-ray spectrum, the column density for a free fit in Γ and N_{H}, and the quality for the free fit (in this order).

4.5.3 Stacking of X-ray spectra

The consortium which carried out the imaging and spectroscopic classification, as well as the analysis of the *XMM-Newton* Serendipitous Medium Sample distributed different scientific tasks to the involved people. As explained in the introduction of this chapter, I became responsible for the analysis of type II QSOs at $z \geq 0.5$. Amalia Corral from the Instituto de Física de Cantabria (CSIC-UC), Santander, Spain is in charge of the development of an X-ray stacking procedure for the consortium. The low count numbers in the X-ray spectra of many of the sources in the *XMM-Newton* Serendipitous Medium Sample do not allow the study of individual spectral features such as an iron line. Based on the assumption that the intrinsic X-ray properties in the sample are nearly the same, a stack of the individual spectra can reveal the presence of such a line. The implementation of the X-ray spectra stacking requires extensive tests and modulations of the X-ray background in order to quantify statistical effects. The code is still in its development phase. Therefore, I sent the extracted X-ray spectra of each source directly to Amalia Corral. Since the number of individual X-ray spectra increases the SNR in the stacked spectrum, we decided to include all type II QSO candidates regardless of the optical flag. The assumption is justified because the secure and tentative sample do not show differences in Fig. 4.2.

Corral et al. (2007) explain the stacking process in detail. Here I outline the essential components of the process. Using the best-fit parameters, unfolded spectra (`eufspec` in `XSPEC`) from the ungrouped observed X-ray spectra (MOS and PN data) are extracted. The unfolded spectra are corrected for Galactic foreground absorption, shifted to the rest-frame and normalised to the same rest-frame flux in the 2-5 keV band. The flux is rebinned into a common energy grid for all spectra. The stacked spectrum is binned to a final energy grid that contains at least 100 counts per energy bin. The final errors of the stacked spectrum are based on Gaussian propagation of the errors in the individual spectra. To distinguish between real spectral features and artefacts from the averaging process the underlying continuum has to be modelled. Each source was simulated 100 times using the same model (absorption plus power law) with the same 2-8 keV flux as observed in the real spectra. The individual simulated X-ray continuum spectra from all different X-ray sources are stacked exactly as the observed X-ray spectra which are used to determine the 1σ and 2σ contours (68% and 95% of all simulated continuum spectra).

The 0.2-12 keV final stacked spectrum contains $\sim$5800 counts. Together with the 1σ and 2σ contours the ratio of the observed spectrum to the average simulated continuum is shown in Fig. 4.9. The stacked spectrum shows positive residuals around 6-7 keV which are likely to correspond to the iron Kα emission line. The central region (narrow core) has been detected at a 99% confidence level while a broad Gaussian line profile is only found at a 95% confidence level. The line energy is $6.4^{+0.3}_{-0.3}$ keV with a $\sigma = 700^{+400}_{-300}$ eV

Table 4.5: Computed properties of type II QSO sample

(1) No	(2) XMMU J	(3) $\log(L_{X_{OBS}})$ 0.5-10keV	(4) $\log(L_{X_{INT}})$ 0.5-10keV	(5) N_{Counts} PN	(6) $N_{H,\Gamma=2.0}$ 10^{22} $[cm^{-2}]$	(7) C-stat/d.o.f $\Gamma = 2.0$	(8) Γ	(9) N_H 10^{22} cm^{-2}	(10) C-stat/d.o.f
Marano 9A	031510.1-551313	44.50	44.55	270	0.6±0.1	435/504	1.7±0.1	0.3±0.1	426/503
Marano 20A	031621.6-551759	44.82	44.99	64	1.7±0.4±0.7	183/227	1.8±0.2	1.4±0.5	182/226
Marano 32A	031547.2-551755	44.88	45.22	129	12.3±1.7	287/292	1.8±0.2	9.8±2.4	285/291
Marano 39A	031339.7-550151	44.04	44.22	36	0.8±0.2±0.4	111/117	1.8±0.3	0.6±0.2	110/116
Marano 47A	031538.8-551043	43.49	43.72	38	1.5±0.5±0.5	149/157	2.4±0.5	2.1±0.9	149/156
Marano 50A	031410.1-551746	43.76	44.05	50	2.5±0.6±0.8	182/190	1.5±0.3	1.4±0.8	180/189
Marano 51A	031630.6-551501	43.27	43.27	47	0.0±0.0±0.1	139/183	1.5±0.2	0.0±0.2	132/182
Marano 63A	031517.1-550602	44.57	44.81	29	4.1±1.4±1.4	125/140	1.5±0.3	1.8±1.6	122/139
Marano 66A	031500.8-550718	43.36	43.45	39	0.3±0.2±0.2	127/130	1.8±0.4	0.2±0.2	126/129
Marano 116A	031620.9-551651	43.31	43.72	28	5.6±1.2±1.0	129/126	0.5±0.4	1.1±1.2	122/125
Marano 133A	031426.4-552113	44.04	44.04	14	0.0±0.8±0.0	87/70	2.3±0.7	0.0±1.2	86/69
Marano 171A	031351.2-550257	43.61	44.00	14	5.4±1.5±1.0	46/51	1.8±0.7	4.9±2.6	46/50
Marano 224B	031304.9-551606	43.71	44.25	8	12.4±3.5±1.7	48/53	2.0±0.9	12.4±7.2	48/52
Marano 253A	031438.2-550648	42.97	43.55	11	14.5±5.0±3.2	64/85	0.6±0.8	3.7±3.9	62/84
Marano 463A	031625.3-550839	44.37	44.53	7	1.6±1.0±0.9	76/45	2.1±0.6	2.0±1.7	76/44
Marano 610A	031552.0-551222	43.23	43.68	17	7.2±1.9±2.1	117/120	2.1±0.9	7.8±3.9	117/119
X21516_135	022626.7-043654	44.73	45.15	29	14.8±5.7±4.8	61/79	2.5±0.8	25.2±14.4	59/78
X00851_154	221541.6-173753	44.48	44.70	261	12.1±2.0	580/622	1.6±0.1	5.6±2.0	572/621
X01135_126	015257.5-140839	43.85	43.85	392	0.1±0.0	371/514	1.7±0.1	0.0±0.1	355/513
X03246_092	004345.8-202955	43.48	43.84	35	3.8±1.2±1.3	74/67	0.2±0.4	0.0±0.5	65/66
phl5200-001	222826.4-051820	44.66	44.92	772	6.3±0.2	854/971	1.6±0.1	4.5±0.4	834/970
sds1b-014	021842.9-050437	44.35	44.45	491	0.5±0.1	549/594	1.8±0.1	0.4±0.1	546/593

and an equivalent width of $EW = (1100 \pm 400)\,\mathrm{eV}$. We suspect that the equivalent width of the line is likely to be overestimated since the fit includes some residuals above $7\,\mathrm{keV}$. We detected significant absorption in some of our type II objects and therefore expect an iron edge at $7\,\mathrm{keV}$ in the stacked spectrum. At the present signal-to-noise ratio this might mimic a large equivalent width of the line.

4.6   Discussion

In Fig. 4.6 I show the fitted intrinsic N_{H} distribution of the sources. A column density peak at $N_{\mathrm{H}} = 4 \times 10^{22}\,\mathrm{cm}^{-2}$ is found. I revealed moderate absorption in the majority of our objects. The significance of the absorption exceeds 2σ in most of the cases (see the confidence contours in Appendix H). Three type II objects with no X-ray absorption were discovered, one of which is from the secure type II sample.

The determination of the intrinsic N_{H} also allows us to compute the de-absorbed intrinsic X-ray luminosity $L_{\mathrm{X_{INT}}}$ of our sources. As mentioned in the introduction of Sect. 4, I define a type II object by the detection of narrow emission lines in the optical spectrum. Figure 4.7 shows the intrinsic column density vs. de-absorbed intrinsic X-ray luminosity plane. The dividing line of $\log(L_{\mathrm{X_{INT}}}\,[\mathrm{erg/s}]) = 44$ is used to distinguish between type II AGN and QSOs. Ten type II objects from the secure sample and four tentative objects are classified as QSOs. I detected one unabsorbed type II QSO but the object belongs to the tentative sample. No obvious trend of absorption in type II QSOs with intrinsic X-ray luminosity is found.

Most of the type II QSOs fall into the same region of the N_{H}-$L_{\mathrm{X_{INT}}}$ diagram where previous studies have also found type II QSOs (Mainieri et al. 2002; Szokoly et al. 2004; La Franca et al. 2005; Ptak et al. 2006). The additional criterion ($N_{\mathrm{H}} > 10^{22}\,\mathrm{cm}^{-2}$, Mainieri et al. 2002) makes only a small difference to our sample selection (two more secure objects).

The N_{H}-redshift plane for type II QSOs and type II AGN is shown in Fig. 4.8. I found no obvious differences between the N_{H} distribution of AGN and QSOs. Although a tentative anticorrelation of N_{H} vs. redshift below $z < 1$ and a direct correlation above $z = 1$ is indicated, when all data are taken together there is no significant trend in N_{H} with redshift. Considering the typical flux and column densities found for the sources, I expect all $z > 1$ type II objects to be classified as QSOs. At lower redshifts $\sim$40% of the type II QSO candidates are actually type II QSOs.

Statistical fluctuations in the X-ray spectrum can lead to high values of spuriously measured N_{H} values at high redshifts (e.g. Akylas et al. 2006). However, Fig. 4.5 shows that objects with intrinsic N_{H} of several $10^{22} - 10^{23}\,\mathrm{cm}^{-2}$ are not significantly influenced by systematic trends in redshift. The fit method is also able to pick up much higher absorptions than found in our sources. The scatter in the mentioned N_{H} range at $z > 2.5$ is consistent with an intrinsic absorption of $N_{\mathrm{H}} = 10^{23}\,\mathrm{cm}^{-2}$ for all sources.
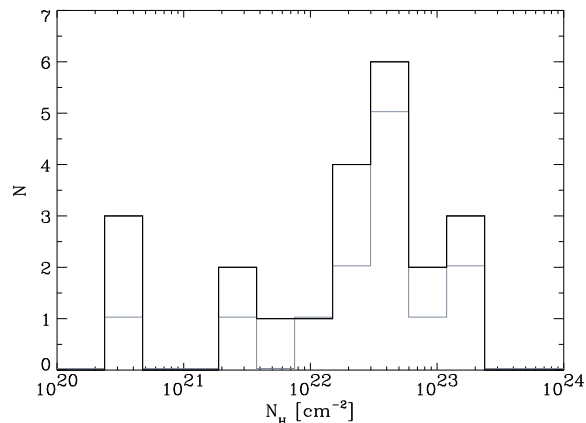
Figure 4.6: Intrinsic N_{H} distribution of all 22 type II QSO candidates (black) and of the 13 secure type II QSO candidates in grey.
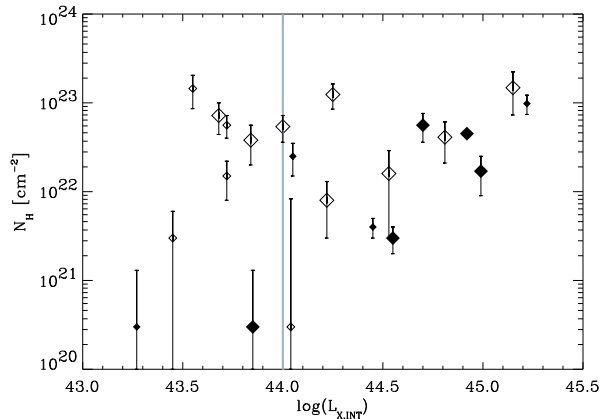
Figure 4.7: Intrinsic N_{H} vs. de-absorbed intrinsic 0.5-10 keV X-ray luminosity. Large symbols represent optical secure type II QSO candidates while small symbols illustrate the tentative sample. Open symbols indicate X-ray sources that have less than 40 net PN counts in the 0.2-8 keV band; filled symbols $\geq$40 net PN counts. The vertical solid line at $\log(L_{\mathrm{X_{INT}}} \, [\mathrm{erg/s}]) = 44$ marks the dividing line between AGN and high luminosity QSOs. Objects with $\log(L_{\mathrm{X_{INT}}} \, [\mathrm{erg/s}]) \geq 44$ and $N_{\mathrm{H}} \geq 10^{22} \, \mathrm{cm}^{-2}$ (upper right corner) fall in the "type II QSO region" as defined by Mainieri et al. (2002).

As a further test of the impact of statistical fluctuations, I plot in Fig. 4.8 the amount of N_{H} that is needed to reduce the 0.5 keV flux by 30% and 50%. The 30%-line agrees well with the 90% contours of unabsorbed sources in Fig. 4.5. Consequently even for the sources at $z > 2.5$, the fitted N_{H} values are unlikely to be caused by statistical fluctuations.

The previous conclusions depend on not having misinterpreted Compton-thick objects ($N_{\mathrm{H}} > 1.5 \times 10^{24} \, \mathrm{cm}^{-2}$) as moderately absorbed objects. Increasing column densities cause a hardening of the X-ray spectrum. This trend stops when the material becomes optically thick to electron scattering. The X-ray spectrum of a Compton-thick source is completely dominated by the reflection component. Their X-ray spectra show soft X-ray radiation but with a much lower photon index ($\Gamma \sim -0.4 - 1.3$, Maiolino et al. 1998; Bassani et al. 1999; Risaliti et al. 2000; Iwasawa et al. 2001; Comastri 2004). I simulate an X-ray spectrum with $\Gamma = 1.0$ as observed in the 3-12 keV band for NGC 1068. When I fit the spectrum with a fixed $\Gamma = 2.0$, I recover values for absorption of $N_{\mathrm{H}} = 0.7 \times 10^{22} \, \mathrm{cm}^{-2}$, $N_{\mathrm{H}} = 1.9 \times 10^{22} \, \mathrm{cm}^{-2}$ and $N_{\mathrm{H}} = 3.8 \times 10^{22} \, \mathrm{cm}^{-2}$ for redshifts of $z = 1, 2, 3$ respectively.

Hence, moderately absorbed sources can be found if intrinsically Compton-thick sources are studied. However, I am able to exclude a general misclassification of objects based on
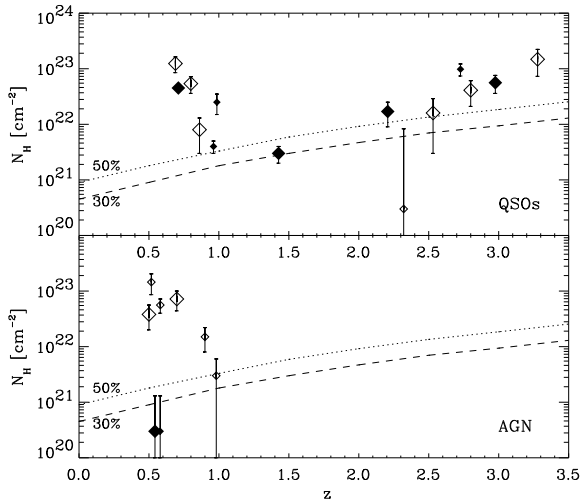
Figure 4.8: Intrinsic N_H vs. redshift diagram for type II QSOs (top panel) and type II AGN (lower panel). Labels as in Fig. 4.7. The dashed and dotted lines represent the N_H values which correspond to a 30% and 50% decrease in the 0.5 keV flux at the given redshift, respectively.
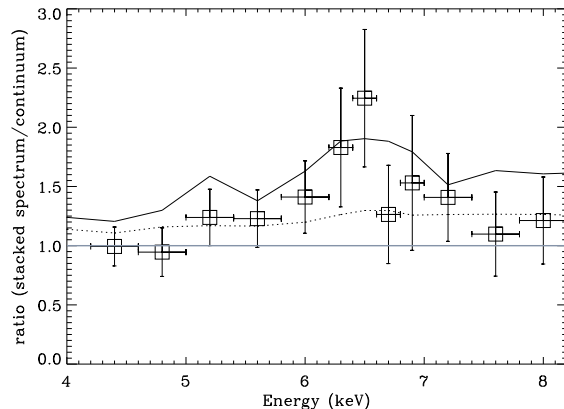
Figure 4.9: Stacked X-ray spectrum of all 22 type II QSO candidates ($\sim$1900 counts in the shown 4-8.2 keV energy range). The squares represent the ratio between the flux of the stacked spectrum and the simulated continuum spectrum. The dotted line shows the 1σ detection error while the solid line represents the 2σ detection error. The solid grey line at a ratio of one illustrates the continuum flux.

the following arguments.

First, I tested if the X-ray spectra are better fitted with an unabsorbed single power law that has a low photon index $\Gamma \lesssim 1$. For 15 out of 22 sources the X-ray spectra are better fitted by a power law plus intrinsic absorption. Only three spectra (Marano 116A, 253A, X03246_092) are better reproduced by a single, hard power law, while four sources (Marano 50A, 63A, 610A, X21516_135) can be equally well fitted with a single hard power law or a power law with intrinsic absorption as given in Table 4.5. However, all suspicious objects have PN net counts of $\leq$50. Simulations of a single power law with 30 net PN counts recovered a peak at $\Gamma = 1.8$ (input value $\Gamma = 2.0$) with a FWHM$\sim$0.9. None of the objects with $N_{PN-Counts} > 100$ has $\Gamma < 1.6$. Therefore the scatter of the recovered Γ can probably explain the finding of low count spectra with typical Compton-thick photon indices.

Secondly, the reflected component of Compton-thick sources is $\sim$50-150 times weaker than the de-absorbed intrinsic X-ray luminosity (Brandt & Hasinger 2005). Hence they are usually found at low values of $f_X/f_{[OIII]}$ (Bassani et al. 1999). For the majority of our objects the [O III] line is redshifted out of our spectral range. As a second best estimator I adopt f_X/f_{opt} rather than $f_X/f_{[OIII]}$. Figure 4.2 shows that almost all objects have high f_X/f_{opt} which is inconsistent with Compton-thick objects. Only X00851_154 has a rather low f_X/f_{opt} ratio, but the best X-ray spectral fit is a moderately absorbed power law with $\Gamma = 1.6$. In addition, the Compton-thick corrected X-ray luminosity would be $\sim$100

times higher than shown in Fig. 4.7. Under the assumption of Compton-thick absorption, all studied objects would be classified as QSOs and our sample would contain the most luminous QSOs ever studied ($\log(L_{X_{INT}} [\text{erg/s}]) \sim 47$).

Another indicator of a Compton-thick object is the detection of the iron line which is normally outshone by the direct component. Due to the reflection of the X-ray radiation from cold material at the torus, an iron Kα fluorescence line with an equivalent width $EW \gtrsim 1\,\text{keV}$ is expected. The line has to be narrow if the reflector is the torus. Although the EW allowing a broadened iron Kα line is $1.1\,\text{keV}$ (Sect. 4.5.3), the contribution of a narrow component is considerably low ($EW \sim 0.3\,\text{keV}$, see Fig. 4.9). This is not consistent with the properties of Compton-thick AGN. Therefore, I conclude that the typical AGN in our stacked spectrum is not Compton-thick absorbed.

Chapter 5

Conclusion

In this chapter I summarise the main conclusion of this thesis. First, I will review the results of the *XMM-Newton* Marano field survey (Sect. 5.1) and then the study of absorption in distant type II QSOs (Sect. 5.2). Finally, I will discuss the results of the thesis in respect to the main questions in Sect. 2 and in the context of deep X-ray surveys. An outlook is presented in Sect. 5.4.

5.1 Conclusion for the XMM-Newton Marano field survey

With a total of 120 ksec good observation time we detected 328 X-ray sources ($ML \geq 5$) in the *XMM-Newton* Marano field survey. Among 140 spectroscopic classifications of 187 optical counterparts (with a $3\sigma_X$ position error and $\sigma_{\mathrm{syst.}} = 0.7\,\mathrm{arcsec}$) to 202 X-ray sources, we found 89 broad emission line AGN, 36 narrow emission line AGN, 6 galaxies, and 9 stars. In the central region of the Marano field we reached a classification completeness of 65%. In the 1 Msec *Chandra* Deep Field South Szokoly et al. 2004 detected 349 X-ray sources and spectroscopically classified 44%, while the 2 Msec *Chandra* Deep Field North (Barger et al. 2003) revealed 503 X-ray sources and has a spectroscopic classification ratio of 56%.

While the redshift distribution of the optically selected QSOs in the field is basically flat up to $z \simeq 3$, the distribution of the *XMM-Newton* sources peaks at $z \simeq 1$. Using our sample of *XMM-Newton* sources classified as type I AGN, we investigated possible causes for this tendency of deep X-ray surveys to discover faint populations at comparably low redshifts. We found no significant correlation of the optical to X-ray SED slope α_{OX} with redshift. As widely reported in the literature, α_{OX} is tightly correlated with optical luminosity. A different representation of this correlation is the non-linear relation $L_X(l_{\mathrm{opt}})$. The best-fit regression $\log(L_X) = 0.84 \times \log(l_{2500\,\mathrm{\AA}}) + 19.36$ implies that the optical luminosities in

a typical sample are spread over a wider range than the X-ray luminosities. Therefore, the less luminous objects of the population are more easily detected in X-rays than in the optical. On the other hand, an increase of optical luminosity is, on average, not accompanied by a proportional increase in X-ray luminosity. Hence, the luminous (and more distant) objects are detected more efficiently in optical surveys.

In the core region of the field we classified 31 new type II AGN. Most of them were found at redshifts $z < 1.5$; additionally we found five high redshift type II AGN at $z > 2.2$. Fifteen objects were classified as type II QSOs with intrinsic X-ray luminosities $L_X > 10^{44} \, \mathrm{erg \, s^{-1}}$.

We showed that the optical identification of type II AGN is very difficult in the redshift range $z = 1 - 2$ due to the absence of suitable emission lines in the optical window. Therefore, their intrinsic redshift distribution remains unclear. We demonstrated that the use of K-band data for MXU slit positioning reveals type II AGN or XBONGs that would have likely been missed in R-band images. The X-ray selected type II AGN have a very similar redshift distribution to non-X-ray emitting narrow emission line galaxies, which were spectroscopically classified in the same field as a control sample.

The intrinsic hydrogen column densities, as derived from X-ray hardness ratios, show that the fraction of intrinsically absorbed X-ray sources is much higher for type II AGN than for type I. Nevertheless, we found a few unabsorbed type II AGN and some evidence for absorption in high redshift type I AGN. However, due to the faintness of the sources, the significance of absorption in the individual type I AGN is low. Furthermore, at high redshifts statistical fluctuations in the X-ray spectrum can lead to high values of spuriously measured N_H values (e.g., Akylas et al. 2006). If we only include 2σ detections of intrinsic N_H in our analysis, only 4 absorbed type I AGN remain and no dependency of absorbed fraction on redshift is obvious. In the *Chandra* data from *Chandra* Deep Field South (CDFS), Tozzi et al. (2006) found hints for the increase of intrinsically absorbed fraction with redshift. However, these data probably also suffer from the uncertainties mentioned above. Using *XMM-Newton* data in the same field, Dwelly & Page (2006) found little evidence that the absorption distribution is dependent on either intrinsic X-ray luminosity or redshift. Our type I and type II AGN cover the same range in absorption-corrected X-ray luminosity. However, the mean corrected X-ray luminosity is smaller for type II AGN than for type I AGN. This result can be explained by an observational bias effect. The survey missed a significant fraction of the X-ray luminous type II AGN at $z > 1$, since their optical identification and classification is very difficult to achieve due to missing emission lines over a wide range of the optical spectrum. The argument is supported by Fig. 3.14 which clearly shows the so-called redshift desert for type II AGN at $1 < z < 2$. The analysis of AGN below $z = 1$ resulted in a very similar intrinsic absorption-corrected X-ray luminosity distribution for type I and II AGN.

Three of the *XMM-Newton* classifications are X-ray bright optically normal galaxies (XBONGs), which show X-ray luminosities typical for AGN, but no optical emission lines. Their X-ray luminosities of $\log(L_X \, [\mathrm{erg/s}]) \sim 43 - 44$ are comparable to the mean type II AGN X-ray luminosity. They do not show harder X-ray spectra and do not reveal higher hydrogen column densities than the average type II AGN. We concluded that the objects are very similar to type II AGN. However, their narrow emission lines were not detected,

since they are either intrinsically weak or obscured by dust.

5.2 Conclusion for the absorption of distant type II QSOs

We selected 51 spectroscopically classified type II objects from the *XMM-Newton* Marano field survey, XWAS, and AXIS. We re-investigated the optical spectra for narrow AGN high excitation lines, as well as verified the X-ray counterpart determination. 22 sources met our selection criteria (13 secure classifications, 9 tentative). All sources have $z \geq 0.5$ and observed 0.5-10 keV luminosities (not corrected for intrinsic absorption) of $\log(L_{\mathrm{X_{OBS}}}\,[\mathrm{erg/s}]) \sim 43 - 45$. The sample is not flux limited.

Since the distribution of net PN counts peaks at $\sim$40, the X-ray spectral analysis has to account for this very low numbers of counts. We extensively simulated and studied such low count number X-ray spectra. A binning with at least one count per bin combined with the Cash-statistic recovered the input values best. We proved that the method is able to find absorption up to $N_{\mathrm{H}} = 10^{24}\,\mathrm{cm}^{-2}$.

However, we discovered only moderately absorbed type II QSOs. Only one QSO is consistent with being unabsorbed but it belongs to the tentative sample. Compton-thick sources may be detected as moderately absorbed but we can exclude this scenario for the majority of our sources. Their values of $f_{\mathrm{X}}/f_{\mathrm{opt}}$ and the photon index Γ give evidence that we have not misclassified Compton-thick sources.

The column density distribution found by us agrees well with those in deep *Chandra* and *XMM-Newton* surveys (Mainieri et al. 2002; Szokoly et al. 2004; Mateos et al. 2005; Ptak et al. 2006). These authors also reported a few cases of unabsorbed type II AGN, as well as evidence for some heavily absorbed sources ($N_{\mathrm{H}} \sim 10^{24}\,\mathrm{cm}^{-2}$). La Franca et al. (2005) studied column density trends with X-ray luminosity in different redshift bins. They classified type II AGN as all sources that do not show any emission lines with FWHM $> 2000\,\mathrm{km/s}$. Independent of X-ray luminosity and redshift bins, they discovered type II AGN with an average absorption of $N_{\mathrm{H}} \sim 10^{23}\,\mathrm{cm}^{-2}$, slightly above the column density peak of our survey ($N_{\mathrm{H}} = 4 \times 10^{22}\,\mathrm{cm}^{-2}$). The present study of strictly classified type II AGN/QSOs, based on the optical spectra, verified that there is no obvious trend with redshift or X-ray luminosity.

Our results contradict studies of the local universe. Bassani et al. (1999) and Risaliti et al. (2000) found 75% of the local, X-ray bright Seyfert II galaxies with high absorption ($N_{\mathrm{H}} > 10^{23}\,\mathrm{cm}^{-2}$) and 25-45% with $N_{\mathrm{H}} > 10^{24}\,\mathrm{cm}^{-2}$. Either the column density properties change dramatically from the local to distant universe or the majority of the heavily absorbed distant sources are missed in our surveys. Indeed even the most luminous Compton-thick sources in the local universe, such as NGC 6240, could not have been detected by our survey if they were at $z \gtrsim 0.4$. Norman et al. (2002) claim that for the most distant type II QSO ever detected ($z = 3.7$), there is strong evidence for heavy or even Compton-thick absorption. However, our survey rules out high numbers of Compton-

thick sources with X-ray luminosities of $L_{X_{INT}} > 10^{47}$ erg/s, based on the assumption that potential Compton-thick objects at high redshifts are likely to have similar properties of Compton-thick objects in the local universe.

In summary, the column densities in our survey show no trend in X-ray luminosity and no clear trend in redshift. If we compare our results with studies of AGN in the local universe, the low redshift samples contain significant fractions of heavily absorbed sources ($N_H > 10^{23}$ cm^{-2}), which are not found in our sample. Our survey is biased toward very X-ray luminous QSOs. Deeper X-ray observations are needed to detect high redshift type II QSOs with intrinsic X-ray luminosities of $L_{X_{INT}} > 10^{44}$ erg/s which could be Compton-thick absorbed and have only observable X-ray luminosities of $L_{X_{OBS}} \gtrsim 10^{42}$ erg/s. Since we are missing these sources, a dramatic evolution in column density among type II AGN/QSOs cannot be excluded.

5.3   Conclusions of the thesis

In Sect. 2 I identified the main issues to be addressed by this thesis. Here I summarise these main points.

We were able to spectroscopically classify 65% of the X-ray sources in the central *XMM-Newton* Marano field survey. About 90% of the classified X-ray sources are powered by accretion onto super-massive black holes at different cosmic times. We therefore confirmed the results of other much deeper X-ray surveys such as Mainieri et al. (2002), Barger et al. (2002), and Szokoly et al. (2004). They showed that more than 90% of soft (< 2 keV)and 60% of the hard (2-8 keV) cosmic X-ray background can be resolved into single sources. The higher sensitivity of these surveys allows the classification of more low-luminosity X-ray sources. Interestingly, most of the additional X-ray sources are found at low redshifts. However, very deep X-ray surveys do not discover further X-ray source populations than found in the *XMM-Newton* Marano field survey.

The X-ray and optical properties of the different X-ray source populations are spread over a wide range for different parameters. In the optical they cover an R-band magnitude range of $R \sim 12$ down to undetected in the R-band images ($R \sim 24$, for the *XMM-Newton* Marano field survey). In terms of X-ray fluxes they extend over almost three decades ($f_X = (0.16 - 54) \times 10^{-14}$ erg cm^{-2} s^{-1}). However, the different X-ray source populations separate in different optical and X-ray parameter spaces. Low X-ray emitting normal galaxies and X-ray active stars can be clearly distinguished from accretion onto super-massive black holes (type I and type II AGN) by different combinations of parameters, such as hardness ratio vs. X-ray luminosity and X-ray flux vs. R-band magnitude. These diagnostic plots were known previously and are widely used in the literature (e.g., Mainieri et al. 2002, Szokoly et al. 2004).

The *XMM-Newton* Marano field survey classified a significant number of optically secure type II objects over a wide range of redshifts. Type I and type II AGN are more difficult to distinguish in their X-ray and optical properties. In general type II AGN are

found at lower redshifts, are more absorbed in the X-ray, have slightly higher f_X/f_{opt} values, and on average lower observed X-ray luminosities than type I AGN. A significant number of exceptions exists in both populations. For example, we found type I AGN with evidence of absorption comparable to type II AGN. We also discovered type II AGN that are unabsorbed. There are type II AGN that have X-ray luminosities comparable to the highest X-ray luminosities found in type I AGN and even a type I AGN with an f_X/f_{opt} value similar to low X-ray luminous normal galaxies that are not powered by accretion onto super-massive black holes. In every studied X-ray and optical parameter space there is considerable overlap between type I and type II AGN. The extreme cases such as X-ray absorbed type I AGN (optically classified) can be explained by advanced unification models (Elitzur 2006), which assume a soft edge torus with optically thick clouds. Since the X-ray emission of the AGN originates from a much smaller region in the central part of the AGN than the optical, an optically thick cloud can absorb the X-ray emission but an optical spectrum would reveal a regular type I AGN. However, the advanced unification scenario fails for the observation of unabsorbed type II AGN. Most likely such observations can be explained by different epochs of the X-ray and optical observation. The optical observation was obtained when a significant number of optically thick clouds blocked the direct view on the central engine of the AGN. Since the clouds are expected to move, an X-ray observation at earlier or later times can look directly on the central part and thus finds no X-ray absorption in this optically confirmed type II QSO. The observations of the same X-ray flux before and after a dip in the X-ray light curve in the AGN of NGC 3227 (Lamer et al. 2003) and NGC 1365 (Risaliti et al. 2007) support the picture of crossing clouds. The interpretation as varying accretion rate of the black hole is incompatible with these data.

The wide range of overlap in different parameter spaces between type I and type II AGN is evidence that the same physical processes are involved and a more advanced unification model will be able to explain our observation of a large variety of AGN. The additional use of other wavelength ranges, both deeper and more frequent X-ray observations, as well as simultaneous optical and X-ray observations will be essential to arrive at a final answer to the question. The significant number of exceptions in the strict type I and type II classification scheme suspect that the same, but not yet fully understood, physical model is acting in both X-ray source populations.

The combination of the *XMM-Newton* Marano field survey, the AXIS, and XWAS allowed us to study one of the largest, optically very strict type II QSO sample ever obtained. Type II QSOs are expected to be a main contributor to the cosmic X-ray background. In order to analyse the X-ray spectra, I carefully studied the fit results of simulated X-ray spectra as a function of fit statistic and binning method. The proper fitting of spectra with relatively few counts is a notorious problem in X-ray astronomy. This thesis contains the most extensive analysis of optically secure identifications published in that field. I only detected moderately absorbed type II QSOs and some unabsorbed objects. Although the importance of possible bias effects is not known completely, the absorption in distant type II QSOs shows no significant trend in redshift or X-ray luminosity. The moderate absorption found in these objects gives evidence that distant type II QSOs ($L_{X_{OBS}} > 10^{44} \, \mathrm{erg \, s^{-1}}$)

are not contributing significantly to the hard cosmic X-ray background.

5.4   Outlook

ROSAT was only able to study the X-ray background up to 2 keV. *XMM-Newton* and *Chandra* gave access to the X-ray sky in an energy range of 2-12 keV by discovering a large population of absorbed, low-luminosity, low-redshift X-ray sources. However, the understanding of the cosmic X-ray background peak at ∼30 keV is still insufficient. Synthesis models of the cosmic X-ray background need a further large Compton-thick population, but the observational evidence in the high-redshift universe is missing.

X-ray surveys such as the *XMM-Newton* Marano field survey, AXIS, and XWAS are able to significantly improve the sample size of X-ray source populations that are thought to contribute to the cosmic X-ray background, but are only found in low numbers in the energy range of current X-ray missions. In chapter 4 we followed this approach and studied the amount and evolution of absorption in type II QSOs. The moderate absorptions found in these objects suggests that their contribution to the cosmic X-ray background peak is overestimated.

Future satellite missions that are able to image the energy range around the peak of the cosmic X-ray background are needed to improve our understanding. *SIMBOL-X*, a joint French-Italian mission, is planned to carry the first 0.5-80 keV imaging telescope that takes advantage of the spacecraft formation flying technology. *XEUS*, ESA's X-Ray Evolving Universe Spectrometer, is proposed to be launched in 2018 and will possibly be equipped with an instrument sensitive in the 10-40 keV energy range. In addition, NASA is also considering to configure its future X-ray mission *Constellation X* with a hard X-ray telescope (6-40 keV). These missions will help to solve the question of the cosmic X-ray background peak's origin. Current X-ray missions find a significant decrease of the resolved fraction of the X-ray background with higher energies (Worsley et al. 2005). Up to now there is still room for a considerable fraction of a diffuse cosmic X-ray background above 10 keV.

In terms of the unification model *XMM-Newton* and *Chandra* helped to improve our understanding substantially. Due to the enlarged high sensitivity energy range compared to *ROSAT*, the physical processes of cold and warm absorbers, emission and absorption lines, as well as iron lines and edges could be studied. X-ray observations offer the unique possibility to study the immediate vicinity of the black holes. Small scale structures such as optically thick clouds in the proximity of the accretion disk can be investigated on very small time scales in the X-ray regime. Based on these observations more advanced unification models have been developed that are able to explain the mismatch between optical and X-ray observations of AGN. A precise knowledge about the statistics of mismatches and further X-ray observations of transient objects (AGN that change their Seyfert classification), will constrict the parameter space in the new unification models further. A detailed understanding of the unification scheme for AGN can also influence our knowledge of the cosmic X-ray background, since AGN are the primary contributors. To use existing X-ray

telescopes more effectively for answering our basic questions in X-ray astronomy, theorists and observers must improve their cooperation.

X-ray astronomy developed over the past 50 years to become one of the strongest research fields in modern astronomy. In the 1950s scientists considered the Sun to be the only detectable source in the X-ray universe. Today we recognise the potential of X-ray missions. Comets, planets, stars, star forming regions, galaxies, active galaxy nuclei, and galaxy clusters can be studied in the X-ray regime. With future missions such as *eRosita* which will even map the distribution of the dark matter in the universe, X-ray astronomy is still extending its importance in modern astronomy in almost every research field. The rapid improvement of new technologies for X-ray missions and future cornerstone missions of ESA and NASA will ensure X-ray astronomy's remarkable significance in astronomy.

Appendix A

X-ray source list of the XMM-Newton Marano field

Table A.1: X-ray source list of the Marano field. The detailed explanation of the individual columns follows the table in this Appendix.

(1) ID	(2) Name XMMU J...	(3) CR $[ks^{-1}]$	(4) ML	(5) σ_X [arcsec]	(6) $HR1$	(7) $HR2$	(8) $HR3$	(9) Flux $[10^{-14}\mathrm{ergs}^{-1}\mathrm{cm}^{-2}]$
1	XMMU J031549.7-551810	101.0±2.1	6918.8	0.72	0.195±0.033	-0.617±0.032	-0.524±0.081	16.31
2	XMMU J031547.5-552902	296.3±6.4	7886.9	0.72	0.316±0.034	-0.681±0.030	-0.362±0.087	47.85
3	XMMU J031732.8-552025	181.3±8.7	2130.2	0.77	0.788±0.066	-0.587±0.083	-0.381±0.198	29.27
4	XMMU J031334.1-552642	232.7±6.3	4202.8	0.74	-0.037±0.040	-0.760±0.038	-0.672±0.133	37.56
5	XMMU J031650.3-551109	51.1±2.6	1326.8	0.78	0.075±0.089	-0.750±0.099	-0.985±0.410	8.244
6	XMMU J031605.9-551538	37.0±1.3	1763.4	0.76	0.061±0.053	-0.690±0.057	-0.519±0.197	5.966
7	XMMU J031505.7-550942	24.6±1.0	1197.7	0.78	-0.095±0.061	-0.606±0.073	-0.864±0.200	3.967
8	XMMU J031456.2-552006	24.6±1.0	1025.1	0.78	0.760±0.070	-0.186±0.074	-0.287±0.098	3.967
9	XMMU J031510.1-551313	21.3±0.9	1151.4	0.77	0.564±0.056	-0.554±0.056	-0.520±0.133	3.438
10	XMMU J031328.3-551019	60.3±2.2	1627.3	0.77	0.570±0.051	-0.541±0.051	-0.281±0.105	9.740
11	XMMU J031511.4-550927	24.7±1.0	1123.8	0.77	0.206±0.061	-0.664±0.060	-0.616±0.187	3.984
12	XMMU J031432.4-551440	21.1±0.9	988.4	0.81	0.325±0.057	-0.984±0.026	−	3.405
13	XMMU J031351.1-551837	29.3±1.4	796.3	0.81	0.041±0.074	-0.702±0.078	-0.189±0.233	4.733
14	XMMU J031638.1-550635	33.6±1.8	727.7	0.83	0.184±0.085	-0.740±0.083	-0.504±0.327	5.419
15	XMMU J031552.8-550816	17.6±1.0	563.1	0.82	0.526±0.087	-0.552±0.091	-0.363±0.200	2.847
16	XMMU J031538.3-550140	41.4±2.0	916.2	0.80	0.332±0.073	-0.575±0.072	-0.359±0.168	6.678
17	XMMU J031528.6-551029	24.9±1.0	1053.5	0.80	0.381±0.054	-0.690±0.052	-0.446±0.181	4.022
18	XMMU J031421.3-552403	18.9±1.2	403.9	0.87	0.454±0.093	-0.669±0.091	-0.614±0.344	3.056
19	XMMU J031525.3-551827	13.2±0.8	460.7	0.84	0.399±0.082	-0.648±0.080	-0.393±0.247	2.129
20	XMMU J031621.6-551759	17.1±1.3	380.8	0.87	0.569±0.119	-0.432±0.117	-0.507±0.253	2.758
21	XMMU J031626.3-552250	19.3±1.5	314.2	0.94	0.529±0.118	-0.703±0.106	-0.819±0.353	3.110
22	XMMU J031519.9-550230	24.4±1.5	473.6	0.89	0.238±0.101	-0.540±0.107	-0.128±0.223	3.936
23	XMMU J031432.3-551959	15.5±1.0	400.6	0.87	0.313±0.092	-0.691±0.098	-0.118±0.273	2.499
24	XMMU J031703.7-550513	43.9±3.5	339.3	0.97	0.326±0.128	-0.480±0.123	-0.669±0.228	7.091
25	XMMU J031534.9-551925	14.7±1.0	448.3	0.85	0.352±0.093	-0.611±0.097	-0.608±0.254	2.373
26	XMMU J031436.1-551402	11.0±0.7	326.8	0.90	0.340±0.101	-0.732±0.109	-0.275±0.390	1.770
27	XMMU J031538.9-552219	13.1±1.0	285.5	0.92	0.290±0.121	-0.862±0.124	-0.227±0.801	2.116
28	XMMU J031507.7-550456	15.6±1.0	404.5	0.89	0.166±0.088	-0.702±0.094	-0.711±0.349	2.524
29	XMMU J031511.2-551530	11.0±0.7	448.1	0.86	0.312±0.080	-1.000±0.042	−	1.780
30	XMMU J031659.7-551622	14.9±1.3	207.6	0.99	1.000±0.095	0.085±0.167	-0.237±0.188	2.408
31	XMMU J031706.8-551948	32.0±2.6	297.5	0.97	0.650±0.135	-0.251±0.133	-0.551±0.190	5.159
32	XMMU J031547.2-551755	12.5±0.9	279.1	0.88	0.908±0.090	-0.344±0.098	-0.523±0.177	2.018
33	XMMU J031319.5-551616	19.9±1.4	295.1	0.93	0.531±0.118	-0.551±0.122	-0.566±0.277	3.212
34	XMMU J031559.3-552637	28.2±1.9	476.3	0.88	-0.240±0.095	-0.668±0.122	-0.675±0.413	4.560
35	XMMU J031503.3-551906	9.4±0.7	249.8	0.90	0.931±0.101	-0.292±0.134	0.094±0.166	1.513
36	XMMU J031411.5-551830	8.5±0.8	164.2	1.01	0.601±0.174	-0.459±0.160	-0.481±0.319	1.365
37	XMMU J031236.3-545314	67.1±5.3	256.9	1.04	0.233±0.126	-0.513±0.123	-0.542±0.270	10.84
38	XMMU J031630.2-551909	21.6±1.4	414.3	0.89	0.254±0.087	-0.819±0.075	-0.398±0.429	3.481
39	XMMU J031339.7-550151	19.8±1.5	249.8	1.00	0.769±0.122	-0.402±0.122	-0.338±0.209	3.201
40	XMMU J031558.0-545549	30.9±3.1	180.8	1.12	0.433±0.140	-0.819±0.117	-0.271±0.658	4.982
41	XMMU J031608.1-551723	8.7±0.9	151.6	1.01	0.194±0.128	-0.947±0.100	−	1.410
42	XMMU J031548.8-552245	12.3±1.0	216.1	0.96	0.231±0.120	-0.647±0.123	-0.693±0.396	1.992
43	XMMU J031332.4-551050	12.2±1.0	179.3	1.03	0.549±0.102	-0.933±0.085	-1.000±0.982	1.973
44	XMMU J031346.7-550031	14.1±1.4	119.6	1.18	0.366±0.154	-0.769±0.132	0.364±0.325	2.279
45	XMMU J031451.5-551932	5.3±0.6	89.0	1.13	1.000±0.087	-0.301±0.168	-0.363±0.293	0.853
46	XMMU J031607.4-552322	13.2±1.2	183.7	1.07	0.052±0.155	-0.582±0.174	-0.514±0.479	2.131

Table A.1: X-ray source list (continued)

(1) ID	(2) Name XMMU J...	(3) CR $[ks^{-1}]$	(4) ML	(5) σ_X [arcsec]	(6) $HR1$	(7) $HR2$	(8) $HR3$	(9) Flux $[10^{-14}\mathrm{ergs^{-1}cm^{-2}}]$
47	XMMU J031538.8-551043	4.5±0.5	82.4	1.12	0.925±0.124	-0.407±0.158	-0.886±0.260	0.731
48	XMMU J031458.5-545732	21.7±1.9	183.1	1.09	0.551±0.126	-0.925±0.093	–	3.502
49	XMMU J031638.4-552013	13.5±1.2	167.9	1.03	1.000±0.050	-0.413±0.134	-0.430±0.248	2.172
50	XMMU J031410.1-551746	7.6±0.7	112.1	1.11	0.969±0.087	-0.367±0.157	-0.117±0.245	1.233
51	XMMU J031630.6-551501	10.4±1.0	154.6	1.05	0.617±0.145	-0.411±0.147	-0.530±0.334	1.687
52	XMMU J031451.7-545713	15.6±2.0	89.9	1.26	0.033±0.209	-0.662±0.231	–	2.518
53	XMMU J031358.9-551754	6.7±0.8	75.4	1.20	0.574±0.185	-0.478±0.179	-1.000±0.487	1.078
54	XMMU J031612.7-545910	11.3±1.5	68.3	1.34	0.175±0.222	-0.852±0.197	0.242±0.888	1.820
55	XMMU J031457.3-552027	4.6±0.6	45.0	1.31	0.421±0.203	-0.759±0.256	-0.219±0.899	0.741
56	XMMU J031250.9-551728	28.2±2.6	208.6	1.07	0.142±0.172	-0.208±0.174	-0.940±0.192	4.559
57	XMMU J031344.2-551922	8.2±0.9	74.9	1.22	0.349±0.179	-0.547±0.168	-0.259±0.358	1.329
58	XMMU J031301.8-552224	21.0±2.1	103.4	1.20	0.128±0.157	-0.412±0.170	-0.862±0.253	3.389
59	XMMU J031339.6-551426	10.9±0.9	138.7	1.06	0.126±0.120	-0.640±0.135	0.252±0.253	1.753
60	XMMU J031426.4-551746	6.5±0.6	97.6	1.14	0.211±0.155	-0.468±0.165	-0.493±0.336	1.042
61	XMMU J031238.7-550232	2.9±1.1	9.6	2.26	1.000±0.892	-1.000±0.643	–	0.465
62	XMMU J031442.0-545555	22.3±3.0	82.8	1.35	0.625±0.149	-0.795±0.128	-0.043±0.495	3.595
63	XMMU J031517.1-550602	7.2±0.7	130.2	1.07	0.651±0.143	-0.398±0.132	-1.000±0.197	1.164
64	XMMU J031334.0-551021	7.3±0.9	44.9	1.43	0.240±0.187	-0.620±0.182	0.128±0.361	1.179
65	XMMU J031402.2-552756	2.2±1.3	9.9	2.07	–	–	–	0.360
66	XMMU J031500.8-550718	4.0±0.6	51.4	1.24	0.720±0.184	-0.585±0.167	-0.458±0.488	0.652
67	XMMU J031310.6-551312	12.0±1.1	109.4	1.09	0.232±0.153	-0.609±0.154	0.062±0.323	1.945
68	XMMU J031338.2-552303	12.1±1.2	107.1	1.13	0.105±0.181	-0.569±0.200	-0.183±0.442	1.954
69	XMMU J031415.4-551910	3.1±0.6	19.3	1.54	0.639±0.293	-0.867±0.260	0.676±0.595	0.500
70	XMMU J031620.8-550648	2.9±1.0	13.4	1.84	-0.259±0.652	–	0.959±0.482	0.464
71	XMMU J031714.1-550131	17.9±2.5	61.4	1.45	0.643±0.182	-0.856±0.146	-0.304±0.861	2.892
72	XMMU J031660.0-545855	4.9±2.1	9.5	2.38	-0.145±0.860	-1.000±0.872	–	0.787
73	XMMU J031321.3-552046	12.9±1.5	87.6	1.24	0.379±0.155	-0.806±0.133	0.399±0.371	2.086
75	XMMU J031601.3-550516	5.6±0.7	56.6	1.25	0.391±0.195	-0.521±0.200	-0.874±0.360	0.909
76	XMMU J031549.7-550908	4.9±0.6	67.5	1.28	0.472±0.179	-0.819±0.170	0.177±0.655	0.798
78	XMMU J031502.2-552611	4.6±1.1	19.0	1.50	1.000±0.332	-0.561±0.316	0.263±0.505	0.748
79	XMMU J031343.7-552007	1.8±0.6	5.4	1.98	–	0.479±0.739	-0.832±0.777	0.295
80	XMMU J031359.8-545716	11.7±1.8	52.1	1.45	0.156±0.257	-0.825±0.253	–	1.886
81	XMMU J031343.7-550153	12.7±1.3	98.6	1.20	0.510±0.136	-0.625±0.132	-0.931±0.224	2.046
83	XMMU J031448.2-552231	6.5±0.8	87.9	1.16	0.417±0.142	-0.737±0.148	-0.682±0.632	1.046
84	XMMU J031621.8-552038	5.8±1.1	42.0	1.41	0.979±0.154	-0.739±0.275	-0.087±0.845	0.934
85	XMMU J031523.1-545919	1.4±0.7	6.4	2.28	-1.000±0.502	–	–	0.222
86	XMMU J031345.0-551612	5.6±0.7	49.8	1.32	0.558±0.194	-0.403±0.193	-1.000±0.389	0.911
87	XMMU J031454.9-551411	1.8±0.3	15.9	1.53	0.743±0.362	-0.453±0.416	-1.000±0.746	0.285
88	XMMU J031316.3-550311	10.4±1.2	67.0	1.38	0.289±0.165	-0.700±0.174	-0.293±0.501	1.672
90	XMMU J031205.6-545831	17.7±2.9	35.7	1.77	-0.349±0.287	-0.525±0.443	0.334±0.597	2.864
92	XMMU J031200.1-550224	22.2±2.8	430.8	1.47	0.492±0.210	-0.583±0.191	-0.722±0.410	3.590
94	XMMU J031530.5-552558	5.3±0.9	33.6	1.37	-0.460±0.210	-0.098±0.367	-1.000±0.708	0.856
96	XMMU J031654.4-550625	0.9±0.7	6.4	2.63	–	–	–	0.143
98	XMMU J031247.8-550535	14.4±1.7	79.7	1.33	0.841±0.120	-0.550±0.148	-0.711±0.297	2.325
99	XMMU J031358.1-545510	12.5±2.1	30.5	1.66	0.358±0.256	-0.410±0.257	-0.327±0.407	2.020
100	XMMU J031243.9-551100	13.8±1.7	63.3	1.39	0.256±0.192	-0.628±0.193	-1.000±0.496	2.233
101	XMMU J031719.1-550535	4.2±2.0	5.2	2.37	–	–	–	0.678
102	XMMU J031259.3-550934	4.3±1.1	12.1	2.23	1.000±0.341	-1.000±0.256	–	0.689
104	XMMU J031647.2-551029	2.7±0.9	7.9	2.16	0.944±0.438	-0.692±0.412	–	0.430
106	XMMU J031510.1-550516	3.5±0.7	24.9	1.69	0.286±0.354	-0.404±0.323	–	0.566
108	XMMU J031450.7-545541	18.1±2.6	62.5	1.51	-0.218±0.184	-1.000±0.098	–	2.920
111	XMMU J031505.0-552947	6.1±1.7	8.9	2.17	-0.206±0.499	0.029±0.584	-0.900±0.655	0.992
115	XMMU J031712.4-551033	2.6±1.2	6.3	2.41	–	–	–	0.421
116	XMMU J031620.9-551651	5.4±0.9	47.8	1.26	1.000±0.552	0.428±0.256	-0.426±0.271	0.867
117	XMMU J031601.7-552819	7.9±1.3	43.4	1.54	0.352±0.288	-0.667±0.296	–	1.274
119	XMMU J031729.1-552051	12.0±5.0	7.9	2.28	–	–	–	1.931
120	XMMU J031313.5-550158	7.9±1.2	32.7	1.50	0.298±0.216	-1.000±0.296	–	1.279
121	XMMU J031703.7-550840	4.2±1.4	15.1	1.79	0.894±0.423	-0.174±0.430	–	0.685
124	XMMU J031519.5-550122	5.1±1.0	24.7	1.63	0.997±0.143	-0.211±0.262	-0.856±0.370	0.818
125	XMMU J031623.4-550326	3.9±1.4	6.6	2.02	–	–	–	0.622
126	XMMU J031355.9-545353	8.1±2.5	8.5	2.23	0.282±0.485	-1.000±0.490	1.000±0.745	1.305
128	XMMU J031532.9-553100	4.9±1.7	6.7	2.26	–	–	–	0.793
130	XMMU J031537.4-552409	4.3±0.8	28.7	1.61	0.997±0.146	-0.626±0.272	–	0.693
131	XMMU J031703.4-552500	6.0±1.5	10.9	1.96	0.549±0.357	-1.000±0.163	–	0.970
132	XMMU J031614.5-551728	4.3±0.9	27.7	1.45	0.652±0.330	-0.365±0.277	-0.290±0.519	0.686
133	XMMU J031426.4-552113	2.7±0.6	11.4	1.82	-0.339±0.354	-0.490±0.606	0.160±0.934	0.429
134	XMMU J031258.4-550235	7.2±1.2	30.9	1.60	-0.504±0.268	-0.070±0.447	-0.209±0.572	1.162
135	XMMU J031315.3-552623	12.8±2.5	31.0	1.70	0.134±0.243	-0.695±0.241	-1.000±0.701	2.065
136	XMMU J031607.7-553423	34.9±5.3	299.1	1.59	0.872±0.211	-0.564±0.265	-0.023±0.522	5.629
138	XMMU J031315.2-550136	4.4±1.0	10.1	1.85	0.460±0.472	-0.037±0.405	-0.631±0.491	0.704
140	XMMU J031433.1-552517	6.8±0.9	46.4	1.35	0.294±0.183	-0.762±0.212	-0.815±0.842	1.105

Table A.1: X-ray source list (continued)

(1) ID	(2) Name XMMU J...	(3) CR $[ks^{-1}]$	(4) ML	(5) σ_X [arcsec]	(6) $HR1$	(7) $HR2$	(8) $HR3$	(9) Flux $[10^{-14}\mathrm{ergs^{-1}cm^{-2}}]$
142	XMMU J031240.2-545342	14.2±3.4	19.2	1.97	0.463±0.290	-0.630±0.249	-1.000±0.552	2.294
144	XMMU J031420.9-551023	2.9±0.5	21.6	1.68	0.597±0.260	-0.633±0.279	-0.769±0.816	0.463
145	XMMU J031537.1-551713	1.3±0.3	13.7	1.71	–	1.000±0.447	-1.000±0.604	0.213
149	XMMU J031254.9-551551	13.3±1.8	60.0	1.42	0.171±0.206	-0.634±0.217	-0.871±0.543	2.148
150	XMMU J031429.6-550605	3.7±0.6	32.8	1.43	1.000±0.160	-0.814±0.220	0.079±0.860	0.598
151	XMMU J031650.1-551059	10.3±2.4	5.2	2.16	-0.076±0.232	-0.654±0.281	0.053±0.597	1.665
153	XMMU J031537.7-552243	3.6±0.7	18.7	1.65	0.472±0.277	-0.870±0.248	–	0.583
157	XMMU J031627.9-550541	2.3±0.7	8.6	2.42	-1.000±0.738	–	–	0.369
159	XMMU J031435.7-553128	9.4±2.3	20.0	1.77	0.032±0.640	-0.566±0.726	–	1.520
163	XMMU J031506.7-550113	2.8±0.8	8.7	1.98	1.000±0.383	-1.000±0.249	–	0.451
164	XMMU J031326.5-550906	3.2±0.8	11.9	1.88	0.951±0.447	-0.715±0.517	0.617±0.674	0.514
165	XMMU J031532.4-551649	1.0±0.4	7.0	1.93	–	-0.027±0.636	-0.531±0.757	0.161
166	XMMU J031456.0-551811	2.0±0.4	11.6	1.68	1.000±0.607	0.135±0.318	-0.296±0.388	0.327
171	XMMU J031351.2-550257	5.8±0.8	46.7	1.40	1.000±0.128	0.162±0.222	-1.000±0.119	0.942
172	XMMU J031624.4-551905	5.9±0.8	57.5	1.30	0.719±0.186	-0.583±0.193	-0.425±0.494	0.959
175	XMMU J031541.5-553019	11.7±2.4	22.7	1.77	0.711±0.245	-1.000±0.244	–	1.887
178	XMMU J031455.2-545745	7.1±1.5	12.2	2.08	0.323±0.208	-0.752±0.175	-1.000±0.680	1.146
183	XMMU J031246.1-550523	8.5±1.5	25.3	1.61	0.668±0.219	-0.482±0.236	-0.758±0.370	1.376
184	XMMU J031425.7-552641	3.7±1.1	12.9	1.90	–	0.596±0.559	-0.663±0.523	0.603
185	XMMU J031650.8-552225	7.7±1.4	33.8	1.50	1.000±0.202	-0.456±0.220	-0.961±0.421	1.245
189	XMMU J031326.4-550121	2.6±0.9	8.9	2.12	-0.574±0.482	–	–	0.425
191	XMMU J031438.7-552005	2.9±0.5	24.9	1.55	0.105±0.549	0.308±0.409	-0.772±0.419	0.469
195	XMMU J031522.2-552750	4.7±1.0	16.7	1.70	0.115±0.435	0.196±0.371	-0.628±0.439	0.765
196	XMMU J031455.9-550046	5.3±1.0	24.6	1.96	0.128±0.244	-0.777±0.263	–	0.850
197	XMMU J031428.2-551933	2.5±0.5	16.2	1.67	1.000±0.440	0.565±0.343	-0.089±0.284	0.406
204	XMMU J031424.8-550204	3.5±0.8	12.1	1.99	0.583±0.510	-0.321±0.472	-0.022±0.649	0.558
205	XMMU J031319.1-552511	11.9±2.0	43.2	1.69	0.325±0.256	-0.637±0.252	-1.000±0.671	1.919
209	XMMU J031602.3-550248	4.7±0.8	23.0	1.54	0.349±0.259	-0.493±0.290	-1.000±0.390	0.756
217	XMMU J031419.4-551641	1.8±0.5	5.6	2.15	1.000±0.247	-1.000±0.271	1.000±0.473	0.286
218	XMMU J031405.6-545538	8.1±2.3	11.1	2.04	0.102±0.426	-0.562±0.384	–	1.305
219	XMMU J031308.2-551905	14.7±1.7	82.0	1.30	0.844±0.170	-0.382±0.160	-0.310±0.283	2.370
220	XMMU J031550.3-550144	5.3±1.1	19.7	1.85	0.362±0.261	-0.857±0.229	–	0.863
221	XMMU J031449.1-551433	2.6±0.4	29.1	1.39	–	0.906±0.217	-0.164±0.235	0.417
222	XMMU J031644.2-552006	3.1±0.9	8.0	2.08	-0.445±0.704	0.636±0.485	-1.000±0.343	0.504
223	XMMU J031647.7-551409	7.2±1.1	40.3	1.41	0.694±0.178	-0.439±0.177	-0.076±0.326	1.156
224	XMMU J031304.9-551606	8.9±1.2	55.4	1.52	–	0.827±0.228	-0.207±0.219	1.443
225	XMMU J031332.1-550044	7.7±1.2	29.5	1.61	1.000±0.074	-0.151±0.213	-0.394±0.292	1.239
226	XMMU J031649.7-552508	7.7±1.7	15.7	2.00	0.718±0.280	-1.000±0.156	–	1.243
229	XMMU J031606.1-551443	1.7±0.6	5.4	2.03	-0.858±0.848	0.891±0.659	-1.000±0.547	0.268
232	XMMU J031441.9-550816	4.7±0.6	53.3	1.21	0.563±0.210	-0.563±0.198	0.393±0.266	0.756
236	XMMU J031332.1-545912	4.8±1.2	9.5	1.97	0.924±0.442	-0.543±0.482	0.202±0.777	0.769
237	XMMU J031431.9-553401	22.7±6.1	23.3	1.87	0.790±0.259	-0.356±0.319	-0.413±0.510	3.667
241	XMMU J031322.0-551350	5.8±0.9	30.9	1.59	0.653±0.214	-0.893±0.134	0.468±0.583	0.933
242	XMMU J031604.3-550716	4.1±0.7	36.6	1.47	0.423±0.257	-0.405±0.275	-0.761±0.470	0.668
246	XMMU J031357.0-550108	4.4±1.0	13.2	2.50	1.000±0.199	-0.612±0.279	-0.091±0.640	0.708
247	XMMU J031439.0-551441	1.6±0.4	9.2	1.86	1.000±0.521	0.268±0.574	-1.000±0.434	0.263
248	XMMU J031629.7-551702	5.9±0.9	49.4	1.40	0.430±0.399	0.319±0.241	-0.442±0.281	0.951
251	XMMU J031434.6-552712	3.9±0.9	17.4	1.76	0.755±0.365	-0.682±0.453	–	0.626
253	XMMU J031438.2-550648	2.6±0.5	16.6	1.65	–	1.000±0.372	-0.256±0.312	0.417
255	XMMU J031446.2-550948	2.2±0.4	12.4	1.58	0.307±0.260	-0.512±0.297	–	0.359
256	XMMU J031445.7-551957	2.0±0.5	8.5	1.86	0.727±0.324	-0.269±0.351	-0.384±0.576	0.327
264	XMMU J031643.2-552924	14.5±2.5	30.7	1.68	0.411±0.270	-0.704±0.271	-1.000±0.943	2.338
265	XMMU J031336.6-550018	3.5±1.0	8.7	2.01	1.000±0.379	-0.646±0.322	–	0.572
267	XMMU J031422.9-551708	2.9±0.5	18.9	1.61	0.566±0.336	-0.209±0.311	-0.043±0.380	0.474
268	XMMU J031624.0-551520	3.8±0.7	26.3	1.56	0.332±0.354	-0.214±0.328	-1.000±0.578	0.609
272	XMMU J031650.4-551732	3.3±0.9	9.5	2.33	–	0.838±0.328	-0.607±0.431	0.530
275	XMMU J031534.3-552249	3.2±0.6	21.7	1.50	1.000±0.323	-0.233±0.285	-1.000±0.742	0.519
280	XMMU J031324.8-551118	4.0±0.8	12.5	1.71	0.622±0.474	0.160±0.328	-0.568±0.336	0.642
281	XMMU J031557.9-550601	2.7±0.6	12.2	1.74	–	0.568±0.338	-0.847±0.323	0.438
282	XMMU J031530.4-552509	3.0±0.7	13.4	1.78	-0.142±0.354	-0.706±0.455	–	0.491
286	XMMU J031207.3-550932	13.7±2.5	29.6	2.06	0.684±0.392	-1.000±0.195	–	2.208
290	XMMU J031201.9-550729	20.2±2.8	57.0	1.41	-0.104±0.239	-0.383±0.323	-0.756±0.428	3.257
292	XMMU J031449.4-545817	14.1±2.1	75.1	1.40	0.930±0.159	-0.549±0.189	-1.000±0.525	2.272
298	XMMU J031549.8-550248	3.1±0.8	6.6	2.17	-0.490±0.474	-0.569±0.853	0.752±0.504	0.493
300	XMMU J031501.6-551413	1.2±0.3	5.7	2.04	0.666±0.399	-0.872±0.351	–	0.187
305	XMMU J031434.4-551502	1.9±0.5	6.2	2.10	0.579±0.161	-0.807±0.142	-1.000±0.676	0.306
306	XMMU J031417.7-550748	1.7±0.5	5.5	1.93	1.000±0.594	-0.342±0.645	0.646±0.389	0.279
308	XMMU J031318.0-551551	4.2±1.1	8.3	2.29	0.410±0.257	-0.473±0.288	-0.720±0.451	0.675
309	XMMU J031709.8-550750	4.9±1.5	9.7	2.12	1.000±0.293	-0.329±0.574	-1.000±0.747	0.797
310	XMMU J031458.4-551323	1.4±0.4	6.6	1.90	0.266±0.511	-0.223±0.504	-1.000±0.525	0.218

Table A.1: X-ray source list (continued)

(1) ID	(2) Name XMMU J...	(3) CR [ks^{-1}]	(4) ML	(5) σ_X [arcsec]	(6) $HR1$	(7) $HR2$	(8) $HR3$	(9) Flux [10^{-14}ergs^{-1}cm^{-2}]
311	XMMU J031630.2-551103	2.4±0.7	7.1	2.00	–	–	-0.018±0.526	0.380
313	XMMU J031607.1-552522	4.6±1.2	8.5	1.99	1.000±0.237	-0.284±0.507	-0.025±0.679	0.748
317	XMMU J031333.2-550322	4.5±0.9	17.9	2.13	1.000±0.682	0.683±0.249	-0.805±0.242	0.721
318	XMMU J031449.2-545941	4.2±1.2	9.4	2.32	0.615±0.490	-1.000±0.453	–	0.677
321	XMMU J031422.9-550842	1.7±0.4	7.4	2.03	0.406±0.439	-1.000±0.191	–	0.272
325	XMMU J031443.4-552029	3.6±0.7	16.3	1.59	0.498±0.269	-0.346±0.266	0.085±0.360	0.574
332	XMMU J031402.0-552720	7.1±1.5	17.0	1.80	0.332±0.266	-0.665±0.279	-1.000±0.706	1.139
334	XMMU J031631.7-551228	6.4±1.0	73.4	1.29	0.844±0.154	-0.761±0.141	-0.262±0.654	1.032
335	XMMU J031357.2-550432	2.6±0.7	7.7	1.95	1.000±0.421	-0.147±0.350	-1.000±0.677	0.415
338	XMMU J031227.1-551221	10.2±2.4	13.3	1.91	0.040±0.380	-0.290±0.406	-1.000±0.586	1.647
339	XMMU J031432.3-552927	6.0±1.4	9.8	2.42	-0.321±0.359	0.271±0.385	-1.000±0.665	0.964
345	XMMU J031316.7-552239	13.3±1.7	63.6	1.33	0.103±0.172	-0.457±0.192	-1.000±0.632	2.153
346	XMMU J031633.5-550412	2.9±0.8	17.0	2.13	–	–	–	0.462
349	XMMU J031541.0-552227	4.1±0.9	14.9	1.75	0.635±0.231	-0.540±0.210	0.145±0.352	0.655
355	XMMU J031517.8-545953	6.1±1.3	13.2	2.13	0.156±0.463	0.340±0.317	-0.382±0.340	0.979
356	XMMU J031519.6-552333	2.2±0.7	5.7	2.06	-1.000±0.523	–	-0.305±0.894	0.349
360	XMMU J031312.0-551718	5.5±1.3	15.6	1.79	1.000±0.931	-0.096±0.459	-0.207±0.585	0.881
361	XMMU J031314.6-550320	5.5±1.1	12.4	1.93	0.254±0.427	0.069±0.362	-0.210±0.372	0.882
364	XMMU J031412.3-552555	6.7±1.0	29.9	1.64	0.379±0.196	-0.611±0.204	-1.000±0.530	1.077
365	XMMU J031526.1-551937	2.5±0.6	7.3	2.37	0.746±0.381	-0.052±0.345	-0.068±0.417	0.401
367	XMMU J031635.1-550352	11.4±2.2	50.7	1.87	0.825±0.226	-0.455±0.243	-0.263±0.430	1.848
371	XMMU J031620.5-550330	3.5±0.9	13.1	1.94	–	1.000±0.734	0.341±0.401	0.561
373	XMMU J031502.6-550508	2.3±0.6	6.5	2.00	-0.264±0.417	0.061±0.488	-0.237±0.555	0.373
375	XMMU J031447.2-553258	15.2±3.3	19.6	2.06	0.602±0.376	-1.000±0.515	1.000±0.575	2.459
376	XMMU J031717.8-551948	5.1±1.5	12.9	1.96	0.659±0.487	-0.229±0.534	–	0.819
377	XMMU J031653.3-550838	4.6±1.1	18.4	1.74	0.479±0.358	-0.525±0.361	-0.442±0.755	0.743
380	XMMU J031449.7-552336	2.1±0.7	5.0	2.24	1.000±0.312	-1.000±0.486	–	0.335
381	XMMU J031644.6-552707	25.5±2.8	162.7	1.15	0.386±0.159	-0.698±0.158	0.220±0.358	4.112
382	XMMU J031247.4-551653	8.9±1.8	28.2	1.89	0.848±0.270	-0.927±0.167	–	1.445
385	XMMU J031318.2-550537	5.6±1.0	24.9	1.57	0.844±0.364	0.346±0.239	-0.369±0.247	0.910
388	XMMU J031401.2-545957	100.7±5.8	775.3	0.71	0.128±0.063	-0.652±0.060	-0.284±0.162	16.26
389	XMMU J031539.0-550336	2.5±0.7	7.3	1.96	0.710±0.326	-0.352±0.349	-0.904±0.570	0.399
397	XMMU J031638.3-545924	15.7±2.5	57.8	1.50	0.560±0.235	-0.506±0.228	-0.603±0.441	2.529
403	XMMU J031225.8-550554	18.6±2.2	67.9	1.41	0.151±0.182	-0.448±0.187	-0.730±0.309	3.005
408	XMMU J031554.2-551004	2.3±0.5	7.9	1.85	1.000±0.214	-0.051±0.327	-0.129±0.376	0.365
410	XMMU J031502.0-552742	4.1±1.1	5.8	2.17	0.146±0.623	-0.383±0.684	0.204±0.830	0.662
412	XMMU J031218.4-550648	7.0±1.9	6.9	2.72	0.623±0.300	-1.000±0.137	–	1.134
413	XMMU J031723.0-550222	9.5±2.4	14.0	2.20	0.187±0.796	0.502±0.448	-0.799±0.401	1.526
421	XMMU J031431.3-550943	1.9±0.4	10.1	2.21	0.842±0.241	-1.000±0.238	–	0.304
422	XMMU J031531.6-551049	2.3±0.4	14.5	1.80	0.520±0.452	0.229±0.283	-0.923±0.295	0.371
431	XMMU J031540.9-545649	6.6±1.3	16.1	1.84	0.706±0.284	-0.531±0.254	-1.000±0.426	1.060
433	XMMU J031436.4-552739	3.7±1.0	7.6	2.33	–	0.933±0.255	-0.762±0.330	0.595
437	XMMU J031534.0-550259	3.6±0.7	14.9	1.64	0.645±0.221	-0.609±0.236	-1.000±0.440	0.582
438	XMMU J031521.8-552338	2.1±0.6	6.2	2.22	0.223±0.412	-1.000±0.181	1.000±0.318	0.340
444	XMMU J031318.1-550600	3.9±0.9	11.5	1.95	1.000±0.999	0.617±0.307	-0.358±0.276	0.628
447	XMMU J031448.7-550037	3.6±1.0	6.4	2.71	0.641±0.401	-0.355±0.362	-1.000±0.732	0.587
449	XMMU J031543.3-550742	2.2±0.6	6.4	2.40	-0.022±0.395	-0.065±0.412	-1.000±0.655	0.357
452	XMMU J031618.2-545649	11.0±2.2	23.9	1.77	0.545±0.220	-0.595±0.205	-0.921±0.578	1.781
453	XMMU J031323.6-550445	3.9±1.0	5.2	2.46	1.000±0.160	0.019±0.339	-0.773±0.395	0.635
456	XMMU J031632.5-552743	7.5±1.7	15.3	1.85	0.464±0.272	-1.000±0.100	1.000±0.257	1.218
460	XMMU J031342.7-550700	5.4±0.8	36.6	1.44	0.410±0.190	-0.982±0.124	–	0.872
461	XMMU J031714.5-551252	4.2±1.6	6.1	2.29	–	1.000±0.285	-0.407±0.440	0.675
462	XMMU J031506.2-551626	1.9±0.4	9.2	1.79	1.000±0.587	0.165±0.269	-0.384±0.343	0.301
463	XMMU J031625.3-550839	3.1±0.8	18.8	1.61	0.979±0.305	-0.592±0.441	–	0.506
464	XMMU J031250.3-550430	4.9±1.2	11.4	2.05	0.083±0.378	-1.000±0.865	–	0.791
468	XMMU J031253.7-551005	9.3±1.4	82.7	1.29	-0.984±0.057	–	–	1.506
470	XMMU J031521.4-552123	3.0±0.6	15.0	1.69	1.000±0.186	-0.038±0.259	-0.675±0.414	0.477
473	XMMU J031532.5-551116	1.3±0.4	5.3	3.35	1.000±0.523	0.039±0.347	-1.000±0.163	0.216
475	XMMU J031352.3-550347	3.6±0.8	10.9	2.05	0.245±0.323	-1.000±0.206	1.000±0.677	0.586
479	XMMU J031600.2-545812	4.5±1.4	8.2	2.13	0.829±0.281	-0.437±0.298	-0.848±0.639	0.729
480	XMMU J031653.5-551234	4.8±1.2	11.1	2.30	0.667±0.354	0.041±0.285	-0.604±0.408	0.777
481	XMMU J031535.4-551616	2.0±0.4	12.3	1.69	0.959±0.599	0.075±0.463	0.291±0.326	0.319
483	XMMU J031405.7-550708	4.1±0.9	15.6	1.60	0.309±0.353	-0.267±0.334	-1.000±0.539	0.670
485	XMMU J031527.4-551618	1.4±0.4	5.6	1.95	–	0.652±0.587	0.071±0.426	0.229
489	XMMU J031452.6-550054	3.5±0.9	5.0	2.36	-0.004±0.274	-0.611±0.329	-1.000±0.842	0.563
496	XMMU J031245.3-551648	10.2±2.1	21.8	1.84	0.189±0.281	-0.850±0.212	–	1.649
497	XMMU J031457.7-550934	1.7±0.4	7.0	1.92	0.357±0.317	-0.841±0.305	–	0.267
498	XMMU J031506.3-551400	1.6±0.4	6.1	2.41	-0.091±0.317	-1.000±0.467	–	0.264
500	XMMU J031642.0-552839	6.3±1.8	5.4	2.37	1.000±0.469	0.353±0.368	-1.000±0.232	1.025
501	XMMU J031355.0-545622	6.3±1.7	7.5	2.57	0.325±0.345	-1.000±0.170	1.000±0.516	1.018

Table A.1: X-ray source list (continued)

(1) ID	(2) Name XMMU J...	(3) CR $[ks^{-1}]$	(4) ML	(5) σ_X [arcsec]	(6) $HR1$	(7) $HR2$	(8) $HR3$	(9) Flux $[10^{-14}\mathrm{erg s^{-1}cm^{-2}}]$
505	XMMU J031539.6-550801	2.6±0.6	8.5	1.76	0.026±0.294	-0.435±0.341	-0.052±0.573	0.416
511	XMMU J031528.1-551313	1.8±0.4	11.0	1.65	0.181±0.285	-0.758±0.363	–	0.299
512	XMMU J031348.4-551309	5.2±0.7	38.6	1.63	0.692±0.309	-0.230±0.260	-0.852±0.399	0.839
513	XMMU J031445.6-550016	5.3±1.0	24.5	1.57	0.814±0.220	-0.951±0.186	0.900±0.368	0.854
514	XMMU J031343.5-552901	5.8±2.0	7.8	2.17	0.590±0.447	-0.585±0.420	-0.011±0.885	0.943
516	XMMU J031213.8-551252	7.8±3.0	5.9	2.54	1.000±0.231	-0.556±0.308	-1.000±0.610	1.264
518	XMMU J031457.2-552924	6.8±1.1	33.9	1.49	0.672±0.294	-1.000±0.093	–	1.093
524	XMMU J031314.1-550419	7.6±1.1	50.6	1.34	0.681±0.274	-0.032±0.206	-0.140±0.228	1.222
526	XMMU J031428.6-553307	8.9±2.7	9.2	2.03	0.120±0.511	-0.158±0.472	–	1.443
528	XMMU J031711.5-551228	6.2±1.5	32.3	1.65	-0.453±0.357	-0.236±0.594	–	0.998
531	XMMU J031338.3-550352	20.1±1.8	241.9	1.01	0.183±0.123	-0.527±0.122	-0.453±0.270	3.244
532	XMMU J031521.7-545544	6.3±1.5	10.0	2.26	1.000±0.228	-0.235±0.298	-0.701±0.465	1.015
535	XMMU J031653.5-551154	3.4±1.0	10.0	2.00	0.294±0.371	-0.786±0.430	–	0.554
536	XMMU J031450.3-550410	1.4±0.5	6.9	2.29	-0.072±0.688	–	–	0.223
541	XMMU J031700.8-552131	3.5±1.2	13.7	2.18	–	–	–	0.561
543	XMMU J031250.3-551100	3.4±1.4	6.4	2.16	–	–	-0.032±0.689	0.552
544	XMMU J031528.7-552650	3.0±0.9	5.5	2.34	0.094±0.316	-0.825±0.454	–	0.489
547	XMMU J031527.0-550257	3.2±0.8	9.2	1.80	1.000±0.433	-0.857±0.397	–	0.510
550	XMMU J031648.5-552105	2.3±0.9	9.6	2.32	–	–	1.000±0.236	0.375
551	XMMU J031243.0-551159	6.5±1.5	11.0	2.11	0.507±0.317	-0.904±0.224	0.805±0.442	1.044
557	XMMU J031441.6-552138	1.6±0.5	5.2	2.30	-0.074±0.392	-1.000±0.265	–	0.254
559	XMMU J031617.3-551428	5.2±0.8	37.0	1.51	0.131±0.200	-0.753±0.240	-0.492±0.925	0.832
566	XMMU J031653.3-552155	3.0±1.0	6.7	2.81	–	0.500±0.638	-0.392±0.672	0.487
570	XMMU J031309.8-551224	3.7±1.0	5.4	2.17	0.208±0.690	-1.000±0.493	–	0.605
572	XMMU J031249.6-551539	4.4±1.2	7.8	2.37	-1.000±0.723	–	–	0.718
579	XMMU J031547.2-551419	1.7±0.4	6.8	1.94	0.525±0.270	-0.847±0.237	–	0.282
582	XMMU J031630.6-551130	4.8±0.9	18.3	1.78	0.205±0.220	-0.585±0.238	-0.658±0.603	0.768
584	XMMU J031652.3-553000	9.3±3.0	6.2	2.16	0.262±0.555	-1.000±0.388	–	1.497
585	XMMU J031309.2-551142	10.4±1.3	74.1	1.37	0.542±0.150	-0.919±0.111	–	1.679
593	XMMU J031511.3-551202	2.0±0.4	12.5	1.83	0.572±0.222	-0.878±0.181	–	0.327
595	XMMU J031405.8-550909	2.7±0.7	5.7	2.27	0.565±0.353	-0.410±0.350	-0.421±0.668	0.433
596	XMMU J031707.0-551915	8.4±1.6	20.0	1.59	0.361±0.233	-0.739±0.225	0.014±0.677	1.353
597	XMMU J031454.5-545810	10.3±1.6	57.6	1.40	0.480±0.214	-0.821±0.155	-1.000±0.768	1.662
607	XMMU J031651.3-551306	7.7±1.2	39.9	1.47	-0.218±0.221	-0.468±0.319	0.042±0.511	1.248
608	XMMU J031349.8-551259	4.3±0.7	28.4	1.36	0.456±0.197	-0.557±0.205	-0.099±0.424	0.691
610	XMMU J031552.0-551222	3.6±0.6	39.7	1.39	0.426±0.404	0.302±0.262	-0.538±0.289	0.584
611	XMMU J031335.8-545657	17.9±2.3	80.3	1.27	0.103±0.165	-0.822±0.151	-0.638±0.785	2.893
615	XMMU J031459.8-550356	5.5±0.7	52.0	1.34	0.036±0.233	-0.178±0.265	-0.629±0.363	0.891
616	XMMU J031246.4-545947	12.8±1.9	47.8	1.46	0.458±0.246	-0.604±0.226	-0.173±0.495	2.061
618	XMMU J031521.6-550349	3.1±0.9	8.3	2.67	0.464±0.425	-0.666±0.383	–	0.502
621	XMMU J031529.7-550022	2.1±0.8	11.8	2.15	–	–	1.000±0.717	0.336
627	XMMU J031523.9-550408	2.3±0.6	7.1	2.43	1.000±0.306	-0.805±0.235	–	0.372
630	XMMU J031625.0-551122	1.5±0.8	9.1	2.18	0.619±0.472	-1.000±0.292	–	0.239
631	XMMU J031532.8-551159	2.0±0.4	7.5	1.72	0.673±0.320	-0.634±0.308	0.328±0.504	0.323
632	XMMU J031624.5-552135	1.2±0.6	5.5	2.25	–	–	–	0.193
633	XMMU J031532.5-545909	4.0±1.1	8.0	2.01	-0.788±0.346	0.437±0.829	0.131±0.699	0.641
652	XMMU J031530.3-550437	14.0±1.0	328.4	0.89	0.350±0.106	-0.765±0.096	0.269±0.262	2.262
653	XMMU J031647.5-551229	6.9±1.1	46.2	1.31	0.397±0.212	-0.615±0.227	-0.298±0.616	1.119
654	XMMU J031706.1-552716	34.8±3.6	150.3	1.18	0.649±0.137	-0.632±0.138	-0.098±0.344	5.627
656	XMMU J031326.1-550427	35.3±3.1	320.8	0.98	1.000±0.033	-0.183±0.096	-0.470±0.135	5.695
660	XMMU J031537.2-545947	3.5±1.0	5.1	2.59	0.730±0.448	-0.080±0.414	-1.000±0.320	0.568
661	XMMU J031706.8-552435	7.9±2.3	12.7	2.53	0.805±0.490	-1.000±0.568	1.000±0.494	1.275
664	XMMU J031611.1-552117	2.7±0.7	6.2	2.23	0.249±0.330	-0.631±0.380	–	0.444
665	XMMU J031645.7-545900	5.9±1.8	7.5	2.44	0.728±0.354	-0.909±0.316	–	0.958
667	XMMU J031348.0-551205	5.4±1.0	25.1	2.79	-0.244±0.758	-1.000±0.913	–	0.875
673	XMMU J031540.4-551221	11.0±0.8	334.6	0.88	0.788±0.095	-0.534±0.103	-0.068±0.204	1.777
675	XMMU J031624.6-551143	9.8±1.0	122.8	1.07	0.378±0.123	-0.933±0.087	–	1.589
676	XMMU J031641.5-552408	4.1±1.1	6.1	2.08	1.000±0.178	-0.218±0.357	-0.124±0.481	0.656
680	XMMU J031647.6-552142	2.3±0.9	9.9	1.96	0.953±0.891	-1.000±0.441	1.000±0.510	0.375
681	XMMU J031248.9-550705	1.6±0.8	5.6	2.64	0.819±0.903	–	–	0.265
686	XMMU J031346.7-551148	94.0±2.2	4192.0	0.73	0.287±0.035	-0.633±0.033	-0.448±0.089	15.18
687	XMMU J031302.5-552604	16.3±3.1	26.4	1.88	0.252±0.226	-0.450±0.237	-0.952±0.296	2.626
688	XMMU J031145.8-550653	189.3±11.1	775.6	0.94	0.293±0.089	-0.587±0.086	-0.326±0.189	30.56
689	XMMU J031140.1-550613	29.5±4.0	50.3	1.84	0.094±0.186	-0.723±0.174	–	4.761
690	XMMU J031135.6-550314	57.4±9.1	86.2	1.80	0.270±0.132	-0.582±0.135	-0.591±0.326	9.267
691	XMMU J031134.5-550608	28.0±4.3	46.9	1.64	0.579±0.178	-0.794±0.141	-0.462±0.592	4.524
692	XMMU J031136.3-550514	36.3±4.7	73.0	1.49	-0.005±0.198	-0.439±0.227	-0.287±0.405	5.855
693	XMMU J031145.9-550702	336.5±20.0	418.0	0.98	0.191±0.201	-0.586±0.205	-0.458±0.476	54.32
694	XMMU J031146.4-550711	97.3±10.6	53.0	1.24	0.283±0.048	-0.609±0.046	-0.411±0.109	15.71
695	XMMU J031259.1-552556	45.5±6.3	91.5	1.83	0.307±0.139	-0.699±0.130	0.106±0.330	7.347
696	XMMU J031152.2-551049	28.0±4.7	41.8	1.84	0.348±0.193	-0.918±0.147	–	4.527

Description of Table A.1

(1) ID
Classification number of the *XMM-Newton* X-ray source in the Marano field.

(2) Name XMMU J...
XMMU source name of the *XMM-Newton* X-ray source.

(3) CR [ks^{-1}]
Added count rates from all three EPIC cameras.

(4) ML
Maximum detection likelihood.

(5) σ_{X} [arcsec]
Position error of the X-ray source. $\sigma_{\mathrm{X}} = \sqrt{\sigma_{\mathrm{stat.}}^2 + \sigma_{\mathrm{syst.}}^2}$, $\sigma_{\mathrm{syst.}} = 0.7$ arcsec, see Sects. 3.1.3 and 3.2.1.

(6) HR1
PN-detector hardness ratios with errors in the 0.2-0.5 keV & 0.5-2.0 keV band.

(7) HR2
PN-detector hardness ratios with errors in the 0.5-2.0 keV & 2.0-4.5 keV band.

(8) HR3
PN-detector hardness ratios with errors in the 2.0-4.5 keV & 4.5-7.5 keV band.

(9) flux [10^{-14} erg s^{-1} cm^{-2}]
EPIC flux in a 0.2-10 keV energy band. Determined from the sum of MOS1-, MOS2-, and PN-count rates in the 0.2-12 keV via an energy conversion factor of 1.61452×10^{-12} erg cm^{-2}.

Appendix B

Table of optical properties of candidate counterparts of Marano XMM-Newton X-ray sources

Table B.1: Optical properties of candidate counterparts of Marano XMM-Newton X-ray sources. The detailed explanation of the individual columns follows the table in this Appendix.

(1) No	(2) RA	(3) DEC	(4) $Dist_{OX}$	(5) K	(6) R	(7) Class	(8) z	(9) Flags	(10) $log(L_{X_{OBS}})$	(11) M_B	(12) α_{OX}	(13) N_H	(14) $log(L_{X_{INT}})$	(15) Rem.
1A	3 15 49.6	-55 18 12	1.52	17.14	20.39	B	0.808	1 - -	44.70	-22.26	1.32	$0.00^{+0.01}_{-0.00}$	44.70	2,3
2A	3 15 47.5	-55 29 04	1.37	–	19.66	B	0.464	1 - -	44.59	-21.66	1.22	$0.00^{+0.04}_{-0.00}$	44.59	2
3A	3 17 32.7	-55 20 26	1.35	–	–	B	0.406	1 - -	44.24	–	–	$0.28^{+0.10}_{-0.12}$	44.44	2
4A	3 13 34.0	-55 26 43	1.26	–	17.05	B	0.987	111	45.28	-26.04	1.74	$0.00^{+0.01}_{-0.00}$	45.28	1
5A	3 16 50.4	-55 11 09	0.78	–	17.51	B	2.531	1 - -	45.63	-27.79	2.00	$0.00^{+0.01}_{-0.00}$	45.63	1,3
6A	3 16 05.8	-55 15 39	1.12	17.79	20.64	B	0.636	111	44.01	-21.49	1.46	$0.00^{+0.01}_{-0.00}$	44.01	1,3
7A	3 15 05.6	-55 09 42	0.13	18.25	21.98	B	0.501	111	43.59	-19.56	1.30	$0.00^{+0.00}_{-0.00}$	43.59	4
8A	3 14 56.0	-55 20 07	1.17	15.53	19.03	G	0.387	111	43.32	–	–	$2.09^{+0.47}_{-0.73}$	43.90	3,5
9A	3 15 09.9	-55 13 13	1.18	18.81	22.63	N	1.427	111	44.64	–	–	$0.33^{+0.18}_{-0.20}$	44.73	4,C
10A	3 13 28.3	-55 10 18	0.49	16.98	20.24	B	1.378	111	45.05	-23.58	1.45	$0.23^{+0.18}_{-0.16}$	45.12	3
11A	3 15 11.3	-55 09 27	0.35	17.98	21.02	B	1.192	111	44.51	-22.45	1.47	$0.00^{+0.01}_{-0.00}$	44.51	2,3
12A	3 14 32.4	-55 14 40	0.46	8.87	–	S	0.000	1 - -	–	–	–	$0.00^{+0.01}_{-0.00}$	–	3
13A	3 13 50.9	-55 18 38	1.54	18.78	21.35	B	0.500	1 - -	43.66	-20.18	1.37	$0.00^{+0.01}_{-0.00}$	43.66	3
14A	3 16 38.0	-55 06 37	1.71	17.47	20.68	B	0.854	1 - -	44.28	-22.09	1.47	$0.00^{+0.01}_{-0.00}$	44.28	2,3
15A	3 15 51.7	-55 08 17	9.58	–	21.69	N	0.331	000	–	–	–	–	–	4, C
16A	3 15 38.3	-55 01 40	0.41	19.40	21.30	B	1.374	111	44.88	-22.51	1.33	$0.00^{+0.01}_{-0.00}$	44.88	3
17A	3 15 28.9	-55 10 27	3.62	18.49	21.27	B	2.161	111	45.15	-23.69	1.48	$0.00^{+0.19}_{-0.00}$	45.15	2,3,C
18A	3 14 21.1	-55 24 05	2.02	–	21.65	B	0.614	1 - -	43.69	-20.40	1.41	$0.05^{+0.08}_{-0.05}$	43.72	3
19A	3 15 25.2	-55 18 27	0.82	19.78	22.13	B	1.573	111	44.53	-22.03	1.42	$0.00^{+0.16}_{-0.00}$	44.53	3
20A	3 16 21.5	-55 17 59	0.63	17.33	–	N	2.207	111	45.01	–	–	$0.83^{+0.52}_{-0.44}$	45.12	C
20B	3 16 21.1	-55 18 01	4.11	13.28	16.72	S	0.000	011	–	–	–	–	–	3
21A	3 16 26.1	-55 22 51	1.38	12.16	16.50	S	0.000	1 - -	–	–	–	$0.00^{+0.02}_{-0.00}$	–	3
22A	3 15 19.7	-55 02 25	4.63	19.41	23.33	B	1.78	111	44.63	-21.19	1.11	$0.00^{+0.10}_{-0.00}$	44.63	C
22B	3 15 20.1	-55 02 34	4.62	17.36	19.98	B	1.353	111	44.34	-23.79	1.66	$0.00^{+0.06}_{-0.00}$	44.34	1,3,C
23A	3 14 32.1	-55 19 59	1.24	18.32	21.01	B	1.271	111	44.37	-22.62	1.56	$0.00^{+0.02}_{-0.00}$	44.37	1
25A	3 15 34.7	-55 19 26	0.85	18.12	–	B	1.430	111	44.48	–	–	$0.00^{+0.03}_{-0.00}$	44.48	3
26A	3 14 36.0	-55 14 03	0.80	17.90	20.23	B	1.19	111	44.15	-23.24	1.76	$0.00^{+0.03}_{-0.00}$	44.15	4,C
27A	3 15 38.7	-55 22 19	1.74	18.04	21.75	B	1.190	111	44.23	-21.72	1.46	$0.00^{+0.01}_{-0.00}$	44.23	3
28A	3 15 07.6	-55 04 56	0.64	17.75	20.15	B	1.315	111	44.41	-23.56	1.71	$0.00^{+0.01}_{-0.00}$	44.41	2,3
29A	3 15 11.1	-55 15 30	0.42	9.28	–	S	0.000	1 - -	–	–	–	$0.00^{+0.01}_{-0.00}$	–	3
32A	3 15 47.0	-55 17 55	1.44	17.75	22.96	N	2.727	110	45.09	–	–	$14.5^{+7.9}_{-8.2}$	45.55	C

Table B.1: continued

(1) No	(2) RA	(3) DEC	(4) $Dist_{OX}$	(5) K	(6) R	(7) Class	(8) z	(9) Flags	(10) $log(L_{X_{OBS}})$	(11) M_B	(12) α_{OX}	(13) N_H	(14) $log(L_{X_{INT}})$	(15) Rem.
33A	3 13 19.4	-55 16 17	0.62	17.18	19.21	B	2.166	1--	45.05	-25.76	1.88	$0.10^{+0.33}_{-0.10}$	45.07	1
34A	3 15 59.1	-55 26 37	1.72	18.32	20.70	B	0.983	1--	44.36	-22.38	1.50	$0.00^{+0.01}_{-0.00}$	44.36	3
35A	3 15 03.2	-55 19 06	0.67	16.17	19.54	N	0.391	111	42.91	-	-	$1.32^{+0.59}_{-0.58}$	43.39	4, C
35B	3 15 03.2	-55 19 09	3.28	-	19.54	N	0.391	011	-	-	-	-	-	C
36A	3 14 11.1	-55 18 29	3.12	19.91	-	-	-	-	-	-	-	-	-	4
38A	3 16 30.0	-55 19 11	2.28	19.66	22.33	B	1.254	111	44.50	-21.27	1.27	$0.00^{+0.01}_{-0.00}$	44.50	2,3
39A	3 13 39.7	-55 01 51	0.95	19.24	23.41	N	0.862	110	44.07	-	-	$0.76^{+0.63}_{-0.33}$	44.32	
41A	3 16 07.9	-55 17 24	1.58	18.54	22.36	B	0.979	111	43.85	-20.71	1.43	$0.00^{+0.05}_{-0.00}$	43.85	4
42A	3 15 48.7	-55 22 46	0.94	19.37	21.63	B	1.54	111	44.48	-22.47	1.51	$0.00^{+0.02}_{-0.00}$	44.48	4,C
43A	3 13 32.5	-55 10 49	1.14	19.52	23.40	B	2.013	111	44.76	-21.41	1.24	$0.17^{+0.32}_{-0.17}$	44.80	
44A	3 13 46.8	-55 00 31	1.07	17.42	21.40	B	0.785	111	43.82	-21.19	1.51	$0.00^{+0.10}_{-0.00}$	43.82	
44B	3 13 47.4	-55 00 30	6.41	-	22.24	N	0.480	000	-	-	-	-	-	
45A	3 14 51.8	-55 19 32	2.49	-	23.09	N	0.584	100	43.08	-	-	$0.69^{+0.51}_{-0.27}$	43.38	4
46A	3 16 07.0	-55 23 24	4.01	19.16	21.98	B	1.308	111	44.34	-21.71	1.43	$0.00^{+0.09}_{-0.00}$	44.34	C
47A	3 15 38.7	-55 10 44	1.34	19.06	23.94	N	0.900	100	43.47	-	-	$2.09^{+1.54}_{-1.09}$	43.89	C
47B	3 15 39.1	-55 10 42	3.72	19.99	22.76	N	0.89	000	-	-	-	-	-	C
49A	3 16 38.3	-55 20 14	1.66	16.01	20.26	G	0.454	111	43.22	-	-	$1.45^{+0.65}_{-0.63}$	43.70	
50A	3 14 09.9	-55 17 46	1.25	18.35	23.66	N	0.986	110	43.79	-	-	$3.63^{+1.63}_{-1.58}$	44.30	
51A	3 16 30.6	-55 15 03	1.83	16.57	20.95	N	0.58	110	43.37	-	-	$0.05^{+0.08}_{-0.05}$	43.41	
52A	3 14 51.4	-54 57 14	1.82	-	-	B	1.829	1--	44.77	-	-	$0.00^{+0.04}_{-0.00}$	44.77	2
53A	3 13 58.8	-55 17 54	0.67	18.82	23.23	N	1.340	100	44.07	-	-	$3.98^{+2.51}_{-2.93}$	44.50	
54A	3 16 12.4	-54 59 10	2.49	-	-	B	2.744	1--	45.05	-	-	$0.00^{+0.40}_{-0.00}$	45.05	1
56A	3 12 50.9	-55 17 26	1.94	16.65	20.11	B	0.641	111	43.90	-22.04	1.60	$0.01^{+0.08}_{-0.01}$	43.91	1
57A	3 13 44.0	-55 19 24	2.33	17.11	20.12	B	0.281	1--	42.52	-19.93	1.79	$0.01^{+0.08}_{-0.01}$	42.54	3
58A	3 13 01.7	-55 22 23	0.70	-	21.10	B	0.589	111	43.69	-20.85	1.49	$0.00^{+0.02}_{-0.00}$	43.69	
59A	3 13 39.4	-55 14 26	0.77	17.37	21.83	B	0.978	111	43.94	-21.23	1.49	$0.00^{+0.02}_{-0.00}$	43.94	
60A	3 14 26.3	-55 17 47	0.71	17.62	21.77	B	0.957	111	43.69	-21.25	1.59	$0.03^{+0.12}_{-0.03}$	43.71	3,5
63A	3 15 16.9	-55 06 02	1.25	20.37	23.19	N	2.800	110	44.88	-	-	$4.37^{+11.2}_{-2.10}$	45.13	C
64A	3 13 33.7	-55 10 21	2.32	17.21	21.51	B	1.165	111	43.95	-21.91	1.61	$0.00^{+0.08}_{-0.00}$	43.95	
66A	3 15 00.7	-55 07 18	1.23	18.40	21.41	N	0.981	100	43.51	-	-	$0.28^{+0.28}_{-0.20}$	43.63	C
67A	3 13 10.6	-55 13 13	1.22	18.27	21.69	B	0.866	111	43.85	-21.11	1.49	$0.00^{+0.03}_{-0.00}$	43.85	
68A	3 13 37.9	-55 23 03	1.77	18.28	21.80	B	0.839	111	43.82	-20.93	1.47	$0.00^{+0.08}_{-0.00}$	43.82	
69A	3 14 15.3	-55 19 10	0.50	19.37	24.63	B	2.553	111	44.42	-20.69	1.29	$1.20^{+1.21}_{-0.77}$	44.53	5

Table B.1: continued

(1) No	(2) RA	(3) DEC	(4) $Dist_{OX}$	(5) K	(6) R	(7) Class	(8) z	(9) Flags	(10) $\log(L_{X_{OBS}})$	(11) M_B	(12) α_{OX}	(13) N_H	(14) $\log(L_{X_{INT}})$	(15) Rem.
70A	3 16 21.0	-55 06 49	1.98	19.82	23.37	–	–	010	–	–	–	–	–	
70B	3 16 21.0	-55 06 45	3.35	18.96	22.15	N	0.844	111	–	–	–	–	–	
73A	3 13 21.2	-55 20 47	0.51	18.31	20.10	B	2.706	111	45.10	-25.31	1.81	$0.00^{+0.12}_{-0.00}$	45.10	1
75A	3 16 01.2	-55 05 16	0.50	18.96	22.86	B	2.460	111	44.64	-22.38	1.49	$0.00^{+0.34}_{-0.00}$	44.64	
76A	3 15 49.7	-55 09 08	0.16	19.06	23.21	B	1.065	111	43.69	-20.01	1.39	$0.01^{+0.15}_{-0.01}$	43.69	3
78A	3 15 02.0	-55 26 11	1.13	19.17	23.68	–	–	–	–	–	–	–	–	
80A	3 13 59.4	-54 57 17	3.16	–	–	B	1.620	1--	44.51	–	–	$0.00^{+0.05}_{-0.00}$	44.51	1
81A	3 13 44.2	-55 01 52	4.16	18.86	–	–	–	–	–	–	–	–	–	
83A	3 14 47.9	-55 22 31	2.33	19.46	23.68	B	1.650	111	44.27	-20.63	1.29	$0.00^{+0.07}_{-0.00}$	44.27	
83B	3 14 48.8	-55 22 30	5.51	18.40	20.70	N	0.568	010	–	–	–	–	–	3
84A	3 16 21.6	-55 20 38	1.32	18.63	23.47	B	2.094	111	44.48	-21.43	1.37	$1.32^{+1.27}_{-0.75}$	44.64	
84B	3 16 21.9	-55 20 41	3.72	18.73	23.42	S	0.000	011	–	–	–	–	–	
88A	3 13 16.6	-55 03 10	3.31	–	20.85	B	0.739	111	43.62	-21.62	1.67	$0.00^{+0.03}_{-0.00}$	43.62	
92A	3 12 00.3	-55 02 22	1.85	–	–	B	2.425	1--	45.22	–	–	$0.58^{+0.97}_{-0.58}$	45.29	
100A	3 12 43.8	-55 10 58	2.43	–	–	B	1.165	111	44.23	–	–	$0.01^{+0.17}_{-0.01}$	44.24	1
104A	3 16 47.0	-55 10 33	3.80	–	23.86	–	–	–	–	–	–	–	–	
111A	3 15 05.2	-55 29 48	2.42	–	–	–	–	–	–	–	–	–	–	
116A	3 16 20.7	-55 16 52	1.30	16.99	–	N	0.581	111	43.08	–	–	$3.63^{+1.37}_{-1.42}$	43.72	
120A	3 13 13.5	-55 01 59	0.87	–	15.90	G	0.094	1--	41.46	–	–	$0.00^{+0.03}_{-0.00}$	41.46	
132A	3 16 14.3	-55 17 29	1.53	17.65	21.79	N	1.144	100	43.70	–	–	$0.00^{+0.18}_{-0.00}$	43.70	
133A	3 14 26.2	-55 21 13	1.02	–	23.54	N	2.321	110	44.25	–	–	$0.00^{+0.20}_{-0.00}$	44.25	
135A	3 13 14.7	-55 26 19	5.41	–	21.95	B	2.033	111	44.79	-22.88	1.48	$0.00^{+0.10}_{-0.00}$	44.79	C
140A	3 14 33.0	-55 25 18	0.91	–	21.84	–	–	–	–	–	–	–	–	
145A	3 15 37.1	-55 17 14	1.40	16.39	19.77	N	0.497	111	42.31	–	–	100_{-31}	44.11	
150A	3 14 29.5	-55 06 05	0.32	18.15	23.21	–	–	–	–	–	–	–	–	
151A	3 16 50.5	-55 11 01	4.45	–	–	–	–	–	–	–	–	–	–	C
157A	3 16 28.0	-55 05 38	3.46	16.41	19.76	N	0.625	111	42.79	–	–	–	–	
165A	3 15 32.2	-55 16 54	5.06	10.94	12.90	S	0.000	011	–	–	–	–	–	
166A	3 14 55.3	-55 18 15	6.85	17.91	21.45	S	0.000	011	–	–	–	–	–	
171A	3 13 51.4	-55 02 56	2.18	18.59	22.17	N	0.800	111	43.45	–	–	$6.31^{+2.38}_{-2.47}$	44.14	
172A	3 16 24.3	-55 19 08	3.17	–	–	–	–	–	–	–	–	–	–	
185A	3 16 50.8	-55 22 24	1.60	–	–	B	2.768	1--	44.90	–	–	$6.31^{+7.80}_{-4.03}$	45.21	2
189A	3 13 25.4	-55 01 18	8.94	19.34	20.47	N	0.079	011	–	–	–	–	–	
191A	3 14 38.5	-55 20 06	2.27	15.98	17.95	B	1.045	1--	43.44	-25.24	2.40	$5.75^{+3.83}_{-2.81}$	44.01	1,C

Table B.1: continued

(1) No	(2) RA	(3) DEC	(4) $Dist_{OX}$	(5) K	(6) R	(7) Class	(8) z	(9) Flags	(10) $log(L_{X_{OBS}})$	(11) M_B	(12) α_{OX}	(13) N_H	(14) $log(L_{X_{INT}})$	(15) Rem.
197A	3 14 27.9	-55 19 34	2.27	17.94	–	–	–	–	–	–	–	–	–	
204A	3 14 24.6	-55 02 03	1.31	18.14	21.16	G	0.859	110	43.30	–	–	$0.03^{+2.26}_{-0.03}$	43.32	
205A	3 13 18.9	-55 25 12	1.73	–	–	S	0.000	111	–	–	–	$0.00^{+0.01}_{-0.00}$	–	
205B	3 13 18.8	-55 25 07	4.20	–	–	S	0.000	011	–	–	–	–	–	
209A	3 16 02.2	-55 02 48	0.88	19.31	20.63	B	2.735	111	44.67	-24.79	1.90	$1.58^{+2.50}_{-1.17}$	44.80	2
217A	3 14 19.6	-55 16 43	3.81	19.35	22.07	N	0.816	110	42.96	–	–	$3.63^{+2.42}_{-1.77}$	43.51	C
217B	3 14 19.2	-55 16 37	3.66	18.00	21.32	N	0.645	010	–	–	–	–	–	C
220A	3 15 50.4	-55 01 45	1.75	18.48	21.53	B	1.529	111	44.11	-22.55	1.69	$0.00^{+0.10}_{-0.00}$	44.11	
222A	3 16 43.2	-55 20 06	8.05	–	–	G	0.82	000	–	–	–	–	–	
223A	3 16 47.6	-55 14 11	1.37	–	–	N	1.304	100	44.07	–	–	$0.28^{+0.45}_{-0.25}$	44.16	
224A	3 13 04.9	-55 16 07	1.89	18.36	21.46	G	0.688	001	–	–	–	–	–	C
224B	3 13 04.8	-55 16 04	1.70	17.48	21.51	N	0.690	111	43.48	–	–	$17.4^{+7.9}_{-5.1}$	44.48	C
225A	3 13 31.7	-55 00 46	3.12	15.89	–	G	0.420	011	–	–	–	–	–	
225B	3 13 32.2	-55 00 45	1.32	16.06	17.99	S	0.000	011	–	–	–	–	–	
229A	3 16 06.5	-55 14 44	4.07	–	22.23	N	0.98	001	–	–	–	–	–	
232A	3 14 41.7	-55 08 17	1.74	19.48	–	B	2.520	111	44.58	–	–	$1.20^{+16.4}_{-0.95}$	44.71	
241A	3 13 21.9	-55 13 51	0.95	15.81	17.56	G	0.165	111	41.85	–	–	$0.01^{+0.06}_{-0.01}$	41.87	
242A	3 16 04.2	-55 07 16	0.81	18.34	22.57	B	1.147	111	43.69	-20.81	1.54	$0.40^{+0.47}_{-0.25}$	43.82	
246A	3 13 56.6	-55 01 07	2.96	18.50	21.91	N	0.944	110	43.51	–	–	$0.52^{+1.77}_{-0.35}$	43.70	
246B	3 13 57.1	-55 01 13	4.75	20.25	22.64	N	0.688	0--	–	–	–	–	–	6
253A	3 14 38.0	-55 06 50	2.64	18.21	21.84	N	0.517	110	42.64	–	–	$25.1^{+28.5}_{-15.2}$	43.83	C
253B	3 14 38.1	-55 06 45	3.12	–	23.86	N	0.518	010	–	–	–	–	–	C
255A	3 14 46.2	-55 09 52	4.28	14.66	17.51	S	0.00	011	–	–	–	–	–	
265A	3 13 36.7	-55 00 18	0.94	18.89	22.65	B	1.280	111	43.74	-21.00	1.56	$0.91^{+3.29}_{-0.90}$	43.94	
265B	3 13 37.0	-55 00 20	4.04	19.84	21.81	S	0.000	011	–	–	–	–	–	
267A	3 14 22.6	-55 17 09	2.71	18.53	22.46	B	1.495	111	43.83	-21.56	1.64	$8.32^{+6.68}_{-4.06}$	44.37	
268A	3 16 23.8	-55 15 20	1.17	18.06	21.20	B	1.22	111	43.72	-22.34	1.79	$0.00^{+0.10}_{-0.00}$	43.72	4
268B	3 16 23.9	-55 15 21	1.68	17.82	21.20	N	0.983	010	–	–	–	–	–	
280A	3 13 24.8	-55 11 19	0.66	18.93	22.95	B	1.936	110	44.23	-21.78	1.53	$27.5^{+21.1}_{-12.6}$	44.97	C
281A	3 15 57.7	-55 06 02	1.92	–	–	–	–	–	–	–	–	–	–	
300A	3 15 01.8	-55 14 08	4.93	10.21	12.96	S	0.000	111	–	–	–	$0.00^{+0.01}_{-0.00}$	–	
308A	3 13 17.8	-55 15 52	1.71	–	22.13	–	–	–	–	–	–	–	–	
310A	3 14 57.9	-55 13 23	3.21	18.51	22.41	B	1.01	111	43.07	-20.72	1.78	$0.05^{+0.20}_{-0.05}$	43.09	
311A	3 16 29.8	-55 11 02	3.88	18.61	–	–	–	–	–	–	–	–	–	

Table B.1: continued

(1) No	(2) RA	(3) DEC	(4) $Dist_{OX}$	(5) K	(6) R	(7) Class	(8) z	(9) Flags	(10) $log(L_{X_{OBS}})$	(11) M_B	(12) α_{OX}	(13) N_H	(14) $log(L_{X_{INT}})$	(15) Rem.
334A	3 16 31.6	-55 12 27	0.70	19.32	20.17	B	2.536	1--	44.73	-25.13	1.93	$0.52^{+0.69}_{-0.52}$	44.79	2,3
335A	3 13 57.3	-55 04 32	0.91	15.96	17.97	N	0.257	111	41.93	—	—	$1.91^{+1.77}_{-0.96}$	42.54	
345A	3 13 16.6	-55 22 38	0.84	—	21.61	B	2.166	111	44.88	-23.36	1.54	$0.00^{+0.10}_{-0.00}$	44.88	
360A	3 13 11.7	-55 17 18	2.36	20.02	—	B	2.166	111	44.49	—	—	$0.14^{+0.90}_{-0.14}$	44.51	
361A	3 13 14.6	-55 03 18	2.03	—	20.03	B	1.648	111	44.20	-24.28	1.96	$12.0^{+9.7}_{-6.4}$	44.80	
364A	3 14 12.0	-55 25 56	1.82	—	21.10	B	1.821	1--	44.39	-23.48	1.75	$0.23^{+0.36}_{-0.23}$	44.45	2,3
367A	3 16 34.8	-55 03 49	3.92	—	21.08	B	0.981	1--	43.97	-21.99	1.61	$2.29^{+1.97}_{-1.46}$	44.37	2
371A	3 16 20.5	-55 03 33	3.16	—	21.25	N	0.802	110	43.23	—	—	$33.1^{+20.5}_{-10.6}$	44.37	
373A	3 15 02.3	-55 05 07	2.53	—	23.69	B	0.953	101	43.24	-19.33	1.45	$0.00^{+0.06}_{-0.00}$	43.24	
373B	3 15 02.5	-55 05 02	6.11	—	21.87	N	0.573	010	—	—	—	—	—	
377A	3 16 53.4	-55 08 38	0.81	—	22.91	—	—	—	—	—	—	—	—	
381A	3 16 44.3	-55 27 08	2.93	—	19.34	B	1.879	1--	45.01	-25.32	1.80	$0.00^{+0.07}_{-0.00}$	45.01	1
382A	3 12 47.3	-55 16 51	1.46	19.83	20.63	B	1.904	111	44.57	-24.07	1.78	$0.00^{+0.04}_{-0.00}$	44.57	C
388A	3 14 01.3	-54 59 56	0.72	17.27	19.99	B	0.841	1--	44.74	-22.75	1.39	$0.00^{+0.01}_{-0.00}$	44.74	1
408A	3 15 54.6	-55 10 04	4.12	19.92	23.40	—	—	—	—	—	—	—	—	
410A	3 15 02.4	-55 27 45	4.21	11.01	14.68	S	0.000	111	—	—	—	$0.00^{+0.01}_{-0.00}$	—	
422A	3 15 31.6	-55 10 45	4.79	17.22	21.04	N	0.476	111	42.50	—	—	$3.98^{+2.46}_{-1.61}$	43.21	
437A	3 15 33.7	-55 02 58	2.33	20.22	21.78	S	0.00	111	—	—	—	$0.01^{+0.05}_{-0.01}$	—	
449A	3 15 43.8	-55 07 42	4.28	18.62	—	B	1.204	111	43.47	—	—	$7.59^{+6.10}_{-4.04}$	44.08	3
462A	3 15 06.0	-55 16 24	1.99	18.75	—	—	—	—	—	—	—	—	—	
463A	3 16 25.3	-55 08 39	0.55	19.07	—	N	2.531	111	44.41	—	—	$3.63^{+4.27}_{-2.20}$	44.66	
473A	3 15 32.2	-55 11 22	6.40	—	21.64	S	0.000	011	—	—	—	$0.01^{+0.05}_{-0.01}$	—	
473B	3 15 32.9	-55 11 27	11.67	—	17.22	G	0.154	0--	—	—	—	—	—	7
475A	3 13 52.4	-55 03 46	1.77	20.20	23.97	B	1.729	111	44.07	-20.48	1.36	$0.10^{+0.43}_{-0.10}$	44.10	
480A	3 16 53.2	-55 12 32	2.52	—	22.47	N	0.921	100	43.52	—	—	$4.79^{+3.85}_{-2.34}$	44.12	
485A	3 15 27.1	-55 16 14	4.69	17.75	22.85	N	1.263	100	43.33	—	—	$27.5^{+72.5}_{-15.1}$	44.25	
496A	3 12 45.4	-55 16 48	1.38	—	19.74	B	1.906	111	44.63	-24.96	1.91	$0.00^{+0.14}_{-0.00}$	44.63	C
498A	3 15 06.1	-55 14 00	1.09	11.83	13.65	S	0.00	111	—	—	—	$0.01^{+0.06}_{-0.01}$	—	
511A	3 15 28.0	-55 13 14	0.92	19.88	22.58	B	2.623	111	44.22	-22.79	1.75	$0.00^{+0.30}_{-0.00}$	44.22	
512A	3 13 48.2	-55 13 09	1.12	17.90	—	N	0.465	110	42.83	—	—	$1.91^{+1.53}_{-1.02}$	43.36	C
512B	3 13 48.3	-55 13 05	3.57	15.92	—	N	0.584	0--	—	—	—	—	—	3,C
518A	3 14 57.0	-55 29 25	2.01	—	21.53	—	—	—	—	—	—	—	—	
524A	3 13 14.1	-55 04 16	3.54	—	20.46	S	0.000	011	—	—	—	—	—	
531A	3 13 38.2	-55 03 51	1.12	18.31	—	B	0.926	111	44.15	—	—	$0.00^{+0.01}_{-0.00}$	44.15	

Table B.1: continued

(1) No	(2) RA	(3) DEC	(4) $Dist_{OX}$	(5) K	(6) R	(7) Class	(8) z	(9) Flags	(10) $log(L_{X_{OBS}})$	(11) M_B	(12) α_{OX}	(13) N_H	(14) $log(L_{X_{INT}})$	(15) Rem.
535A	3 16 53.5	-55 11 52	1.51	—	21.81	B	0.974	101	43.43	-21.25	1.71	$0.44^{+0.58}_{-0.31}$	43.60	
536A	3 14 50.7	-55 04 10	3.47	—	22.41	N	0.333	111	41.92	—	—	—	—	
543A	3 12 50.3	-55 11 00	0.56	19.85	—	B	2.511	111	44.44	—	—	—	—	
551A	3 12 43.3	-55 12 01	3.16	—	—	S	0.000	011	—	—	—	—	—	
551B	3 12 43.0	-55 11 58	1.20	—	—	B	0.789	111	43.48	—	—	$0.00^{+0.20}_{-0.00}$	43.48	
557A	3 14 41.4	-55 21 37	1.27	15.42	18.07	G	0.16	111	41.26	—	—	$0.00^{+0.02}_{-0.00}$	41.26	
559A	3 16 17.3	-55 14 29	0.99	17.95	21.95	B	1.180	1--	43.82	-21.51	1.60	$0.00^{+0.02}_{-0.00}$	43.82	3
579A	3 15 47.3	-55 14 19	0.88	18.01	20.84	N	0.497	110	42.43	—	—	$0.23^{+0.18}_{-0.12}$	42.60	
582A	3 16 30.5	-55 11 30	0.89	17.23	21.32	S	0.000	111	—	—	—	$0.04^{+0.06}_{-0.04}$	—	
585A	3 13 09.3	-55 11 40	1.80	19.23	23.82	B	1.383	111	44.29	-20.01	1.16	$0.01^{+0.20}_{-0.00}$	44.30	
593A	3 15 11.2	-55 12 02	1.16	18.61	22.12	B	0.964	111	43.19	-20.92	1.75	$0.00^{+0.13}_{-0.00}$	43.19	
607A	3 16 51.2	-55 13 06	0.22	—	19.83	N	0.407	110	42.87	—	—	$0.00^{+0.01}_{-0.00}$	42.87	C
608A	3 13 49.7	-55 12 59	0.57	17.67	22.46	N	1.019	100	43.58	—	—	$0.14^{+0.24}_{-0.14}$	43.64	4
610A	3 15 51.8	-55 12 22	1.25	17.64	21.12	N	0.699	111	43.10	—	—	$8.32^{+3.14}_{-2.45}$	43.90	
615A	3 14 59.5	-55 03 57	1.75	19.15	22.77	B	1.355	101	43.99	-21.01	1.46	$0.00^{+0.06}_{-0.00}$	43.99	C
615B	3 15 00.2	-55 03 53	5.00	17.08	19.23	N	0.096	011	—	—	—	—	—	3, C
631A	3 15 32.7	-55 12 00	0.89	19.65	—	—	—	—	—	—	—	—	—	
632A	3 16 24.6	-55 21 33	2.07	18.97	23.29	?	—	000	—	—	—	—	—	C
632B	3 16 24.7	-55 21 44	9.08	19.04	22.93	N	0.987	011	—	—	—	—	—	
652A	3 15 30.3	-55 04 37	0.52	18.56	20.75	B	2.710	111	45.14	-24.66	1.68	$0.00^{+0.20}_{-0.00}$	45.14	3
653A	3 16 47.4	-55 12 31	1.38	—	23.38	—	—	—	—	—	—	—	—	4,C
654A	3 17 05.7	-55 27 18	3.54	—	—	B	2.105	1--	45.26	—	—	$0.33^{+0.44}_{-0.33}$	45.32	1
656A	3 13 26.1	-55 04 25	1.36	15.35	18.37	N	0.166	111	42.64	—	—	$0.91^{+0.34}_{-0.32}$	43.13	
664A	3 16 10.0	-55 21 20	9.50	18.31	22.60	—	—	—	—	—	—	—	—	
664B	3 16 11.0	-55 21 22	5.17	—	—	—	—	—	—	—	—	—	—	
673A	3 15 40.3	-55 12 21	0.65	18.76	22.00	B	1.062	111	44.03	-21.21	1.45	$0.40^{+0.29}_{-0.19}$	44.18	3
675A	3 16 24.6	-55 11 44	0.66	19.14	21.82	B	1.140	1--	44.06	-21.55	1.50	$0.00^{+0.06}_{-0.00}$	44.06	3
686A	3 13 46.6	-55 11 49	0.67	17.08	19.11	B	1.663	111	45.44	-25.23	1.58	$0.00^{+0.03}_{-0.00}$	45.44	1,3,5
687A	3 13 02.6	-55 26 08	4.54	—	18.83	S	0.000	011	—	—	—	—	—	

Description of Table B.1

(1) No
Classification of a counterpart object consists of the sequence number of the X-ray source list and a suffix (A, B) to discriminate between different candidates.

(2) RA [hh:min:ss] and (3) DEC [deg:min:ss]
Right ascension and declination of the optical candidate counterpart (J2000).

(4) $Dist_{OX}$ [arcsec]
Spatial offset between the X-ray and optical positions.

(5) K
SOFI K-band magnitude of the spectroscopically classified candidate, whenever available.

(6) R
WFI R-band magnitude of the spectroscopically classified candidate, whenever possible.

(7) Class
Spectroscopic classification of the identified object. S – star, G – normal galaxy (no emission lines), N – narrow emission line galaxy with unresolved emission lines (at 6000 Å our spectral resolution of 21 Å corresponds to 1050 km/s), B – broad emission line object (all measured line widths have $v_{\mathrm{FWHM}} > 2500$ km/s), and ? – undefined object.

(8) z
Spectroscopic redshift of the identified object. The redshift is taken from the literature for objects with '1--' and '0--' in Col. *(9) Flags*. Column *(15) Rem.* states the source of redshift determination and classification.

(9) Flags
X-ray identification flag, redshift flag, and classification reliability flag. The first number (0, 1) marks whether a spectroscopically classified object was accepted as X-ray counterpart. Objects which we consider to be the correct identification of the X-ray source are flagged by '1', while '0' flags objects not considered as the X-ray source.

The second (middle) flag states the redshift reliability. A redshift flag '1' means a reliable, well-established redshift determined by several spectral features. '0' marks objects where the redshift determination relies on a single but reasonable spectral feature.

The third (last) flag characterises the classification reliability. A flag '1' marks that the object type as given in '*(7) Class*' is well established and reliable. Flag '0' indicates an uncertain classification of the object type. Either high SNR spectral features of the object do not allow a proper classification or the optical spectra do not allow to give a reliable classification of the object type because of a low SNR and/or insufficient wavelength coverage of the optical spectra. The latter is illustrated, for example, in the optical spectrum of the X-ray counterpart 480A (see Appendix E). The narrow [O II] line indicates a narrow emission line galaxy. However, the SNR of the spectrum does not allow us to judge the existence of a broad Mg II line and, hence, a classification as type I AGN. Since
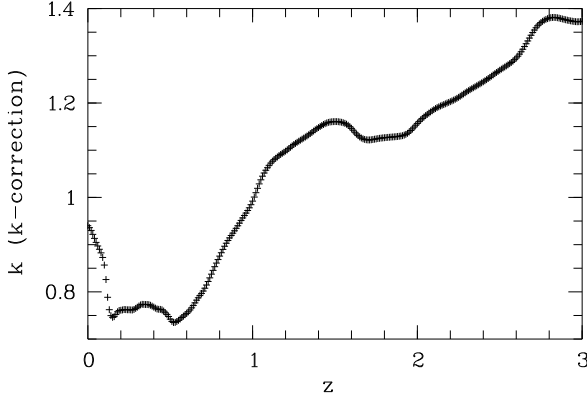
Figure B.1: Adopted mean k-correction from observed R-band to rest-frame M_B for broad emission line AGN.
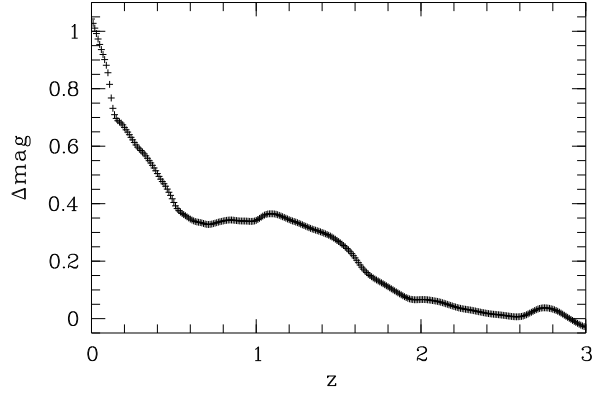
Figure B.2: Adopted conversion term to estimate AB magnitudes at fixed rest-frame wavelength $\lambda = 2500\,\text{Å}$ from observed R-band magnitudes.

C IV and C III] are outside the spectrum's wavelength range, Mg II is the only possible broad-line feature. The most likely classification of this object is a narrow emission line galaxy. However, the given arguments show that a classification as type I AGN cannot be excluded. Therefore, the classification flag for this object is '0'. Objects with '1--' and '0--' have only an X-ray identification flag since their redshift and classification relies on follow-up surveys previously done in the Marano field (see Col. *(15) Rem.*).

(10) $\log(L_{X_{OBS}}\ [erg\ s^{-1}])$
Observed rest-frame X-ray luminosity L_X (logarithmic units) in the 0.2-10 keV energy band calculated by using Eq. B.1. The k-correction vanishes since we assume an energy index $\alpha = -1$ with $F_\nu \sim \nu^\alpha \sim \nu^{1-\Gamma}$ (Γ - photon index) based on Alexander et al. (2003) and Mainieri et al. (2002). The luminosity distance d_L was computed by the analytical fit for flat cosmologies with $\Omega_m = 0.3$, $\Omega_\Lambda = 0.7$, $H_0 = 70\,\text{km}\,\text{s}^{-1}\,\text{Mpc}^{-1}$ following Szokoly et al. (2004).

$$L_X = \frac{4\,\pi\,d_L^2}{(z+1)^{\alpha+1}} f_X \tag{B.1}$$

(11) M_B
Absolute magnitudes M_B (in the Johnson system) were estimated only for type I AGN using the relation

$$M_B = R + 5 - 5\log(d_L/\text{pc}) + K(z)\quad, \tag{B.2}$$

where d_L is the luminosity distance and $K(z)$ is the customary k-correction term. In our case, this term includes the transition from observed-frame R-band to rest-frame B-band,

assuming a mean spectral energy distribution for all sources, and also the $(1 + z)$ bandwidth stretching factor. For the type I AGN we computed $K(z)$ from the composite SDSS quasar spectrum (Vanden Berk et al. 2001). The resulting graph is shown in Fig. B.1. This calculation was kindly provided by Lutz Wisotzki.

(12) α_{OX}

The broad band spectral index $\alpha_{\rm OX}$ roughly characterises the UV–X-ray spectral energy distribution by connecting the rest-frame points at $2500\,\text{Å}$ and $1\,\text{keV}$ with a simple power-law, $F_\nu \propto \nu^{-\alpha_{\rm OX}}$. For each broad emission line AGN we estimated its flux at a fixed rest-frame wavelength of $\lambda = 2500\,\text{Å}$, applying the relation

$$m_{\rm AB}(2500\,\text{Å}) = R + \Delta m(z) \quad , \tag{B.3}$$

where R is the quoted R-band magnitude, $m_{\rm AB}(2500\,\text{Å})$ is the predicted magnitude at $2500\,\text{Å}$ – expressed in the AB system for easy conversion into monochromatic fluxes –, and $\Delta m(z)$ is a redshift-dependent term (similar, but not identical to the k-correction) that also accounts for the zero-point transformation from the Vega to the AB system. Our adopted $\Delta m(z)$ relation, again computed from the SDSS composite quasar spectrum of Vanden Berk et al. (2001), is shown in Fig. B.2. This correction was kindly provided by Lutz Wisotzki as well. Notice that at the typical redshifts of $z \sim 1.5$ of our broad line AGN, the observed R-band approximately traces a rest-frame wavelength of $\lambda_{\rm rest} \sim 2600\,\text{Å}$, implying that the spectral energy distribution corrections are small. The resulting AB magnitudes are then converted into fluxes following the definition of the AB system (Oke & Gunn 1983):

$$m_{\rm AB}(2500\,\text{Å}) = -2.5\log(F_\nu(2500\,\text{Å})) - 48.60 \quad , \tag{B.4}$$

where $F_\nu(2500\,\text{Å})$ is given in $\text{erg}\,\text{s}^{-1}\,\text{cm}^{-2}\,\text{Hz}^{-1}$. The X-ray flux at $1\,\text{keV}$ is computed by:

$$f(0.2 - 10\,\text{keV}) = F_\nu(1\,\text{keV}) \int_{0.2\,\text{keV}}^{10\,\text{keV}} E^\alpha \mathrm{d}E \quad \text{with } \alpha = -1 \quad . \tag{B.5}$$

Hence, the broad band spectral index is obtained as

$$\alpha_{ox} = \frac{\log(F_\nu(2500\,\text{Å})) - \log(F_\nu(1\,\text{keV}))}{\log(\nu(1\,\text{keV})) - \log(\nu(2500\,\text{Å}))}. \tag{B.6}$$

(13) N_H [cm^{-2}]

X-ray absorbing hydrogen column density in units of 10^{22} cm^{-2} (see Sect. 3.3.4).

(14) $\log(L_{X_{INT}}$ [erg s^{-1}])

De-absorbed intrinsic rest-frame X-ray luminosity (logarithmic units) in the 0.2-10 keV energy band after X-ray flux correction for the absorbing hydrogen column density. Calculation uses Eq. B.1.

(15) Rem.

Remarks for individual objects: 1 – optically selected and spectroscopically classified quasar by Marano et al. (1988), 2 – optically selected and spectroscopically classified quasar by Zitelli et al. (1992), 3 – *ROSAT* X-ray source with spectroscopic classification and redshift determination by Zamorani et al. (1999), 4 – *ROSAT* X-ray source with no or wrong identification by Zamorani et al. (1999), 5 – unclassified radio objects within 5.0 arcsec, Gruppioni et al. (1997), 6 – spectroscopic classification and redshift taken from Teplitz et al. (2003), 7 – radio source, spectroscopic classification and redshift taken from Gruppioni et al. (1997), and C – individual comment to an object (see Sect. C).

Appendix C

Comments to individual objects in the Marano field

9A: New redshift determined for this source, formerly known as Zamorani et al. (1999) X043-12.

15A: Object 15A is not regarded as the optical counterpart, since the identification of the line features is uncertain and the positional offset is rather large. A very faint object at the detection limit lies in the X-ray error circle. A lower limit of $f_{\mathrm{X}}/f_{\mathrm{opt}} \sim 65$ for this source was estimated by assuming a limiting magnitude of $R = 24$.

17A: Source 17 is a likely X-ray blend with large contrast between the two individual sources. Object 17A is a unique identification of the brighter X-ray source, whose X-ray flux is likely to be overestimated due to blending.

20A & 20B: Zamorani et al. (1999) identified source 20 with the M star 20B. Some contribution of the M star's X-ray flux cannot be excluded, but the identification with the type II AGN (object 20A) seems more likely, since the X-ray colours indicate a relatively hard spectrum.

22A & 22B: X-ray source 22 is a probable blend. Objects 22A and 22B fall on top of the two suspected point sources. We regard both optical objects as likely counterparts of the X-ray blend and distribute the measured X-ray flux evenly between the two sources.

26A: New redshift determined for this source, formerly known as Zamorani et al. (1999) X301-29.

32A: N v strongest emission line in the spectrum (brighter than Lyα). Narrow emission lines are present and the object is classified as 'N' (narrow emission line galaxy). However, all narrow emission lines have underlying broad components. Therefore, the classification flag is set to '0'.

35A & 35B: Two galaxies at equal redshift, the brighter galaxy 35A is regarded as the X-ray counterpart. The possibility that the X-ray source is a galaxy cluster cannot be completely excluded, but an X-ray extent is not obvious. For 35A a new redshift is determined (update to Zamorani et al. (1999) X022-48).

42A: New redshift determined for this source, formerly known as Zamorani et al. (1999) X031-24.

46A: X-ray blend with major contribution from the south-western component with type I AGN 46A as counterpart.

47A & 47B: Two narrow emission line galaxies at equal redshift. The possibility that the X-ray source is a galaxy cluster cannot be completely excluded, but an X-ray extent is not obvious. 47A is assumed to be the optical counterpart.

63A: Unresolved narrow emission lines are present and the object is classified as 'N' (narrow emission line galaxy). However, the C IV emission line has an underlying broad component. Therefore, the classification flag is set to '0'.

66A: The identification is not unique, since the optical image reveals a possible second object inside the 1σ-X-ray position error circle.

133A: Narrow emission lines are present. The object is classified as 'N' (narrow emission line galaxy). However, Lyα shows a resolved, broad base. Therefore, the classification flag is set to '0'.

151A: Probably a spurious detection of the X-ray source. The source is kept in the source list for the formal reason of having an $ML = 5.2$, but is not considered further.

191A: Optical spectrum in Zitelli et al. (1992) indicates a type I AGN with typical broad emission lines. However, this object shows the lowest X-ray-to-optical flux ratio of all AGN in our sample. $f_X/f_{opt} = 0.04$ suggests an X-ray faint AGN. Since this object was not detected by ROSAT, it is unlikely that the extreme f_X/f_{opt}-ratio is due to a temporary low X-ray state of the object. Furthermore, it is one of the type I objects with intrinsic absorption ($N_H = (5.75^{+3.83}_{-2.81}) \times 10^{22}$ cm^{-2}).

217A & 217B: X-ray blend, the identification of 217A with the south-eastern component seems unambiguous, the identification of 217B with the north-western component is not unique, since a similarly bright, close-by, but still unidentified object is present at the same distance from the X-ray source.

224A & 224B: Two galaxies at equal redshift, no obvious X-ray extent.

253A & 253B: Two objects at similar redshift with 2 mag difference in the optical. The brighter object 253A is regarded as the identification.

280A: Object is classified as 'B' since C III] is well resolved with $\Delta\lambda \sim 72$ Å (FWHM). Lyα and C IV are narrow emision lines, but show strong absorption with broad underlying components. The classification flag is set to '0'. Possible broad absorption line quasar.

361A: Broad absorption line quasar.

382A & 496A: Physical quasar pair, separated by 17 arcsec, at $z = 1.904$, $d_A = 143$ kpc. The spectra are different, i.e., the two objects are not lensed images of the same source.

437A: Spectrum, optical, and X-ray image, and relative soft hardness ratios point undoubtedly to an M star as X-ray source. However, a flux ratio $f_X/f_{opt} = 1.7$ is unusually high for an M star as the X-ray identification.

512A & 512B: Zamorani et al. (1999) identify the NELG 512B with the X-ray source. The 2 mag fainter NELG 512A lies somewhat closer to the X-ray position. While both galaxies may contribute to the observed X-ray flux, we assume object 512A as the counterpart in the following.

582A: Spectrum, optical, and X-ray image, and relative soft hardness ratios point undoubtedly to an M star as X-ray source. However, a flux ratio $f_X/f_{opt} = 1.5$ is unusually high for an M star as the X-ray identification.

607A & 653A: Detected as a single X-ray source by *ROSAT* Zamorani et al. (1999) X404-23, X-ray source 653 is brighter and closer to X404-23 and, therefore, treated as the detected *ROSAT* X-ray source. The broad spectral feature at 7100 Å in the optical spectrum of 607A is spurious due to the zeroth order light of the neighbouring slit.

615A & 615B: Both objects, the broad emission line object 615A and the narrow emission line object 615B, are possible counterparts to the X-ray source. We regard the fainter, but positionally better matching object 615A as the counterpart.

632A: Spectrum suggests a BL-Lac object, but the object is not a radio source, classification unclear.

Appendix D

Marginal X-ray source classification in the Marano field

In this section we include spectroscopic classifications that are possible counterparts to X-ray sources with a detection likelihood $ML < 5.0$. We give the X-ray source list, and the optical/X-ray properties of these sources. The objects given here are included in the optical and X-ray image section (Appendix E).

Table D.1: X-ray source list for marginal X-ray sources in the Marano field. The explanation of the individual columns is given in Appendix A.

(1) ID	(2) Name XMMU J...	(3) CR $[ks^{-1}]$	(4) ML	(5) σ_X [arcsec]	(6) $HR1$	(7) $HR2$	(8) $HR3$	(9) Flux $[10^{-14}\mathrm{ergs}^{-1}\mathrm{cm}^{-2}]$
137	031612.8-550846	1.8±0.6	2.7	2.09	-0.003±0.890	0.289± 0.683	-0.022± 0.636	0.285
160	031644.2-552242	1.4±0.8	3.1	2.29	–	–	–	0.228
289	031648.0-551013	2.4±0.8	4.1	2.10	1.000±0.490	-1.000± 0.187	–	0.390
315	031346.2-550450	1.6±0.6	2.6	2.31	–	0.589± 0.565	-1.000± 0.929	0.252
331	031636.5-550929	1.9±0.7	3.6	2.08	1.000±0.823	0.153± 0.745	-0.278± 0.757	0.313
341	031337.8-552144	4.8±1.9	3.2	15.08	-1.000±0.365	–	–	0.767
366	031538.8-552001	1.5±0.5	2.6	2.26	0.263±0.894	0.146± 0.695	-0.198± 0.734	0.248
386	031339.5-550724	2.4±0.7	2.5	2.51	–	–	-1.000± 0.373	0.382
405	031523.3-551756	0.9±0.3	1.1	2.59	1.000±0.774	0.271± 0.649	-0.887± 0.667	0.139
414	031506.5-553314	6.1±2.3	2.6	2.49	–	-1.000± 0.934	–	0.991
430	031339.0-550706	1.9±0.6	4.8	1.97	0.738±0.432	-0.946± 0.348	–	0.305
432	031555.1-550801	1.7±0.5	3.2	2.08	1.000±0.305	-0.043± 0.374	-1.000± 0.650	0.272
442	031341.0-550038	3.2±1.0	2.4	2.51	0.557±0.472	-0.278± 0.435	-1.000± 0.482	0.518
454	031623.7-551031	2.7±0.8	3.3	2.72	0.364±0.338	-0.689± 0.373	0.229± 0.859	0.429
522	031613.7-550430	1.4±0.7	1.3	2.84	-0.176±0.775	–	–	0.223
529	031622.3-551217	2.1±0.6	2.4	2.58	-0.479±0.401	0.141± 0.586	-0.340± 0.703	0.334
553	031518.0-551722	1.4±0.4	1.4	2.44	0.953±0.276	-0.020± 0.336	-0.319± 0.411	0.224
564	031554.9-551459	1.4±0.4	2.3	2.37	1.000±0.391	-0.193± 0.363	-1.000± 0.580	0.230
581	031638.3-551901	1.7±0.7	4.2	2.44	–	–	1.000± 0.534	0.266
600	031503.3-551656	1.2±0.4	3.1	2.49	-0.347±0.390	-1.000± 0.511	–	0.191
612	031606.8-550423	2.2±0.6	4.2	2.33	-0.340±0.777	0.352± 0.781	-0.676± 0.809	0.347
623	031642.3-551707	2.7±0.8	4.1	2.56	1.000±0.277	-0.407± 0.505	–	0.433
677	031641.2-551934	1.5±0.7	3.6	3.35	–	1.000± 0.710	–	0.234

137A: Broad absorption line quasar.

315A & 315B: As counterpart candidates for X-ray source 315, an M star (315A) and a NELG (315B) are found. The hardness ratios of 315 indicated an obscured X-ray object. Therefore, we regarded 315B as the identification.

Table D.2: Optical properties of candidate counterparts of marginal Marano field XMM-Newton X-ray sources. For a detailed explanation of the individual columns see Appendix B.

(1) No	(2) RA	(3) DEC	(4) $Dist_{OX}$	(5) K	(6) R	(7) Class	(8) z	(9) Flags	(10) $log(L_{X_{OBS}})$	(11) M_B	(12) α_{OX}	(13) N_H	(14) $log(L_{X_{INT}})$	(15) Rem.
137A	3 16 12.9	-55 08 47	1.21	17.55	19.54	B	1.721	111	43.75	-24.90	2.26	$17.4^{+16.7}_{-10.2}$	44.42	1
160A	3 16 43.5	-55 22 40	6.41	–	22.34	–	–	–	–	–	–	–	–	
160B	3 16 44.3	-55 22 43	1.43	–	21.96	N	1.020	100	43.10	–	–	–	–	
289A	3 16 47.7	-55 10 10	4.24	–	23.01	–	–	–	–	–	–	–	–	
315A	3 13 45.5	-55 04 48	6.50	15.92	20.09	S	0.000	011	–	–	–	–	–	C
315B	3 13 46.0	-55 04 46	4.32	–	23.06	N	0.836	110	42.93	–	–	–	–	C
331A	3 16 36.2	-55 09 32	2.72	19.73	22.13	B	1.876	111	43.89	-22.53	1.80	$0.52^{+0.69}_{-0.52}$	44.79	2,5
341A	3 13 38.2	-55 21 38	8.00	19.48	20.64	B	2.784	1--	44.69	-24.81	1.90	–	–	2
366A	3 15 38.8	-55 20 03	2.75	15.50	18.87	S	0.00	011	–	–	–	–	–	
386A	3 13 39.9	-55 07 21	5.11	17.70	20.22	G	0.189	1--	41.59	–	–	$0.00^{+0.17}_{-0.00}$	41.59	3
405A	3 15 23.8	-55 17 59	5.65	10.96	13.14	S	0.000	1--	–	–	–	–	–	
414A	3 15 06.4	-55 33 12	2.36	–	–	B	2.058	1--	44.49	–	–	–	–	2
430A	3 13 38.1	-55 07 06	6.86	17.03	20.04	N	0.390	1--	42.21	–	–	$0.14^{+0.27}_{-0.14}$	42.34	3
430B	3 13 39.0	-55 07 14	7.64	18.52	20.66	N	0.391	0--	–	–	–	–	–	3
432A	3 15 54.9	-55 08 05	4.20	19.19	–	–	–	–	–	–	–	–	–	
442A	3 13 41.4	-55 00 33	5.91	19.23	22.16	N	0.460	010	–	–	–	–	–	
442B	3 13 41.5	-55 00 37	4.60	18.31	22.01	–	–	–	–	–	–	–	–	
454A	3 16 23.8	-55 10 31	1.82	–	–	–	–	–	–	–	–	–	–	
522A	3 16 13.1	-55 04 31	4.89	18.92	20.77	B	3.747	111	44.47	-25.83	1.94	–	–	
529A	3 16 22.4	-55 12 18	1.83	19.03	–	–	–	–	–	–	–	–	–	
553A	3 15 18.8	-55 17 23	7.40	18.78	19.90	N	0.231	010	–	–	–	–	–	
564A	3 15 55.4	-55 15 04	7.40	–	23.37	N	0.633	011	–	–	–	–	–	
600A	3 15 03.9	-55 16 54	5.68	18.38	21.15	N	0.452	110	42.16	–	–	–	–	
612A	3 16 06.9	-55 04 26	3.45	–	23.74	N	0.409	110	42.32	–	–	–	–	
623A	3 16 42.5	-55 17 07	2.56	–	20.18	G	0.073	110	40.76	–	–	$0.01^{+0.11}_{-0.01}$	40.79	
677A	3 16 40.4	-55 19 29	7.85	–	21.93	N	0.131	010	–	–	–	–	–	
677B	3 16 41.5	-55 19 37	4.76	–	–	N	1.354	101	43.41	–	–	–	–	

Appendix E

Optical & X-ray images and optical spectra of X-ray classifications in the Marano field

Optical images

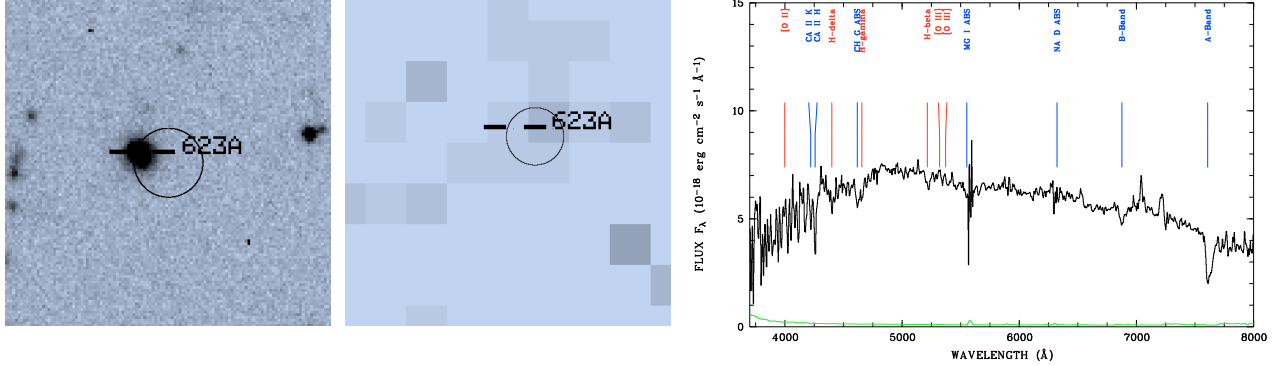The optical images show a 30"×30" section that is centred on the X-ray position (except for images next to the edge of the CCD). The cut levels are set differently for each image. The black circle shows an 1σ-X-ray position error including a 2" systematic error. Black horizontal markers represent the position of the spectroscopically classified object. The nominal orientation of the images is North facing upwards and East to the left (exceptions are marked).

Images were generated using VLT FORS pre-images, WFI-R-band images, or DSSII-images, in this order of availability. The astro-metric correction of VLT FORS pre-images was performed as a 2-stage process, since USNO-stars or stars from similarly well-calibrated catalogues were found to be too sparse or were saturated. I therefore first generated a stellar catalogue of WFI objects (calibrated with the USNO) using this as input catalogue for astro-metric calibration of the VLT images. I typically used stars of the order of 10 that were equally distributed over the field of view and reached an rms accuracy of $\sim$0.2" (0.7 pixels).

X-ray images

The X-ray images show a $\sim$32"×32" section which is nearly centred on the X-ray position. The cut levels are set differently for every image. The black circle shows an 1σ-X-ray position error (2" systematic error). Black horizontal markers represent the position of the spectroscopically classified object. The nominal orientation of the X-ray images is North facing upwards and East to the left.

Labelling of spectra

All spectra are in flux units of $10^{-18}\,\mathrm{erg\,cm^{-2}\,s^{-1}\,\AA^{-1}}$. The black solid line represents the spectrum, the green solid line the error spectrum. Red markers indicate emission lines, blue markers absorption lines. There are exceptions in a few spectra. If no optical spectrum is shown, the redshift and classification is taken from the literature.

Comment

Below every row of optical & X-ray images and optical spectrum a comment for the shown objects is given. This comment states the classification number of the possible counterpart object and the corresponding redshift. If the redshift is only determined by one identification feature in the optical spectra, an additional comment ':@<identification feature>' is shown. The colon marks the uncertainty of the redshift (these objects have a redshift flag of '0' in Table B.1 and Table D.2).
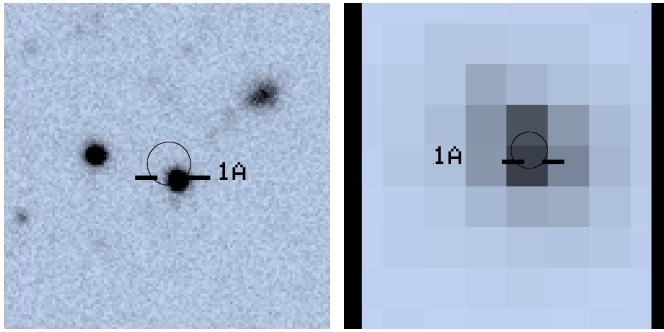
object 1A, z = 0.808
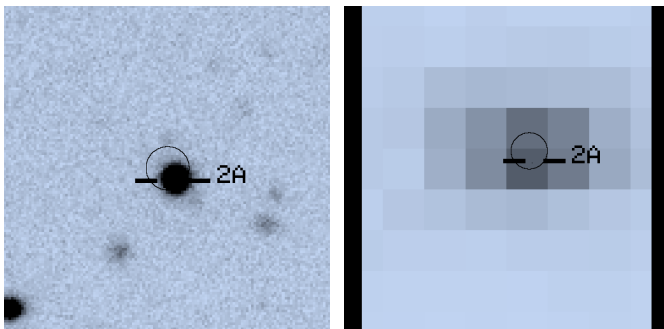
object 2A, z = 0.464
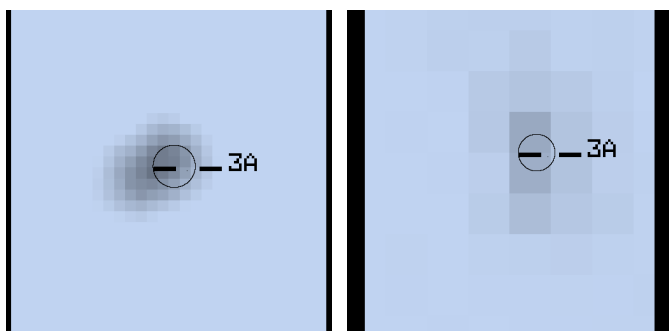
object 3A, z = 0.406
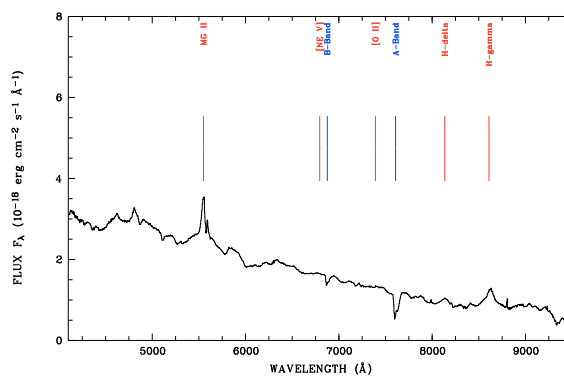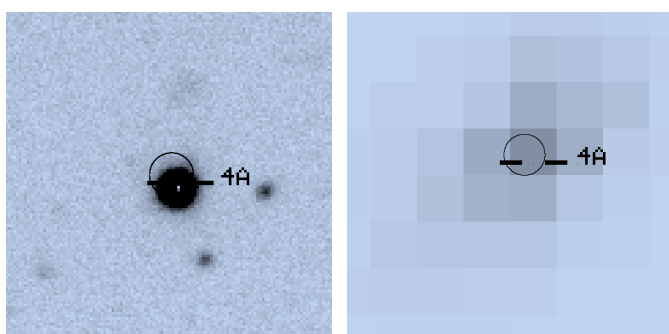
object 4A, z = 0.987
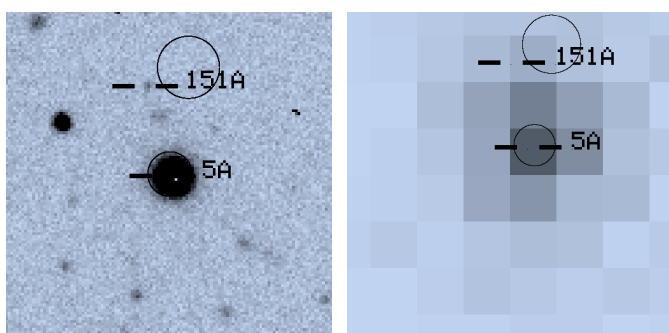
object 5A, z = 2.531
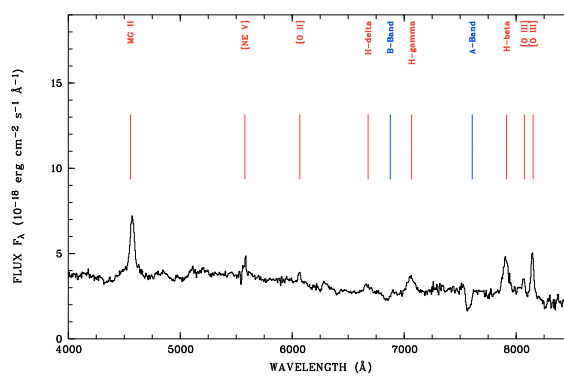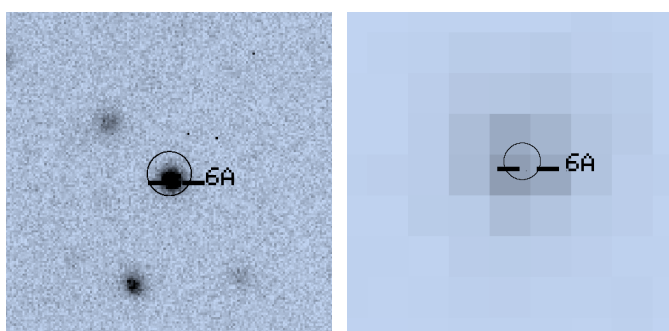
object 6A, z = 0.636
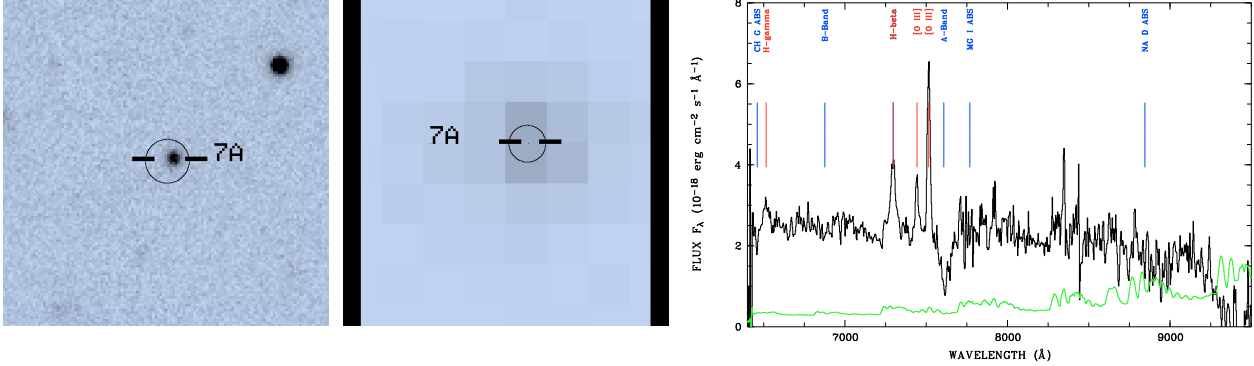
object 7A, z = 0.501
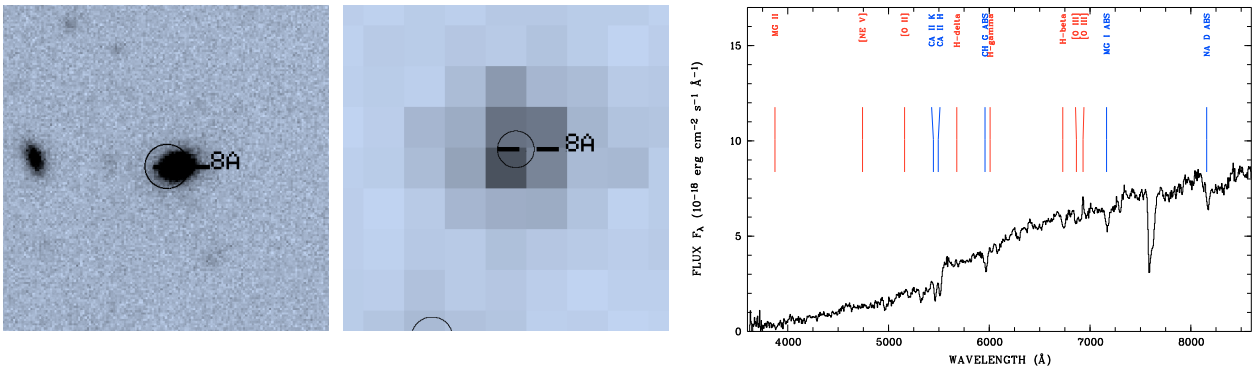
object 8A, z = 0.387
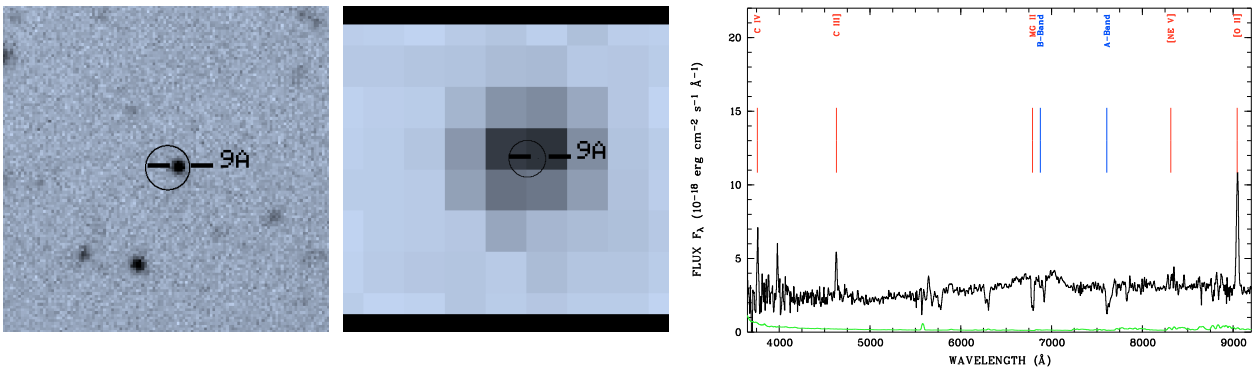
object 9A, z = 1.427
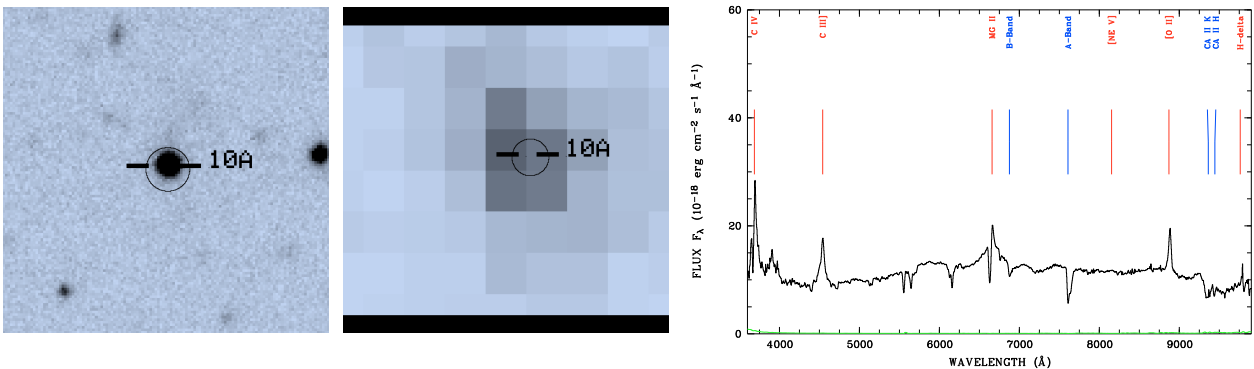
object 10A, z = 1.378
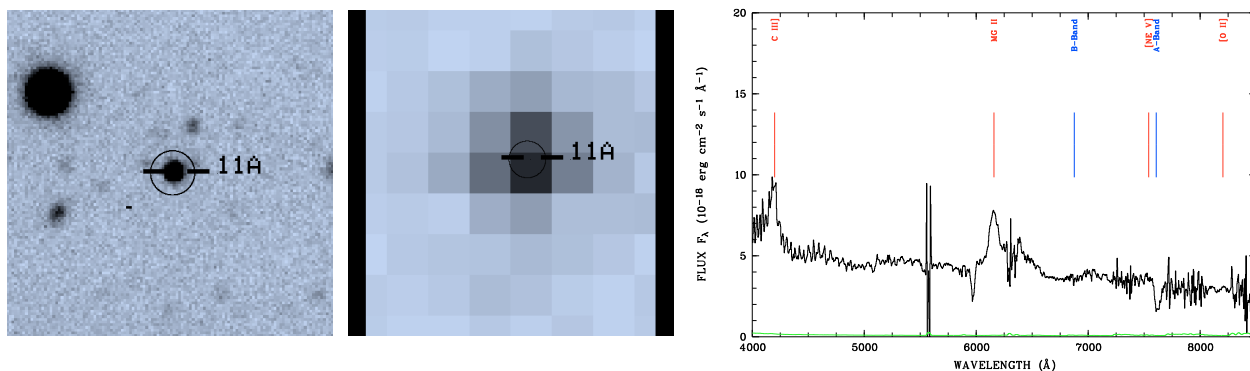
object 11A, z = 1.192
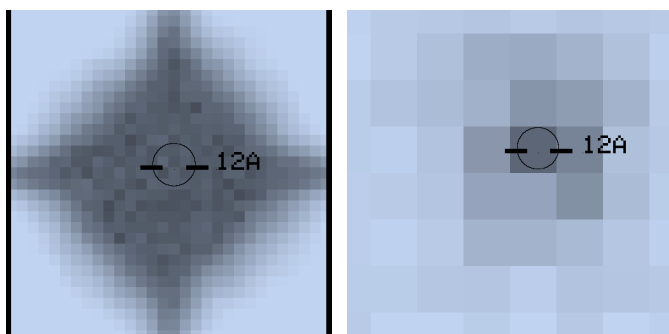
object 12A, z = 0.000
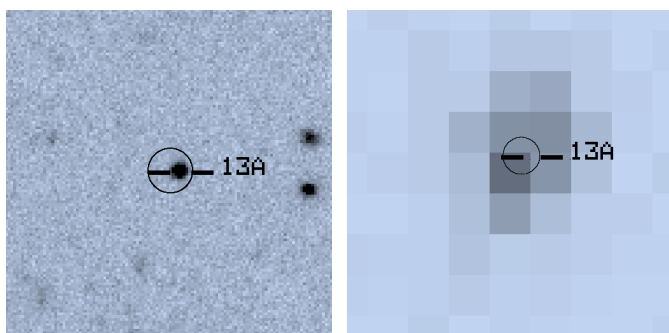
object 13A, z = 0.500
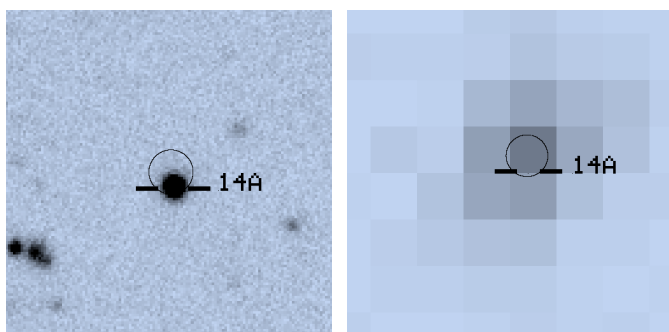
object 14A, z = 0.854
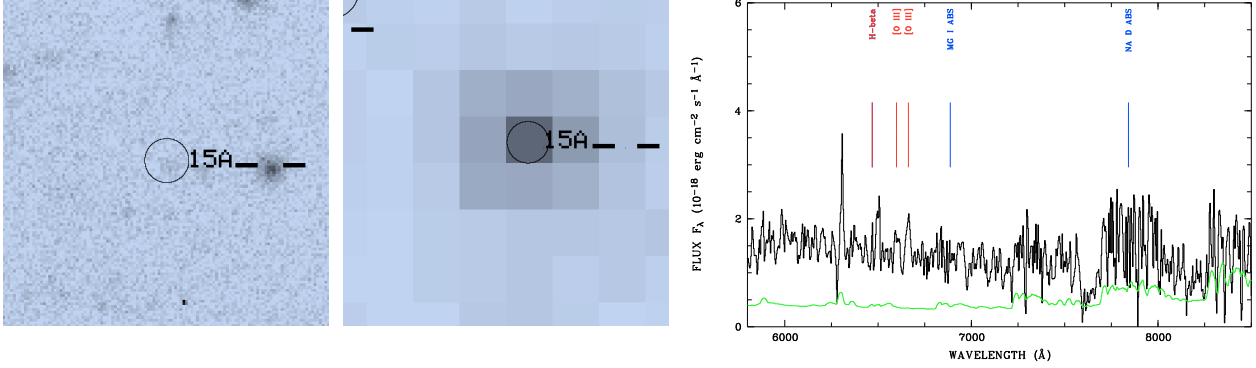
object 15A, z = 0.331:@OIII
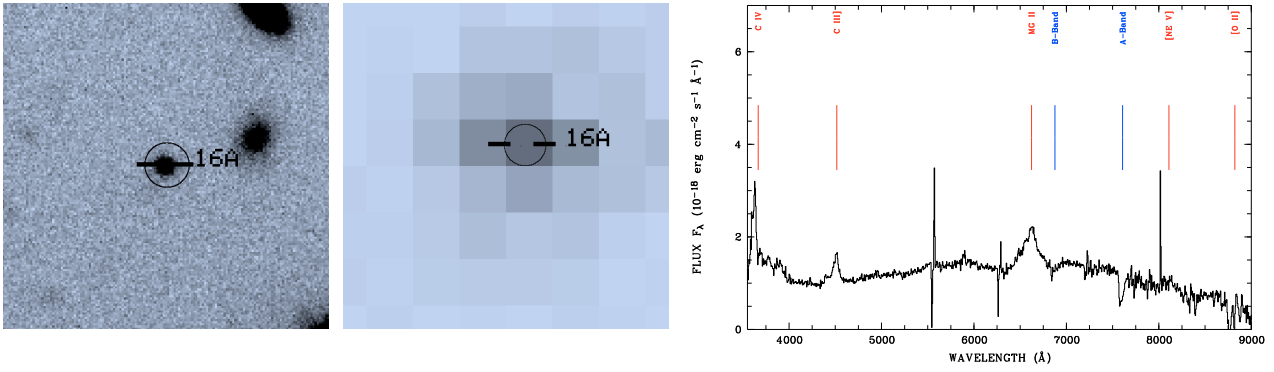
object 16A, z = 1.374
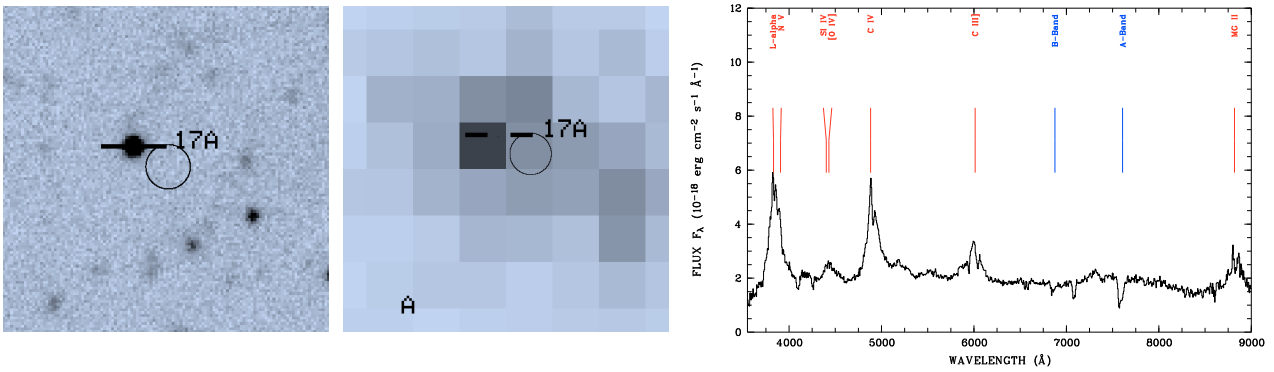
object 17A, z = 2.161
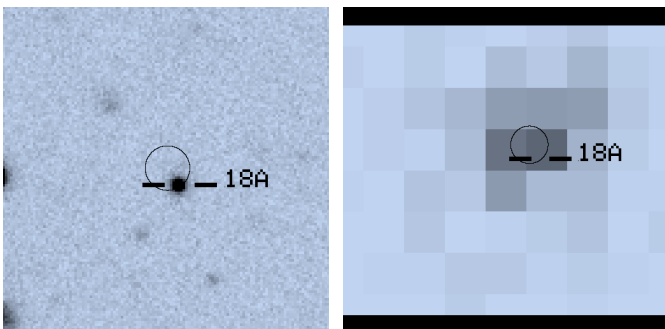
object 18A, z = 0.614
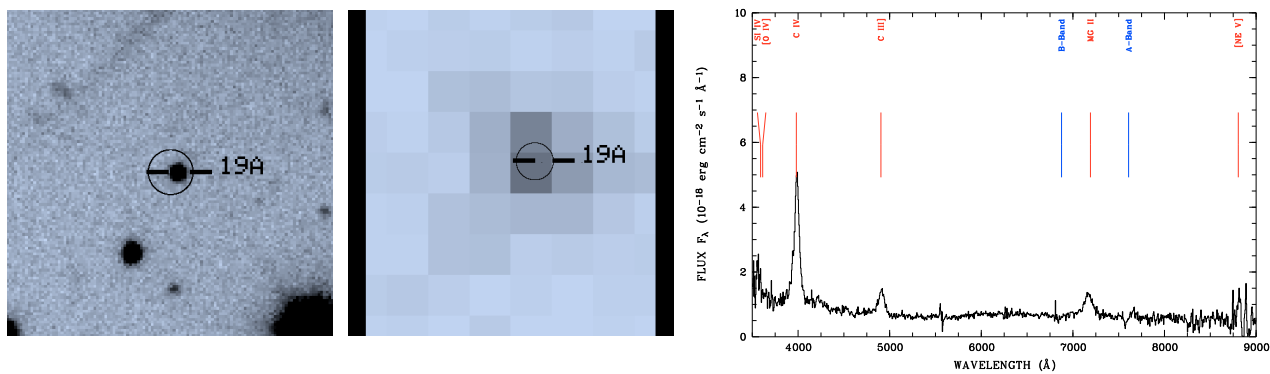
object 19A, z = 1.573
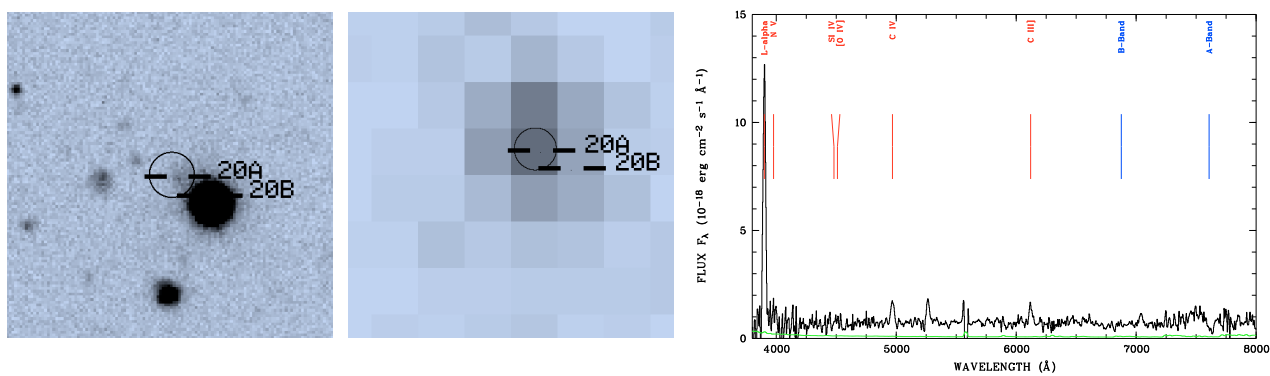
object 20A, z = 2.207
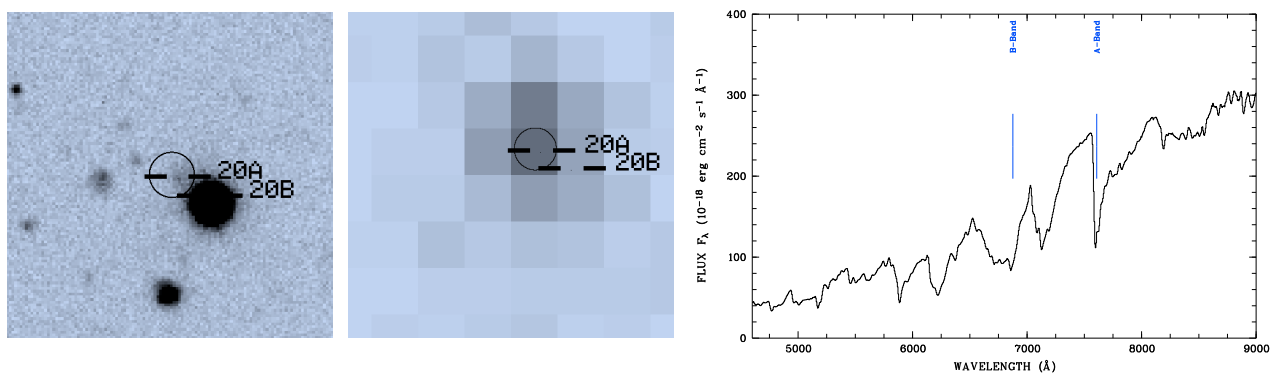
object 20B, z = 0.000
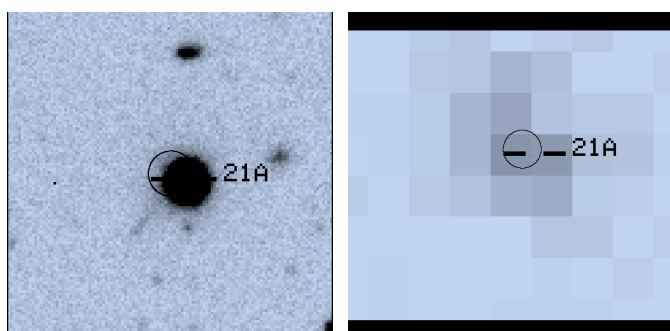
object 21A, z = 0.000
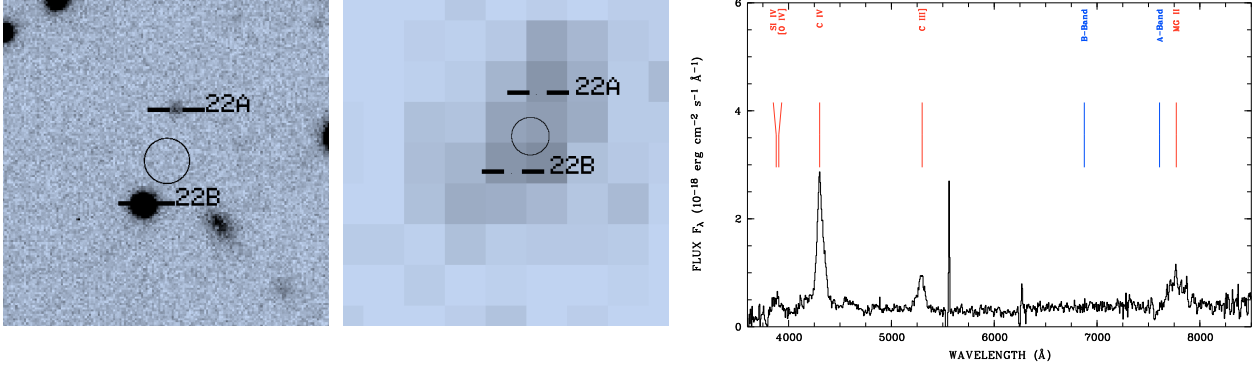
object 22A, z = 1.78
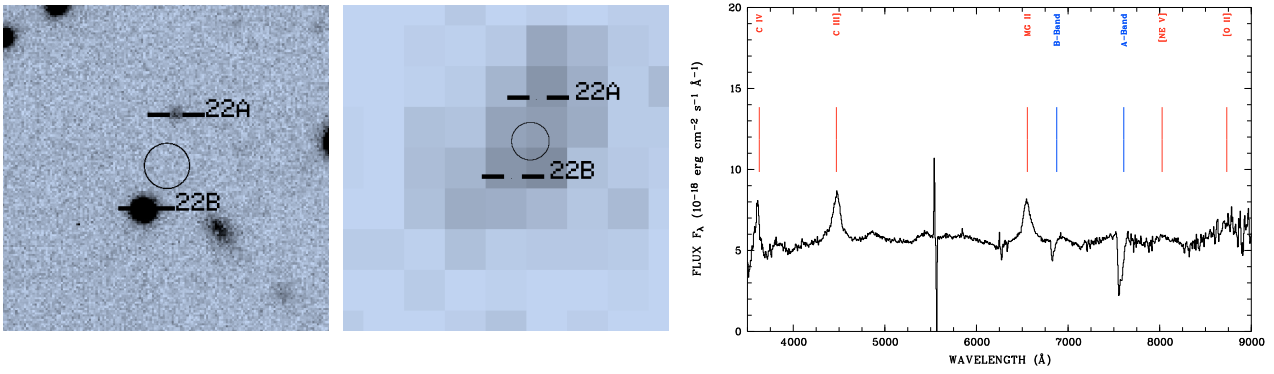
object 22B, z = 1.353
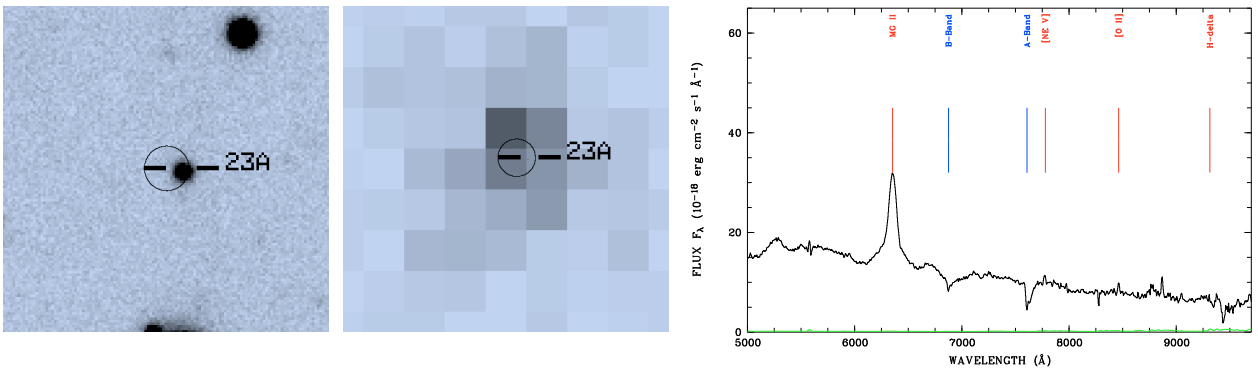
object 23A, z = 1.271
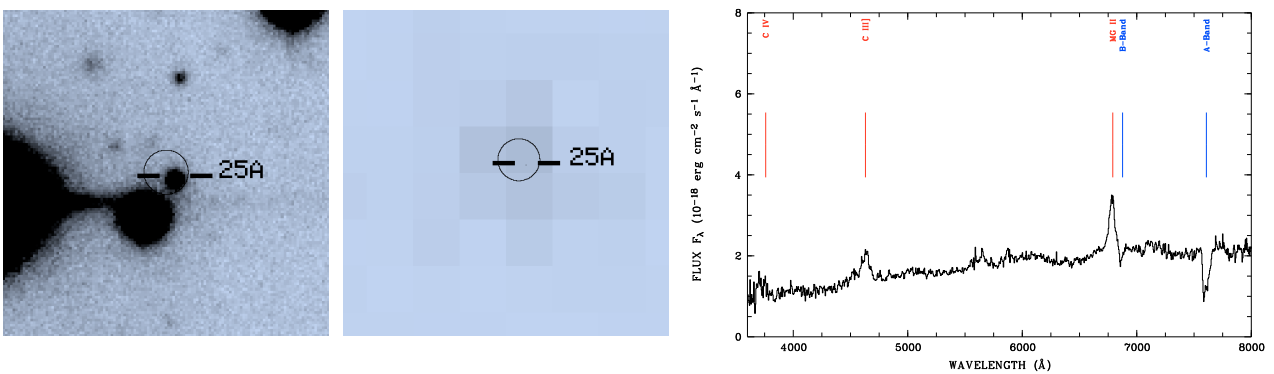
object 25A, z = 1.430
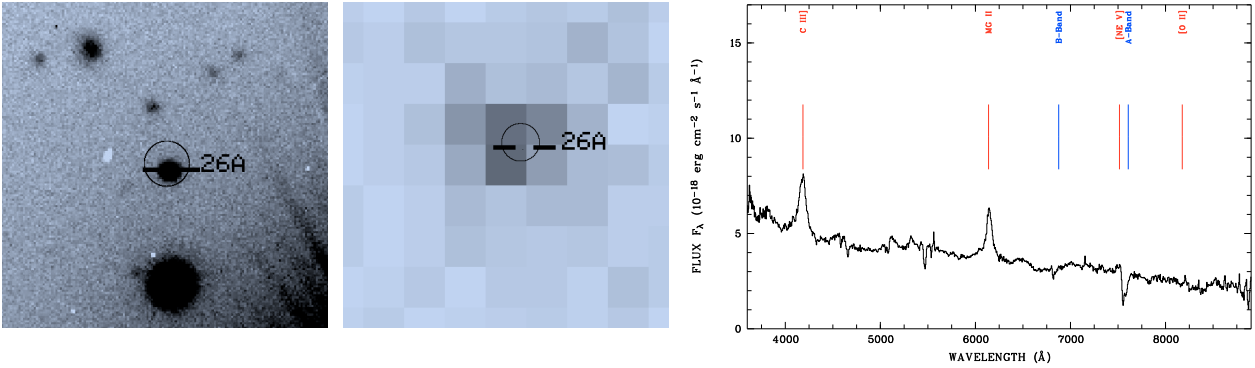
object 26A, z = 1.19
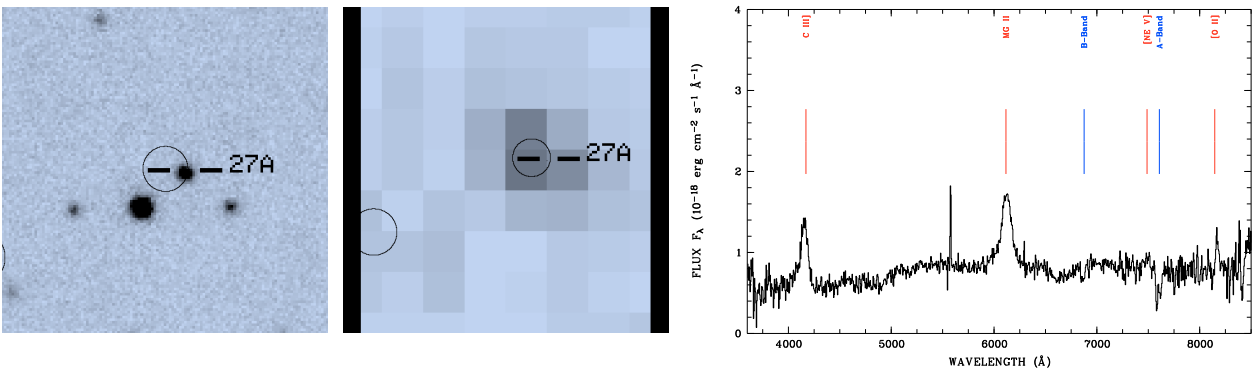
object 27A, z = 1.190
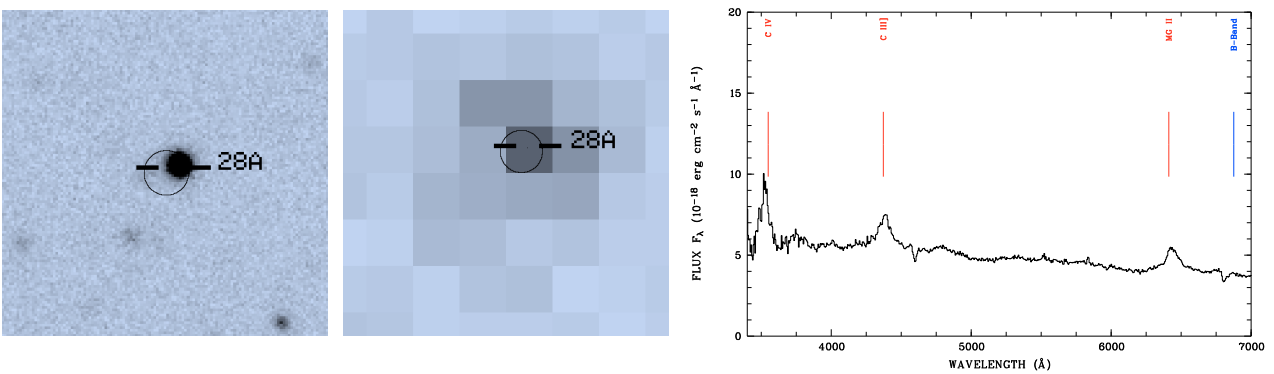
object 28A, z = 1.315
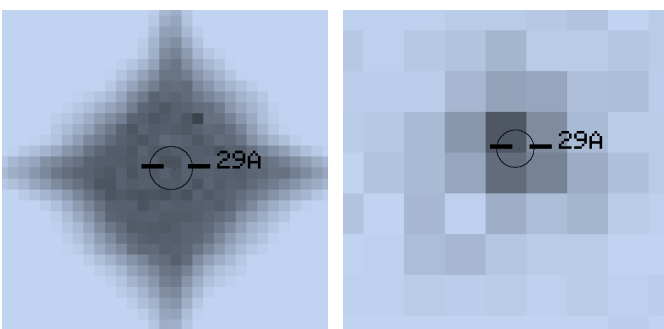
object 29A, z = 0.000

object 32A, z = 2.727

object 33A, z = 2.166

object 34A, z = 0.983
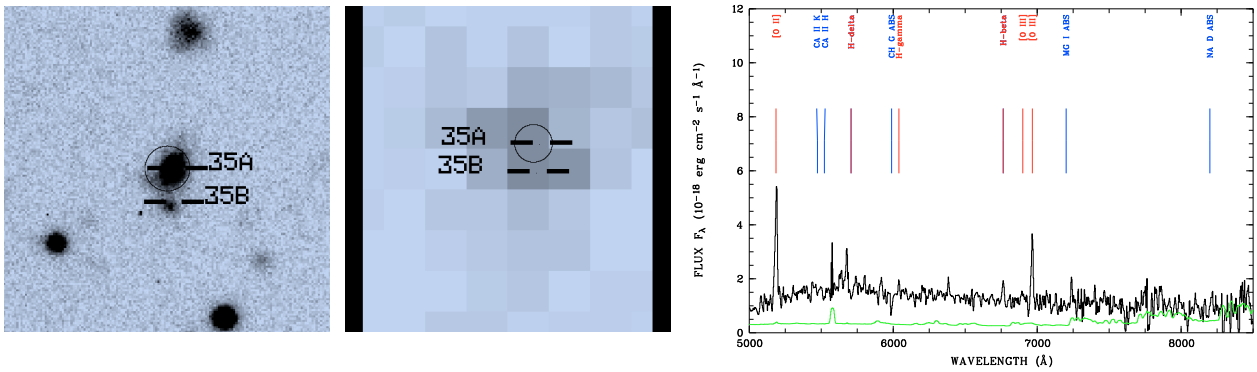
object 35A, z = 0.391

object 35B, z = 0.391
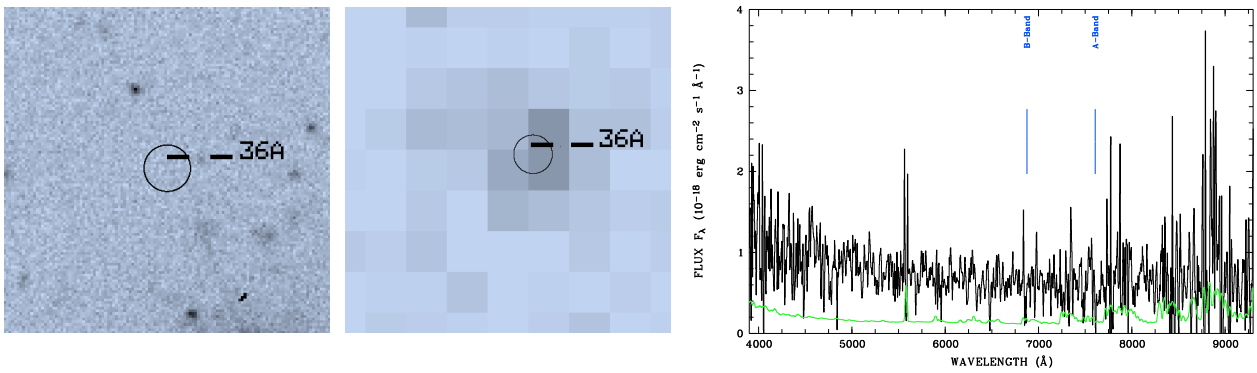
object 36A, no redshift, spectrum too noisy
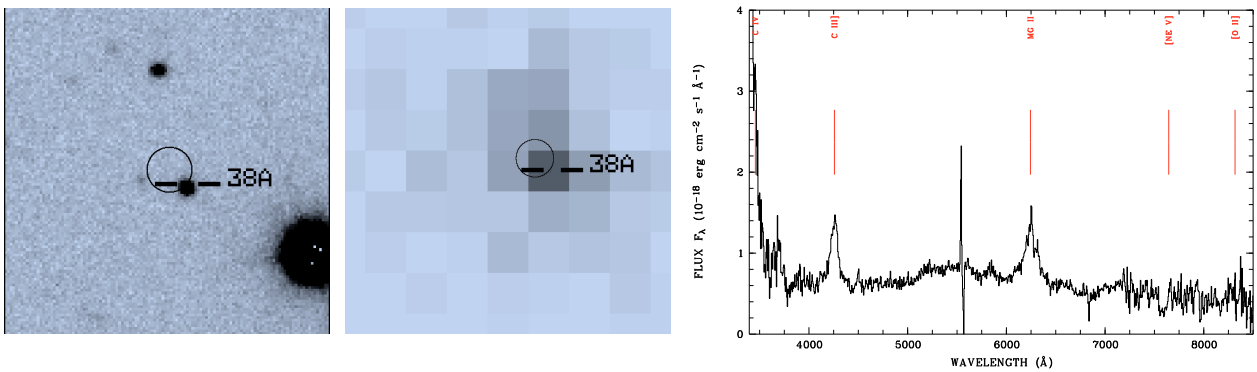
object 38A, z = 1.254
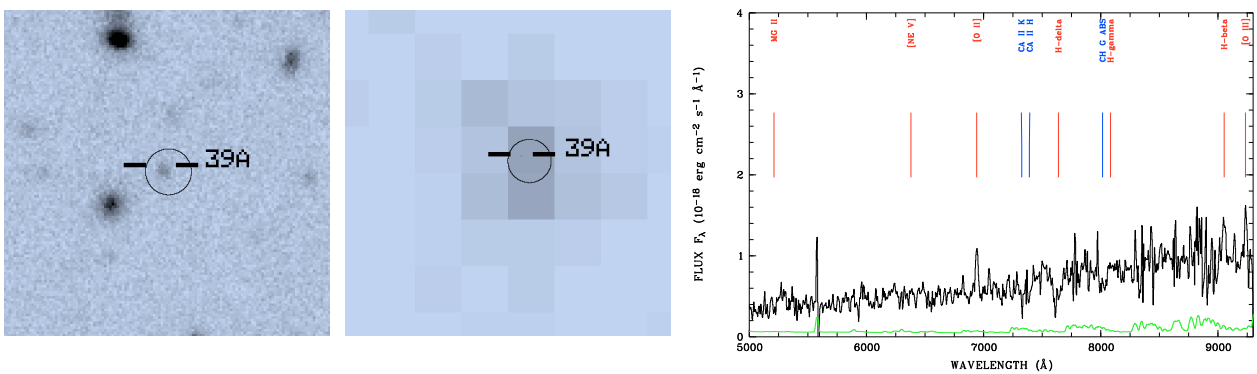
object 39A, z = 0.862
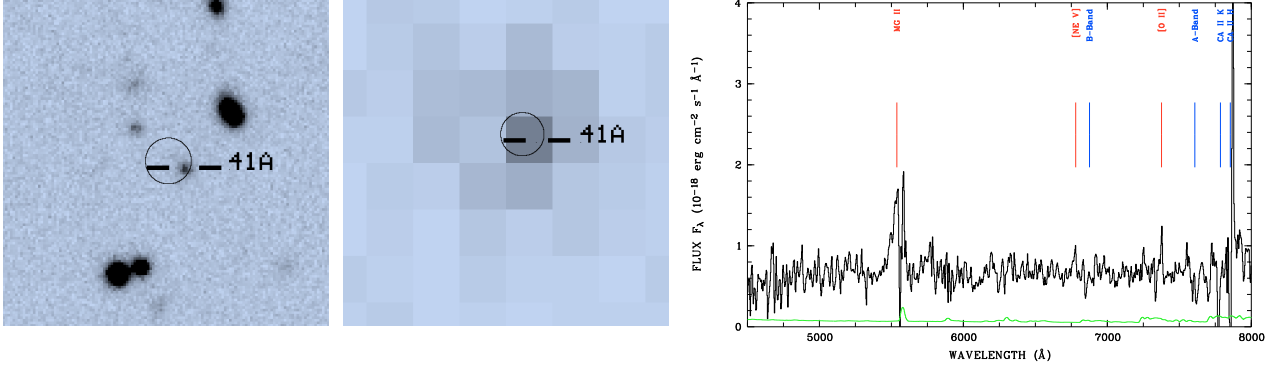
object 41A, z = 0.979
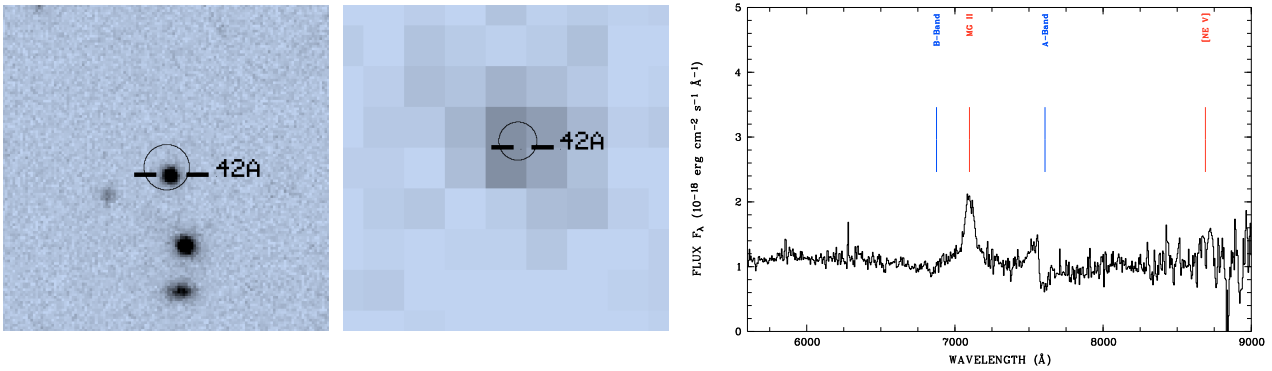
object 42A, z = 1.54
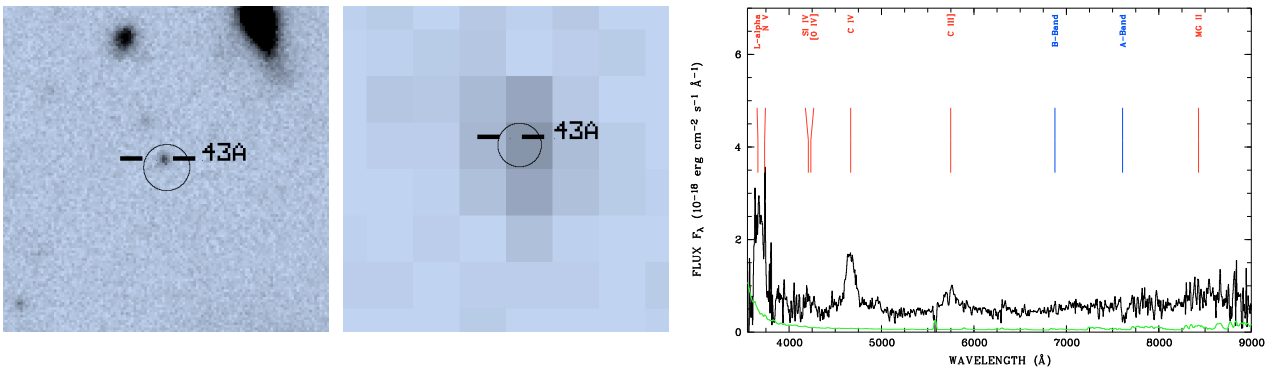
object 43A, z = 2.013
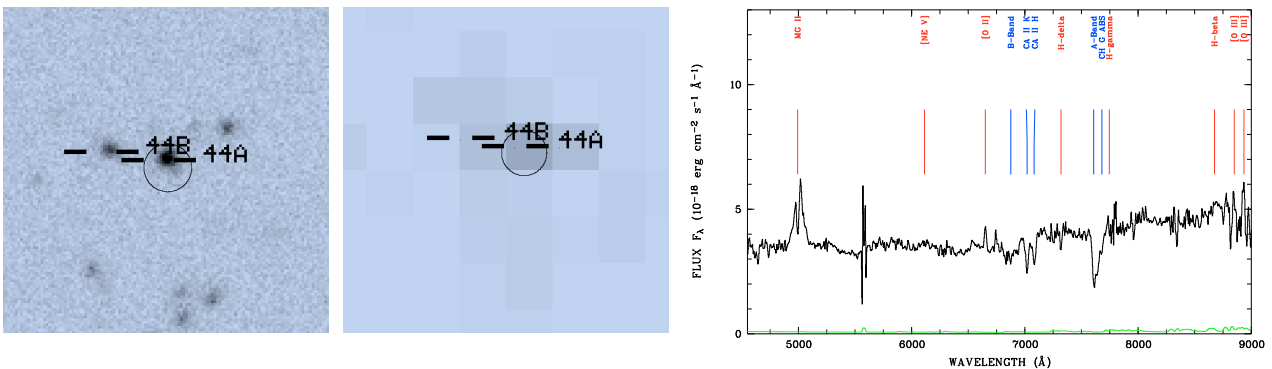
object 44A, z = 0.785
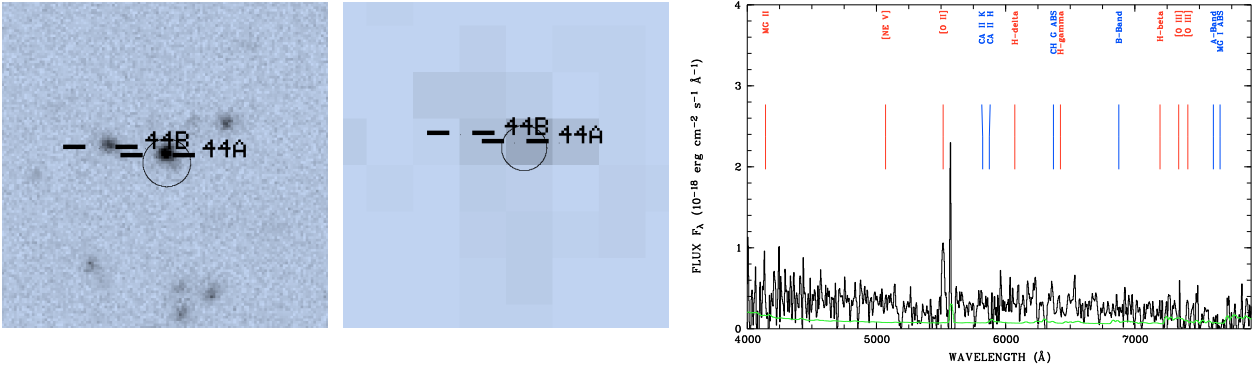
object 44B, z = 0.480:@OII
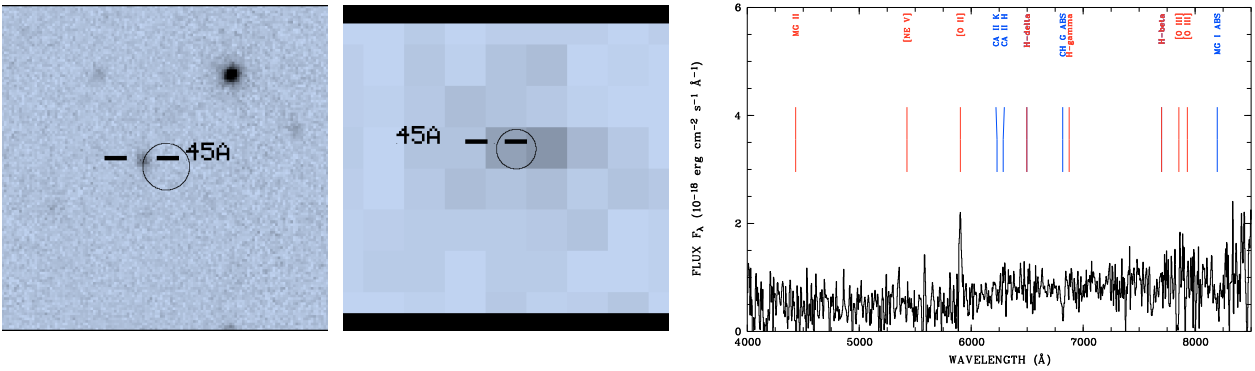
object 45A, z = 0.584:@OII
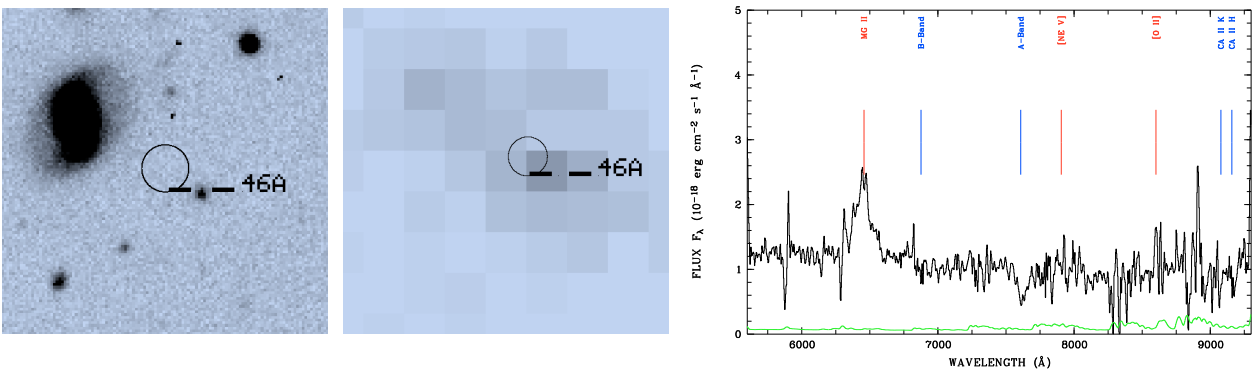
object 46A, z = 1.308
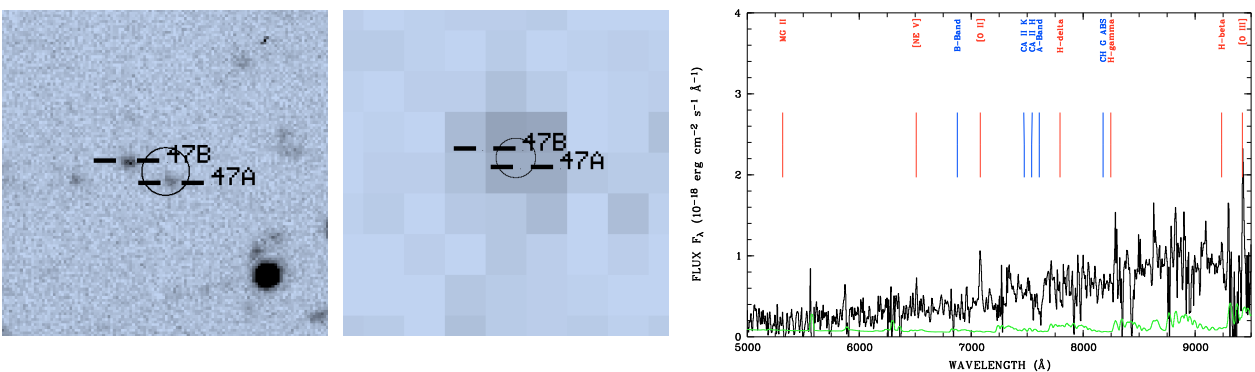
object 47A, z = 0.900:@OII

object 47B, z = 0.89:@OII

object 49A, z = 0.454

object 50A, z = 0.986
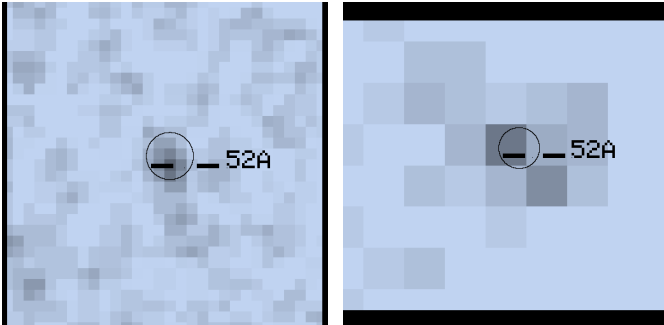
object 51A, z = 0.58

object 52A, z = 1.829
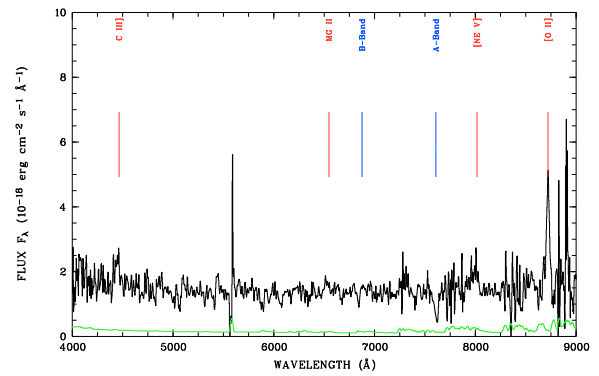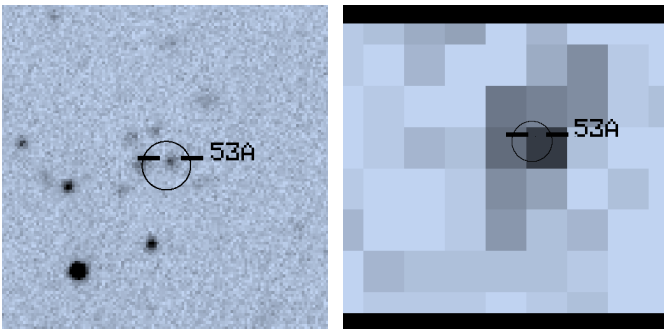
object 53A, z = 1.340:@OII
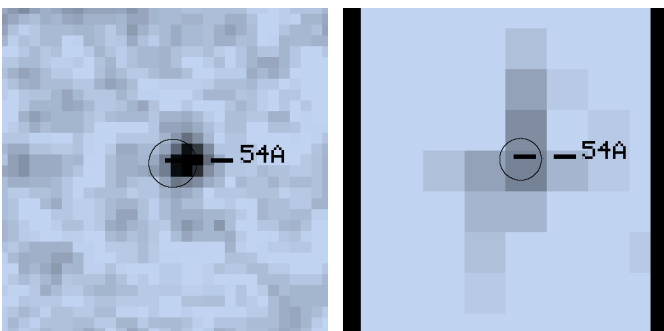
object 54A, z = 2.744
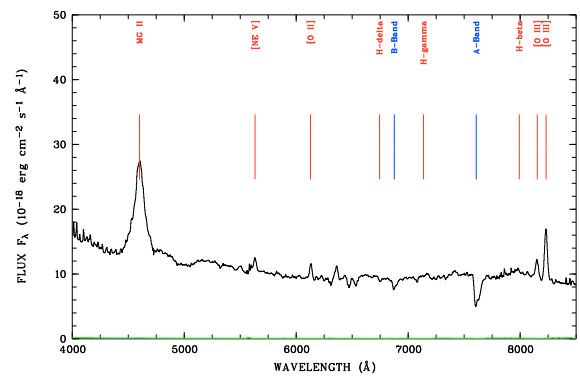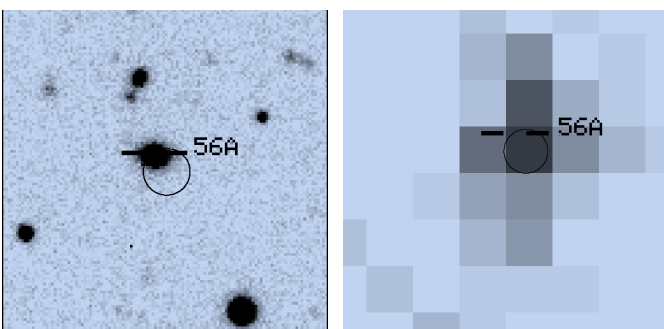
object 56A, z = 0.641
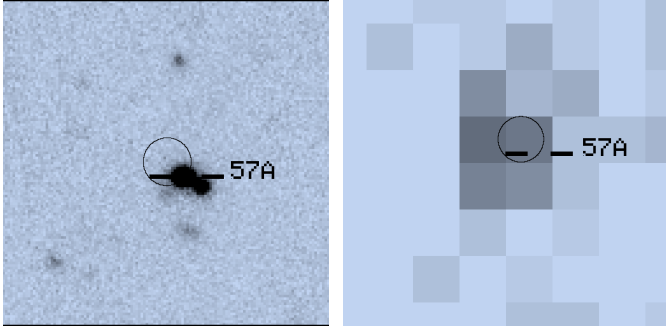
object 57A, z = 0.281
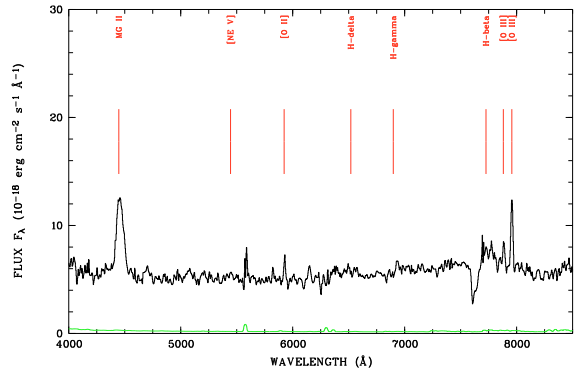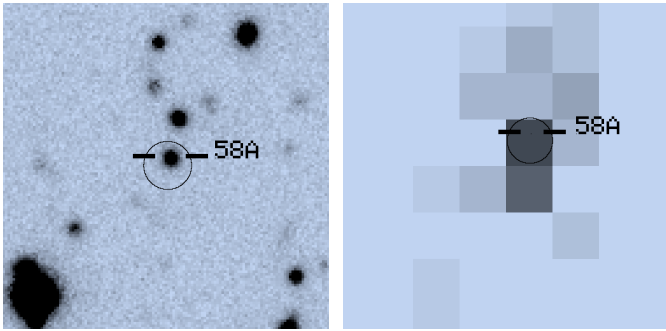
object 58A, z = 0.589
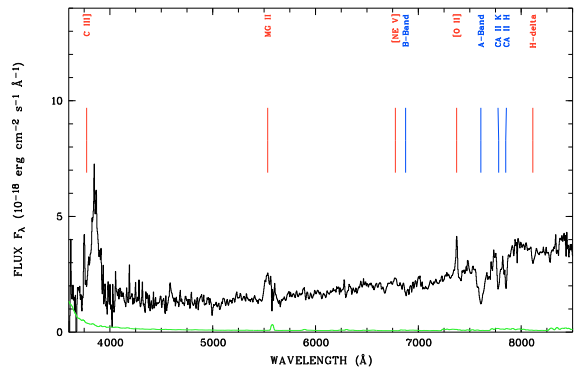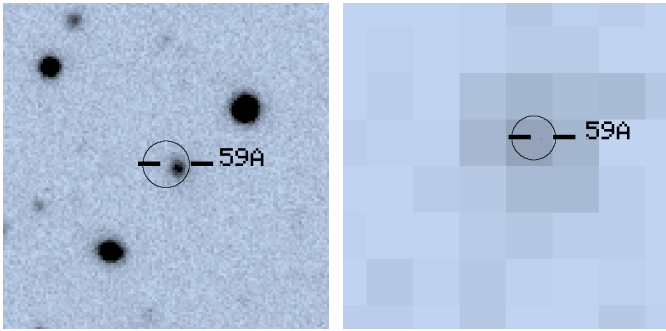
object 59A, z = 0.978
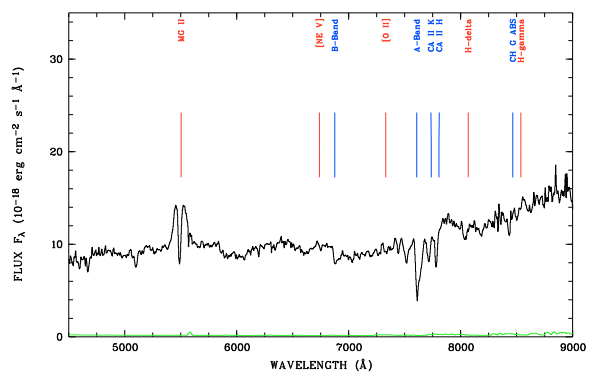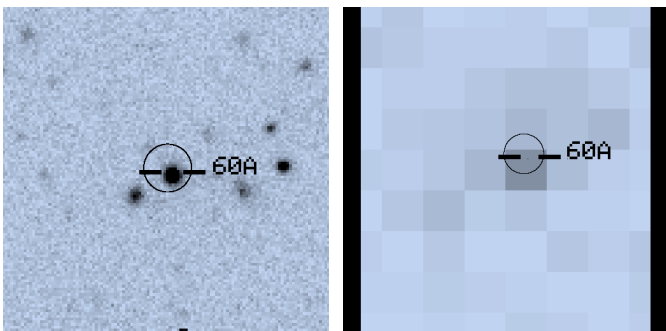
object 60A, z = 0.957
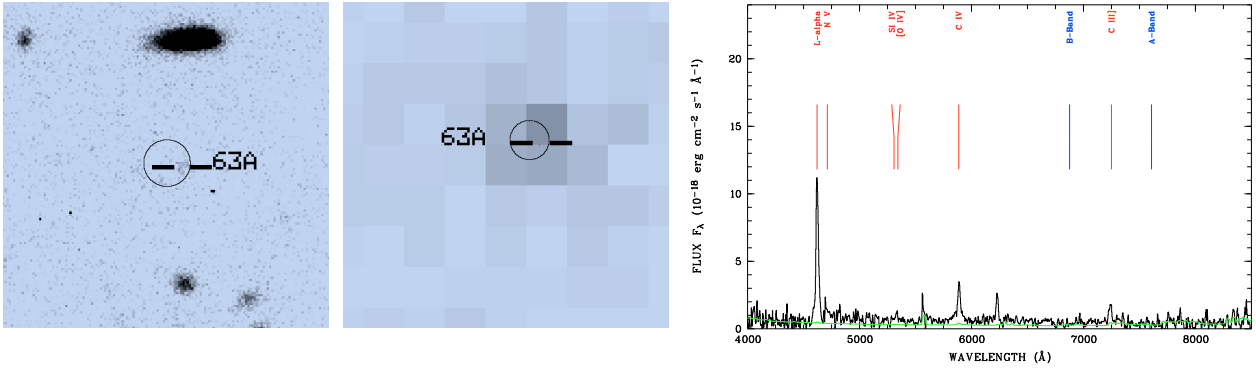
object 63A, z = 2.800
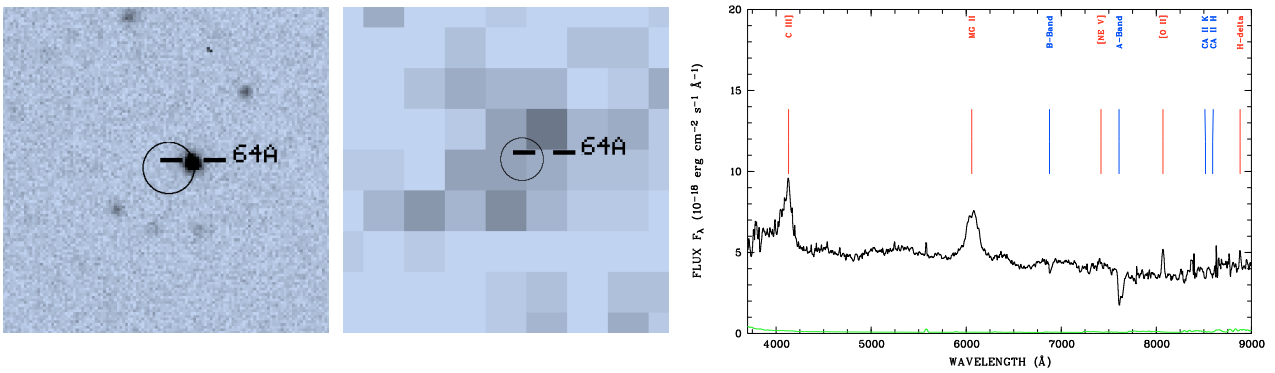
object 64A, z = 1.165
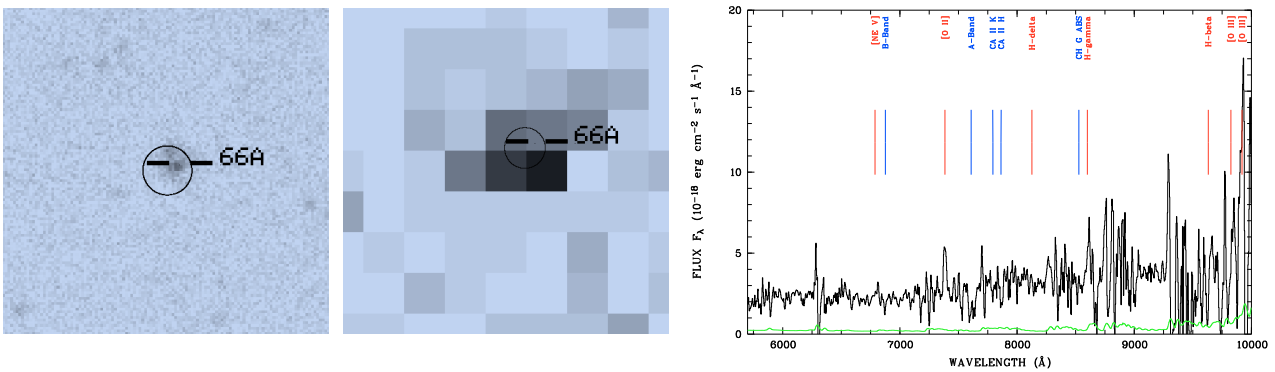
object 66A, z = 0.981:@OII
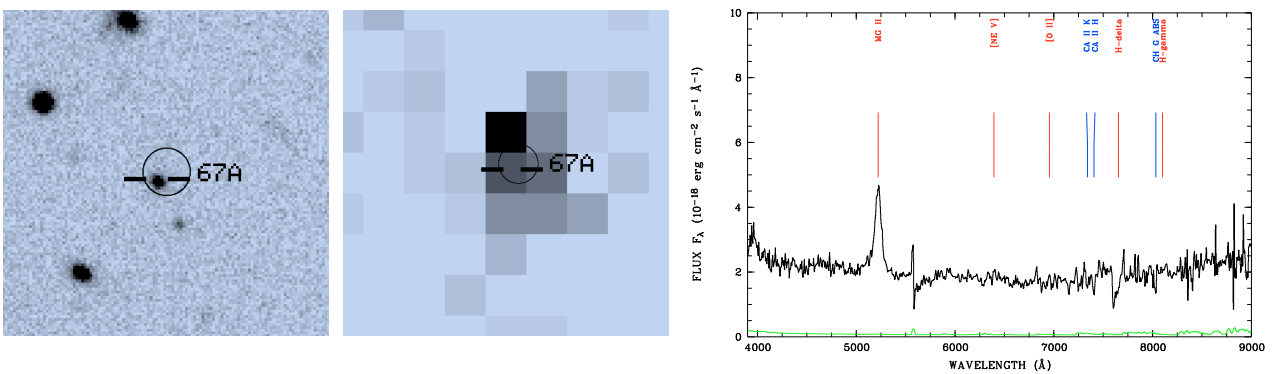
object 67A, z = 0.866
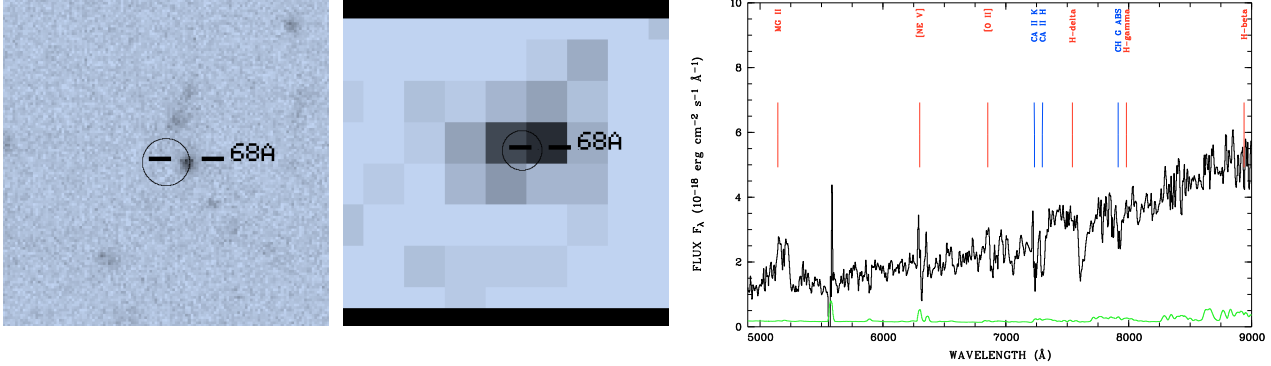
object 68A, z = 0.839
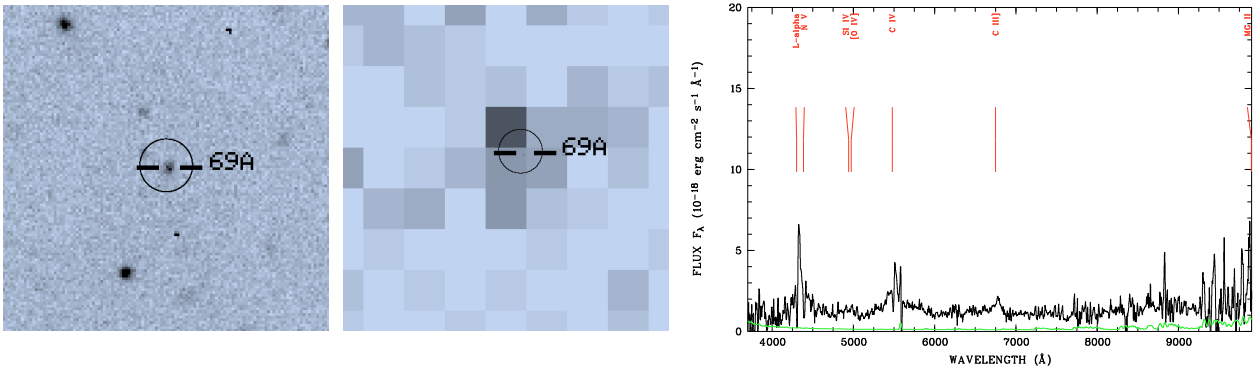
object 69A, z = 2.553
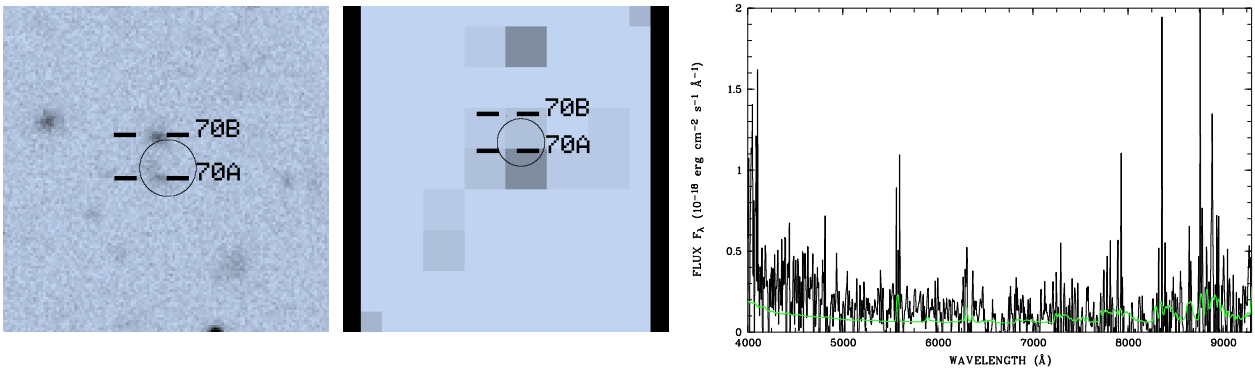
object 70A, no redshift, spectrum too noisy
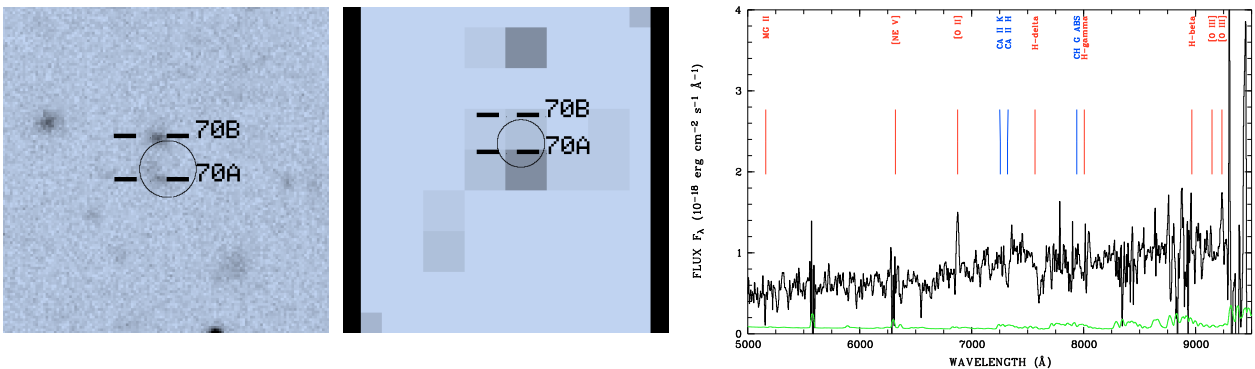
object 70B, z = 0.844
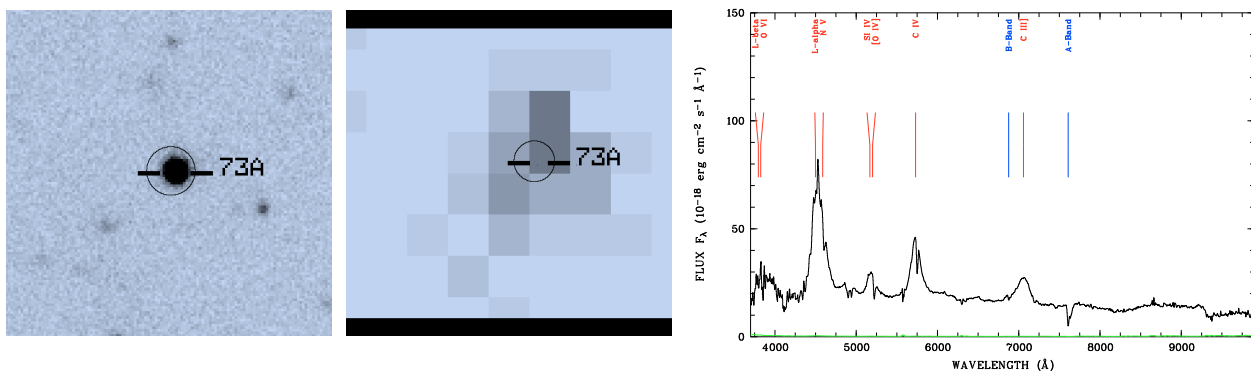
object 73A, z = 2.706
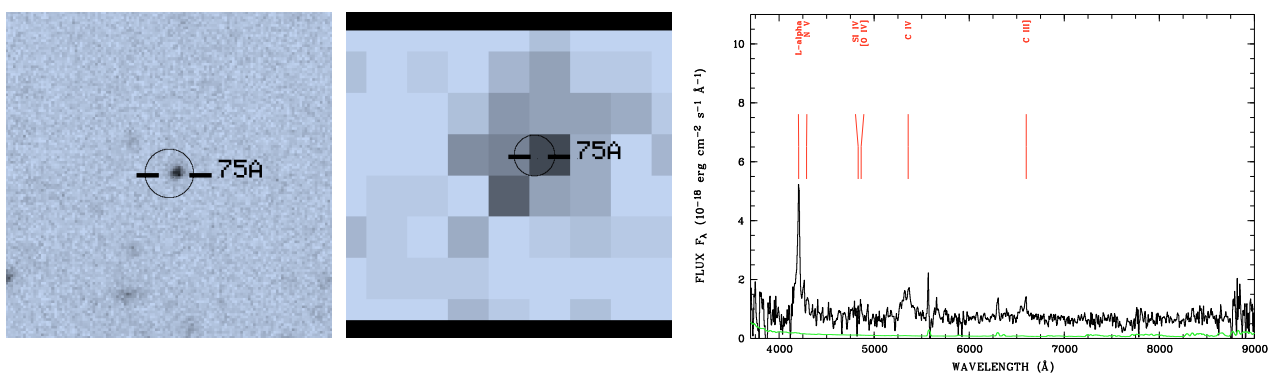
object 75A, z = 2.460
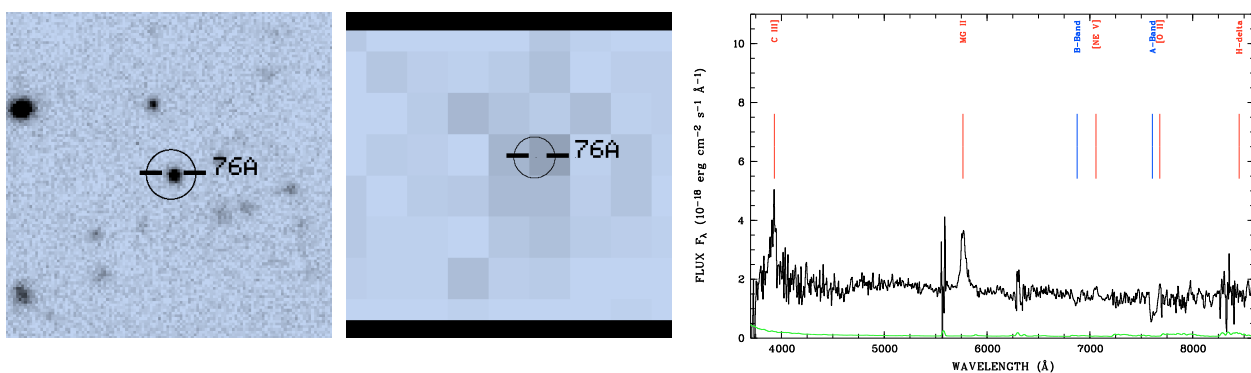
object 76A, z = 1.065
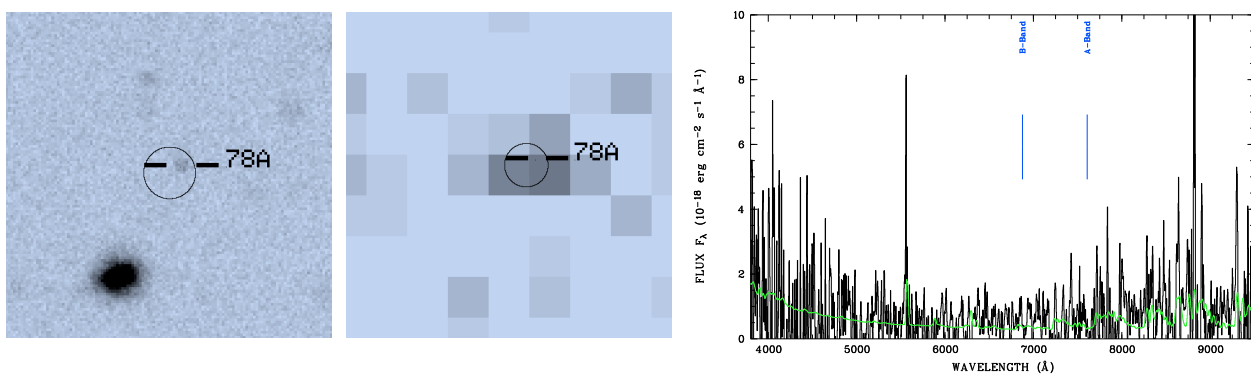
object 78A, no redshift, spectrum too noisy
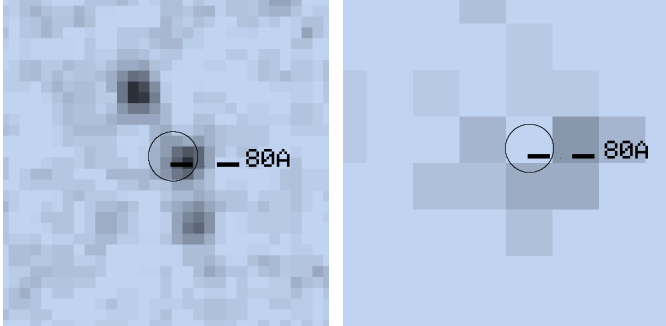
object 80A, z = 1.620
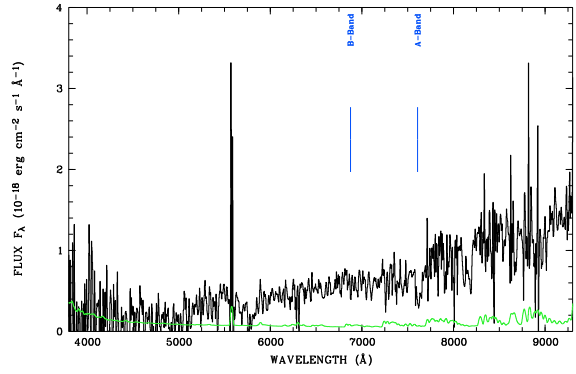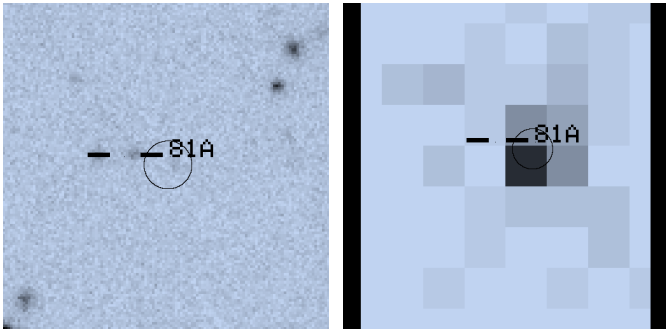
object 81A, no redshift, spectrum too noisy
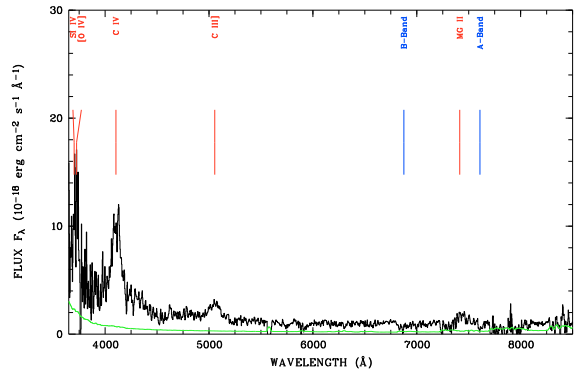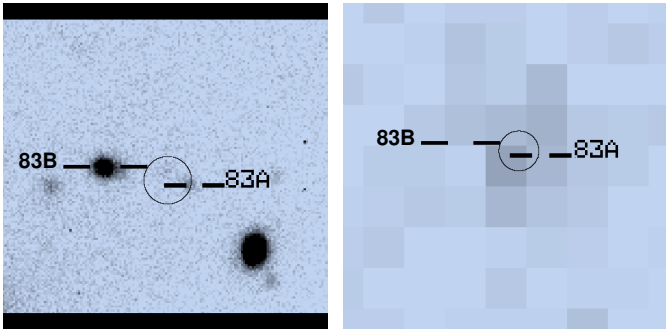
object 83A, z = 1.650
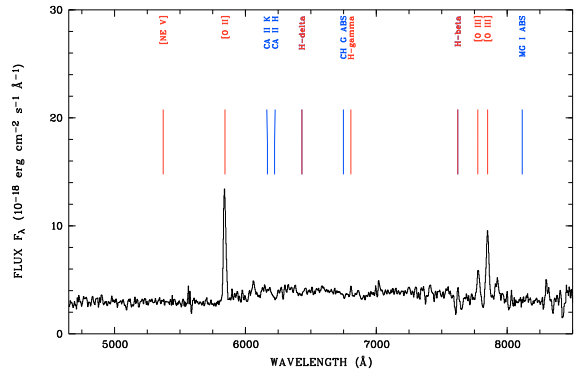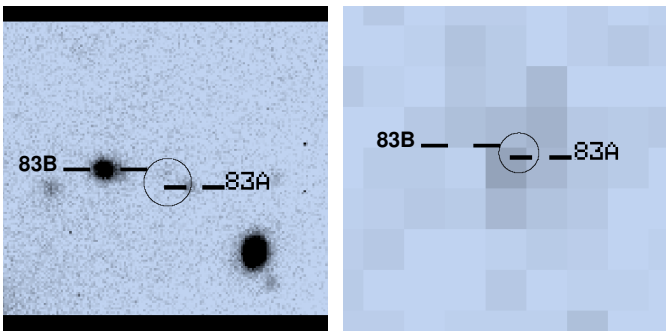
object 83B, z = 0.568

object 84A, z = 2.094

object 84B, z = 0.000

object 88A, z = 0.739

object 92A, z = 2.425
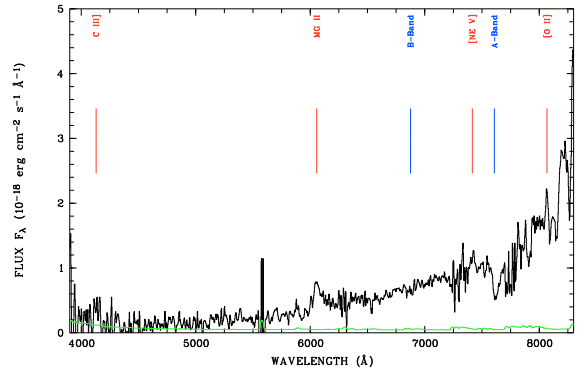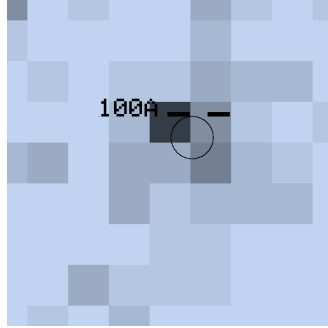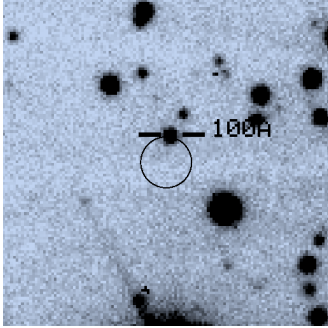
object 100A, z = 1.165
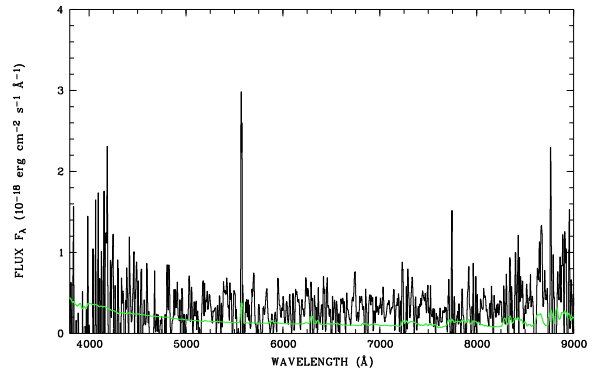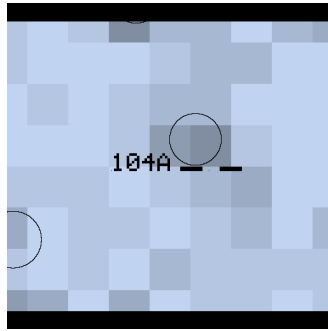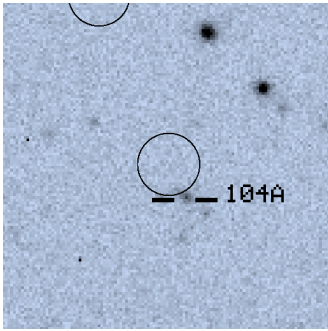
object 104A, no redshift, spectrum too noisy
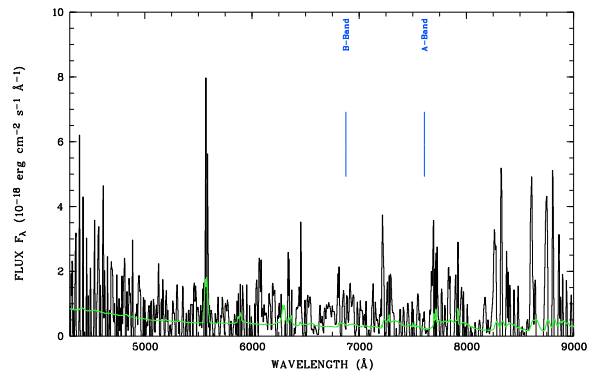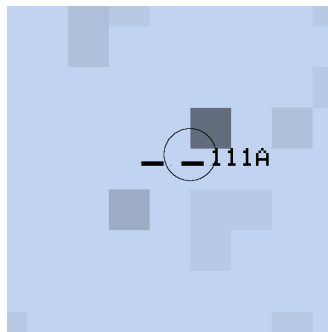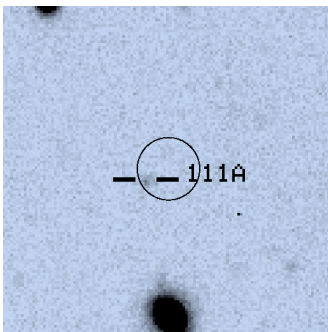
object 111A, no redshift, spectrum too noisy
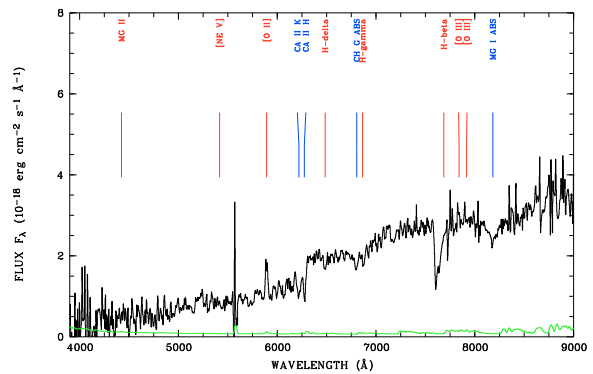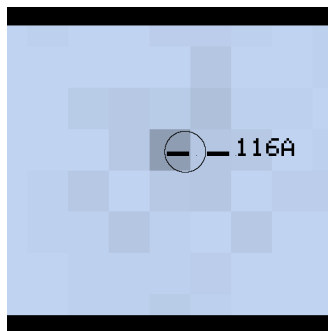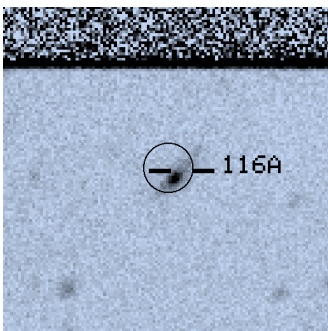
object 116A, z = 0.581
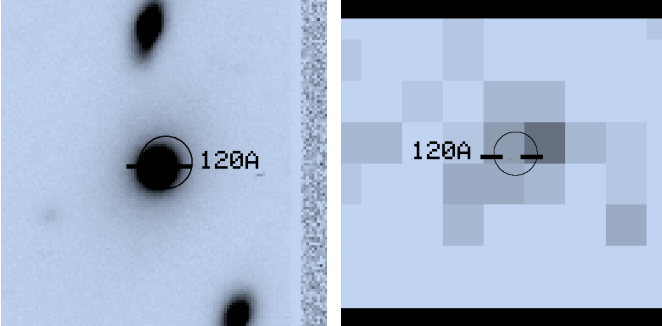
object 120A, z = 0.094
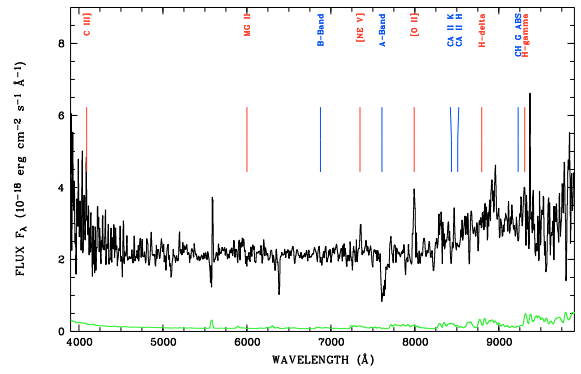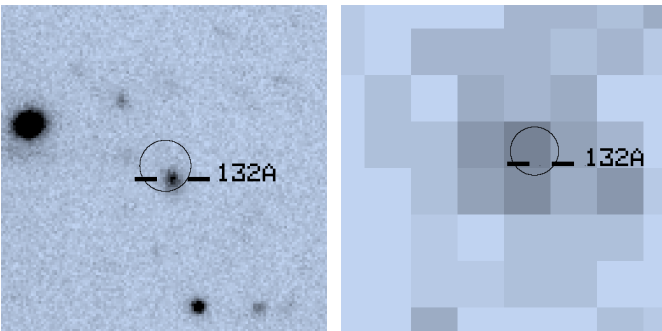
object 132A, z = 1.144:@OII
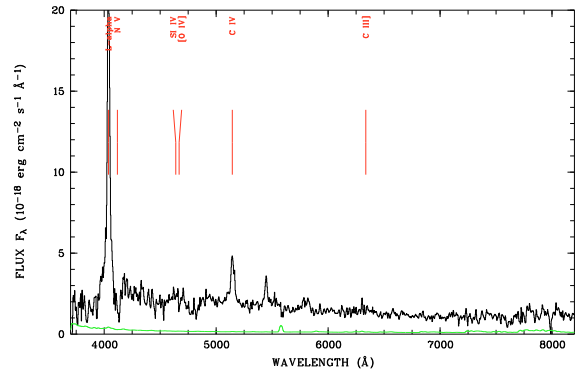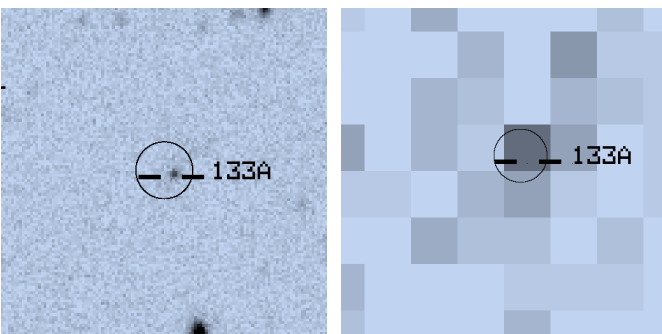
object 133A, z = 2.321
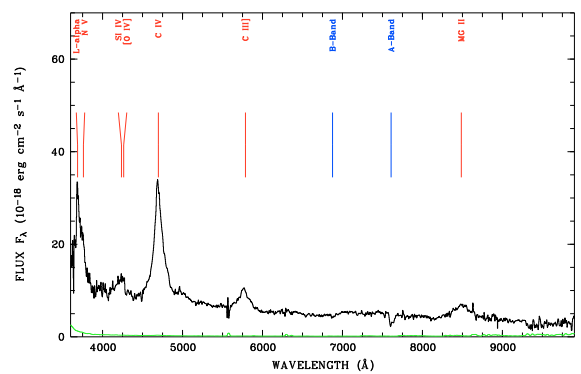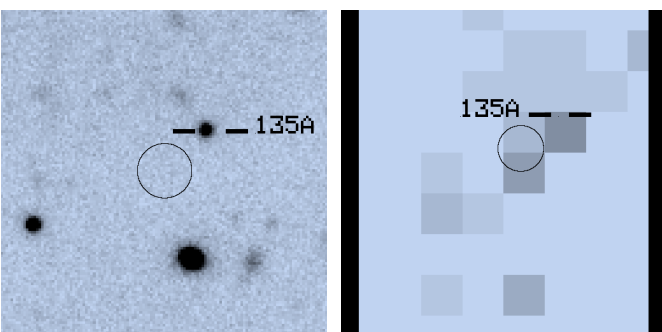
object 135A, z = 2.033
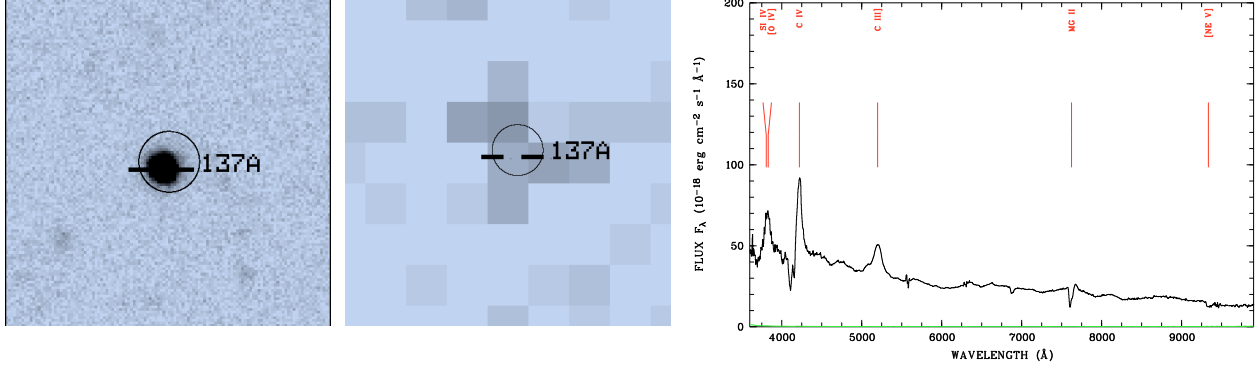
object 137A, z = 1.721
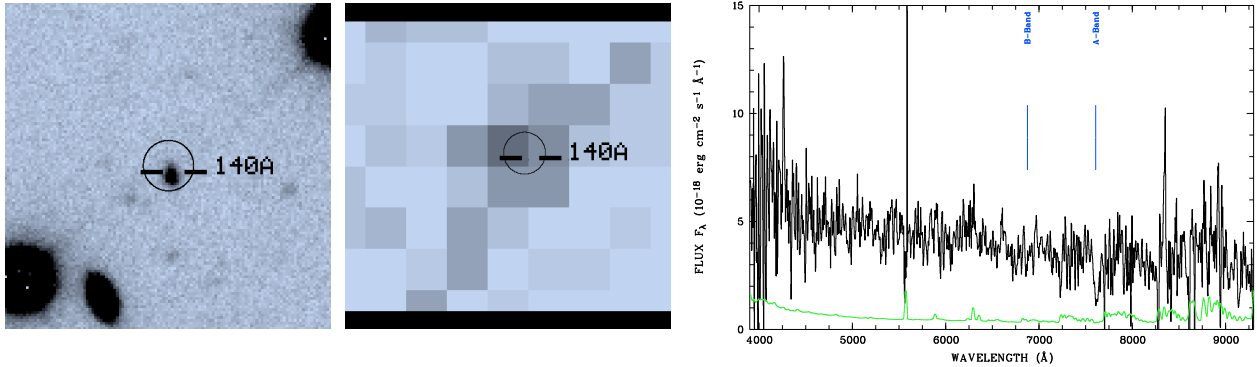
object 140A, no redshift, spectrum too noisy
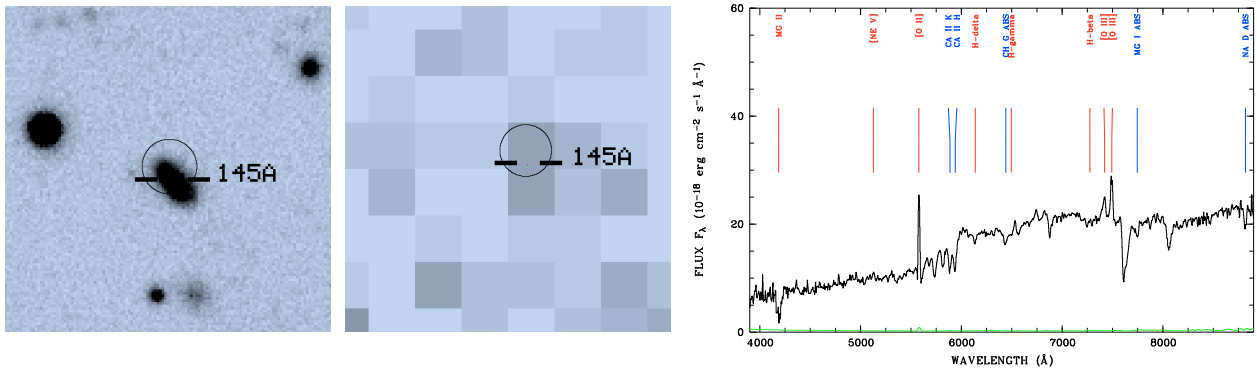
object 145A, z = 0.497
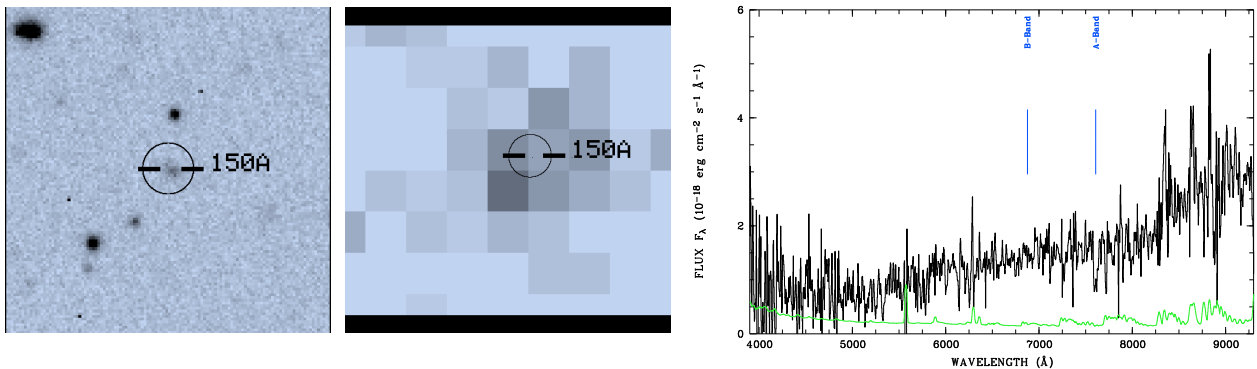
object 150A, no redshift, spectrum too noisy
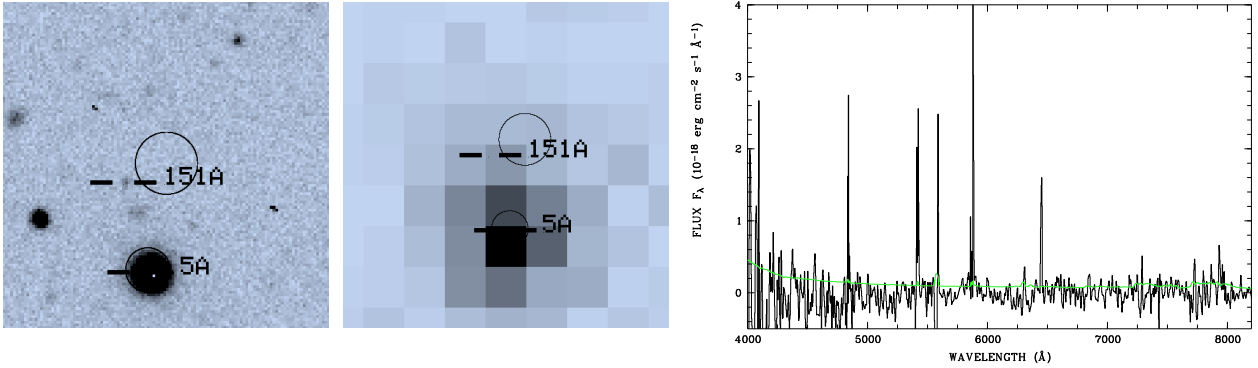
object 151A, no redshift, spectrum too noisy
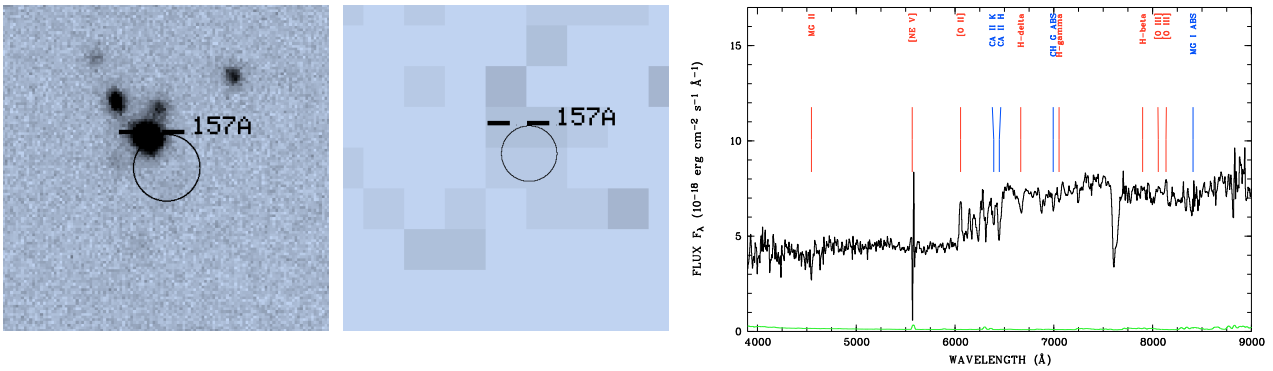
object 157A, z = 0.625
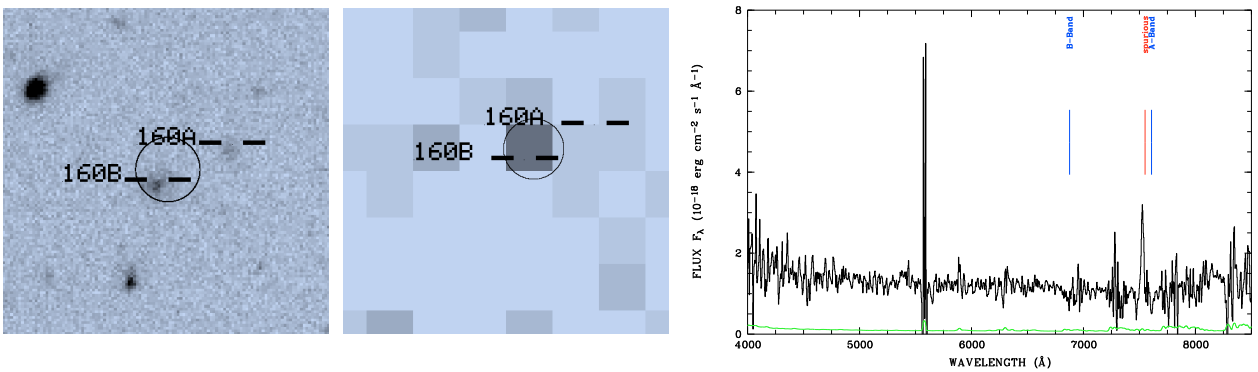
object 160A, no redshift, spectrum too noisy
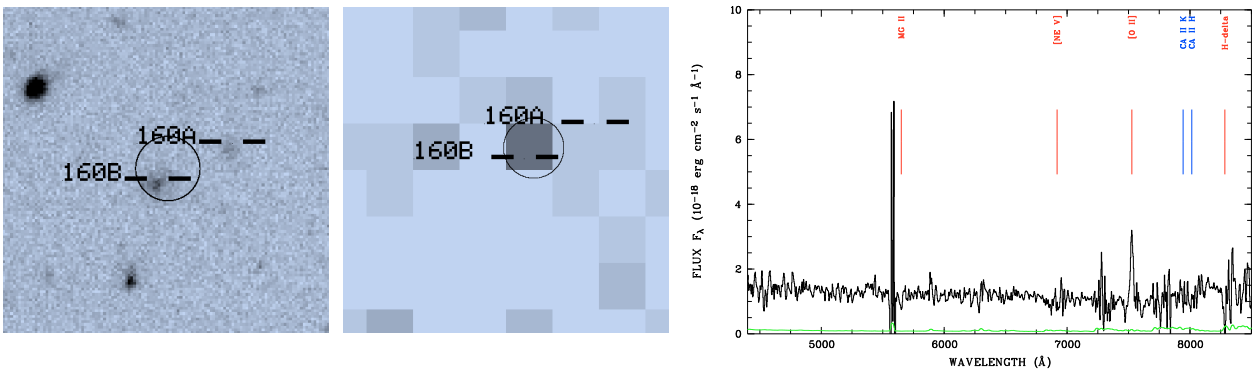
object 160B, z = 1.020:@OII

object 165A, z = 0.000

object 166A, z = 0.000

object 171A, z = 0.800

object 172A, no redshift, spectrum too noisy

object 185A, z = 2.768

object 189A, z = 0.079

object 191A, z = 1.045

object 197A, no redshift, spectrum too noisy
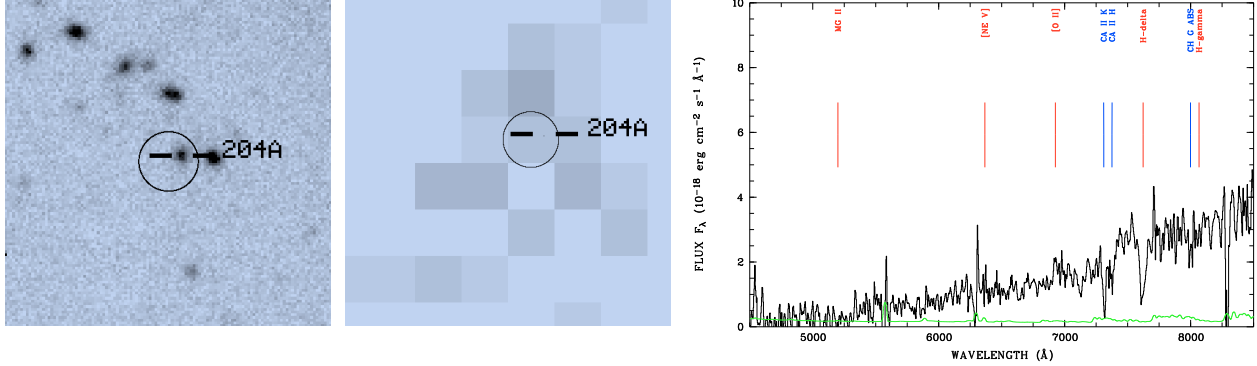
object 204A, z = 0.859
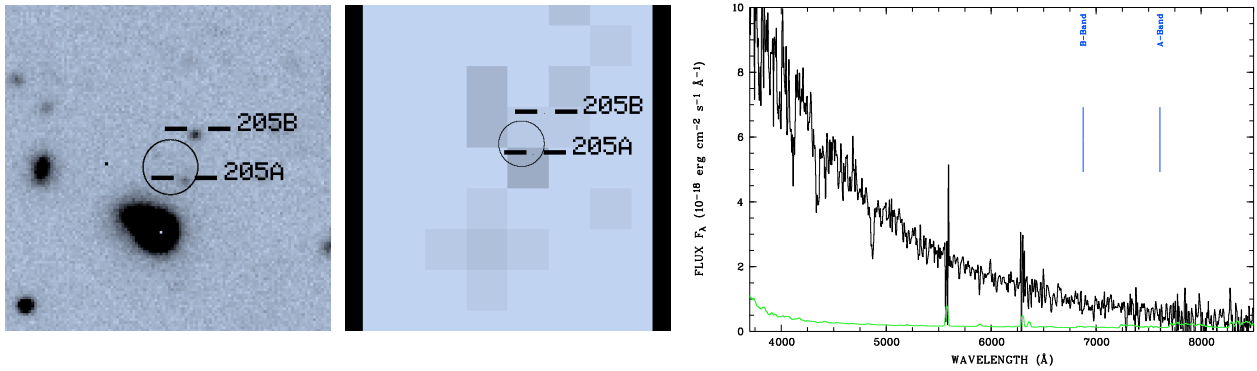
object 205A, z = 0.000
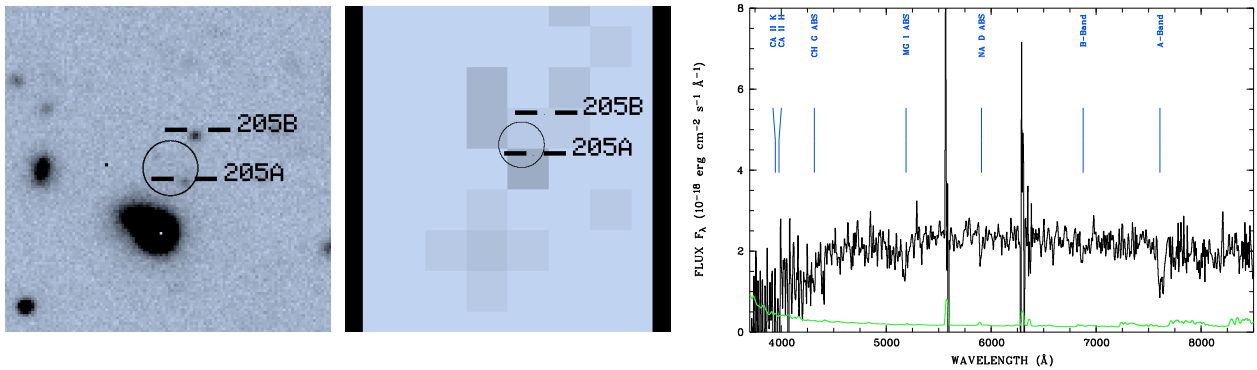
object 205B, z = 0.000
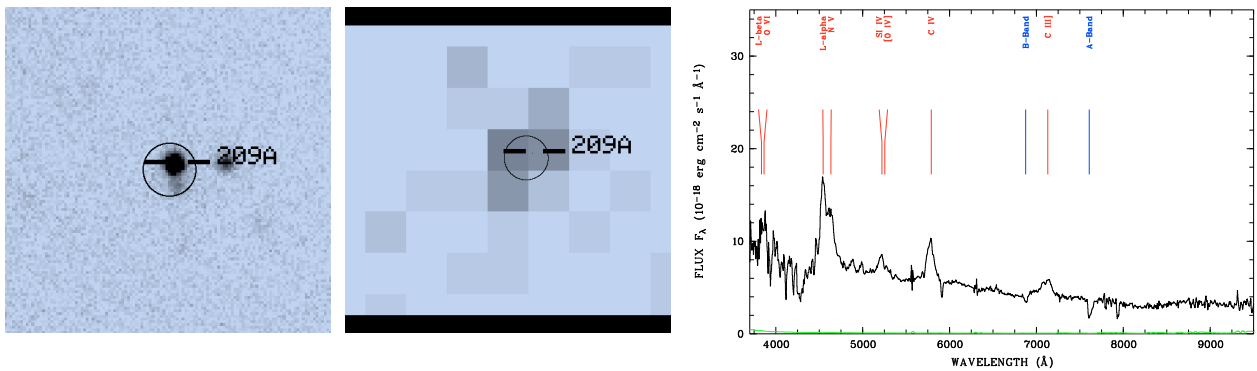
object 209A, z = 2.735
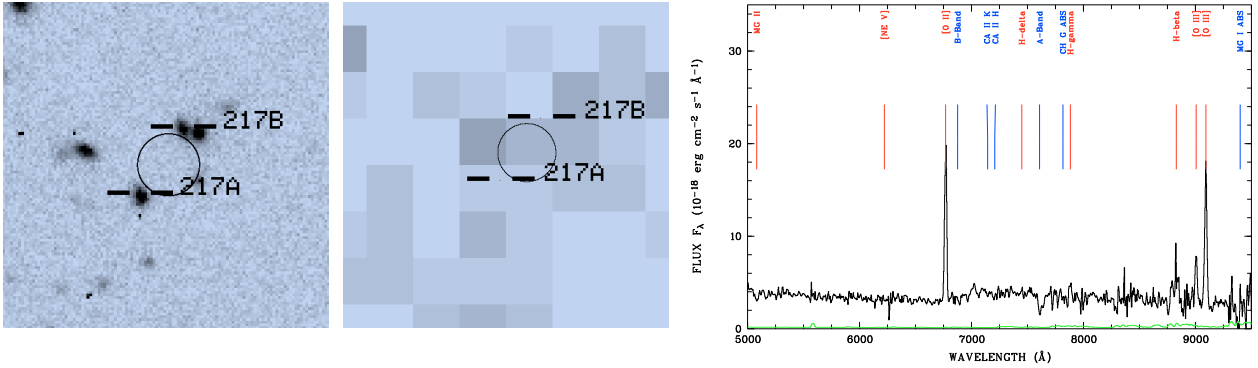
object 217A, z = 0.816
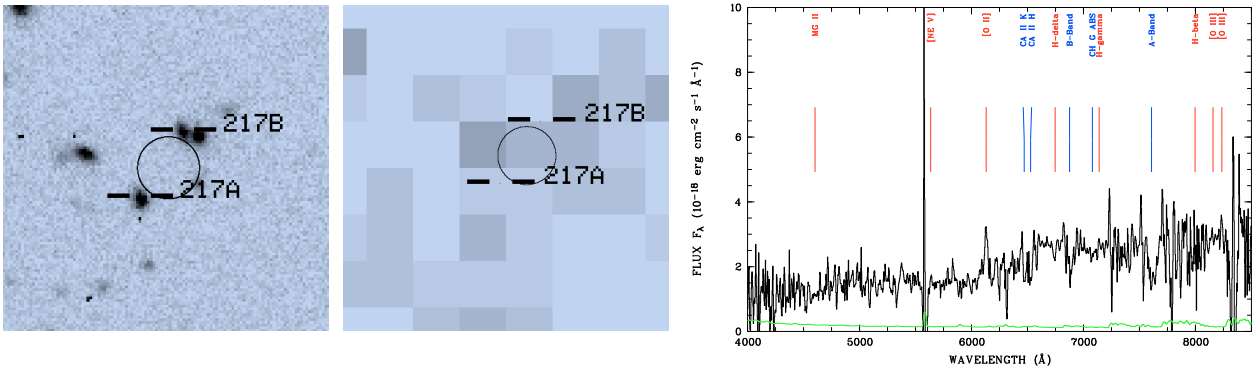
object 217B, z = 0.645
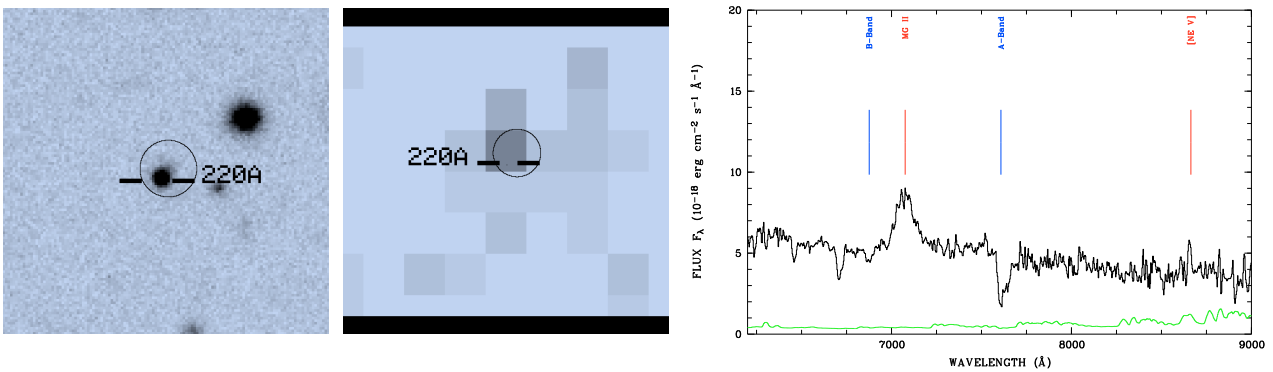
object 220A, z = 1.529
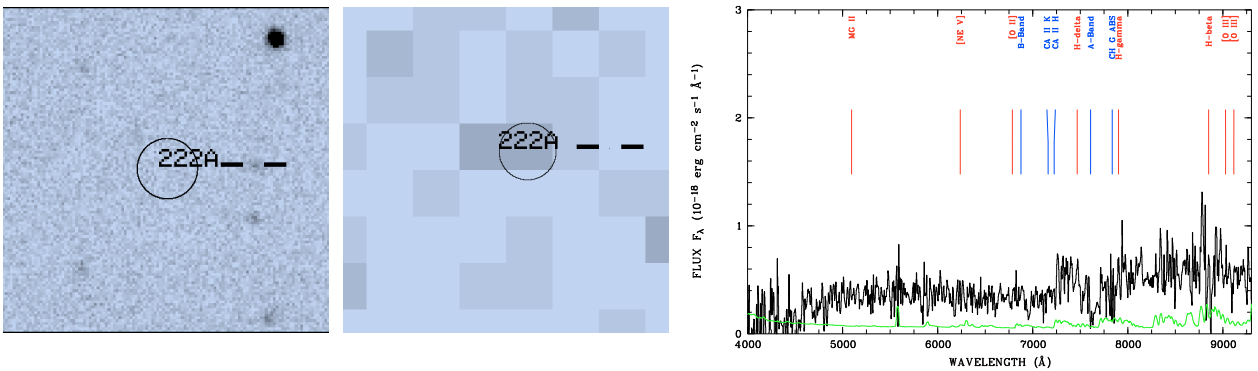
object 222A, z = 0.82:@Ca-Break
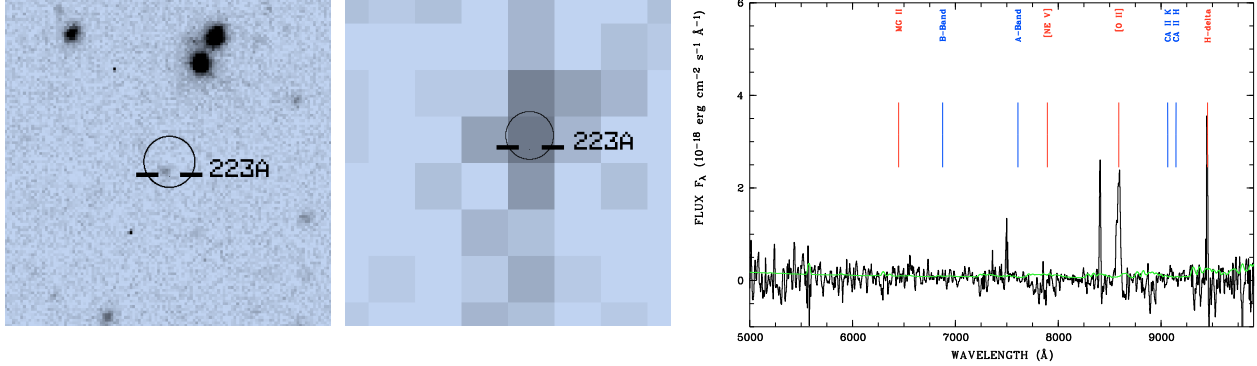
object 223A, z = 1.304:@OII
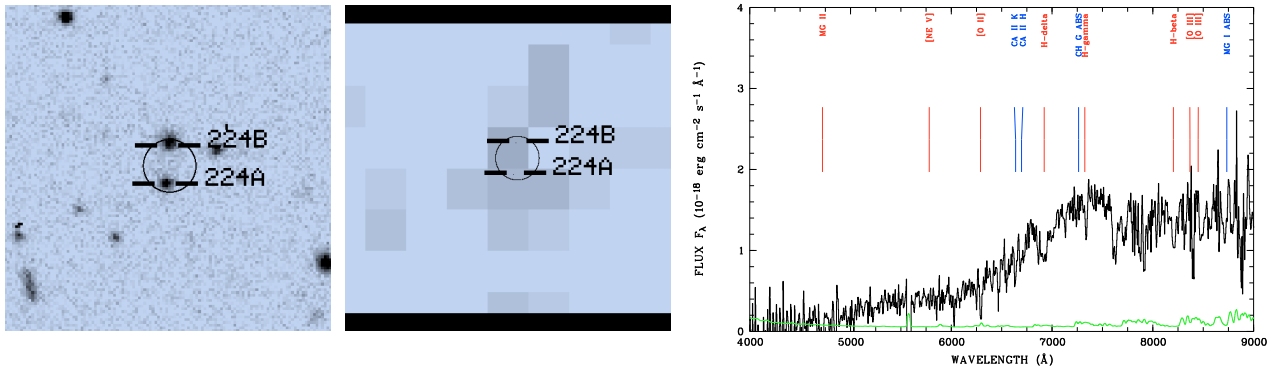
object 224A, z = 0.688:@Ca-Break
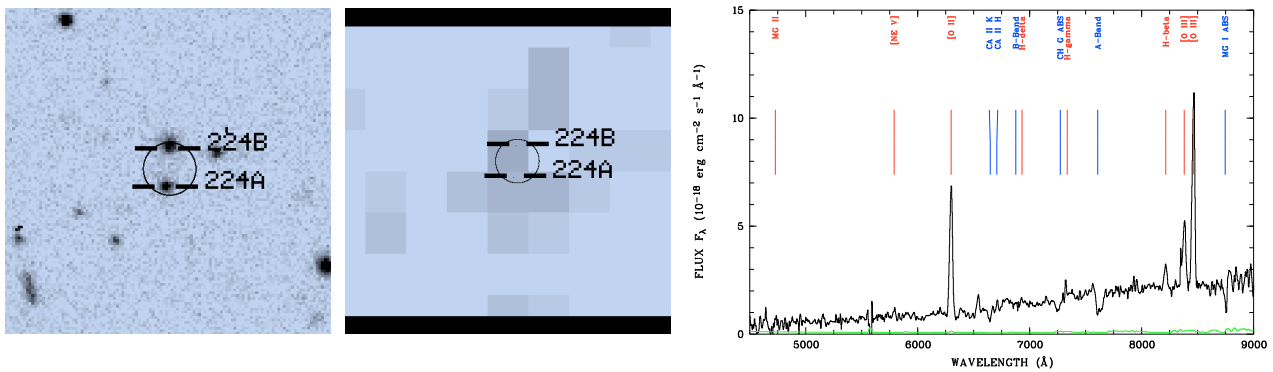
object 224B, z = 0.690
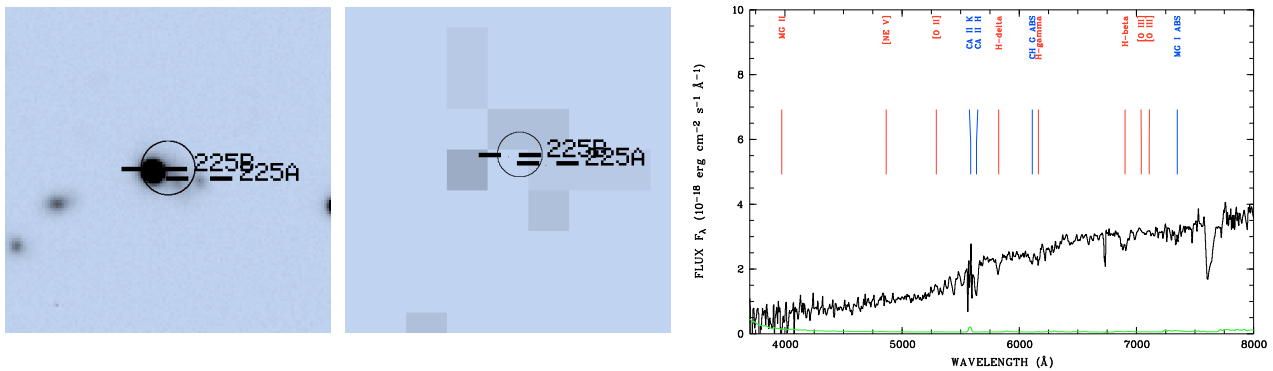
object 225A, z = 0.420
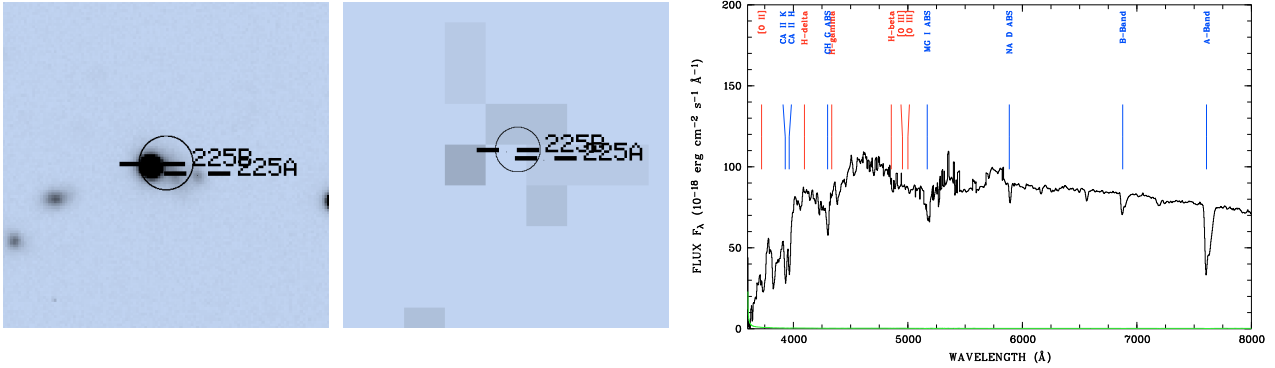
object 225B, z = 0.000
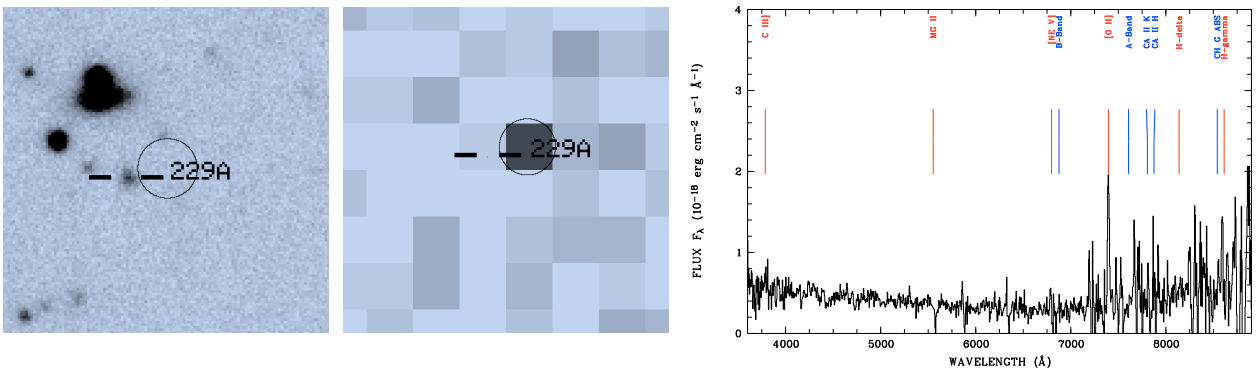
object 229A, z = 0.98:@OII
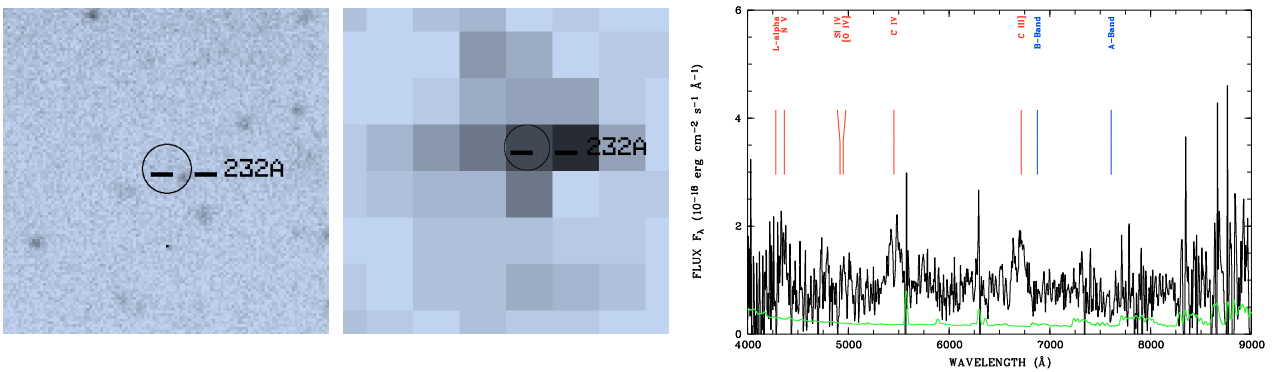
object 232A, z = 2.520
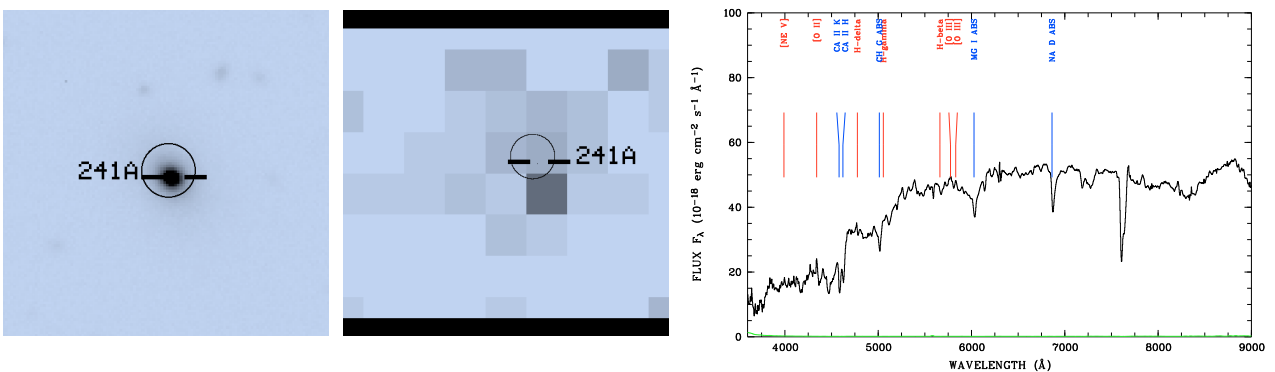
object 241A, z = 0.165
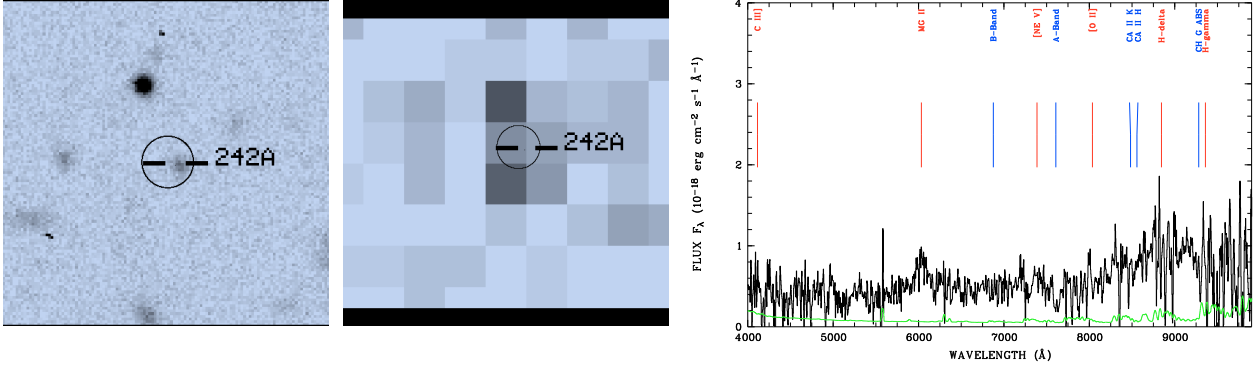
object 242A, z = 1.147
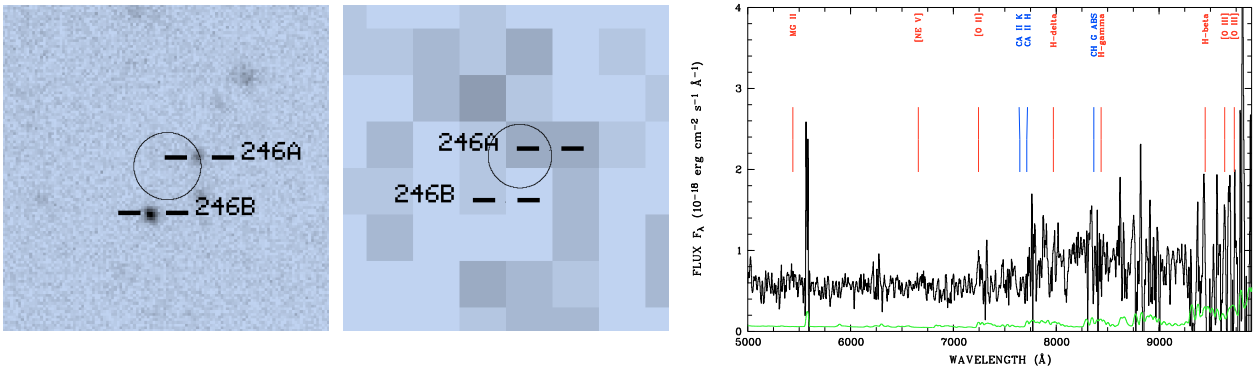
object 246A, z = 0.944
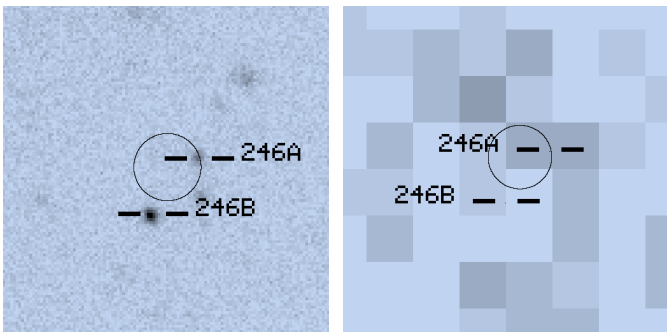
object 246B, z = 0.688
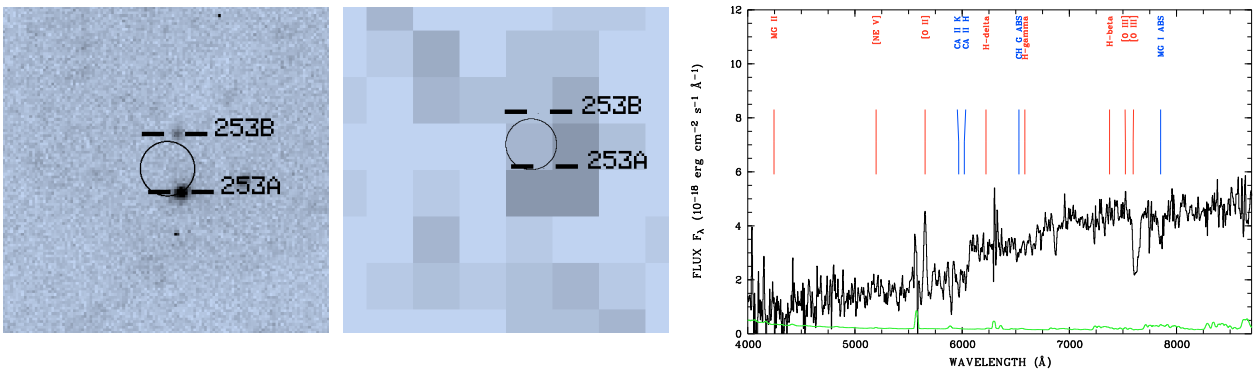
object 253A, z = 0.517
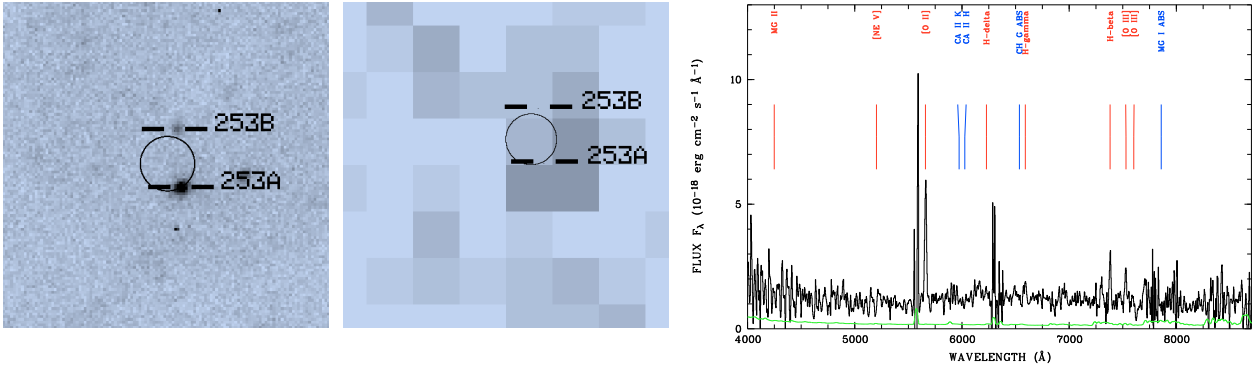
object 253B, z = 0.518
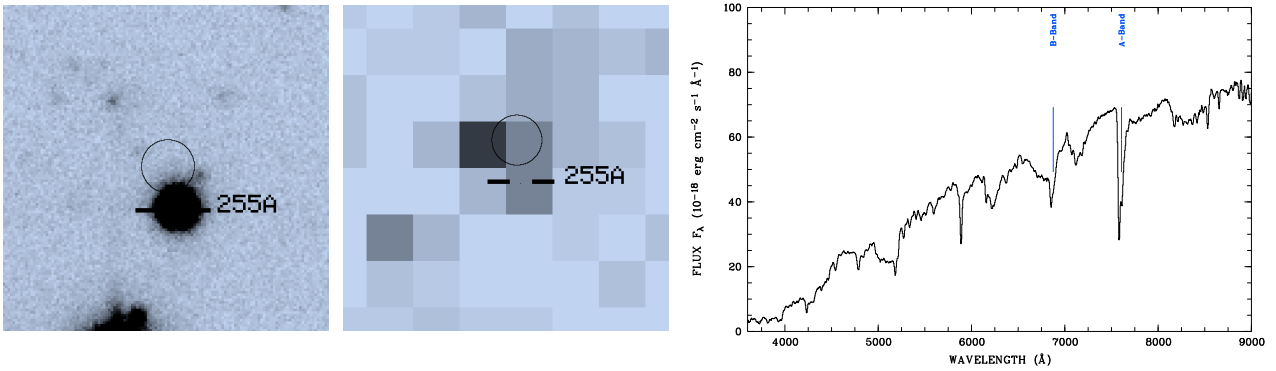
object 255A, z = 0.00
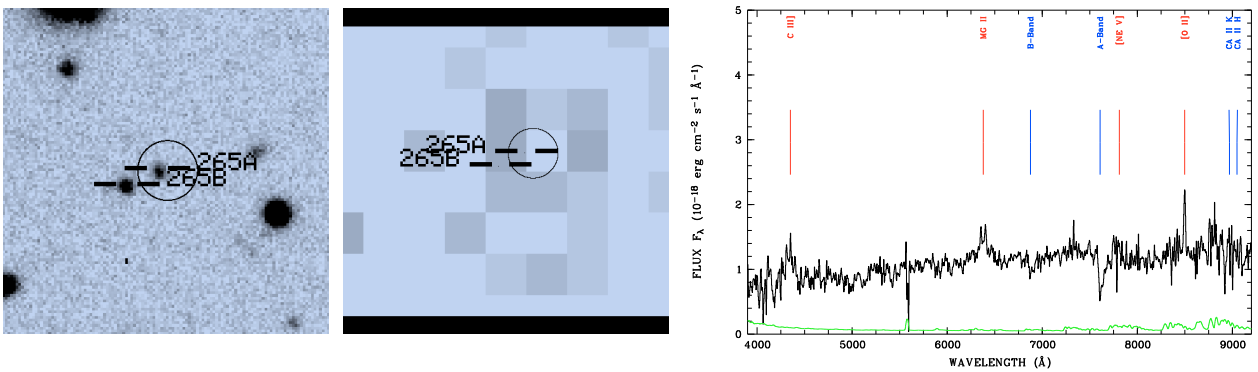
object 265A, z = 1.280
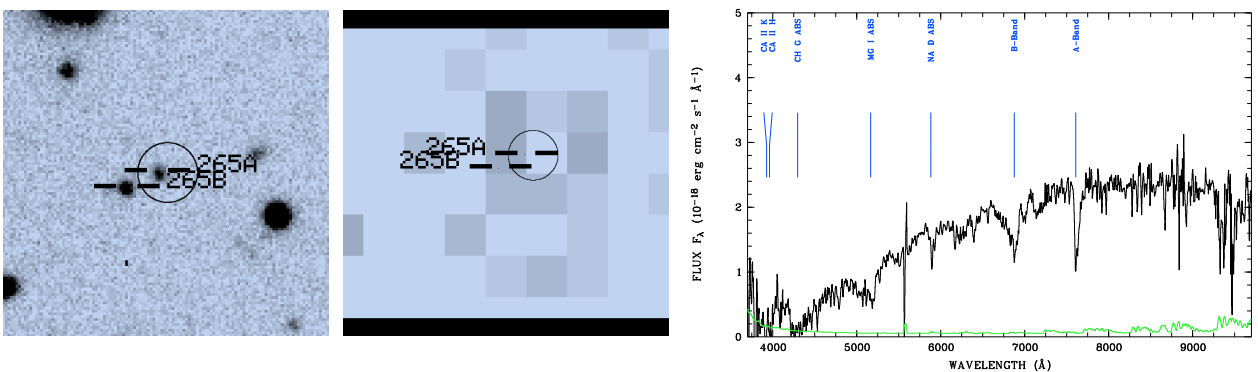
object 265B, z = 0.000
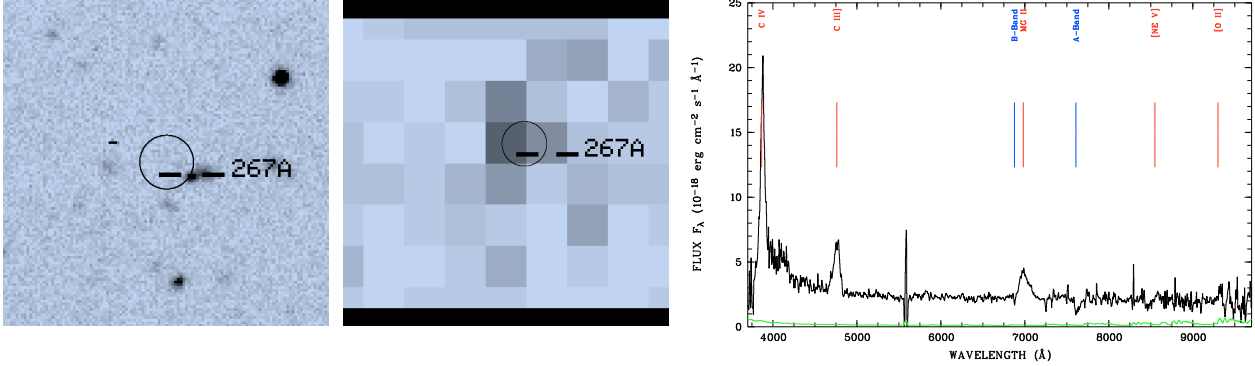
object 267A, z = 1.495
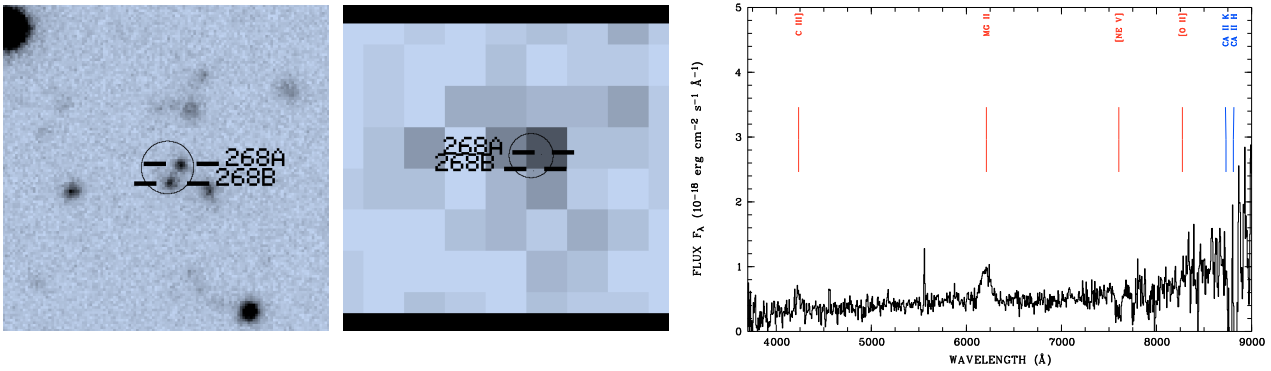
object 268A, z = 1.22
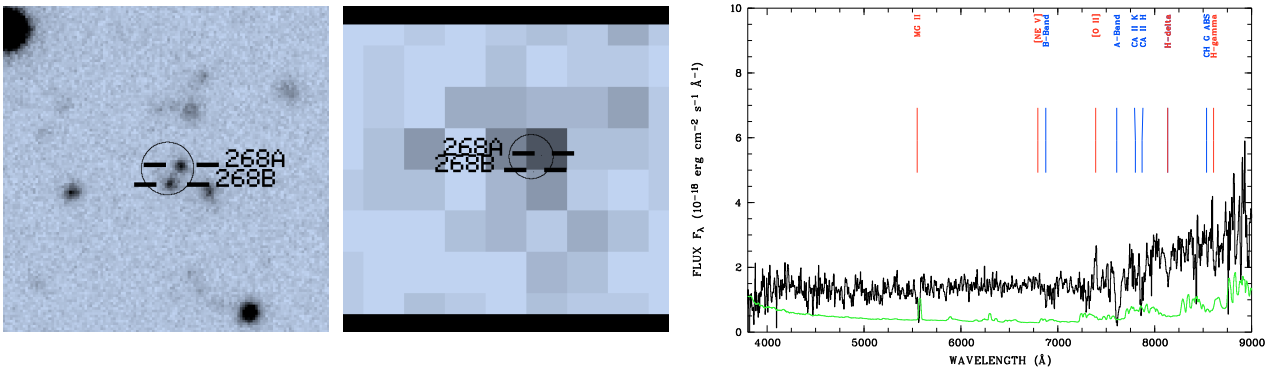
object 268B, z = 0.983
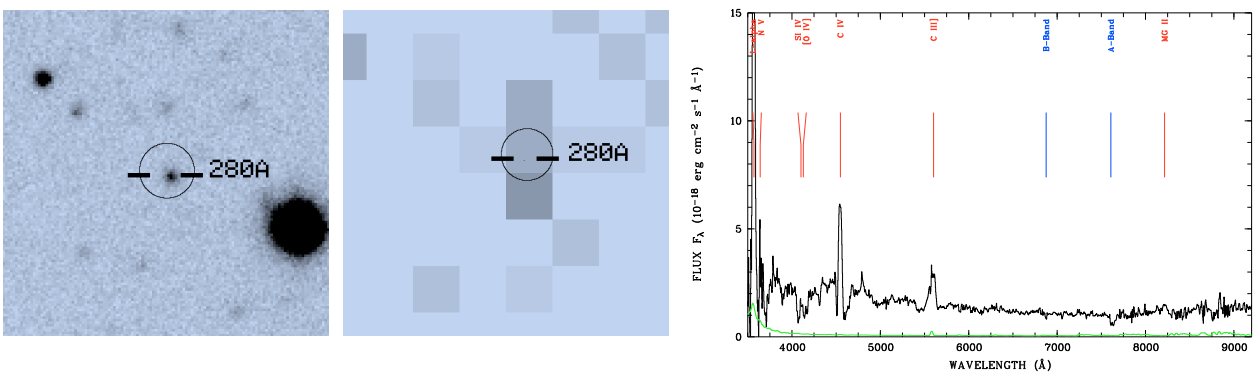
object 280A, z = 1.936
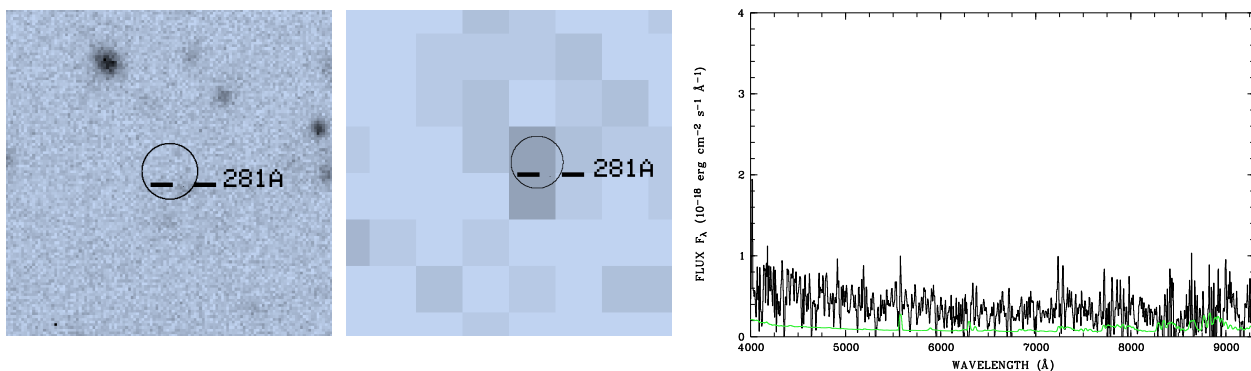
object 281A, no redshift, spectrum too noisy
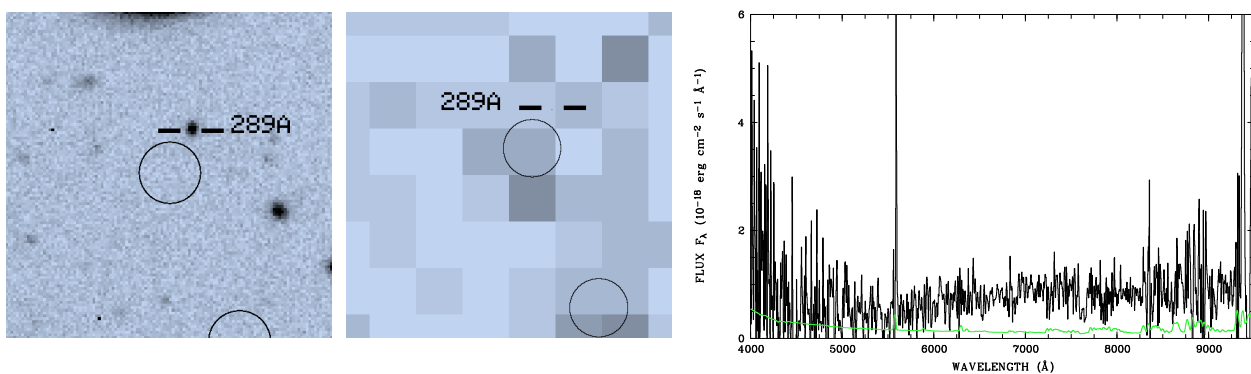
object 289A, no redshift, spectrum too noisy
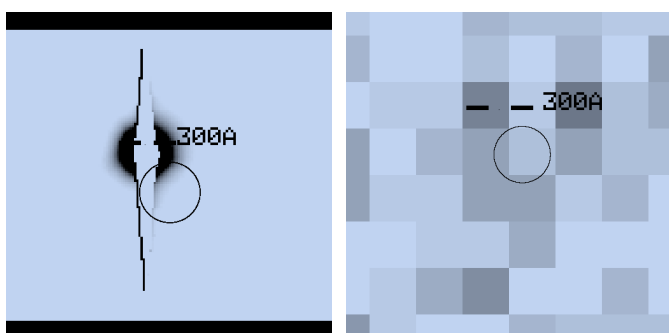
object 300A, z = 0.000
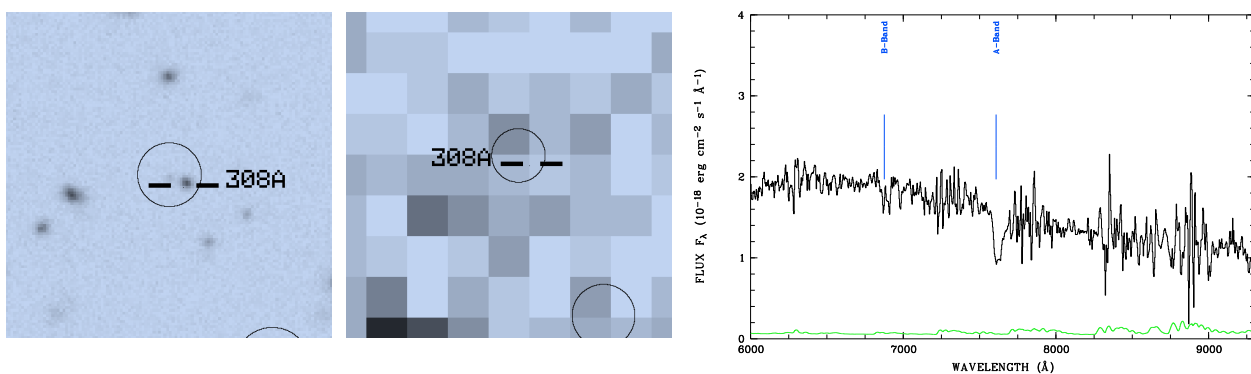
object 308A, no redshift, spectrum inconclusive
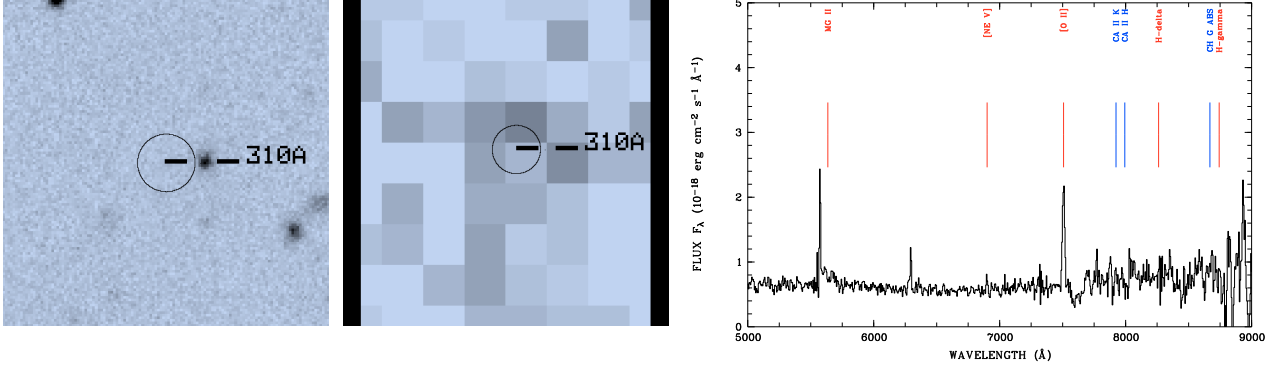
object 310A, z = 1.01
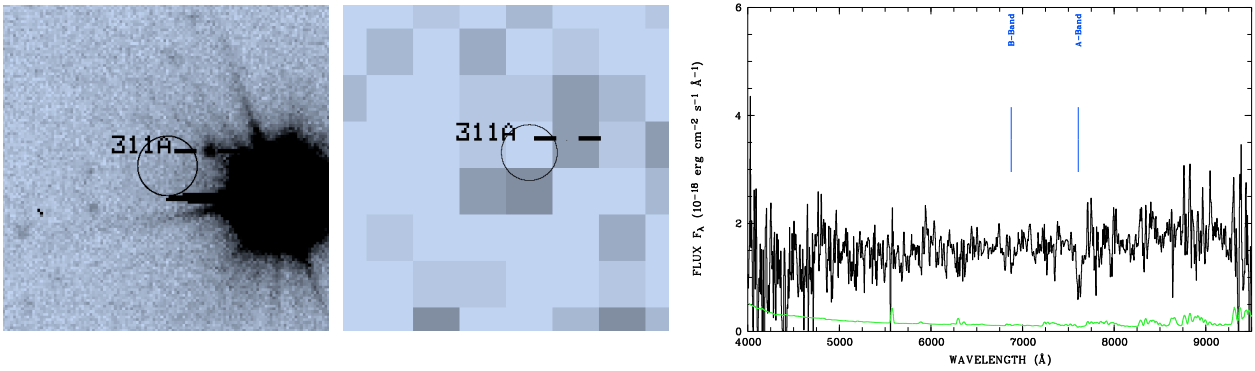
object 311A, no redshift, spectrum too noisy
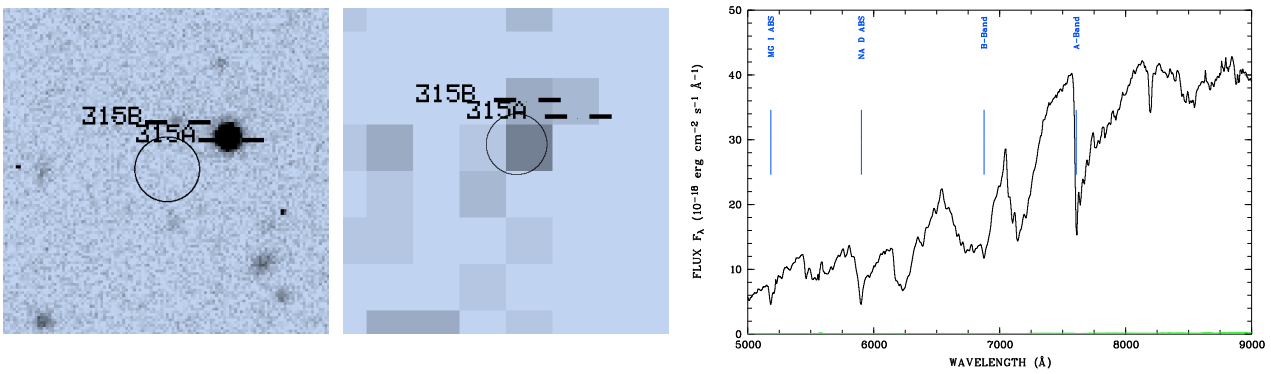
object 315A, z = 0.000
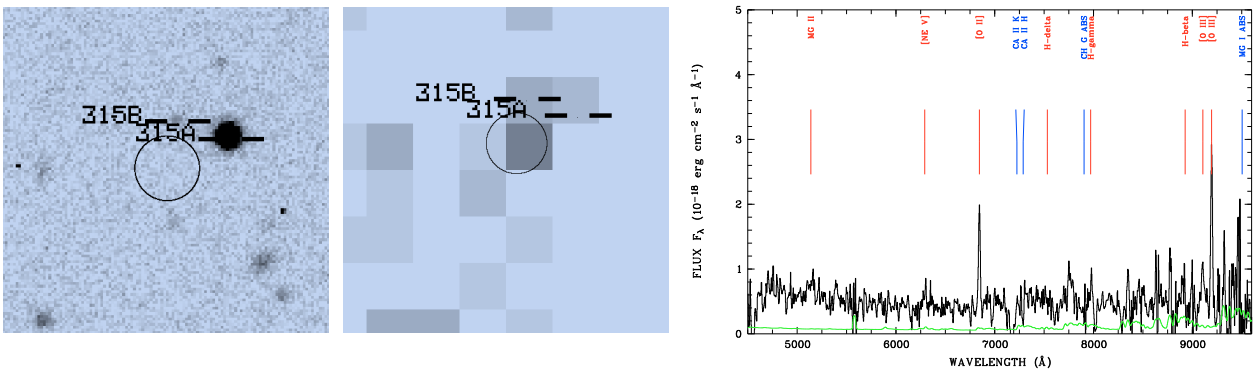
object 315B, z = 0.836
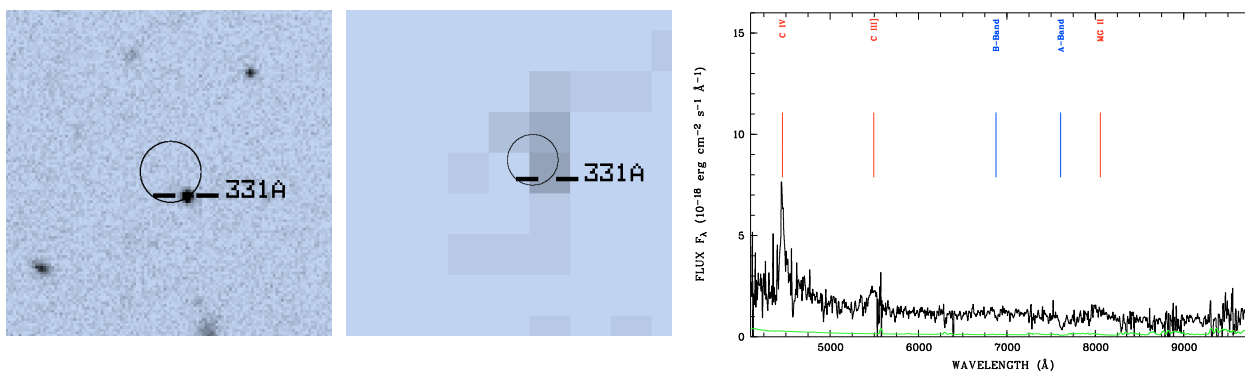
object 331A, z = 1.876
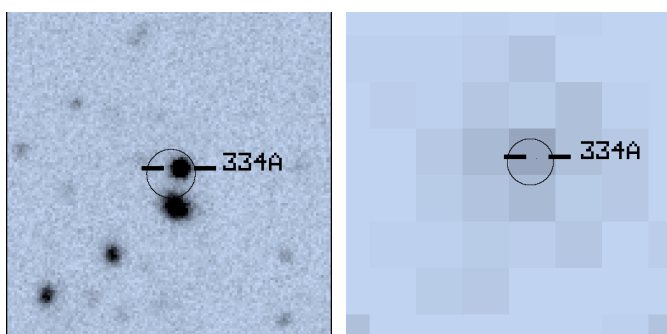
object 334A, z = 2.536
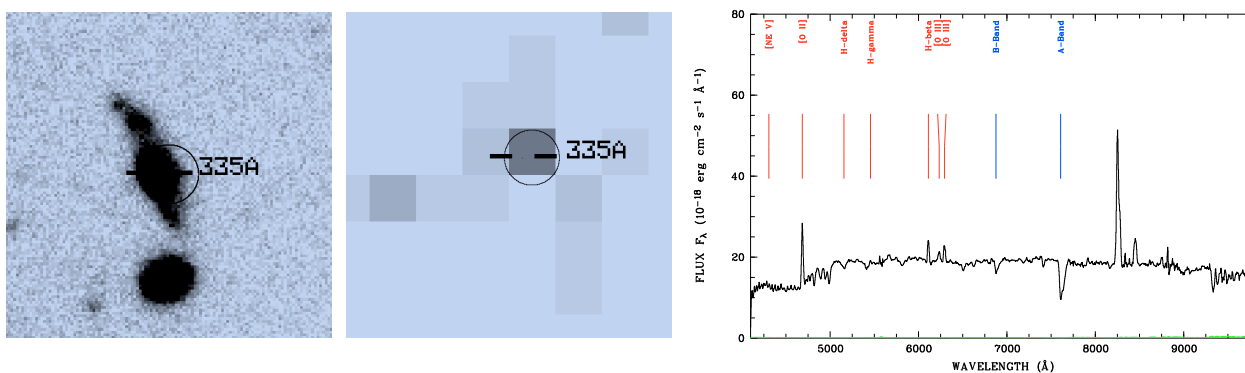
object 335A, z = 0.257
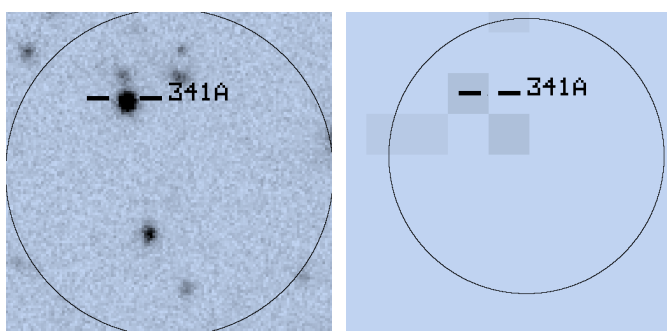
object 341A, z = 2.784
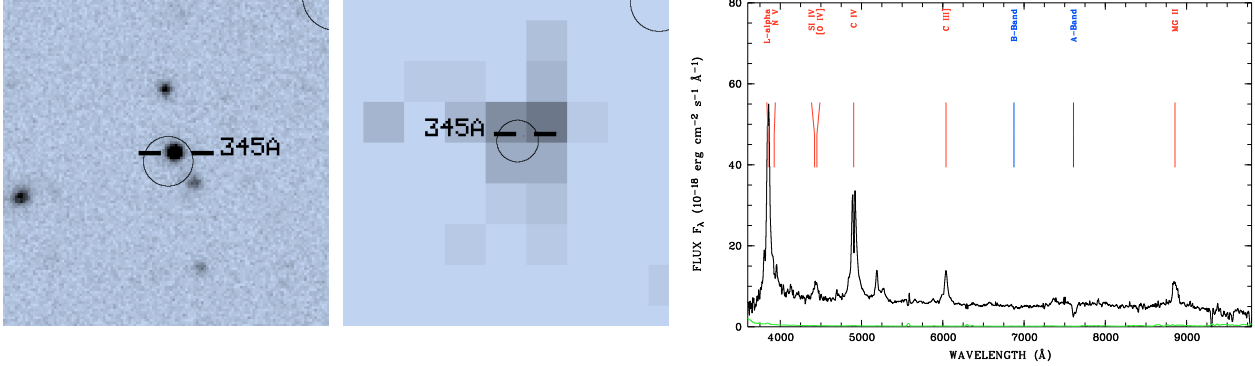
object 345A, z = 2.166
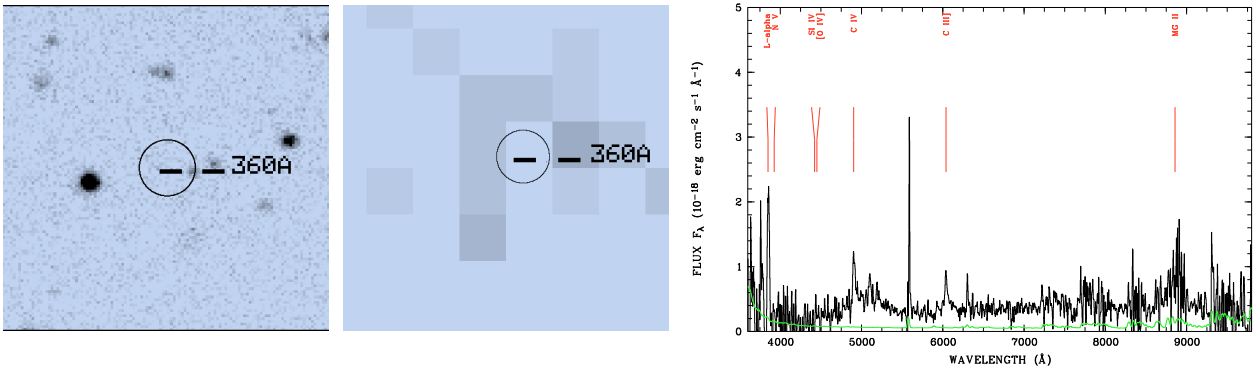
object 360A, z = 2.166
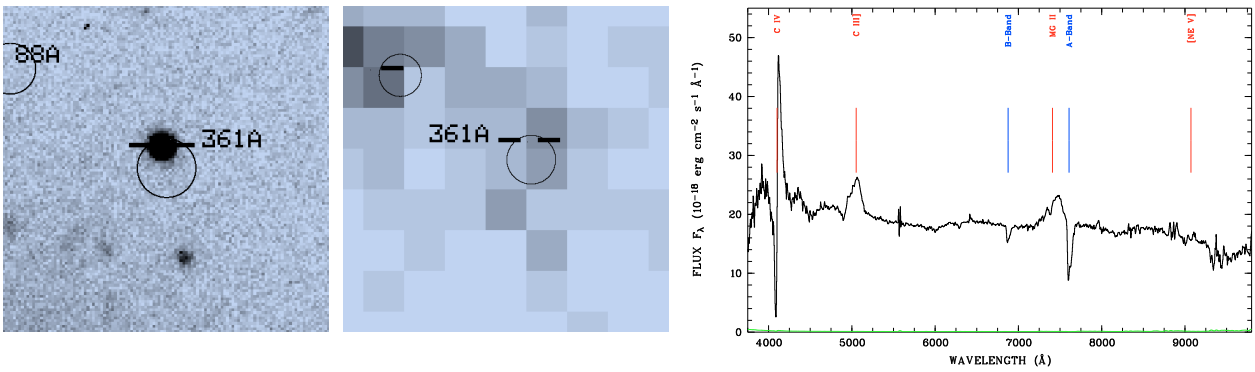
object 361A, z = 1.648
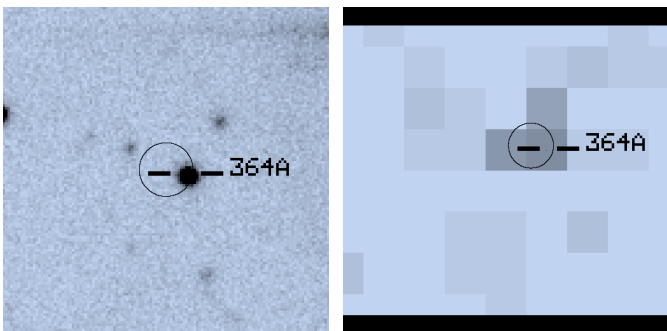
object 364A, z = 1.821
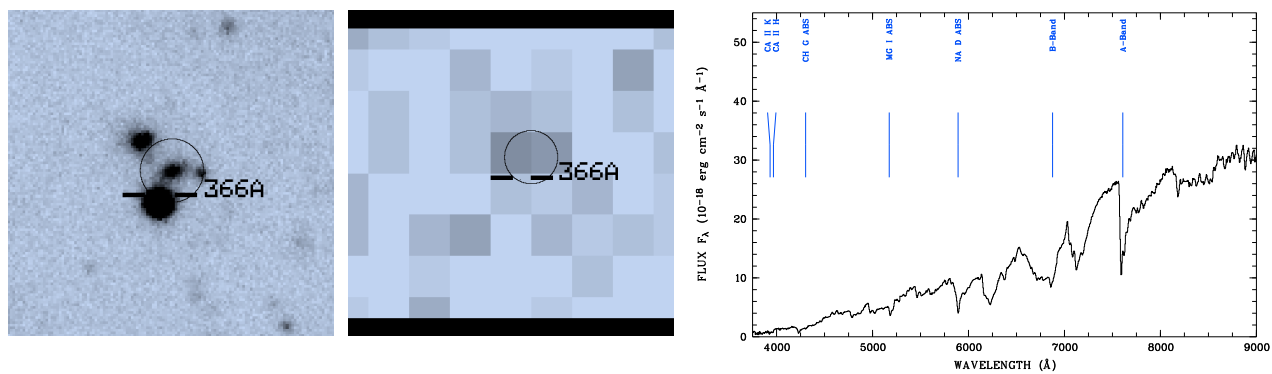
object 366A, z = 0.00
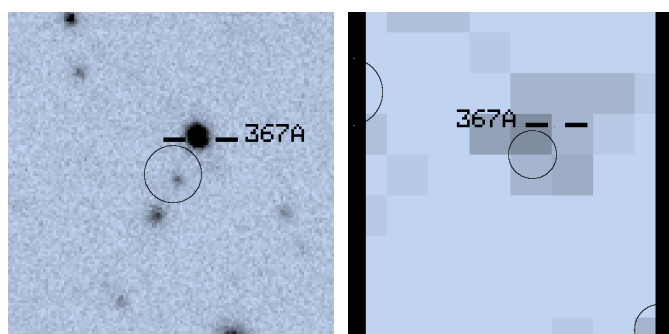
object 367A, z = 0.981
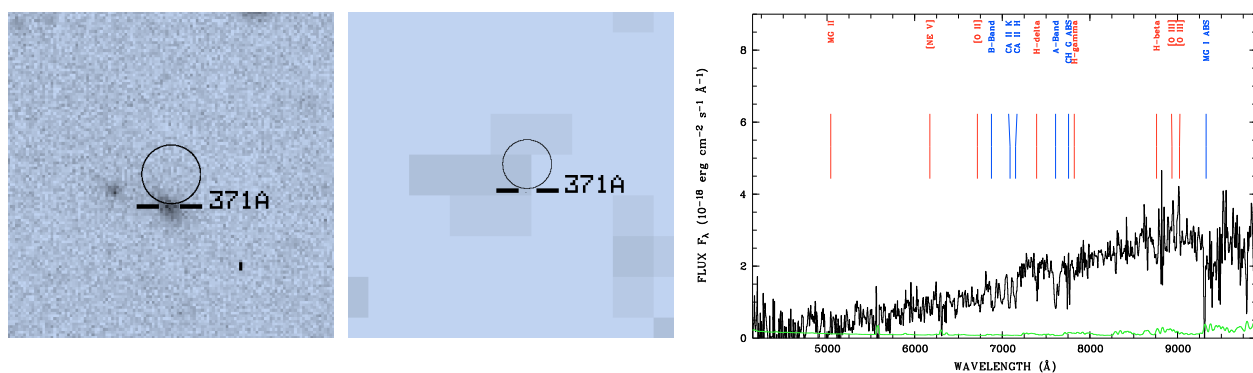
object 371A, z = 0.802
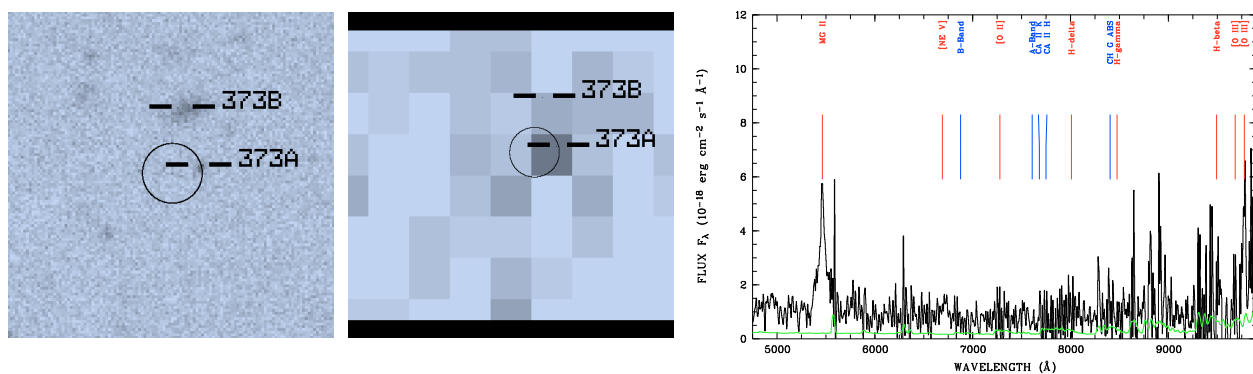
object 373A, z = 0.953:@MgII
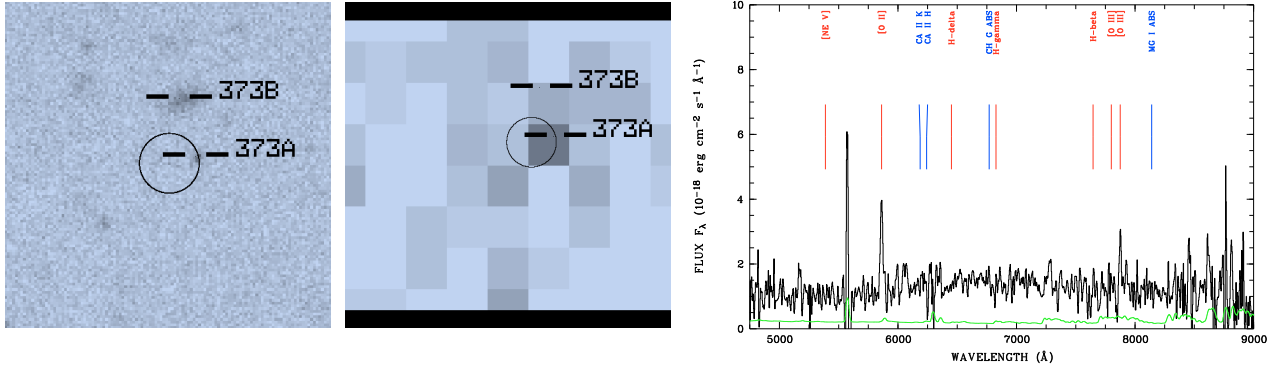
object 373B, z = 0.573
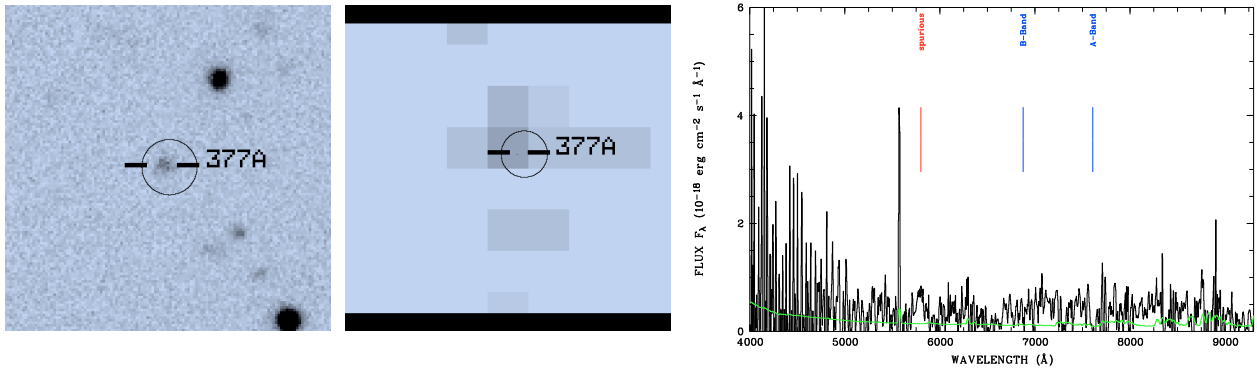
object 377A, no redshift, spectrum too noisy
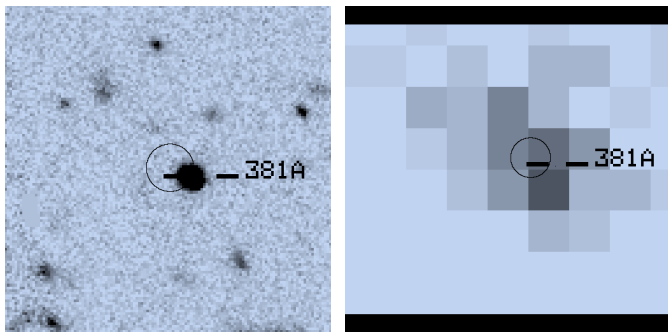
object 381A, z = 1.879
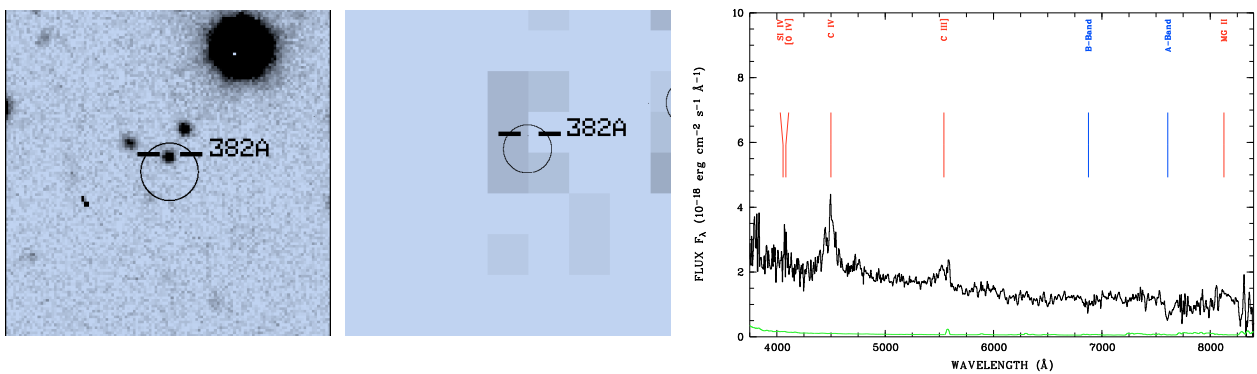
object 382A, z = 1.904
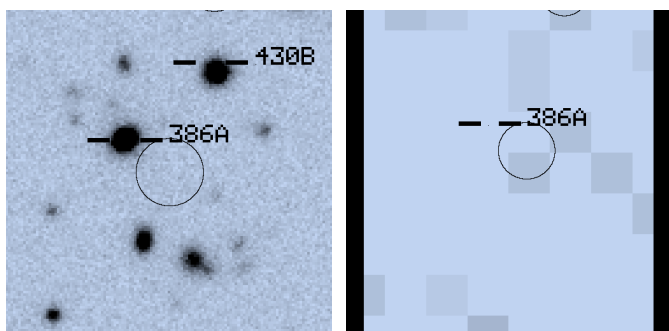
object 386A, z = 0.189
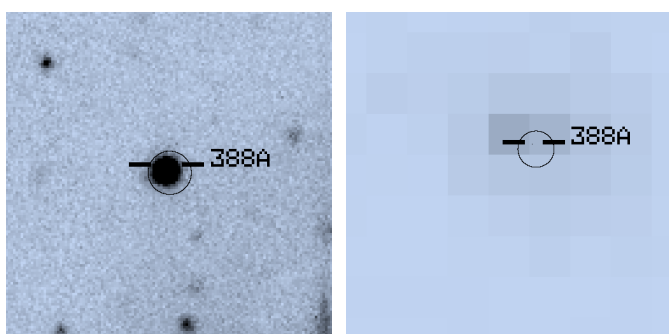
object 388A, z = 0.841
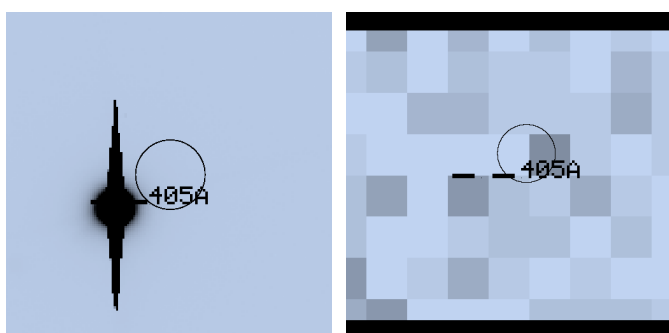
object 405A, z = 0.000
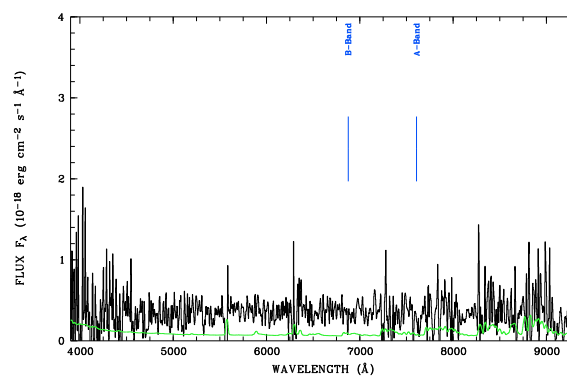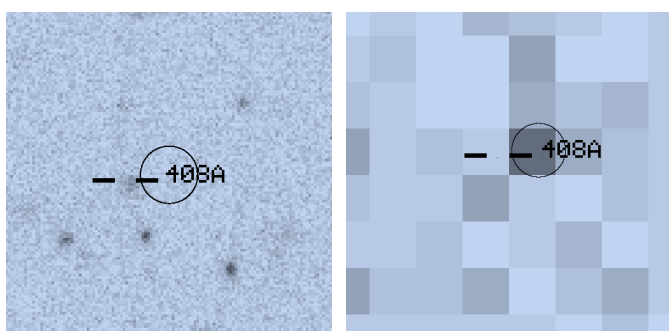
object 408A, no redshift, spectrum too noisy

object 410A, z = 0.000

object 414A, z = 2.058

object 422A, z = 0.476

object 430A, z = 0.390
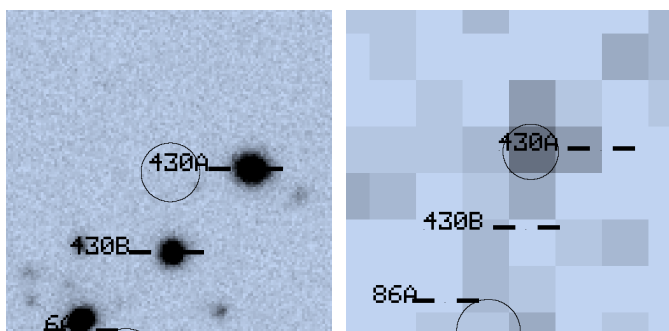
object 430B, z = 0.391
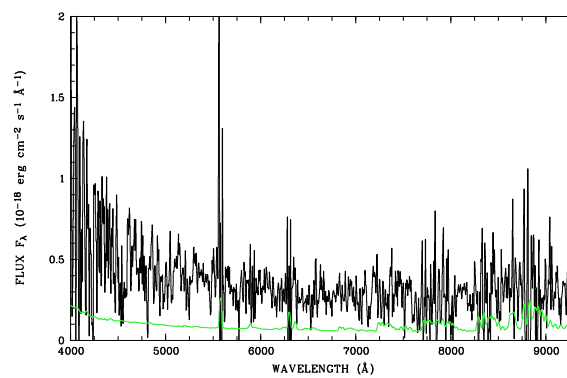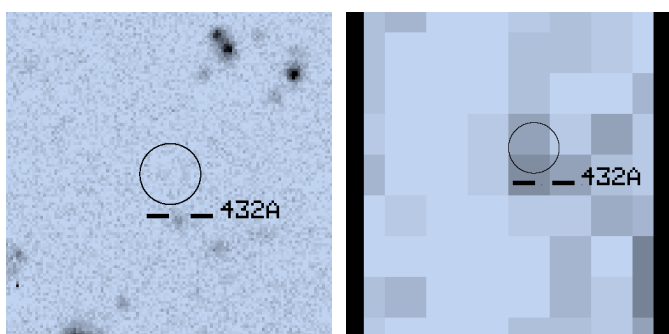
object 432A, no redshift, spectrum too noisy
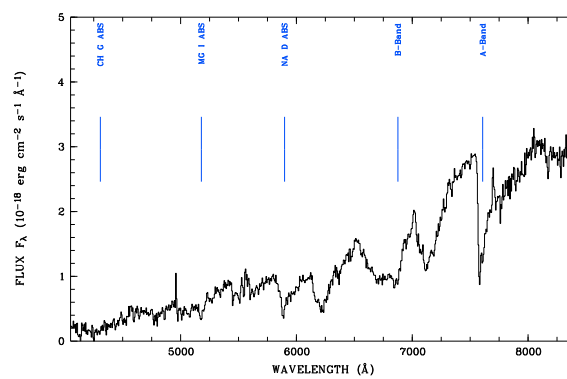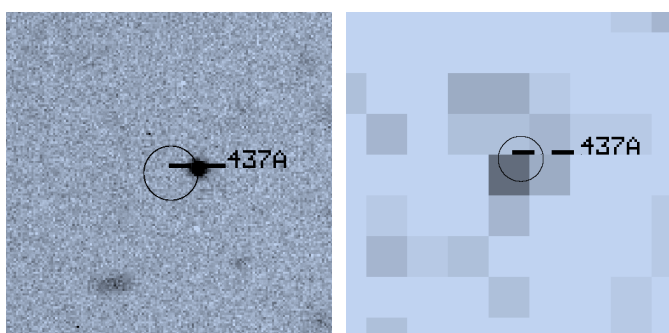
object 437A, z = 0.00
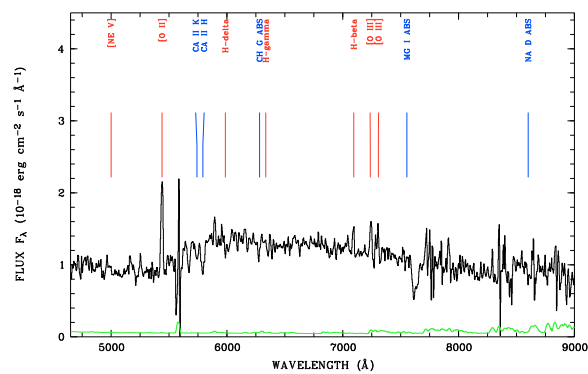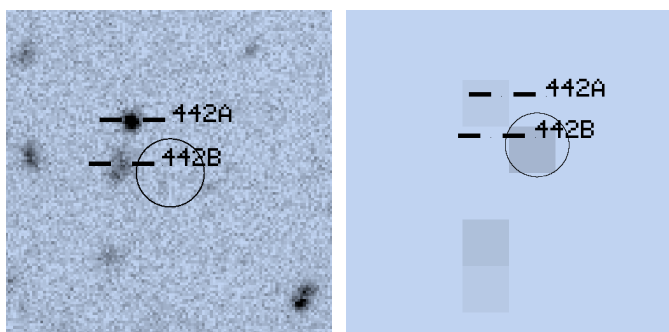
object 442A, z = 0.460
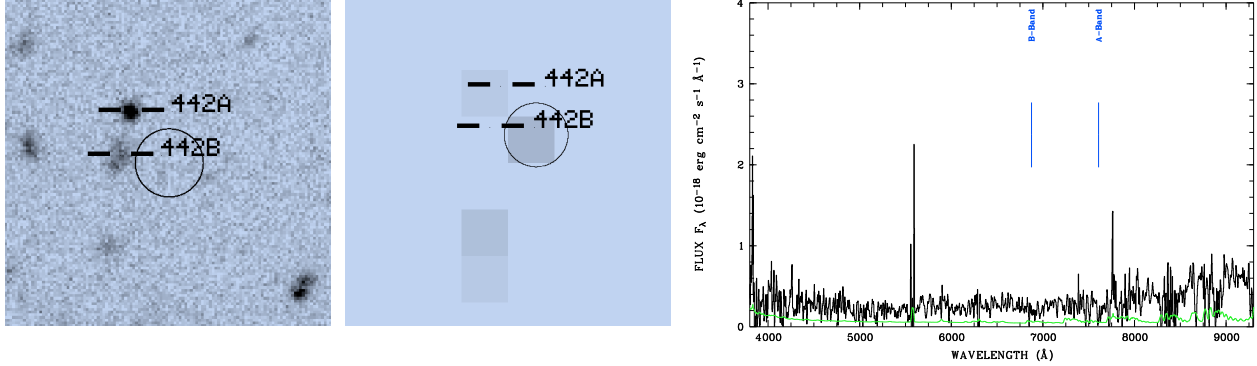
object 442B, no redshift, spectrum too noisy
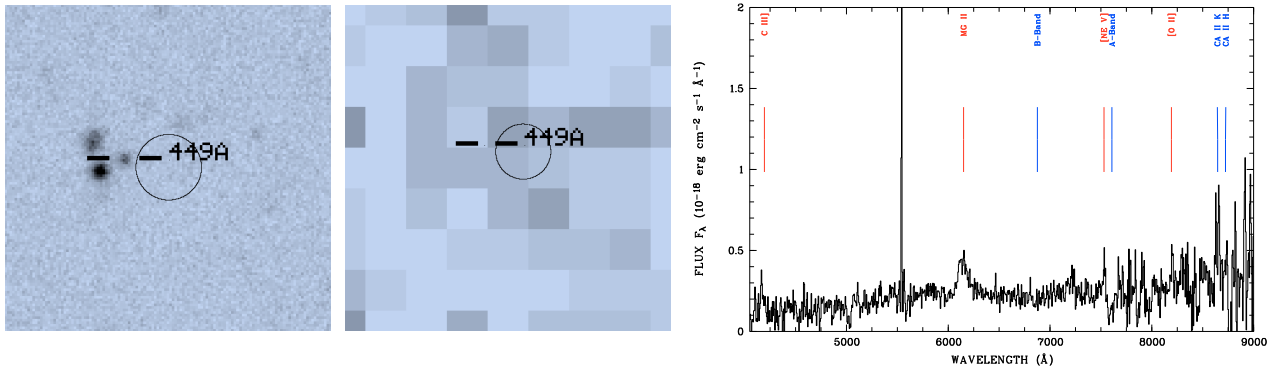
object 449A, z = 1.204
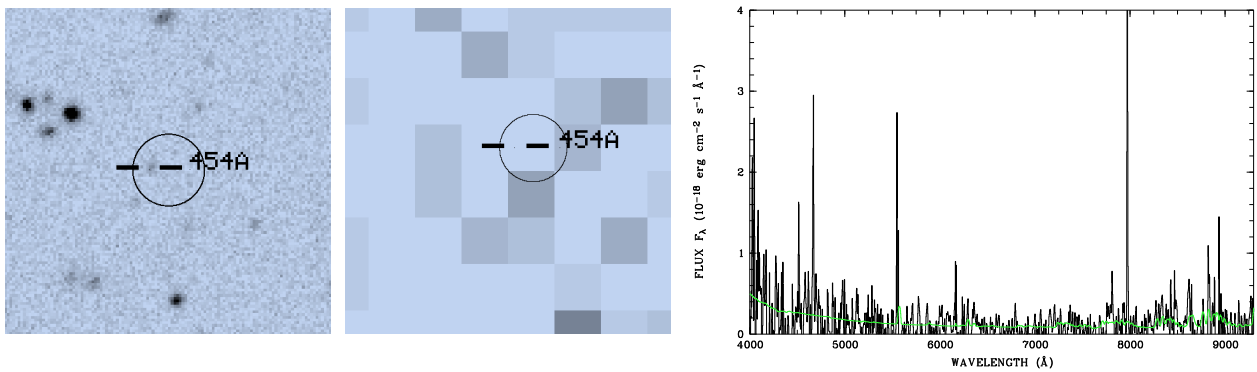
object 454A, no redshift, spectrum too noisy
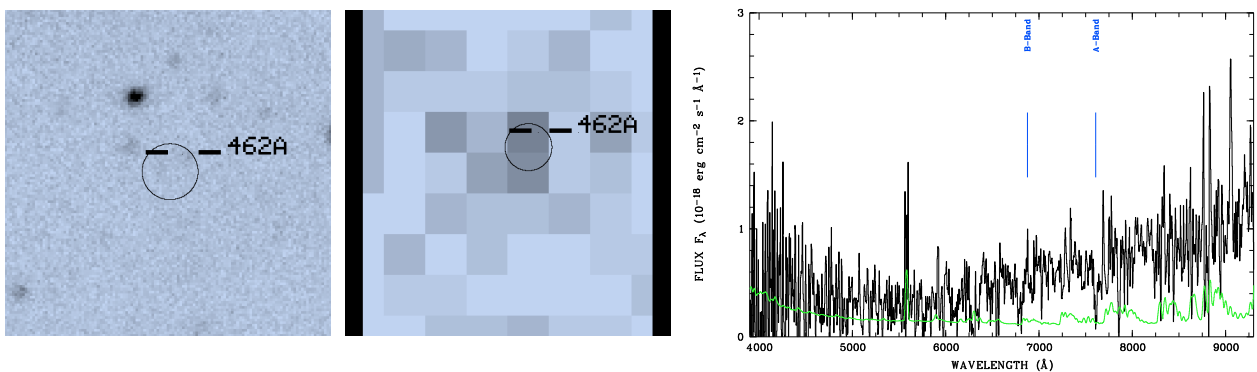
object 462A, no redshift, spectrum too noisy

object 463A, z = 2.531

object 473A, z = 0.000

object 473B, z = 0.154

object 475A, z = 1.729
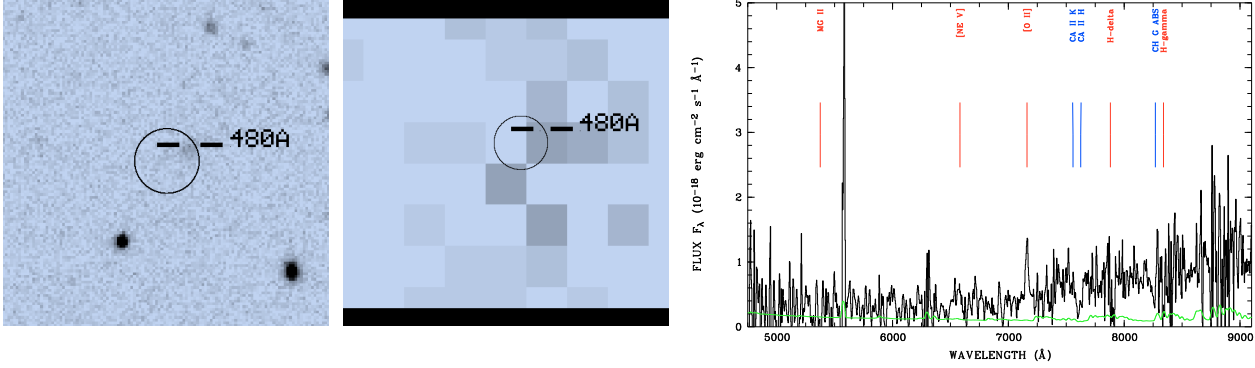
object 480A, z = 0.921:@OII
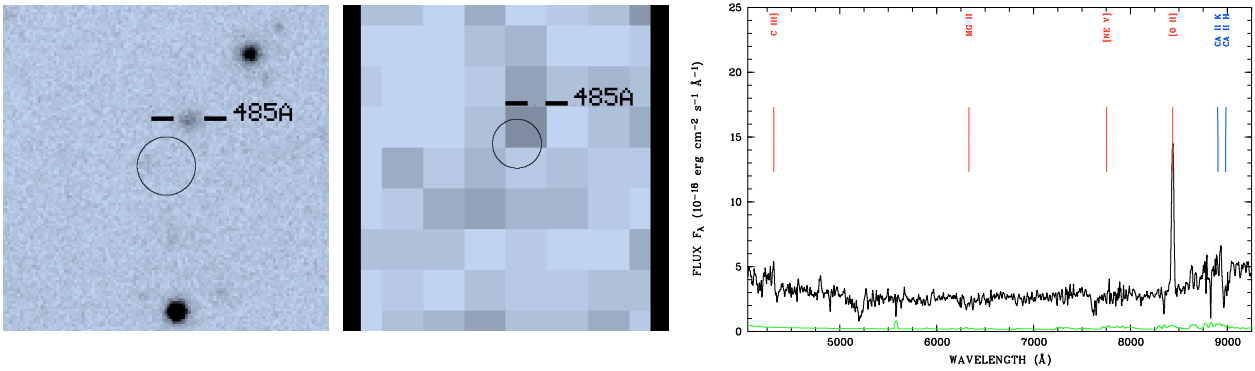
object 485A, z = 1.263:@OII
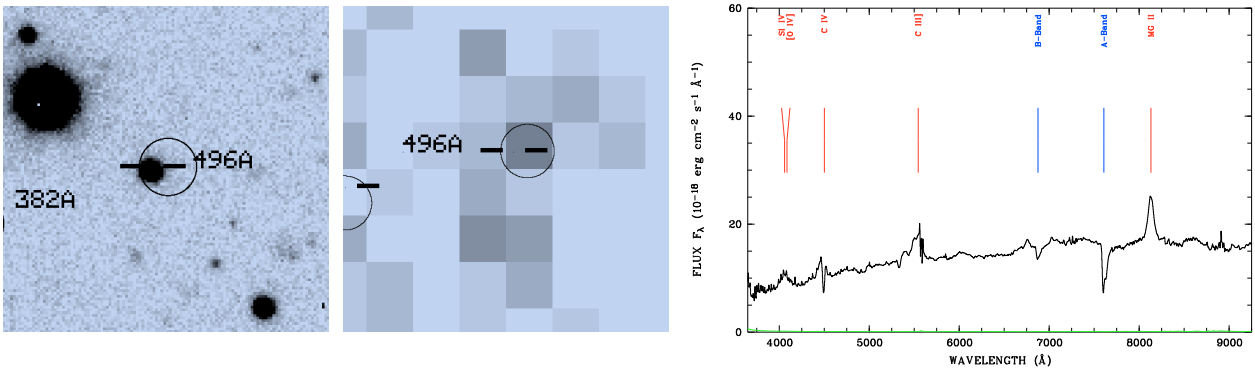
object 496A, z = 1.906
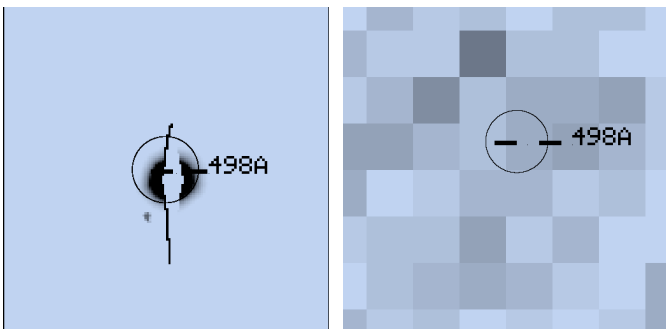
object 498A, z = 0.00
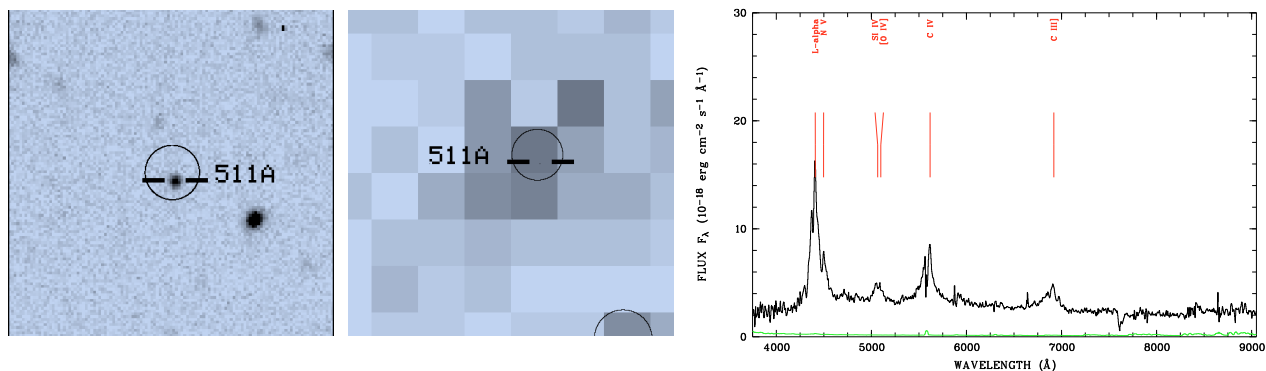
object 511A, z = 2.623
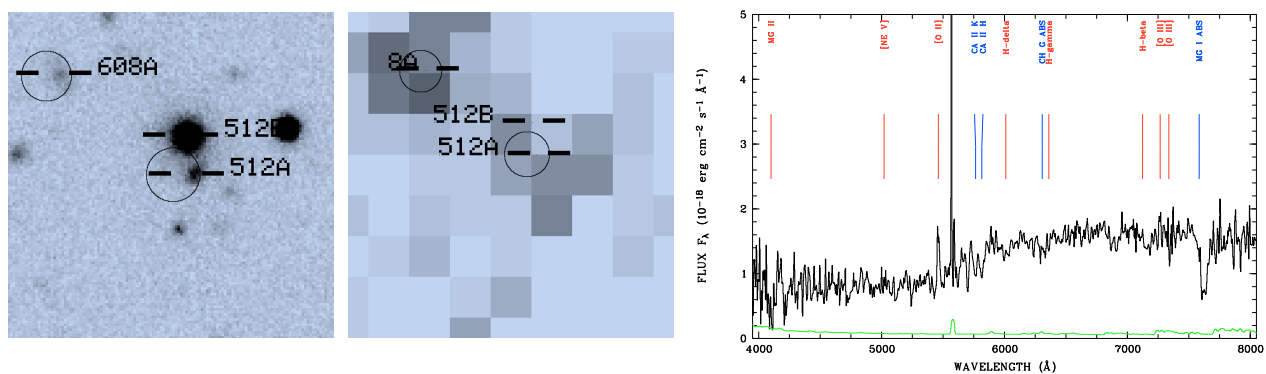
object 512A, z = 0.465
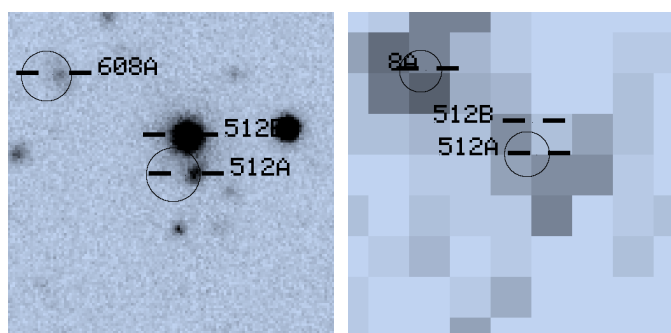
object 512B, z = 0.584
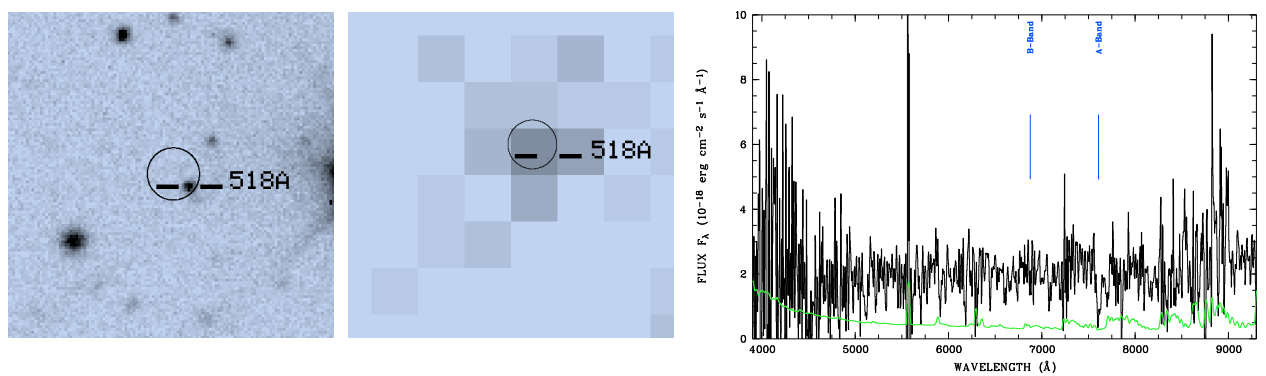
object 518A, no redshift, spectrum too noisy
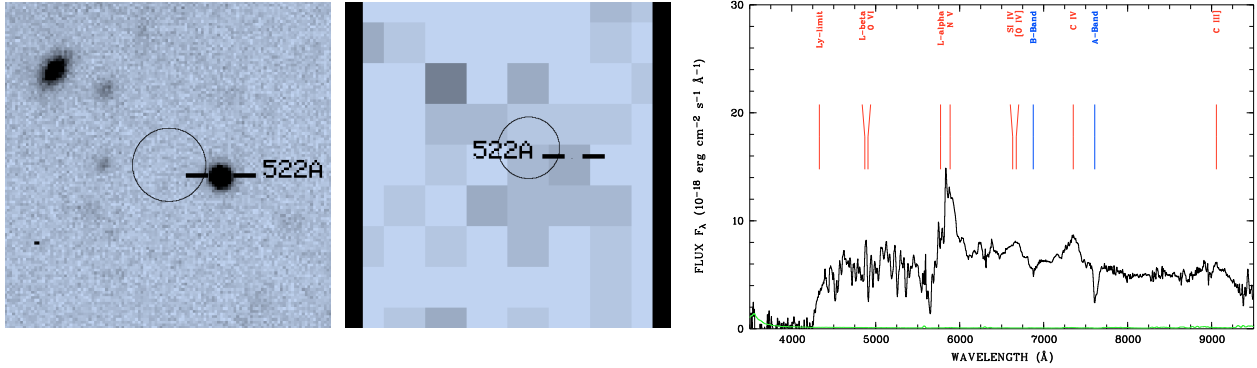
object 522A, z = 3.747
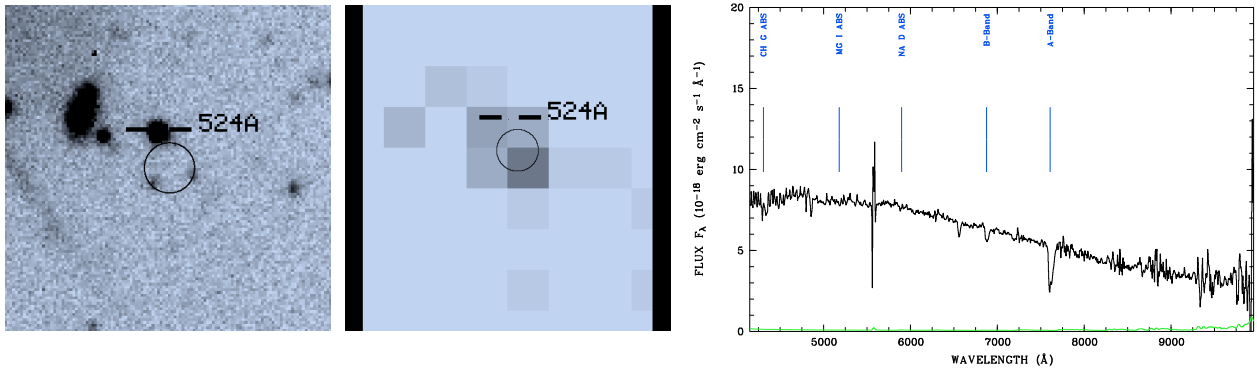
object 524A, z = 0.000
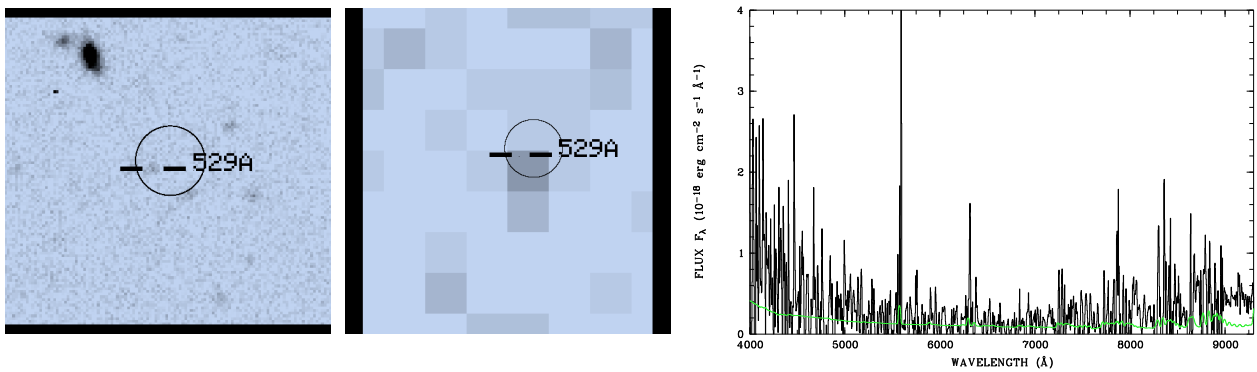
object 529A, no redshift, spectrum too noisy
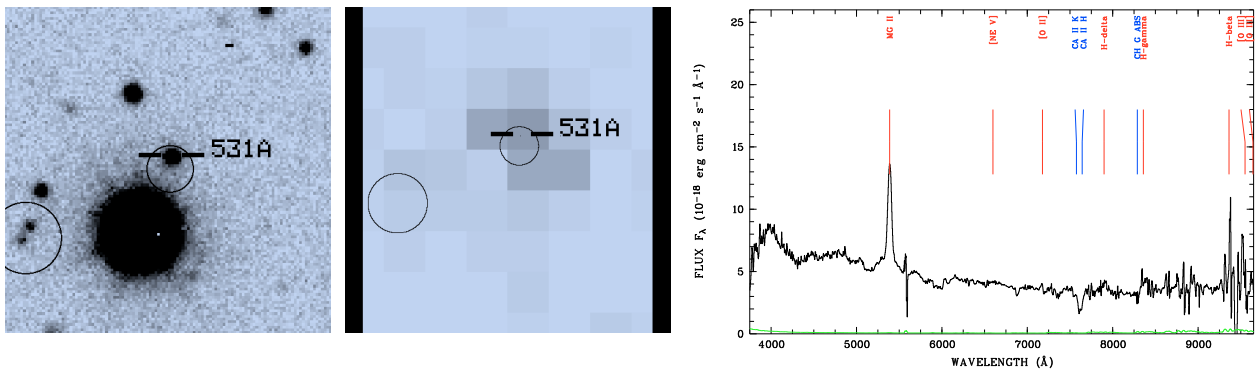
object 531A, z = 0.926
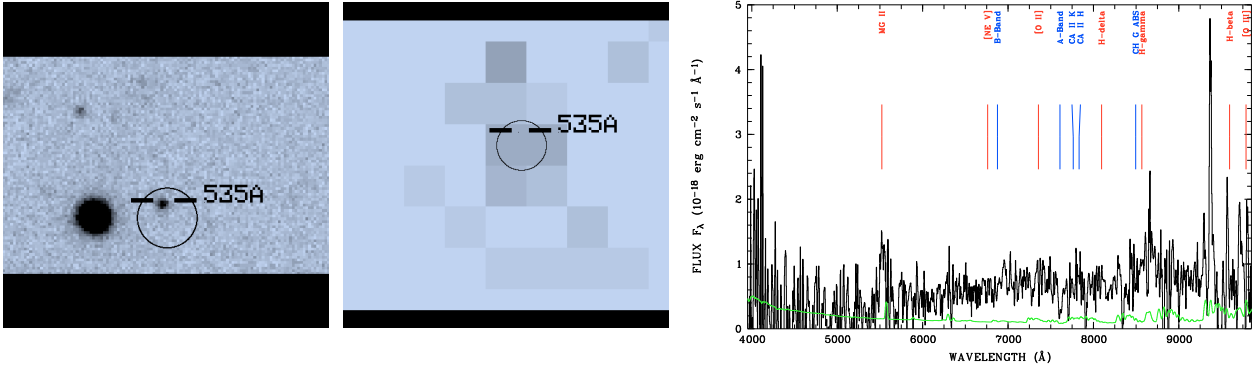
object 535A, z = 0.974:@MgII
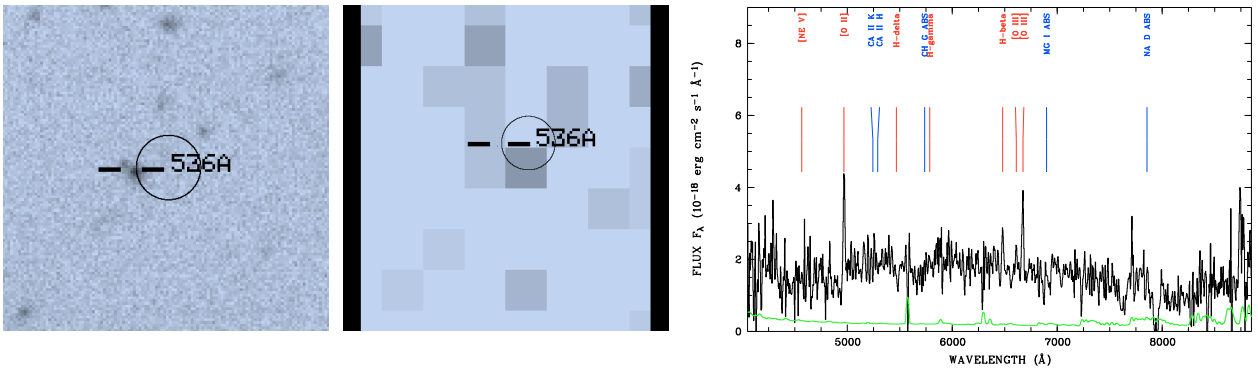
object 536A, z = 0.333
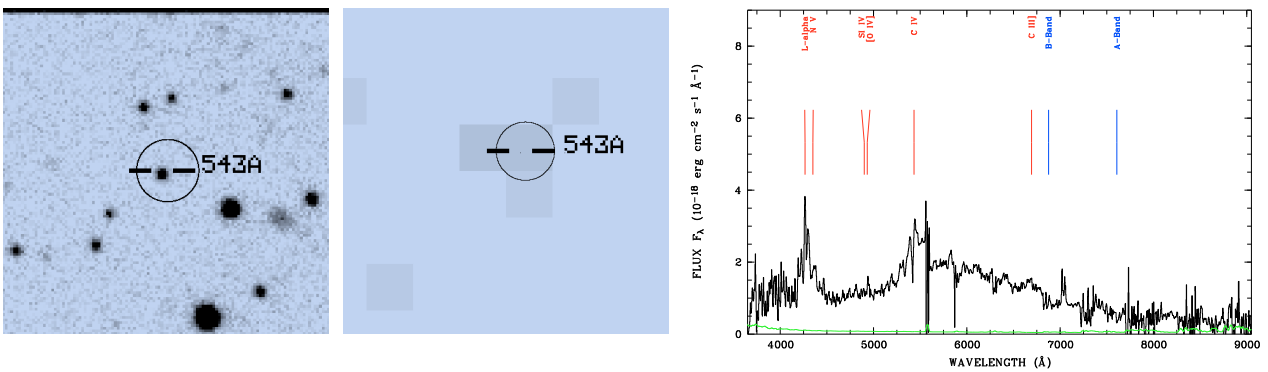
object 543A, z = 2.511
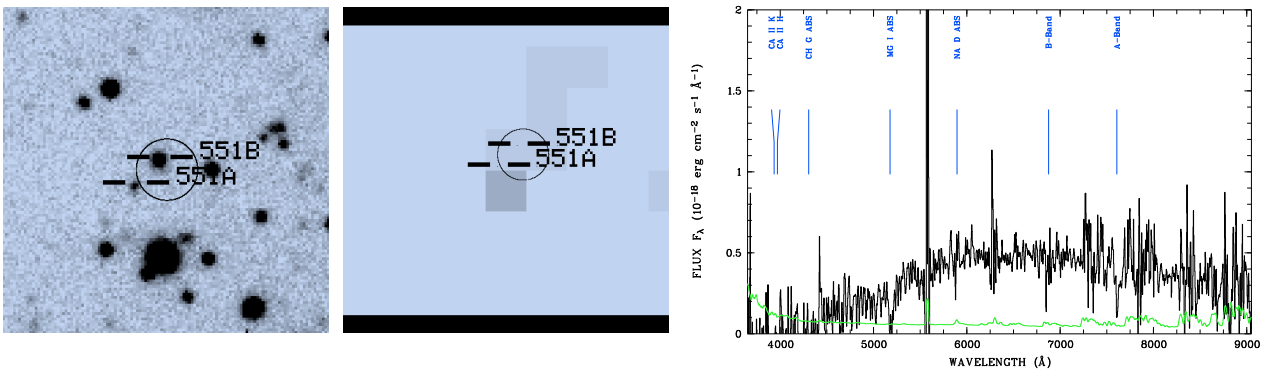
object 551A, z = 0.000

object 551B, z = 0.789

object 553A, z = 0.231

object 557A, z = 0.16

object 559A, z = 1.180
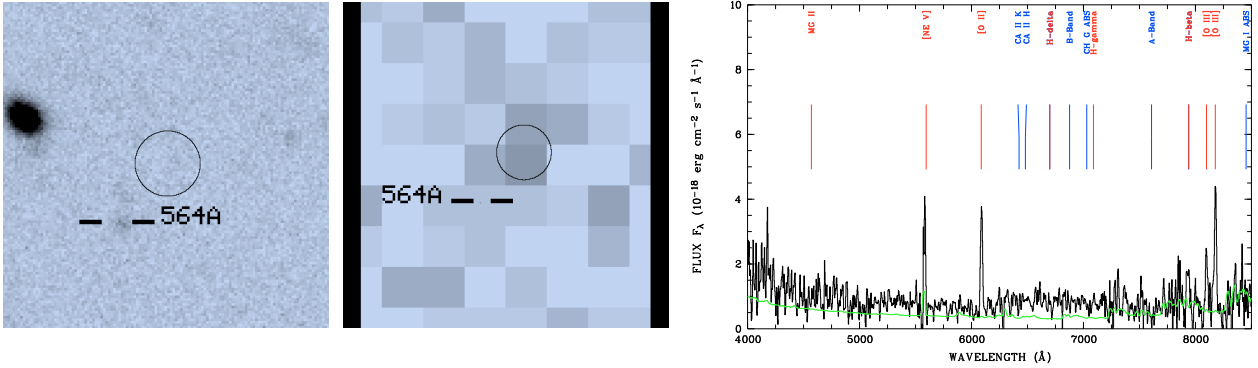
object 564A, z = 0.633
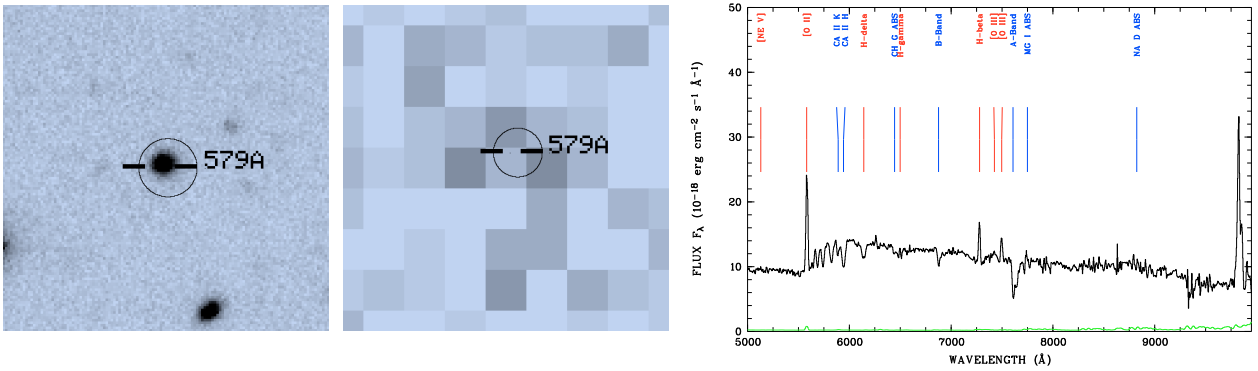
object 579A, z = 0.497
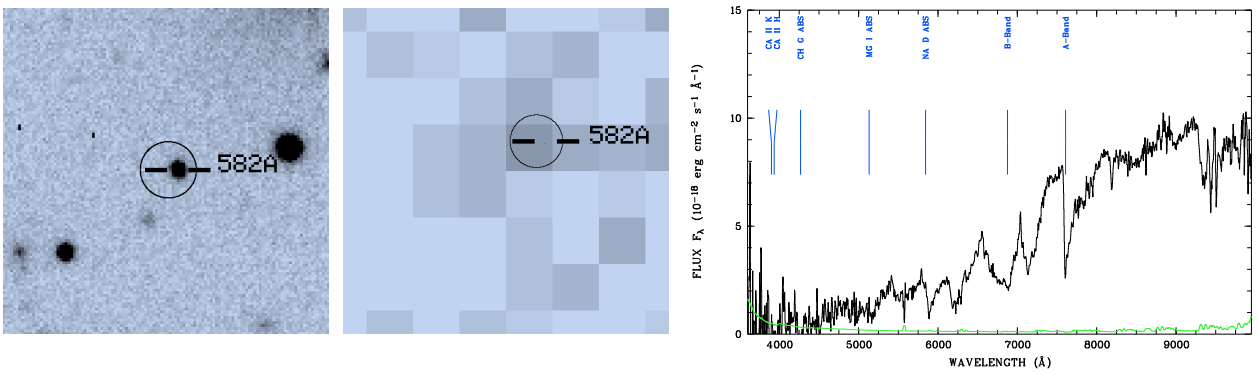
object 582A, z = 0.000
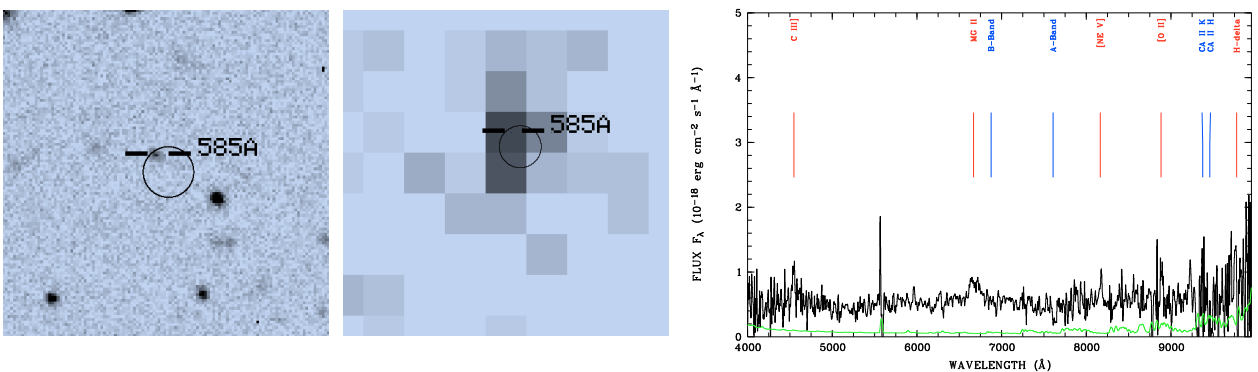
object 585A, z = 1.383

object 593A, z = 0.964

object 600A, z = 0.452

object 607A, z = 0.407

object 608A, z = 1.019:@OII & Ca-Break

object 610A, z = 0.699

object 612A, z = 0.409

object 615A, z = 1.355:@MgII

object 615B, z = 0.096

object 623A, z = 0.073
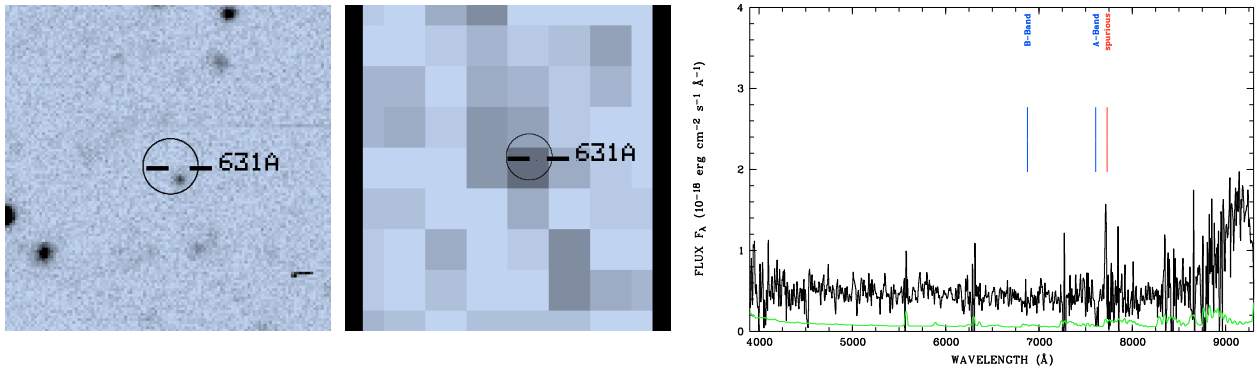
object 631A, no redshift, spectrum too noisy
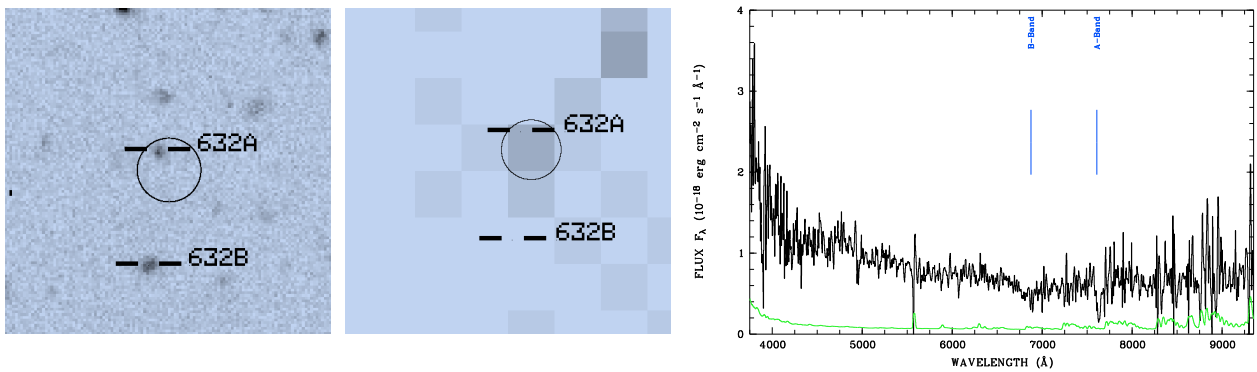
object 632A, no redshift
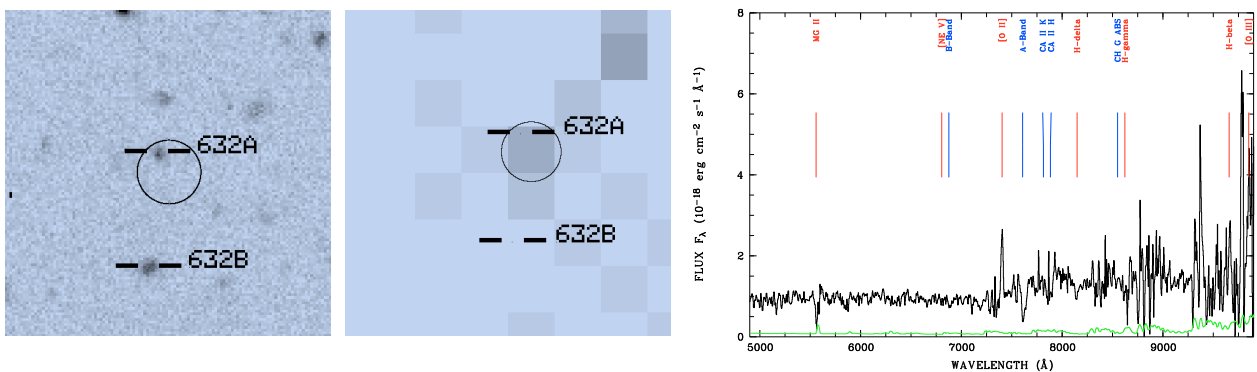
object 632B, z = 0.987

object 652A, z = 2.710

object 653A, no redshift, spectrum too noisy

object 654A, z = 2.105

object 656A, z = 0.166
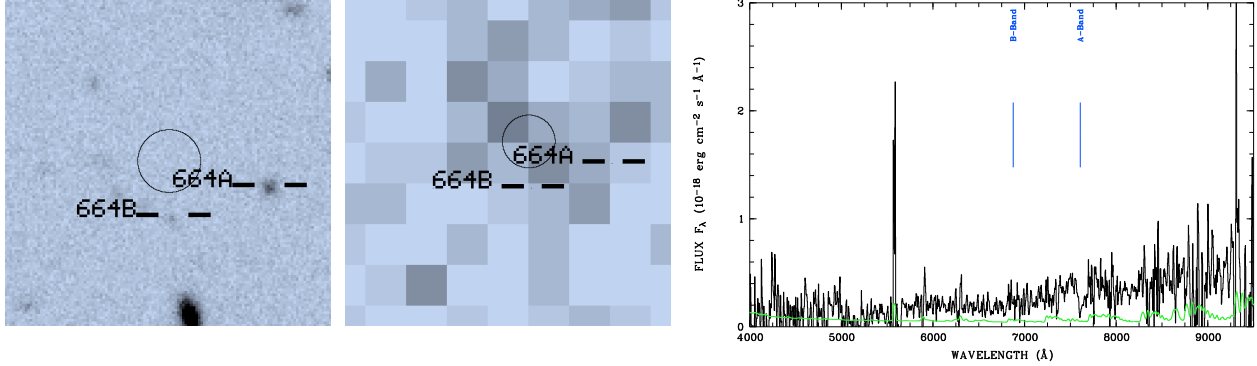
object 664A, no redshift, spectrum too noisy
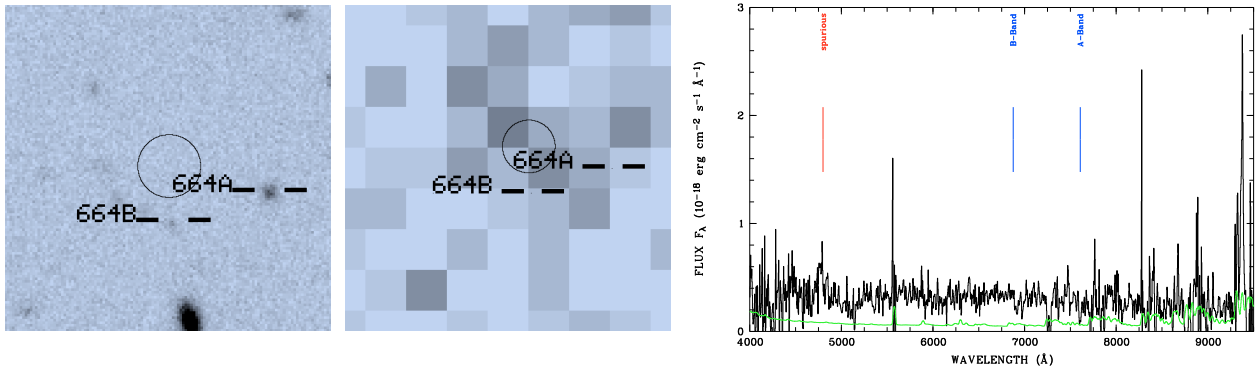
object 664B, no redshift, spectrum too noisy
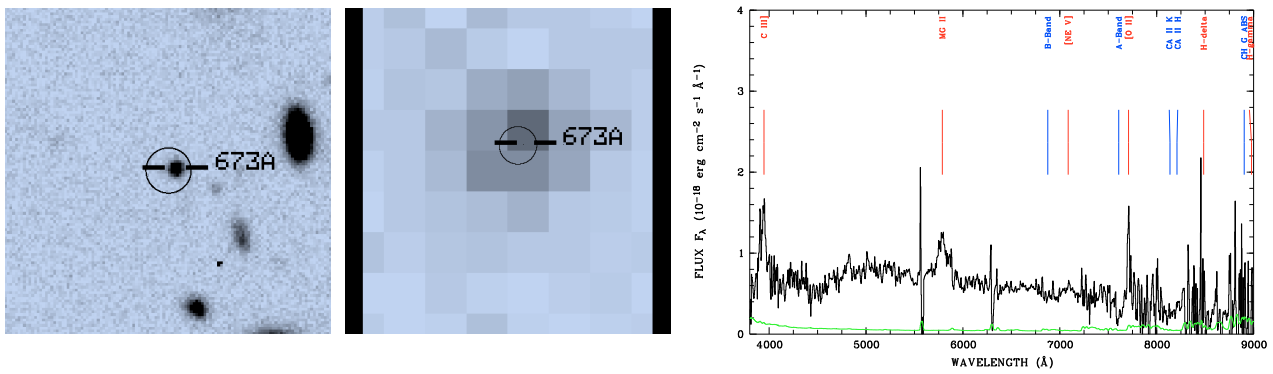
object 673A, z = 1.062
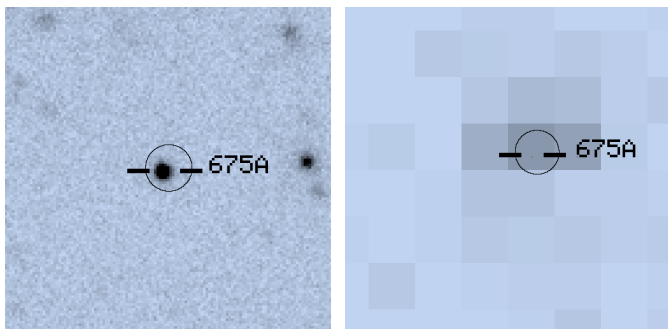
object 675A, z = 1.140
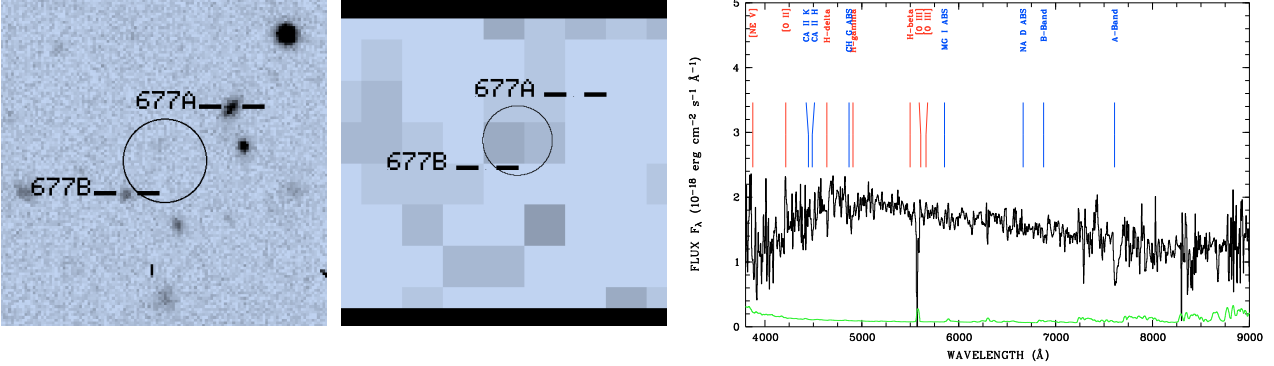
object 677A, z = 0.131
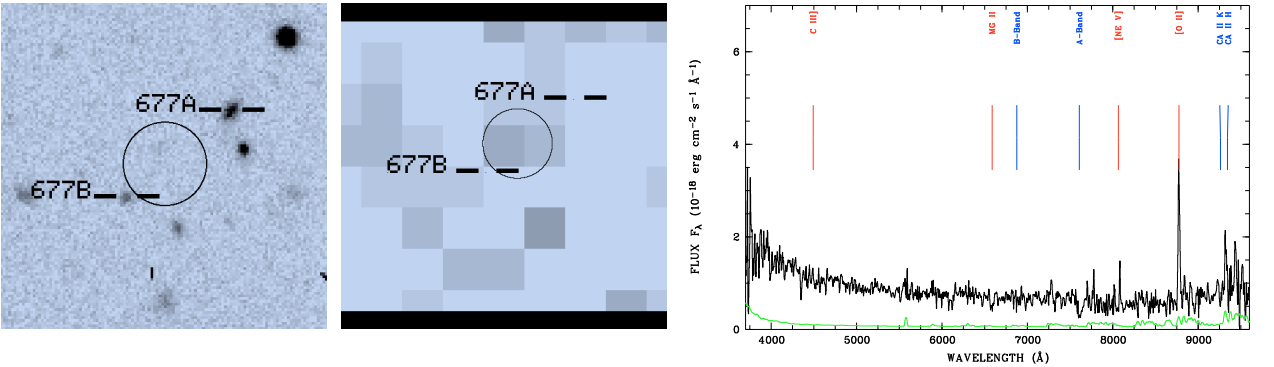
object 677B, z = 1.354:@OII
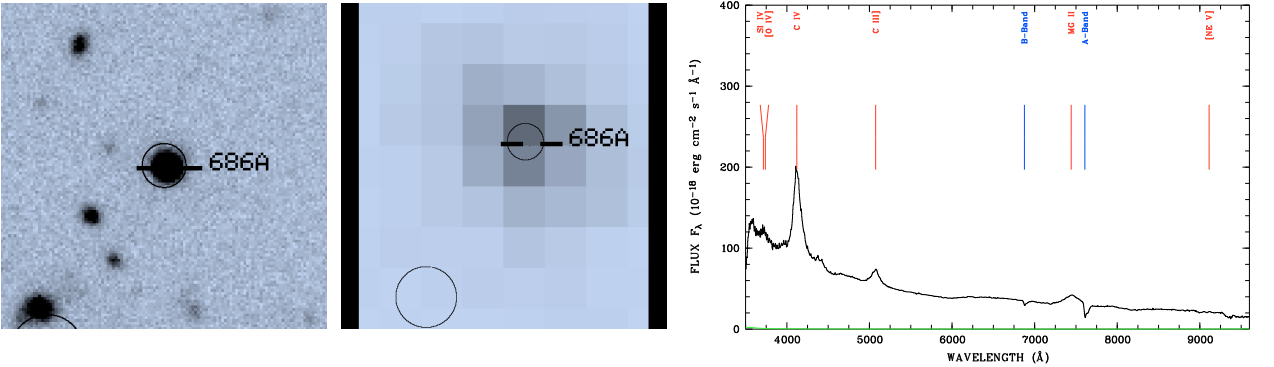
object 686A, z = 1.663
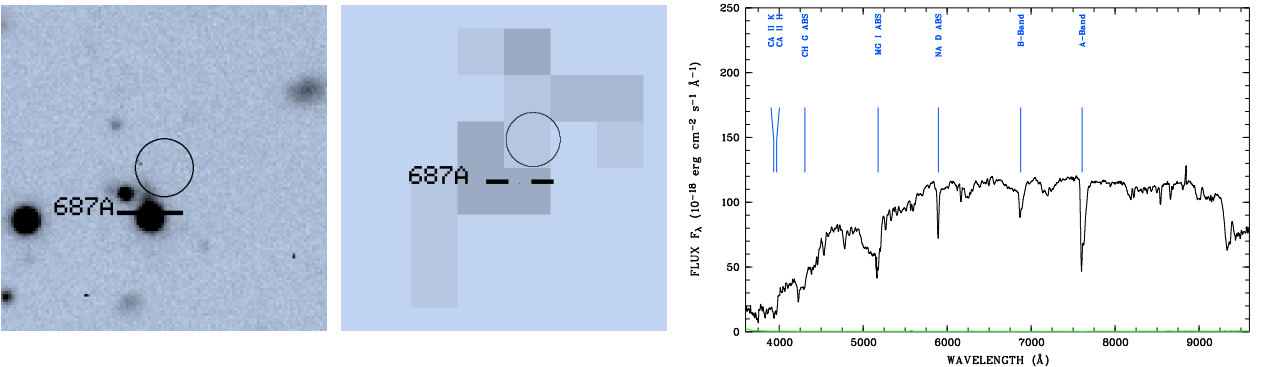
object 687A, z = 0.000

Appendix F

Table of additional optical objects in the Marano field

(1) No
Continuously arbitrary identification number of additional spectroscopically classified sources in the Marano field. These sources are labelled with the suffix '*MA*'.

(2) RA [hh:min:sec] and (3) DEC [degmin:sec]
Right ascension and declination of the spectroscopically classified object.

(4) z
Spectroscopic redshift of the classified object.

(5) K
SOFI K-band magnitude of the spectroscopically classified object, whenever possible.

(6) R
WFI R-band magnitude of the spectroscopically classified object, whenever possible.

(7) Class
Spectroscopic classification of the optical identified object. S – star, G – normal galaxy (no emission lines), and N – narrow emission line galaxy with unresolved emission lines (at 6000 Å our spectral resolution of 21 Å corresponds to 1050 km/s).

Table F.1: Optical data of additional objects in the Marano field.

| (1)	(2)	(3)	(4)	(5)	(6)	(7)
No	RA	DEC	z	K	R	Class
1MA	3 16 08.4	-55 23 06	0.486	17.51	20.41	N
2MA	3 16 19.0	-55 17 34	1.027	18.77	22.52	G
3MA	3 16 21.8	-55 17 42	0.000	–	22.64	S
4MA	3 16 26.8	-55 18 30	1.199	20.23	22.12	N
5MA	3 16 35.0	-55 18 40	1.374	–	23.89	N
6MA	3 16 39.6	-55 18 50	0.491	19.02	21.84	N
7MA	3 16 26.1	-55 08 14	0.158	19.52	20.14	N
8MA	3 16 33.8	-55 12 50	0.486	20.08	22.01	N
9MA	3 16 07.9	-55 05 07	0.786	18.70	21.36	N
10MA	3 16 27.2	-55 04 23	0.235	18.56	18.47	N
11MA	3 16 16.2	-55 02 38	0.420	–	21.28	N
12MA	3 16 23.8	-55 08 56	0.000	17.57	22.10	S
14MA	3 16 26.5	-55 07 35	1.070	18.83	21.94	N
15MA	3 16 24.6	-55 07 25	0.972	17.99	21.02	N
16MA	3 13 31.0	-55 13 56	0.000	–	21.87	S
17MA	3 13 36.7	-55 14 46	0.579	18.09	21.96	B
18MA	3 13 42.3	-55 14 31	0.583	17.61	21.24	N
19MA	3 13 44.3	-55 14 34	0.583	17.68	21.30	N
20MA	3 13 48.8	-55 14 10	0.000	18.95	20.07	S
21MA	3 13 50.4	-55 13 20	0.552	18.26	22.40	N
22MA	3 13 52.8	-55 13 37	0.000	19.82	22.29	S
23MA	3 13 06.8	-55 13 04	0.254	–	20.09	G
24MA	3 13 11.4	-55 11 39	0.000	–	23.10	S
25MA	3 13 18.2	-55 13 04	0.865	–	–	N
26MA	3 13 19.0	-55 11 37	0.000	–	20.81	S
27MA	3 13 24.5	-55 03 11	0.000	18.19	22.54	S
28MA	3 13 28.3	-55 01 38	0.800	19.46	22.14	N
30MA	3 15 14.6	-55 10 33	0.000	–	22.79	S
31MA	3 15 45.7	-55 12 49	0.628	17.12	21.31	G
32MA	3 15 43.7	-55 08 57	0.771	19.42	23.17	G
33MA	3 14 14.4	-55 19 38	0.000	–	23.08	S
34MA	3 14 15.2	-55 21 43	0.813	18.16	22.62	N
35MA	3 14 11.5	-55 21 18	0.869	18.36	22.43	N
36MA	3 14 08.5	-55 20 24	0.000	18.77	22.64	S
37MA	3 13 11.5	-55 21 13	0.907	–	22.25	N
38MA	3 13 14.2	-55 26 32	0.554	–	21.98	N
39MA	3 13 00.8	-55 25 56	0.818	–	21.03	N
40MA	3 13 01.8	-55 25 45	0.816	–	20.85	N
41MA	3 13 05.5	-55 25 28	0.552	–	21.11	N
42MA	3 13 30.3	-55 24 42	0.613	–	22.89	N
43MA	3 13 31.1	-55 24 29	0.000	–	–	S
44MA	3 13 33.3	-55 24 15	0.526	–	21.51	N
45MA	3 14 41.4	-55 04 34	0.704	–	22.15	N
46MA	3 14 48.1	-55 03 04	0.702	16.86	20.67	N
47MA	3 14 52.7	-55 05 49	0.460	16.40	19.32	G
48MA	3 14 52.8	-55 24 39	0.228	–	18.27	G
49MA	3 14 49.0	-55 24 24	0.159	–	17.43	G
50MA	3 15 24.2	-55 14 04	0.774	–	22.16	N
51MA	3 15 32.4	-55 14 19	0.700	–	20.32	N
52MA	3 15 40.1	-55 12 34	0.631	19.22	21.66	N
53MA	3 15 44.6	-55 14 18	0.275	18.94	21.27	N
54MA	3 15 46.3	-55 13 55	0.815	19.17	22.89	N
55MA	3 15 48.6	-55 13 57	0.475	19.91	22.48	N
56MA	3 15 14.0	-55 17 10	0.813	–	20.99	N
57MA	3 15 16.9	-55 17 07	0.000	–	22.09	S
58MA	3 15 20.7	-55 14 17	0.500	–	19.87	N
59MA	3 15 21.8	-55 14 11	0.495	–	22.97	G
60MA	3 15 16.9	-55 06 13	0.840	18.38	21.81	N
61MA	3 16 08.3	-55 23 17	0.071	15.23	17.50	N
62MA	3 15 03.4	-55 16 37	0.000	15.55	17.35	S

Appendix G

Optical charts and spectra of additional optical classifications in the Marano field

For explanation see Appendix E. The only difference is the centring to the optical position, since no X-ray detection is quantified.
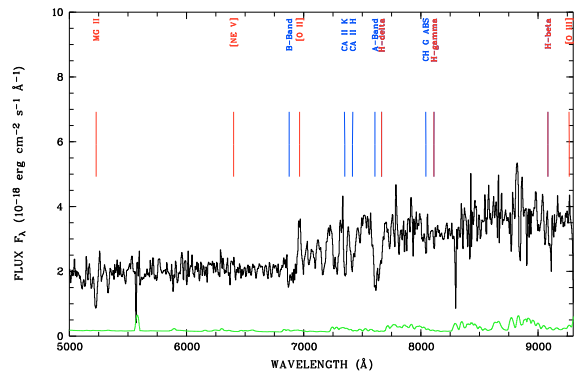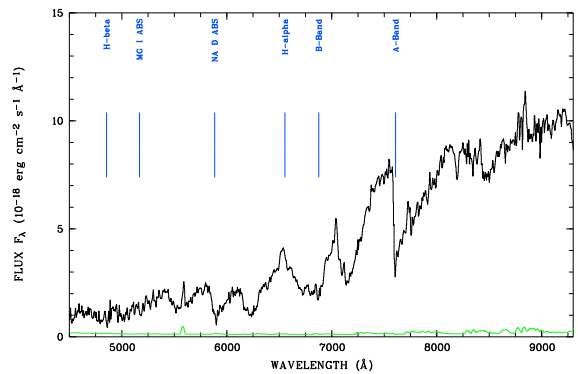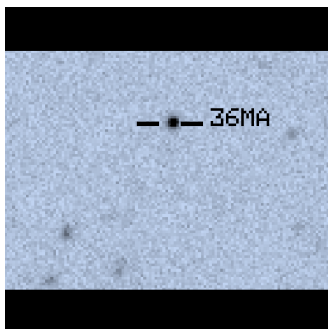

object 1MA, z = 0.486

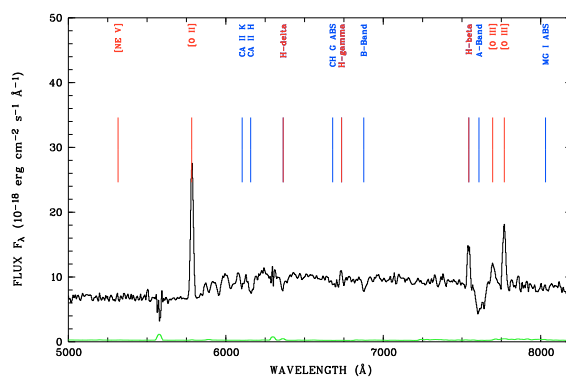object 2MA, z = 1.027
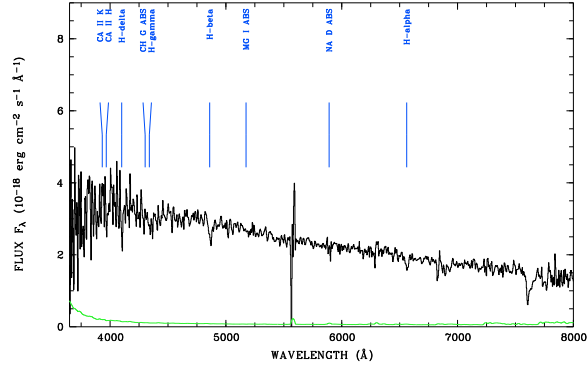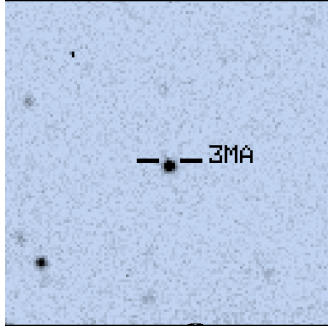
object 3MA, z = 0.000
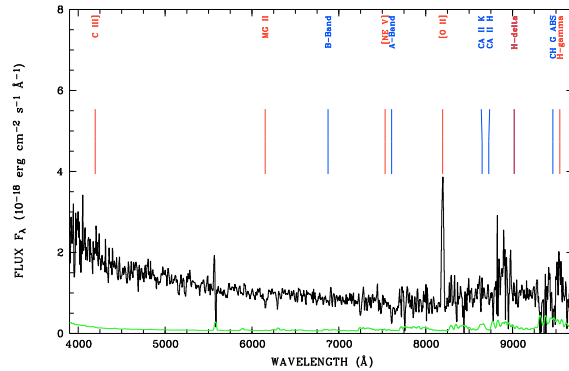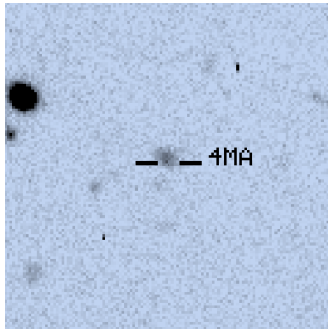
object 4MA, z = 1.199
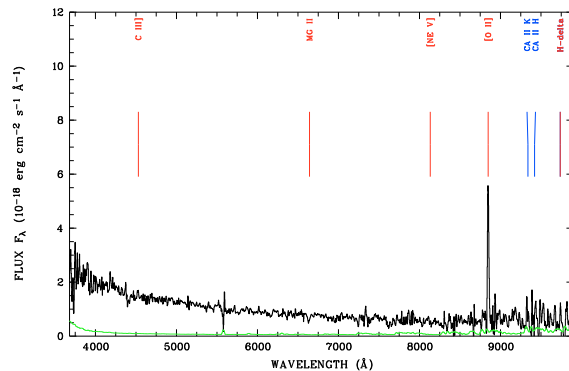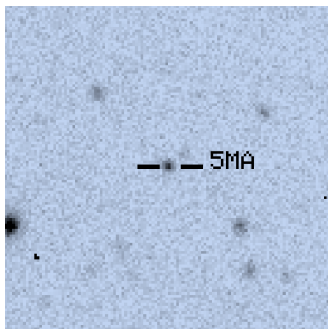
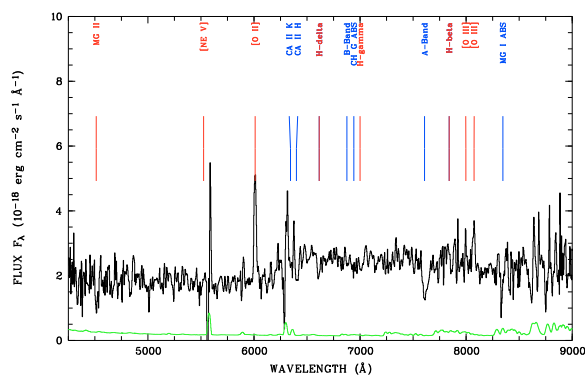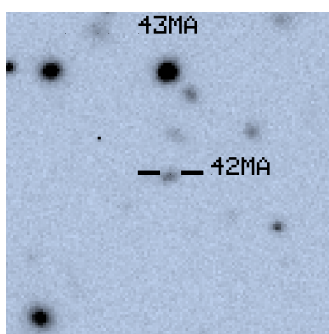object 5MA, z = 1.374
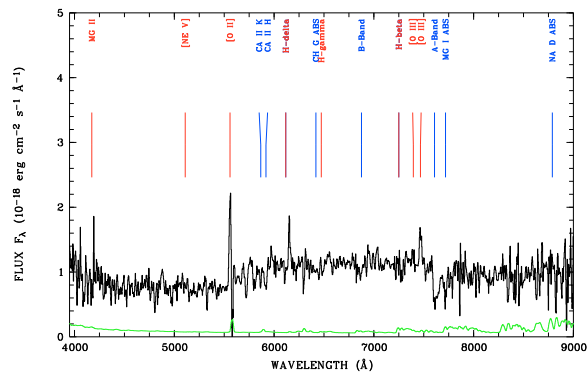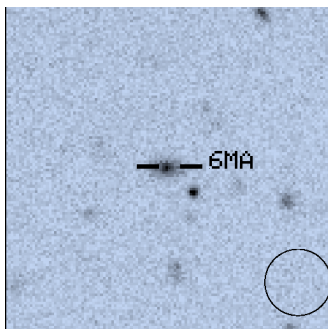
object 6MA, z = 0.491
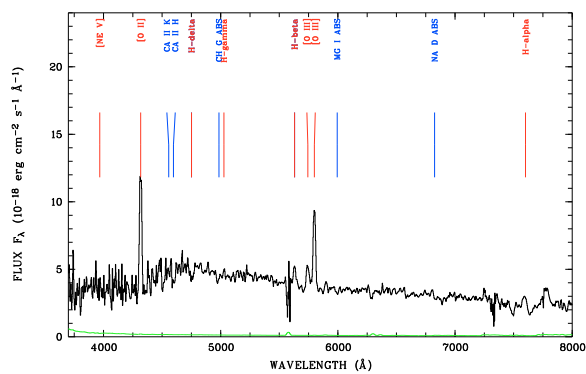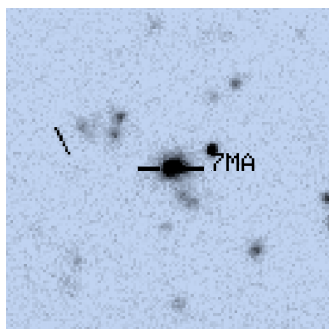
object 7MA, z = 0.158
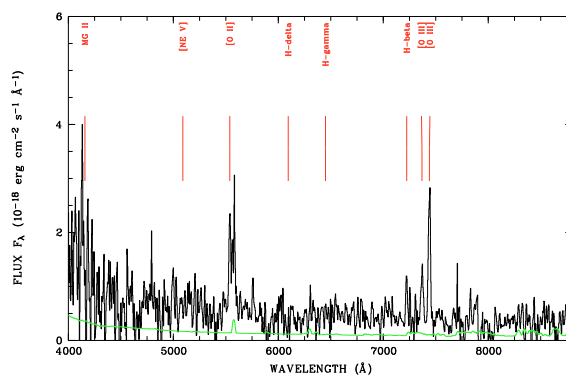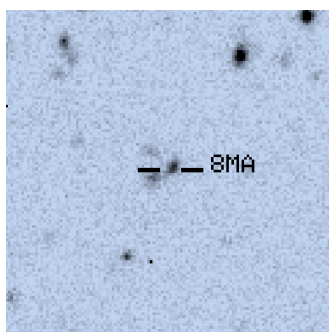
object 8MA, z = 0.486
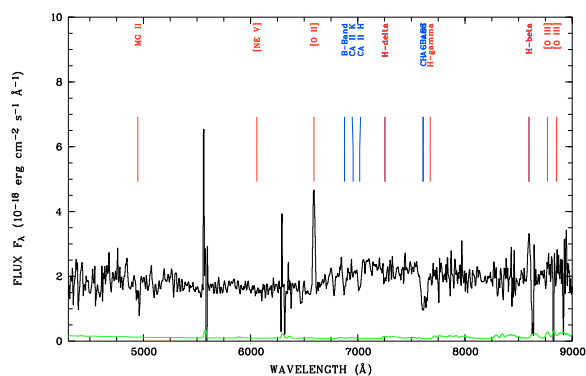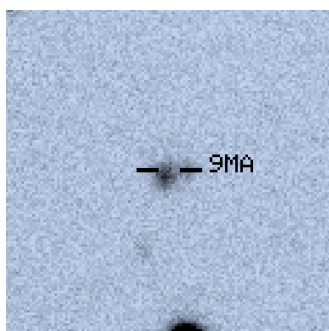
object 9MA, z = 0.786
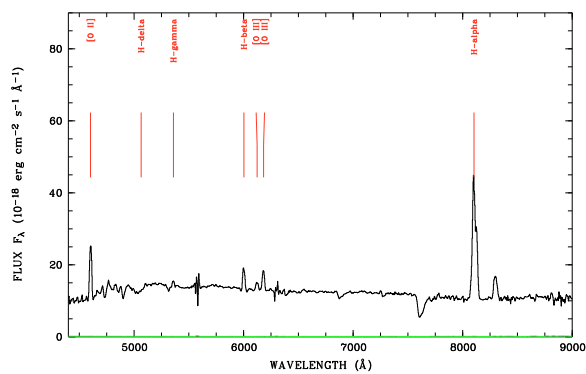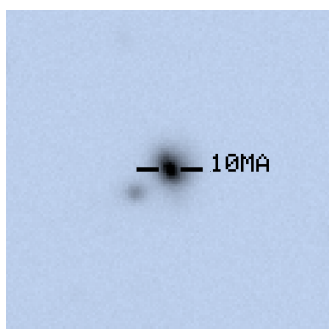
object 10MA, z = 0.235

180
G. Optical charts and spectra of additional optical classifications
in the Marano field
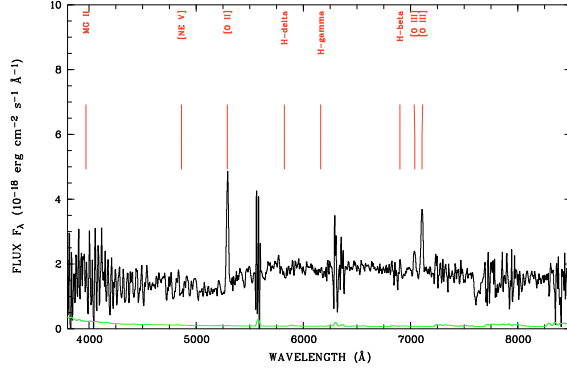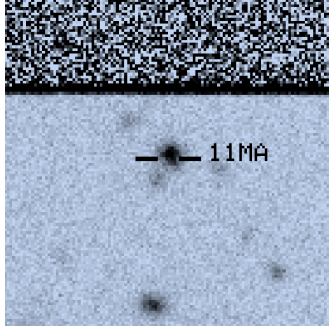
object 11MA, z = 0.420
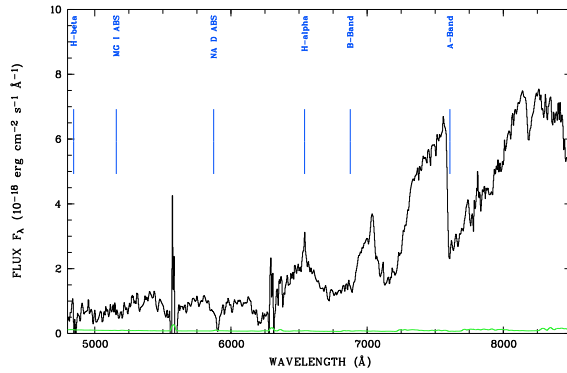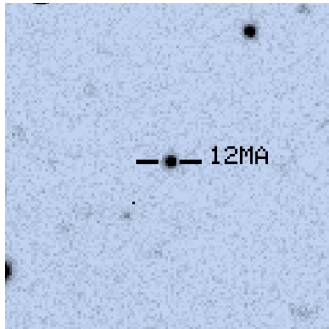
object 12MA, z = 0.000
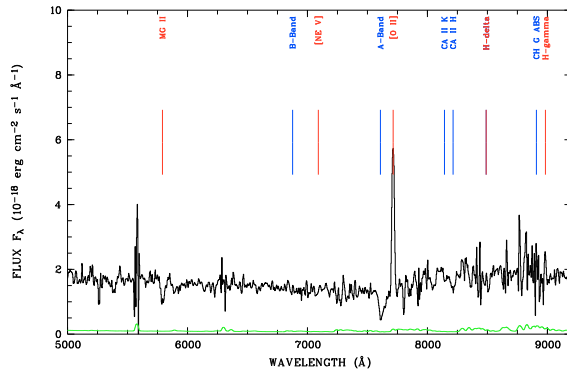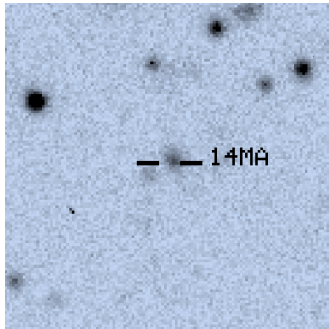
object 14MA, z = 1.070
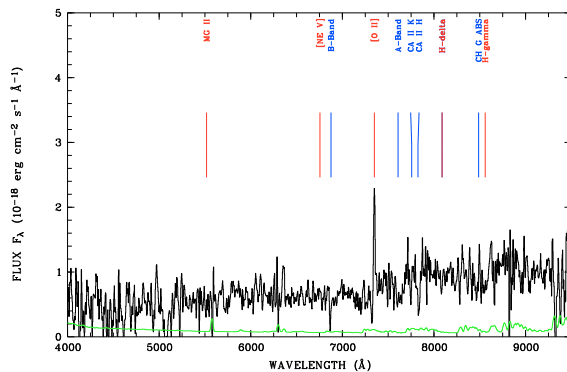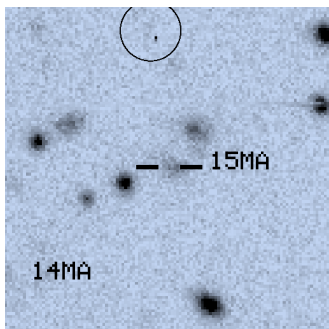
object 15MA, z = 0.972

object 16MA, z = 0.000

object 17MA, z = 0.579

object 18MA, z = 0.583

object 19MA, z = 0.583
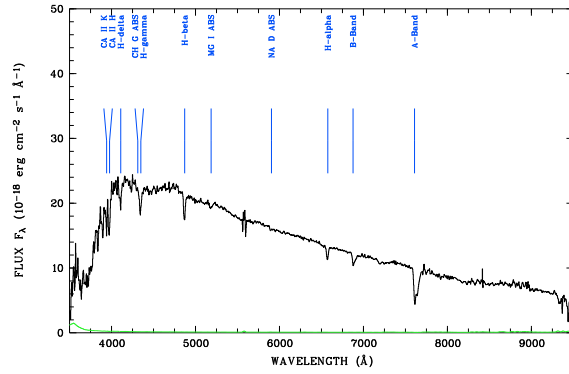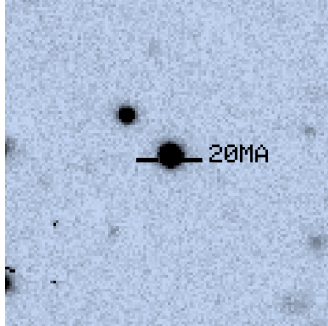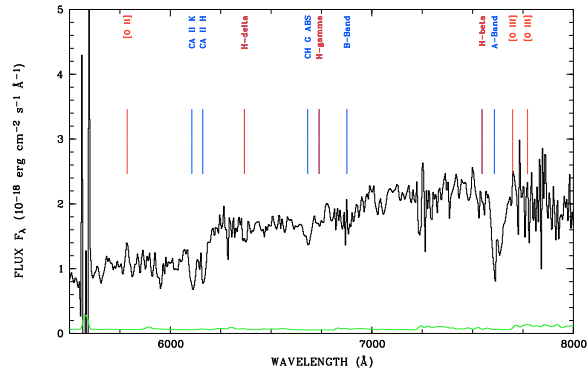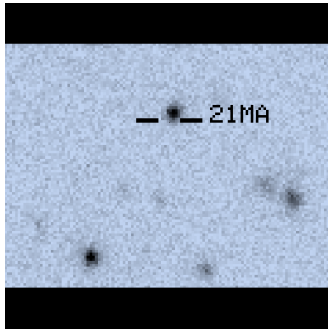
object 20MA, z = 0.000

object 21MA, z = 0.552
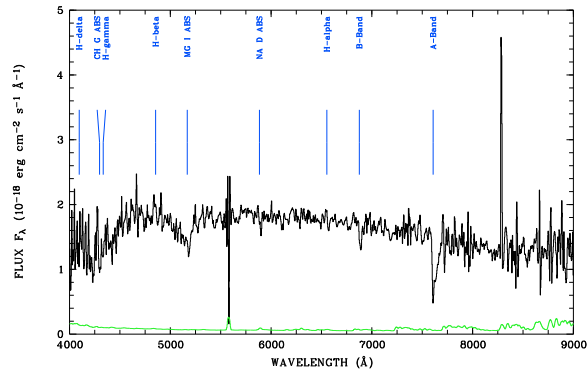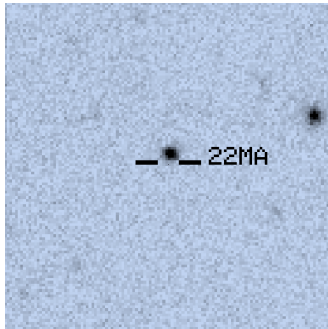
object 22MA, z = 0.000
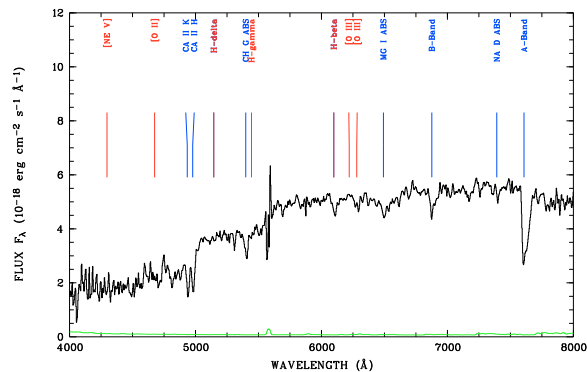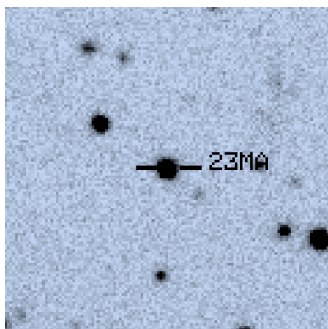
object 23MA, z = 0.254

object 24MA, z = 0.000

object 25MA, z = 0.865

object 26MA, z = 0.000
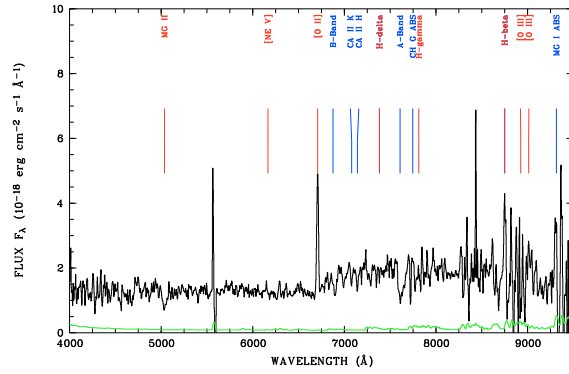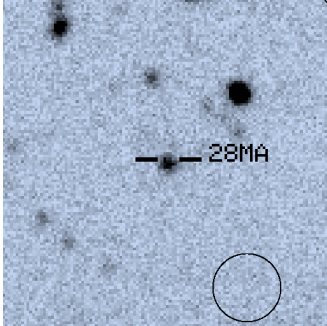
object 27MA, z = 0.000

object 28MA, z = 0.800
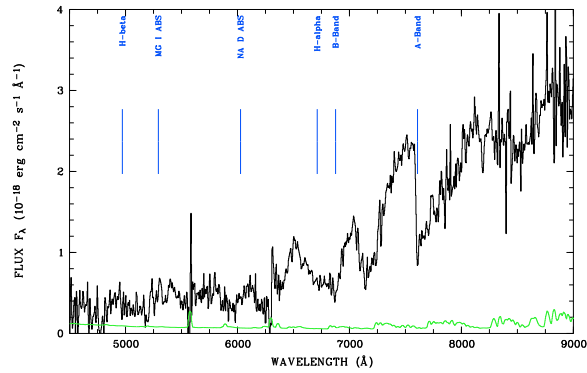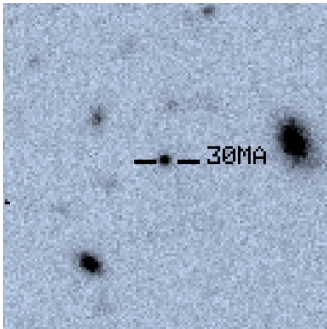
object 30MA, z = 0.000
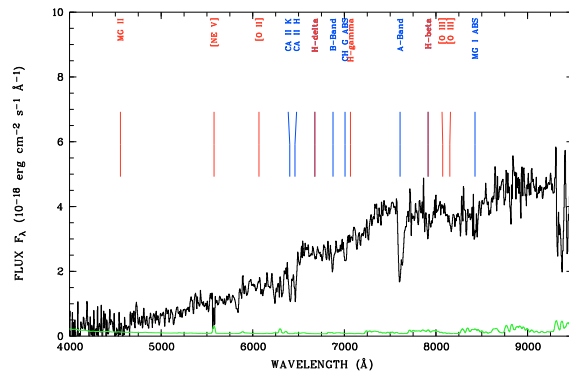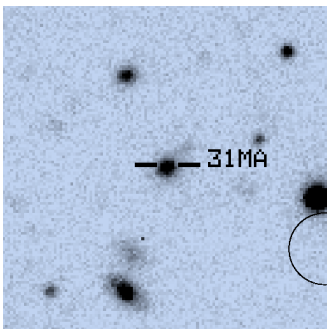
object 31MA, z = 0.628
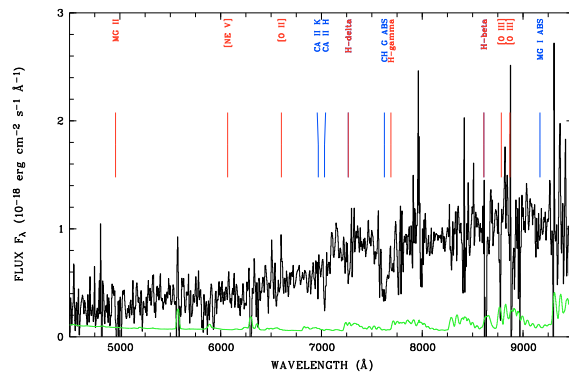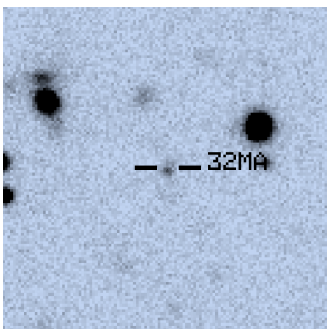
object 32MA, z = 0.771
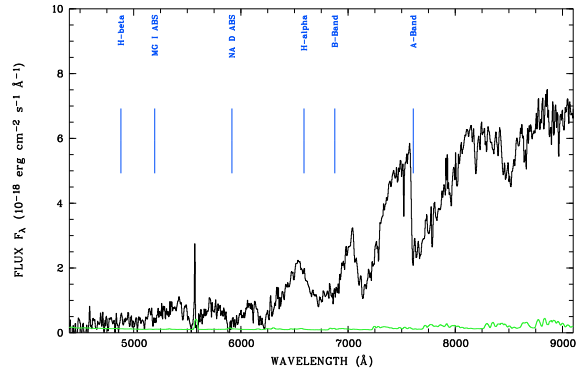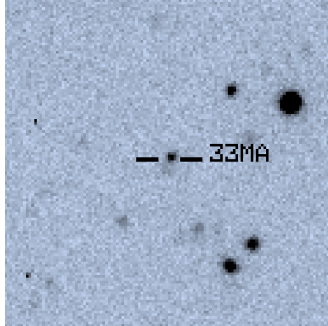
object 33MA, z = 0.000
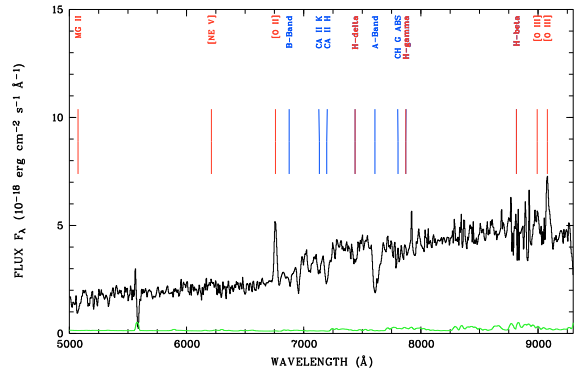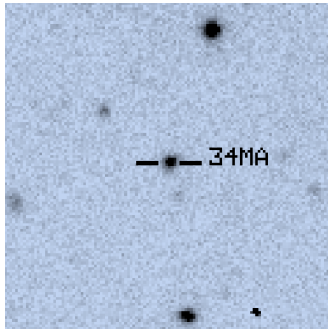
object 34MA, z = 0.813
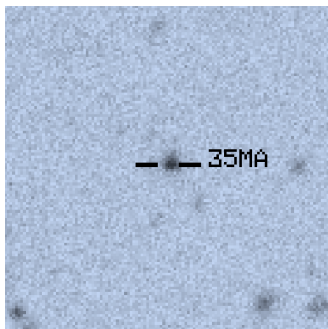
object 35MA, z = 0.869

object 36MA, z = 0.000

object 37MA, z = 0.907

object 38MA, z = 0.554

object 39MA, z = 0.818

object 40MA, z = 0.816
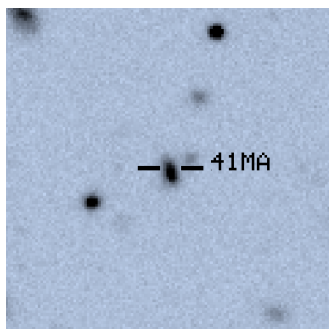
object 41MA, z = 0.552

object 42MA, z = 0.613
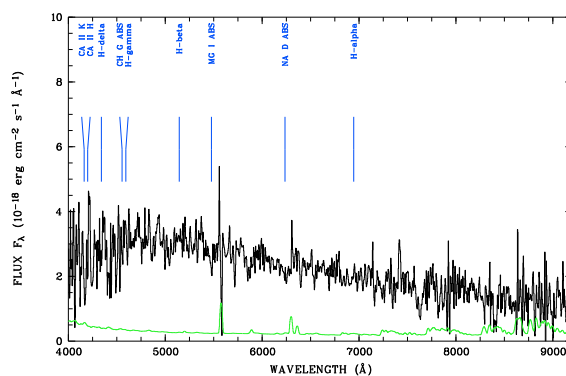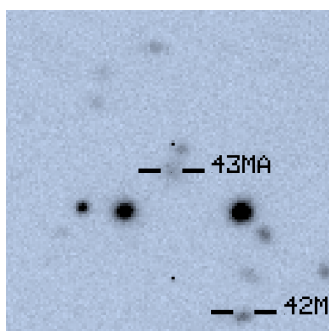
object 43MA, z = 0.000
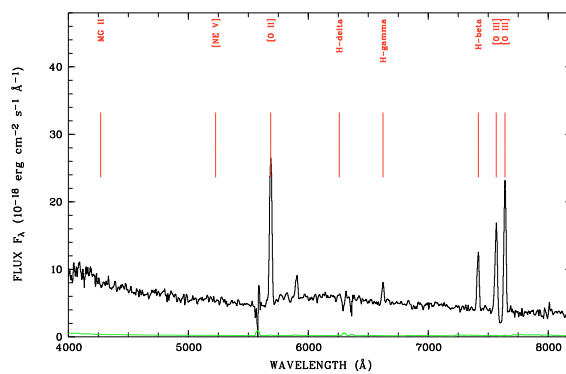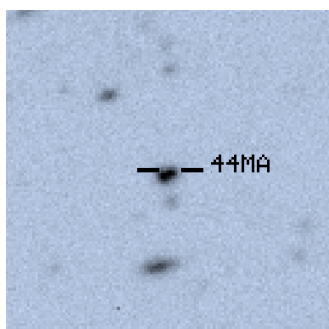
object 44MA, z = 0.526

object 45MA, z = 0.704

object 46MA, z = 0.702

object 47MA, z = 0.460

object 48MA, z = 0.228
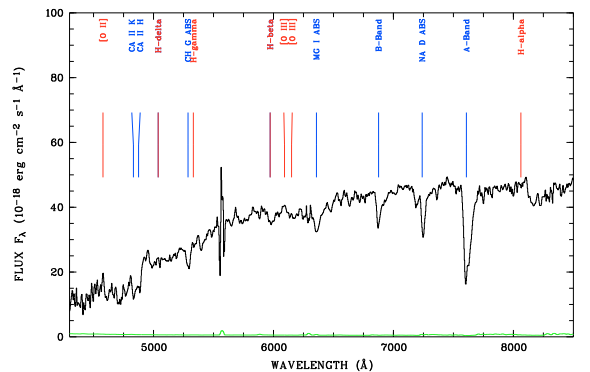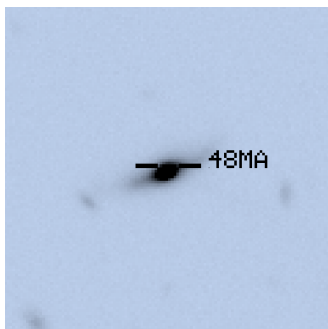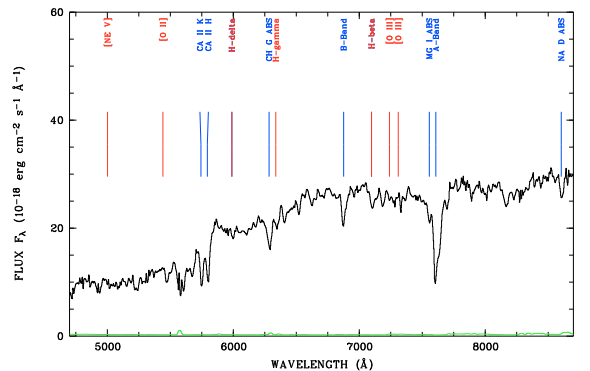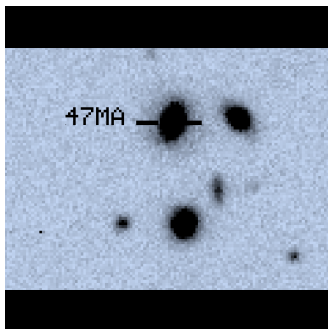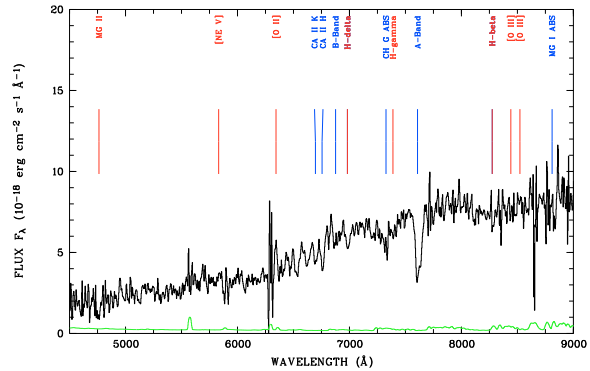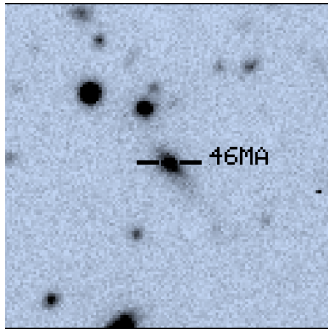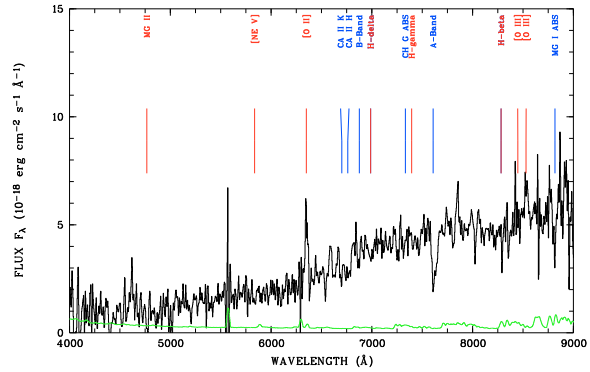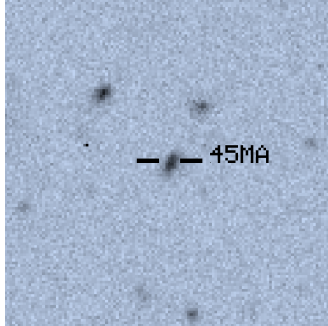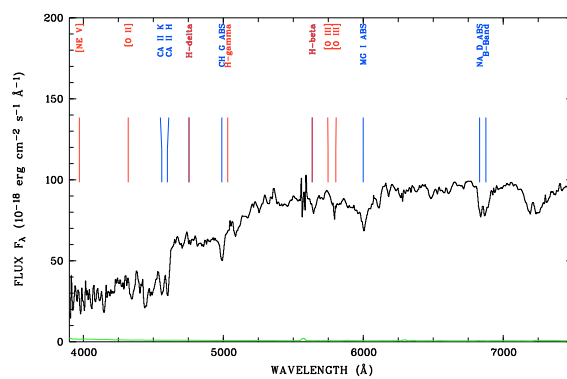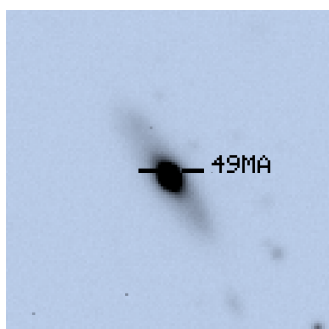
object 49MA, z = 0.159
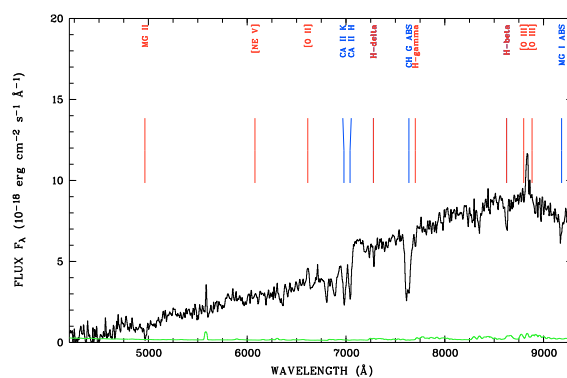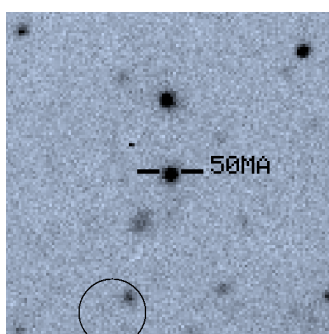
object 50MA, z = 0.774
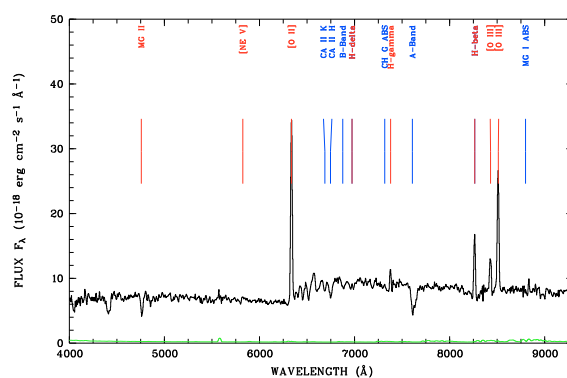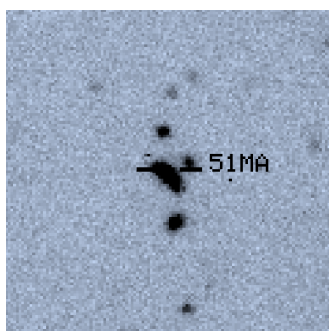
object 51MA, z = 0.700
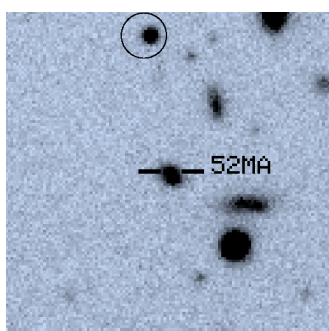
object 52MA, z = 0.631
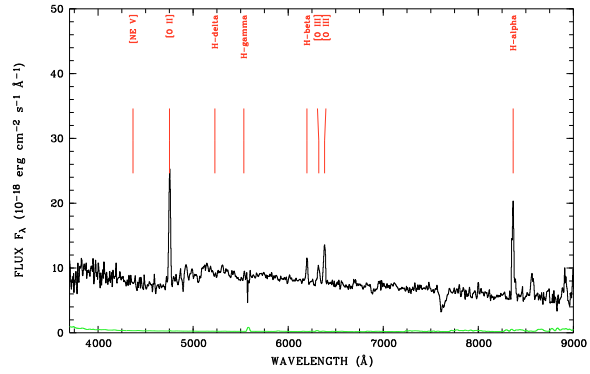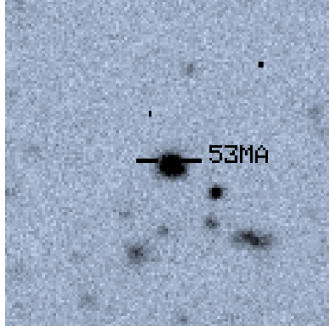
object 53MA, z = 0.275
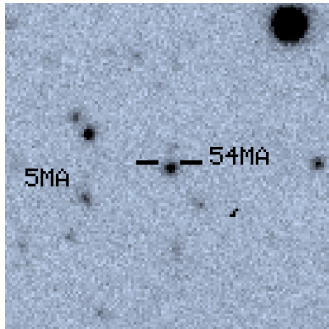
object 54MA, z = 0.815
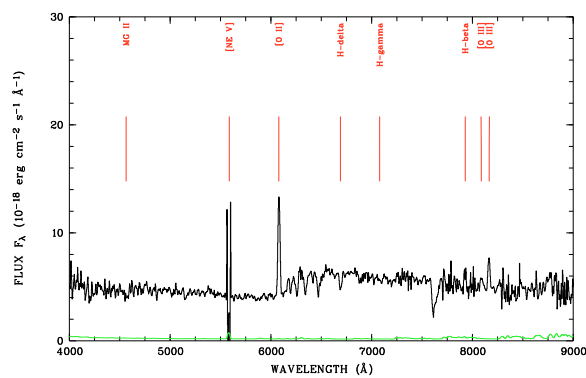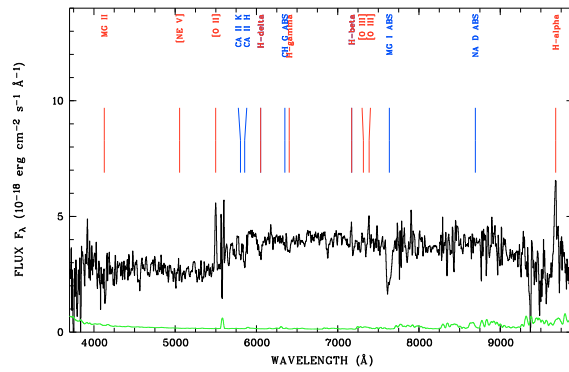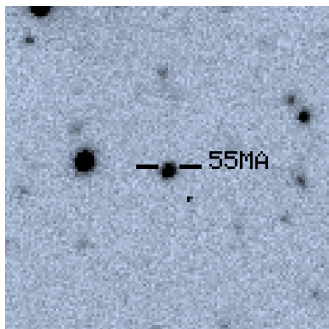

object 55MA, z = 0.475

object 56MA, z = 0.813

object 57MA, z = 0.000

object 58MA, z = 0.500

object 59MA, z = 0.495

object 60MA, z = 0.840

object 61MA, z = 0.071

object 62MA, z = 0.000

Appendix H

Optical & X-ray spectra, confidence contours of type II objects

In this appendix we show the optical and X-ray spectra, as well as the confidence contours of X-ray spectral fits for the parameters N_{H} and Γ.

Optical spectra

The optical atmospheric absorption-corrected, wavelength and flux calibrated spectrum for optical X-ray counterpart is shown. All spectra are in flux 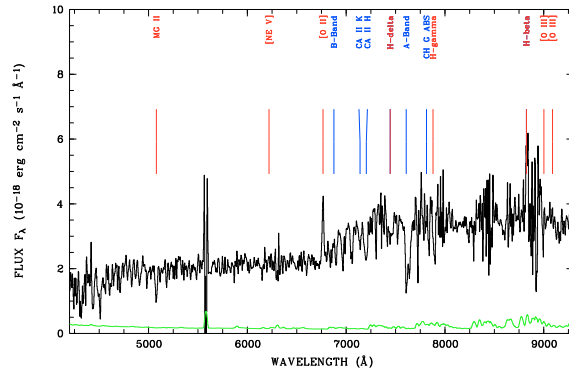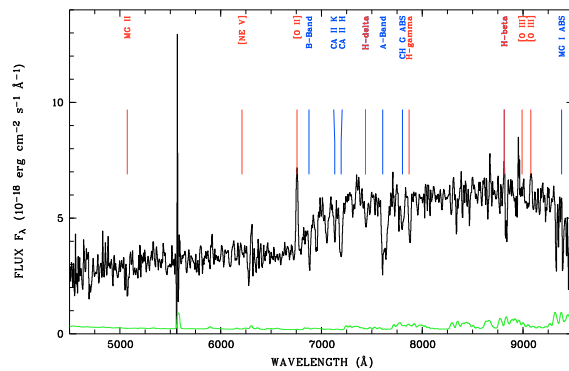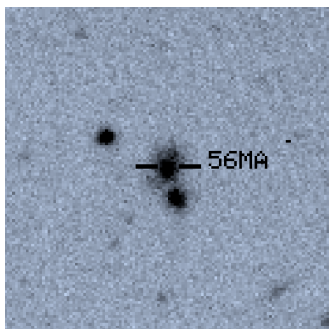units of $10^{-18}\,\mathrm{erg\,cm^{-2}\,s^{-1}\,\mathring{A}^{-1}}$. The black solid line represents the spectrum, the green solid line the error spectrum (not available in all spectra). Red markers indicate possible emission lines, blue markers absorption lines. There are exceptions in a few spectra. Spectral features at 5580 Å are spurious due to incomplete subtraction of a night sky line.

X-ray spectra

The X-ray spectra show the PN and combined MOS data, as well as the best fit model (power law, foreground Galactic absorption, intrinsic absorption at the object's redshift). For objects that have less than 100 PN source counts in the 0.2-8 keV band we fixed the photon index ($\Gamma = 2$). Otherwise free fits in N_{H} and Γ are shown. The fit parameters are given in Table 4.5. For illustration purposes the X-ray data have been rebinned to different signal-to-noise ratio, after grouping to a minimum of one count per bin (min 1).

Confidence contours:

Confidence contours of the absorbing column density in units of $N_{\mathrm{H}} = 10^{22}\,\mathrm{cm^{-2}}$ vs. photon index Γ of the X-ray spectral fits. Confidence contours are plotted for 68% (black), 90% (red) and 99% (green). The contours are based on free N_{H} and Γ X-ray spectral fits for all objects independent of net PN counts.

Comments:

Below every set of optical & X-ray spectra and X-ray contour a comment for the objects shown is given. This comment includes the classification number of the optical counterpart and the corresponding redshift. Furthermore, a short fit description is given. For more details on the properties of the sources and the X-ray spectral fits see Tables 4.2, 4.5.
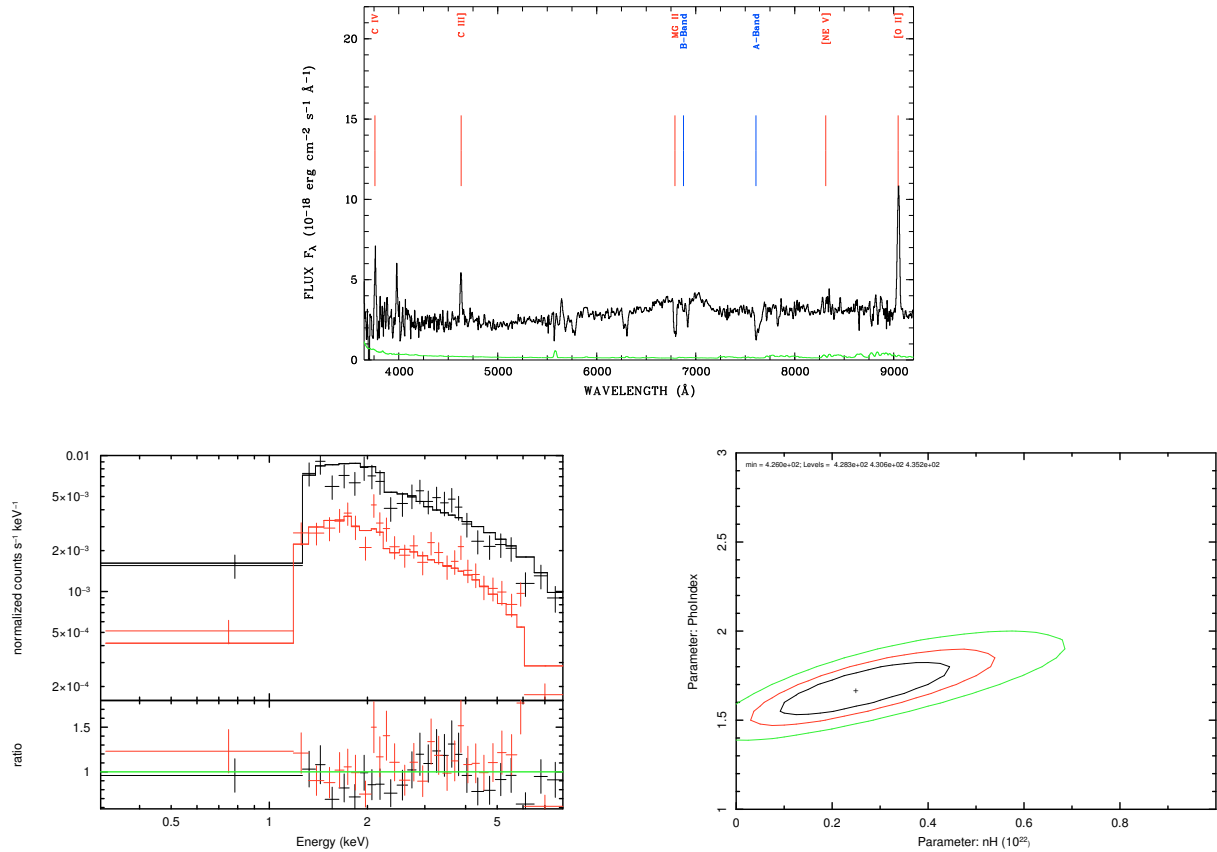
object Marano 9A, z = 1.427, free X-ray spectrum fit
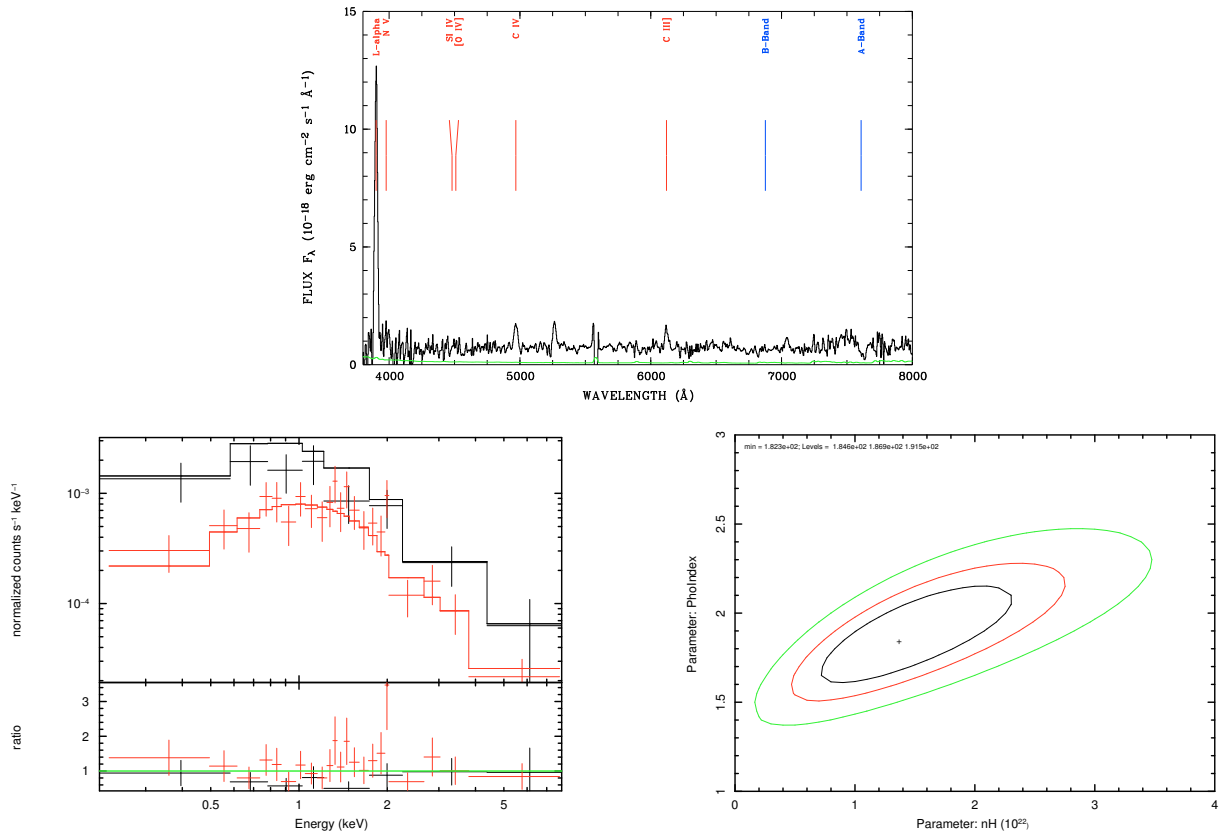
object Marano 20A, z = 2.207, frozen $\Gamma = 2.0$ X-ray spectrum fit
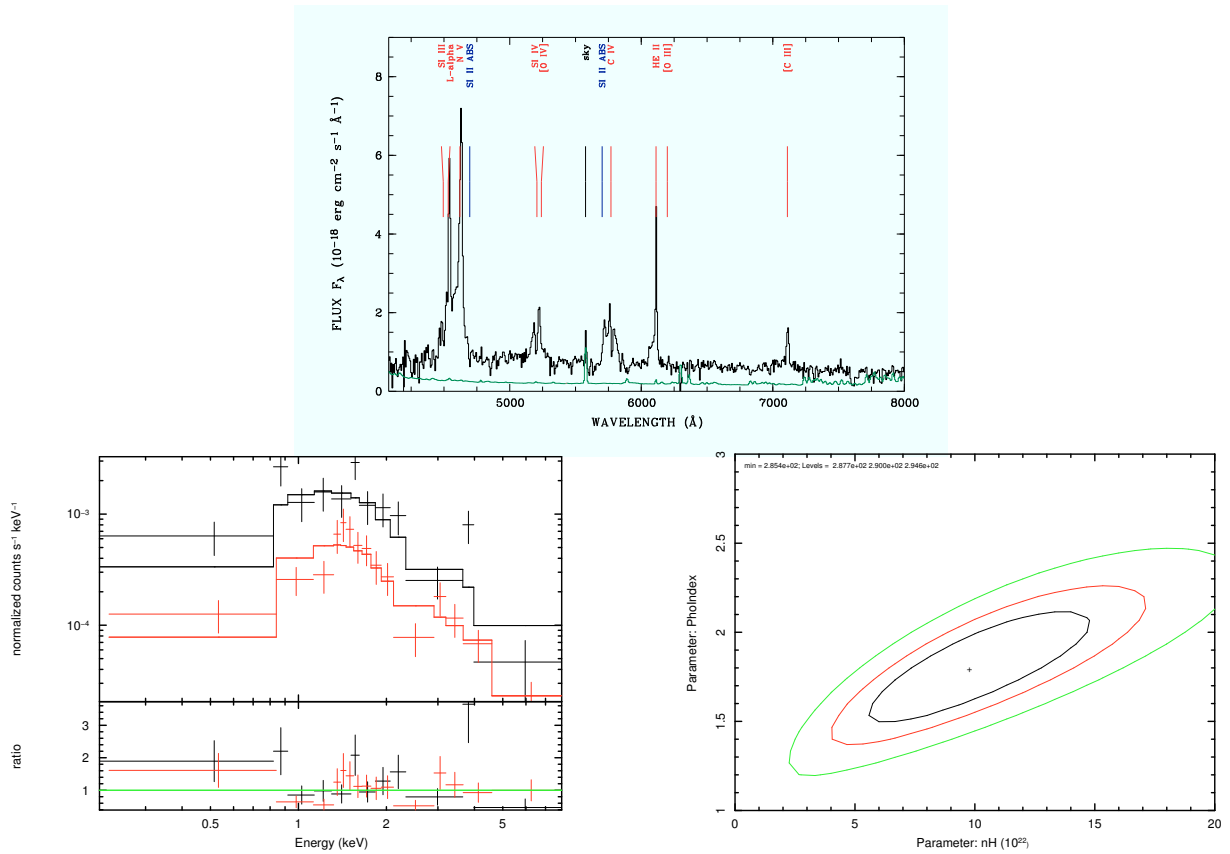
object Marano 32A, z = 2.727, free X-ray spectrum fit
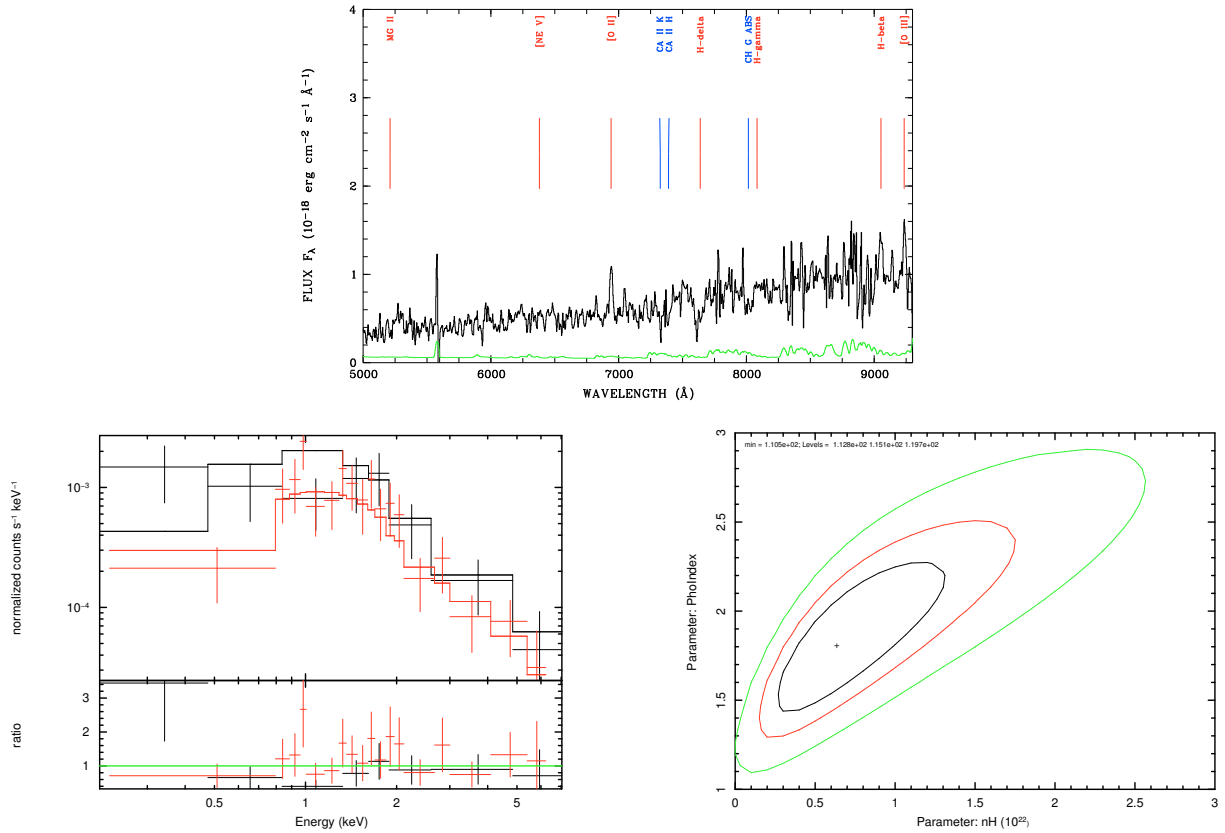
object Marano 39A, z = 0.862, frozen Γ = 2.0 X-ray spectrum fit
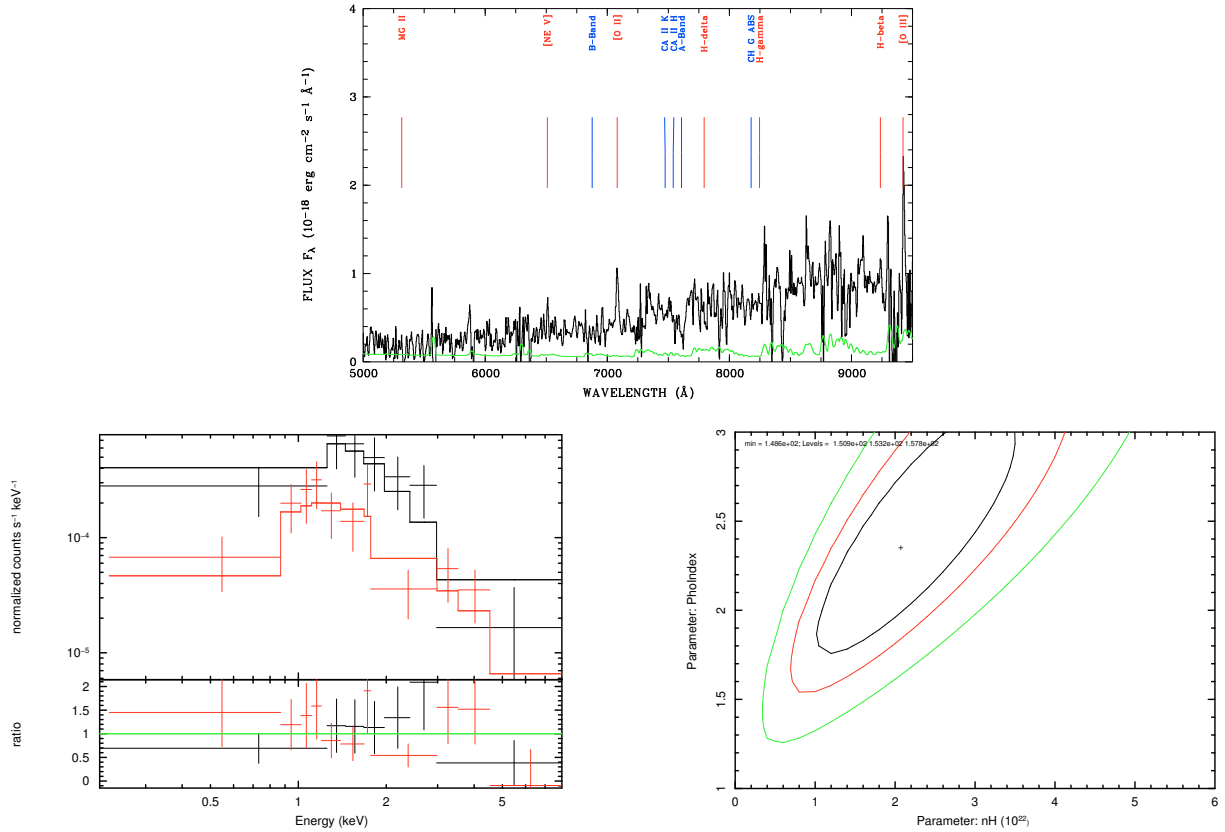
object Marano 47A, z = 0.900, frozen Γ = 2.0 X-ray spectrum fit
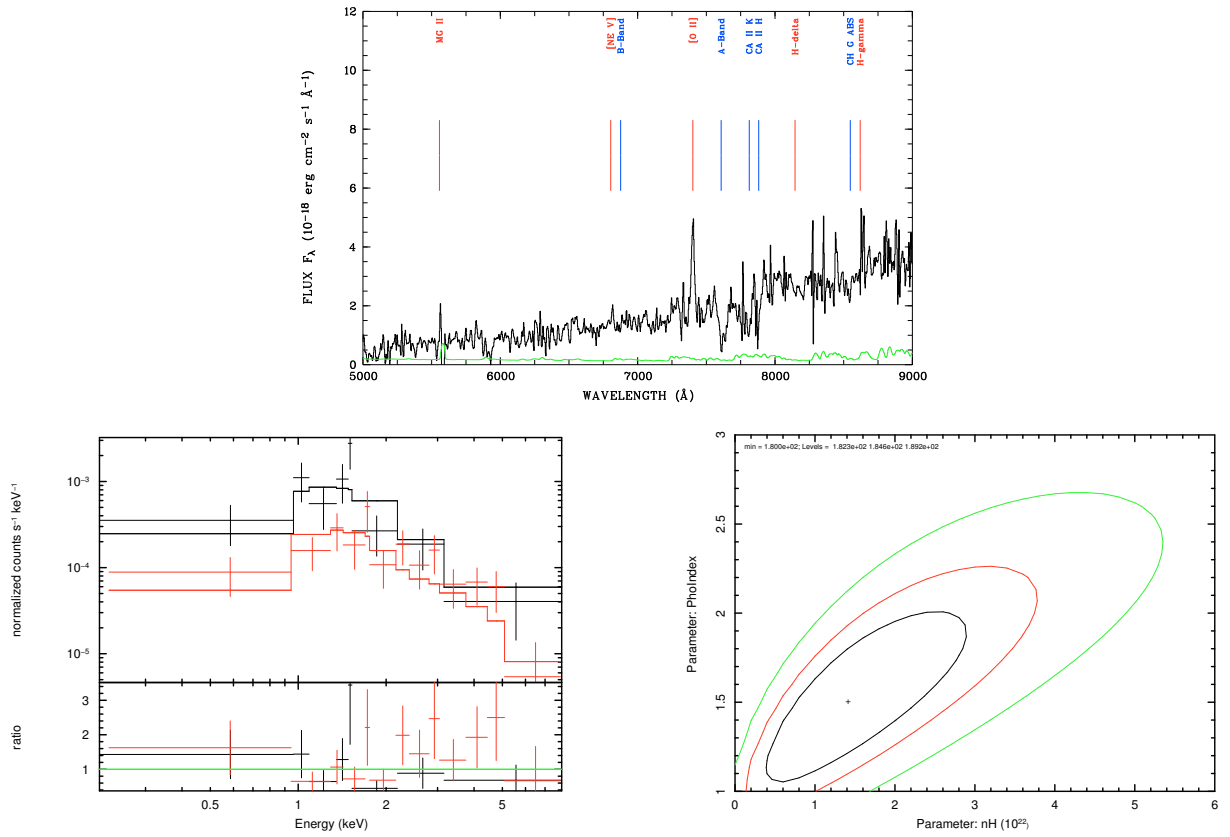
object Marano 50A, z = 0.986, frozen Γ = 2.0 X-ray spectrum fit
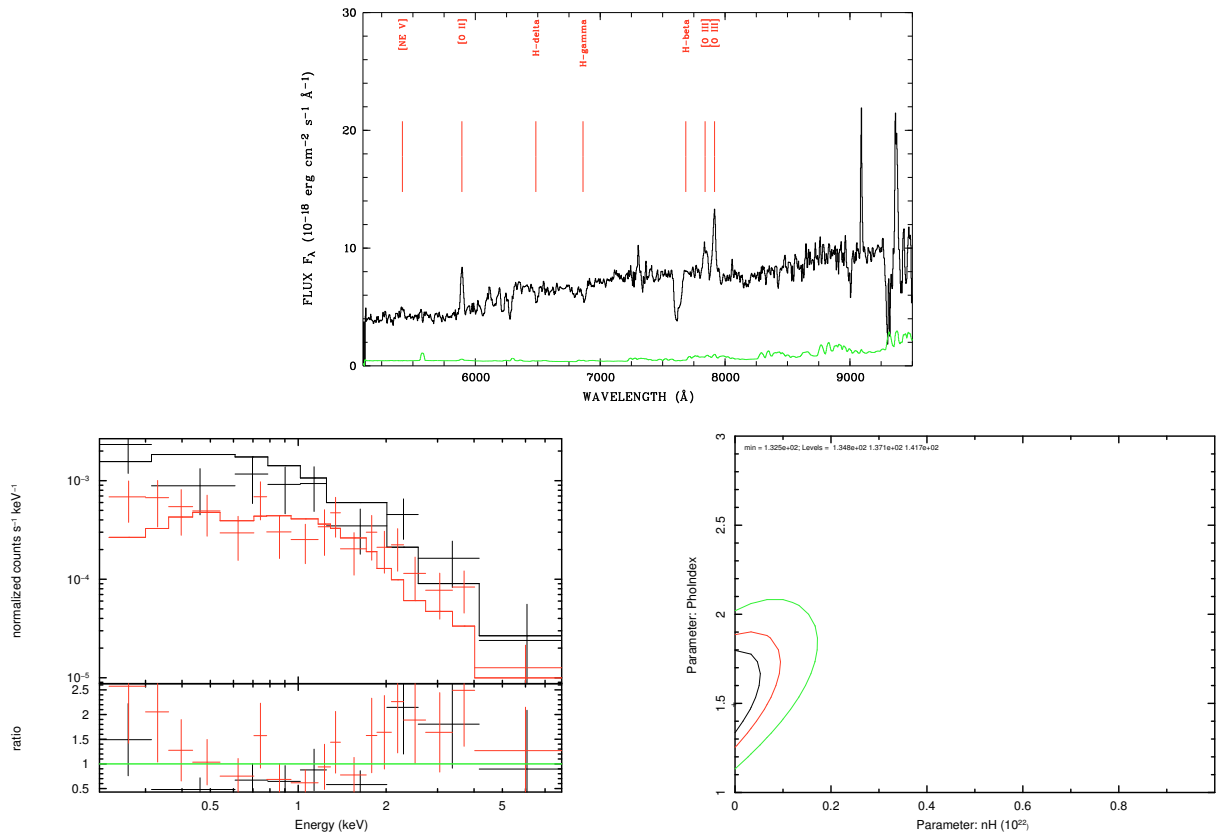
object Marano 51A, z = 0.58, frozen Γ = 2.0 X-ray spectrum fit

object Marano 63A, z = 2.800, frozen Γ = 2.0 X-ray spectrum fit

object Marano 66A, z = 0.981, frozen Γ = 2.0 X-ray spectrum fit
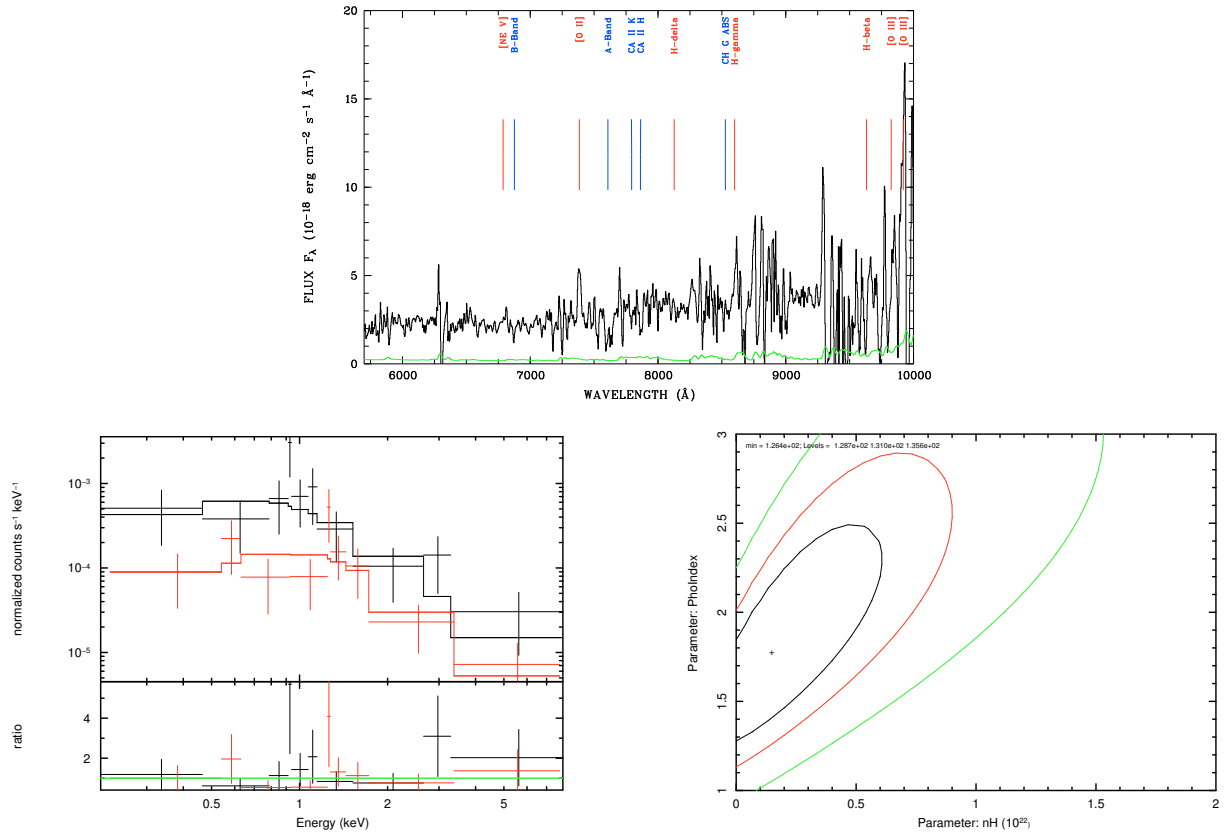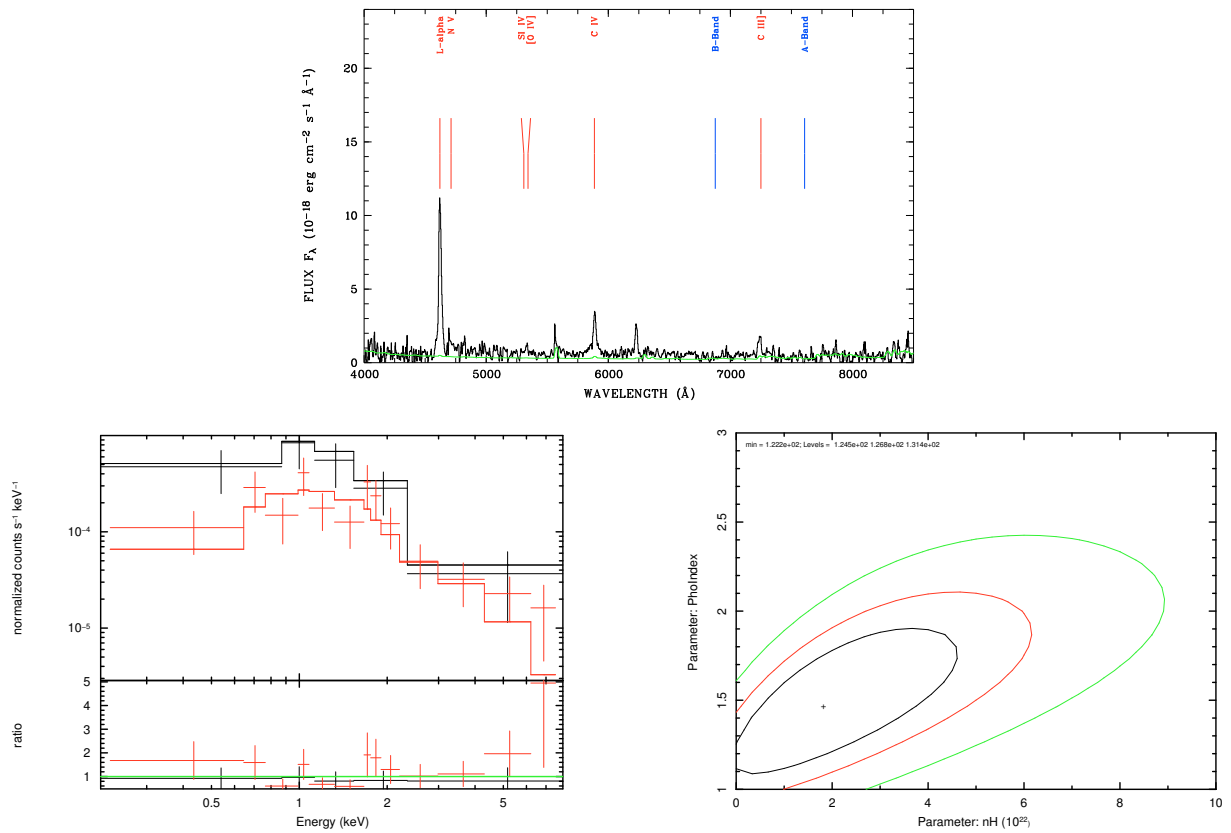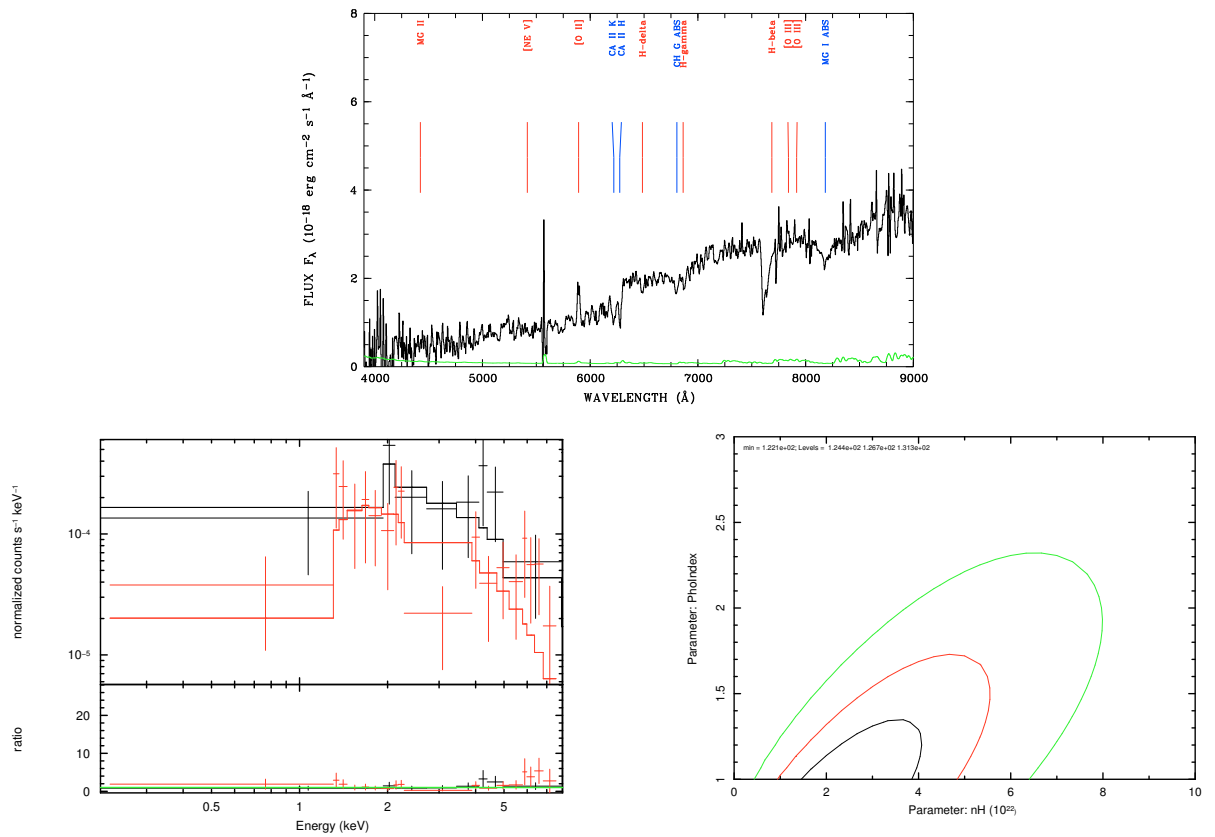
object Marano 116A, z = 0.581, frozen Γ = 2.0 X-ray spectrum fit
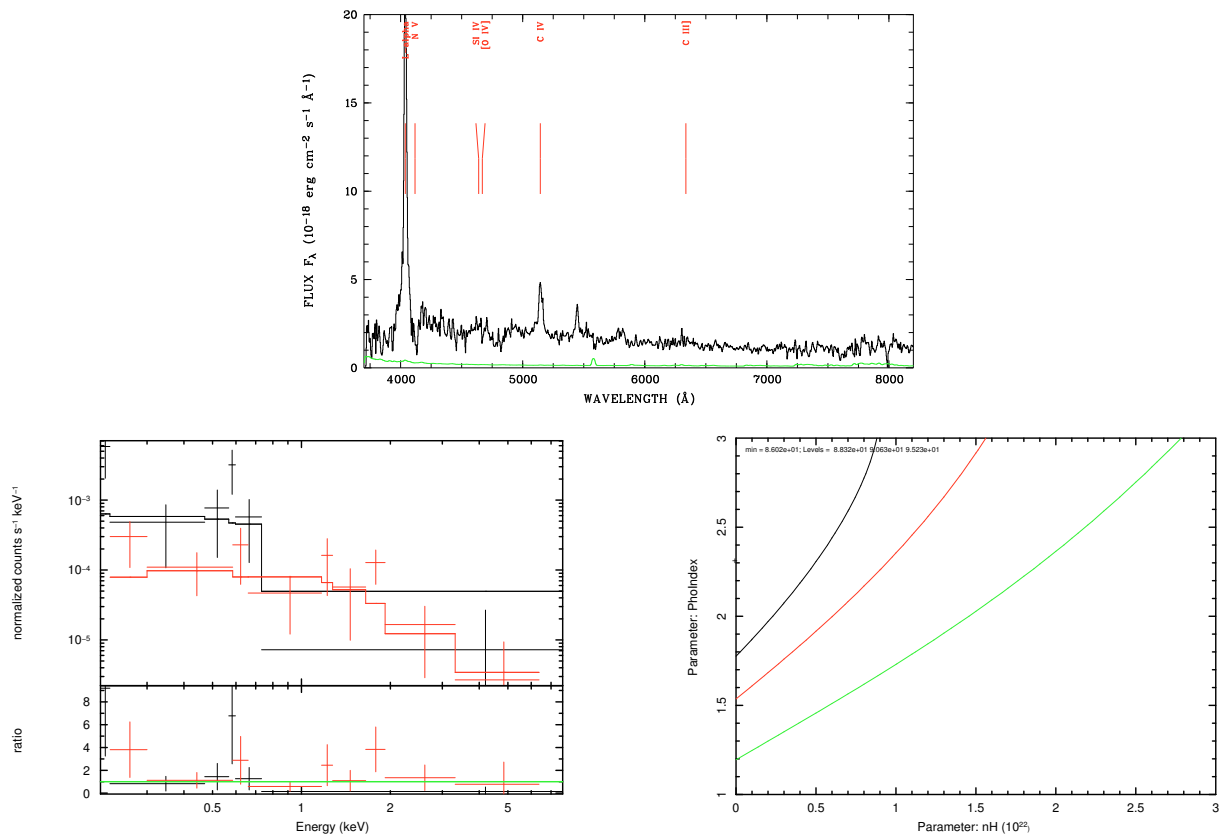
object Marano 133A, z = 2.321, frozen Γ = 2.0 X-ray spectrum fit
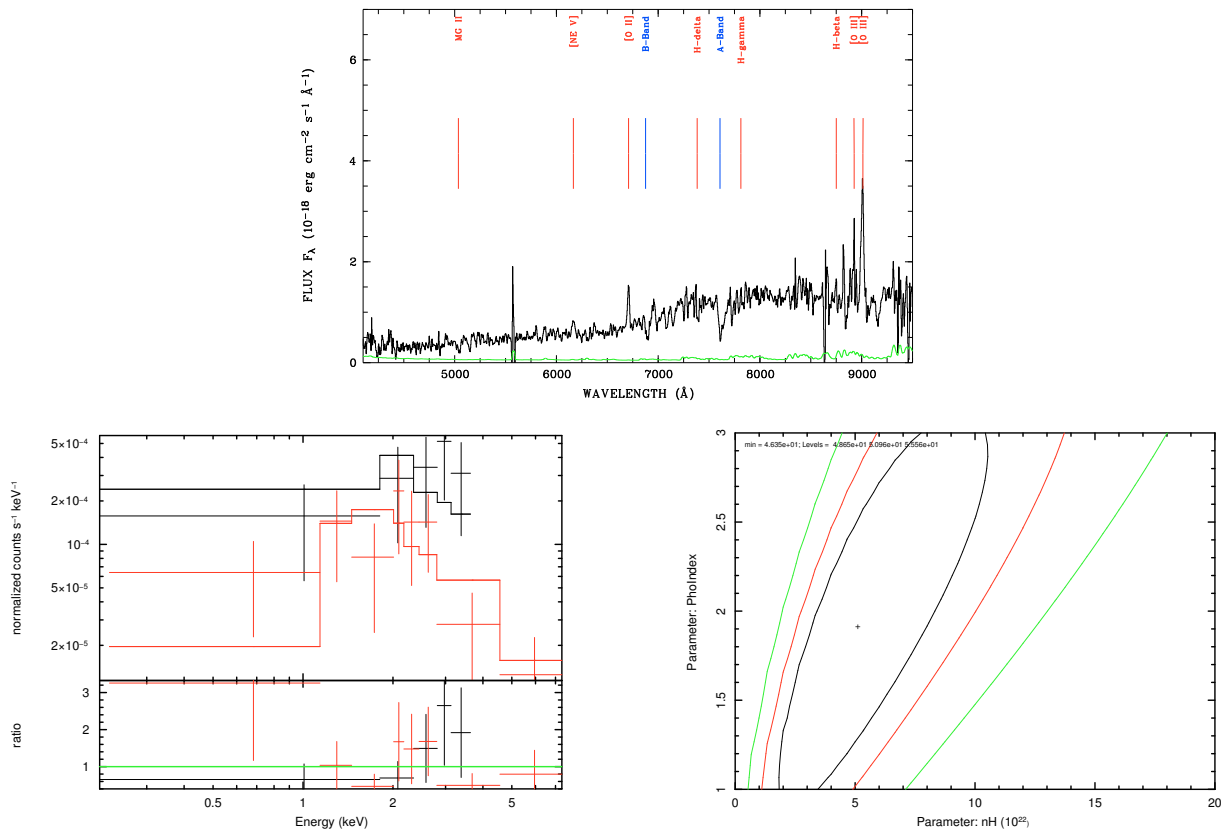
object Marano 171A, z = 0.800, frozen $\Gamma = 2.0$ X-ray spectrum fit
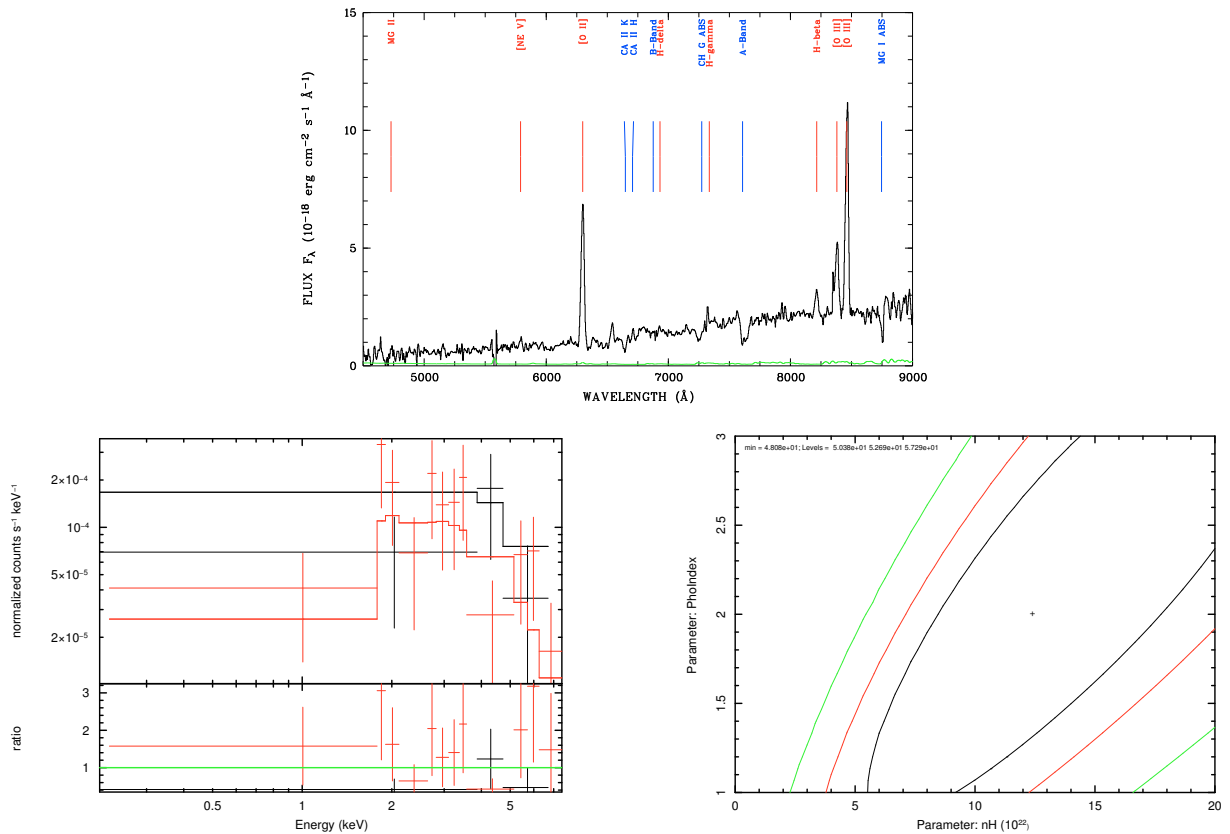
object Marano 224B, z = 0.690, frozen $\Gamma = 2.0$ X-ray spectrum fit
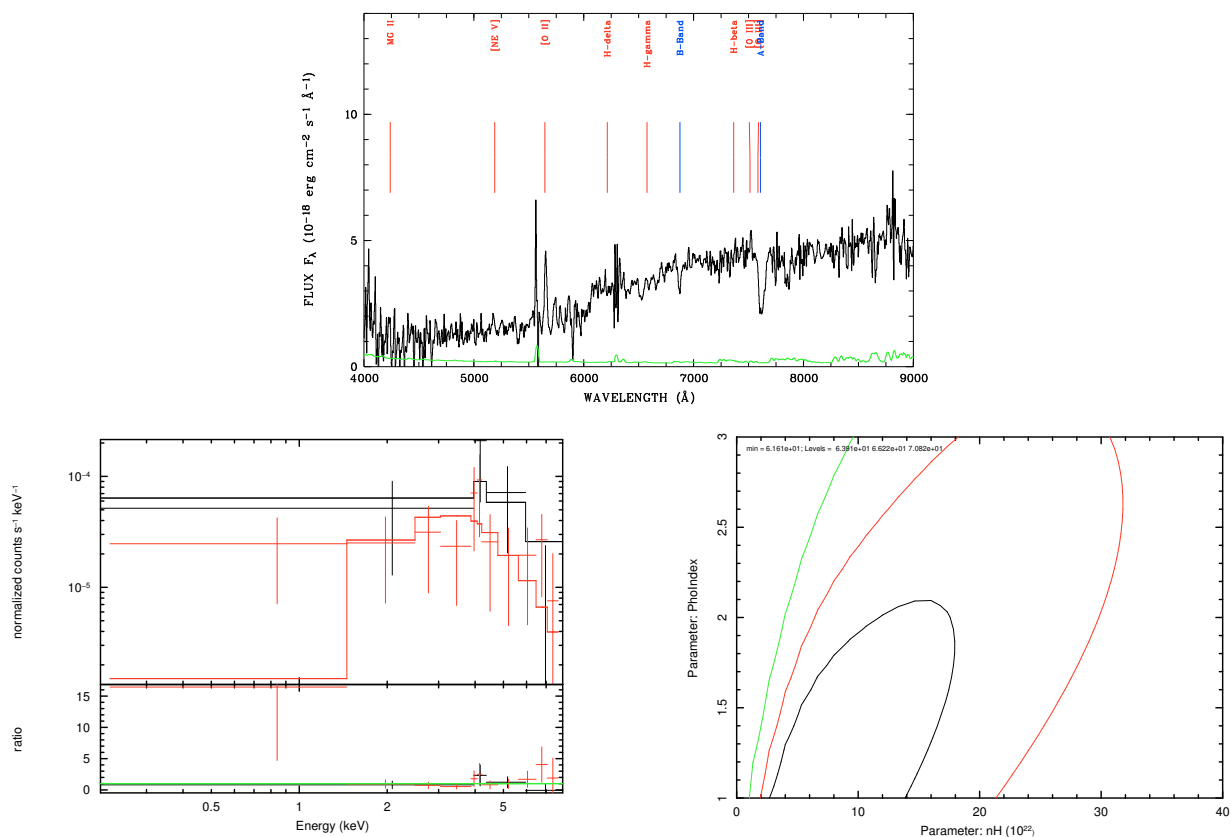
object Marano 253A, z = 0.517, frozen Γ = 2.0 X-ray spectrum fit
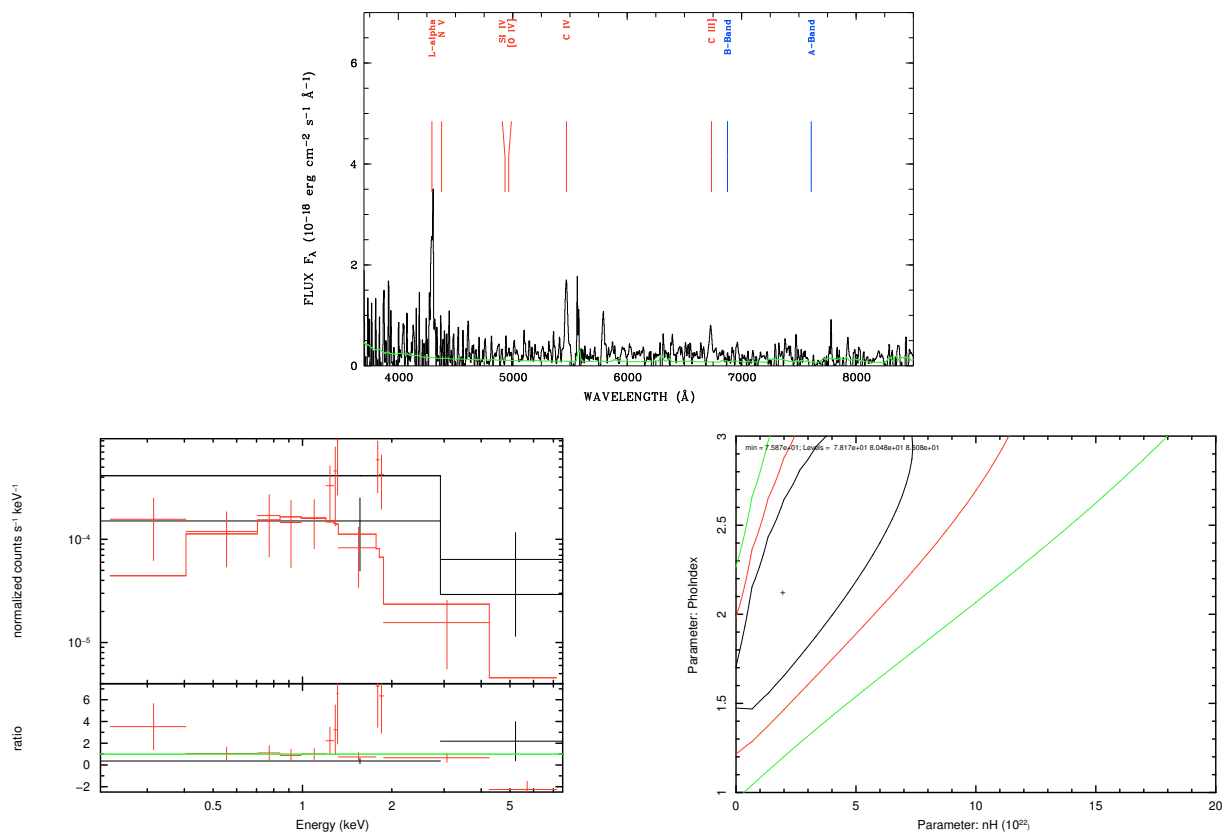
object Marano 463A, z = 2.531, frozen Γ = 2.0 X-ray spectrum fit
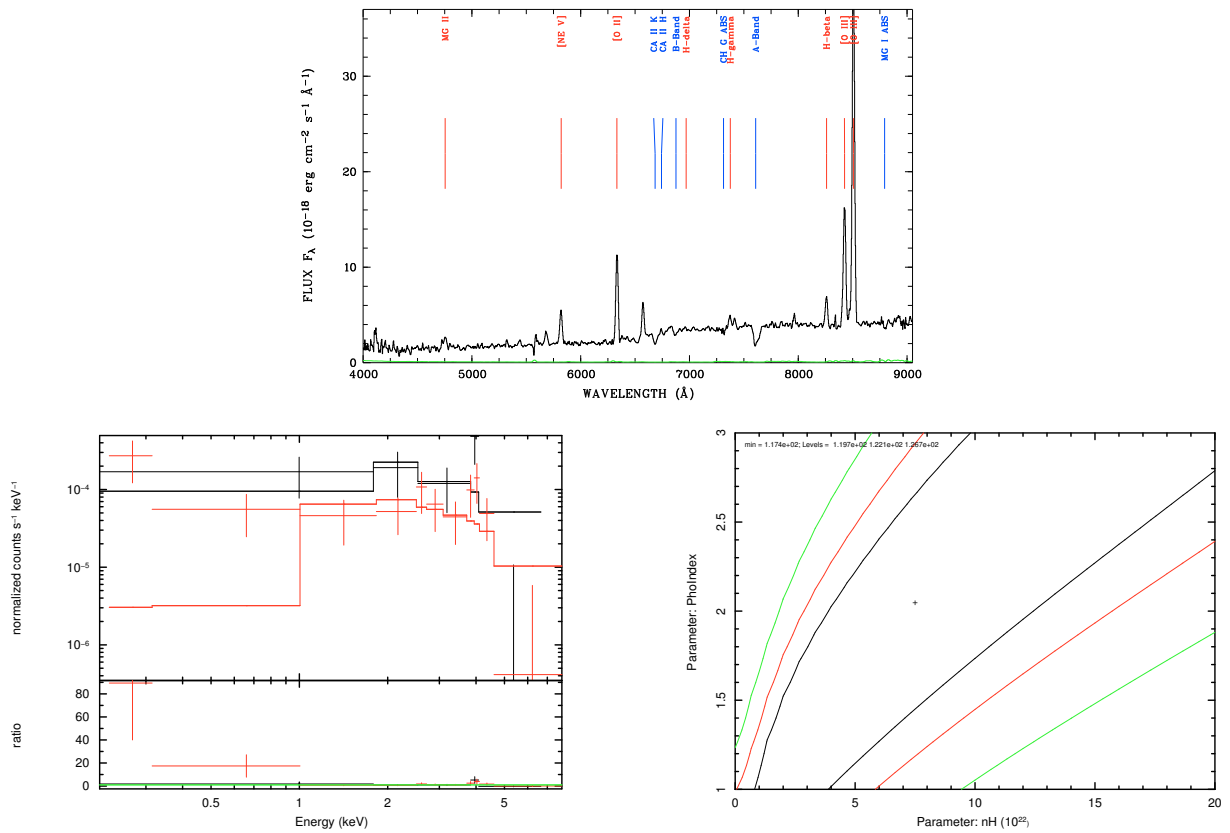
object Marano 610A, z = 0.699, frozen Γ = 2.0 X-ray spectrum fit
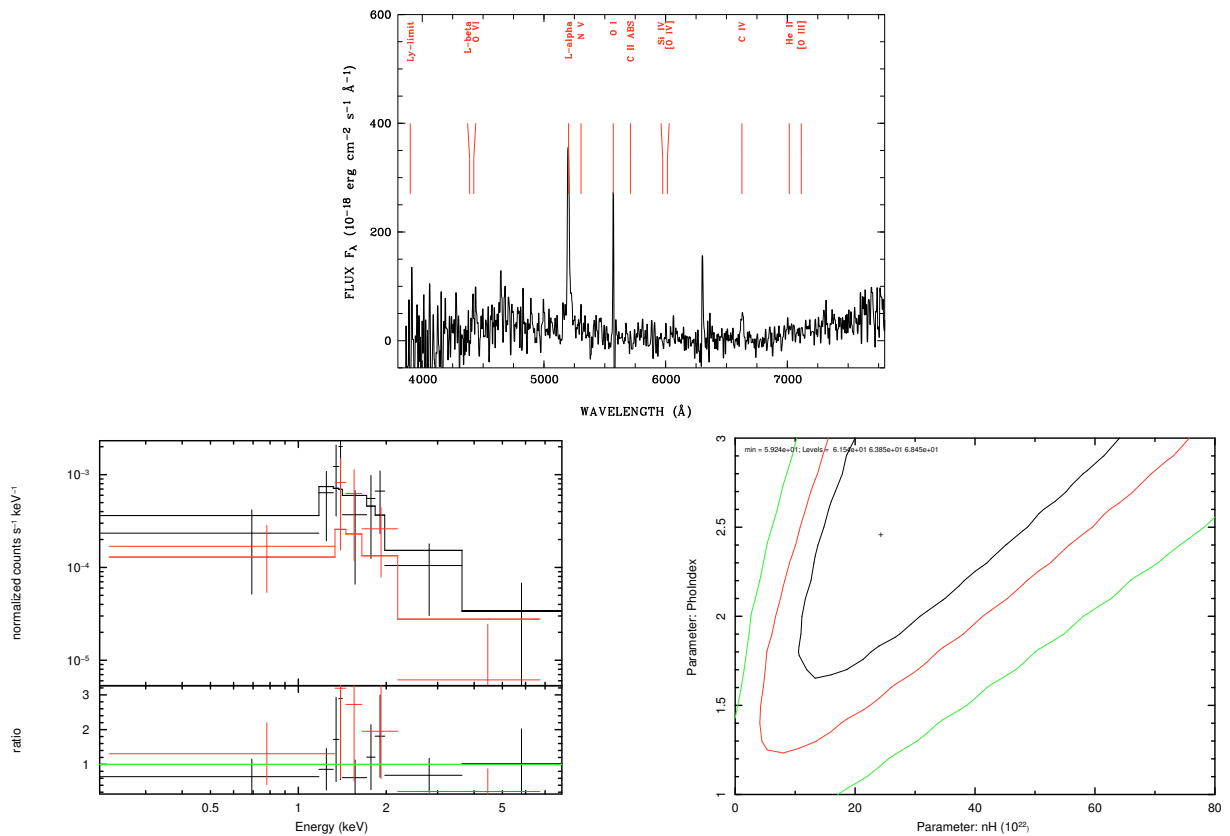
object X21516_135, z = 3.278, frozen Γ = 2.0 X-ray spectrum fit
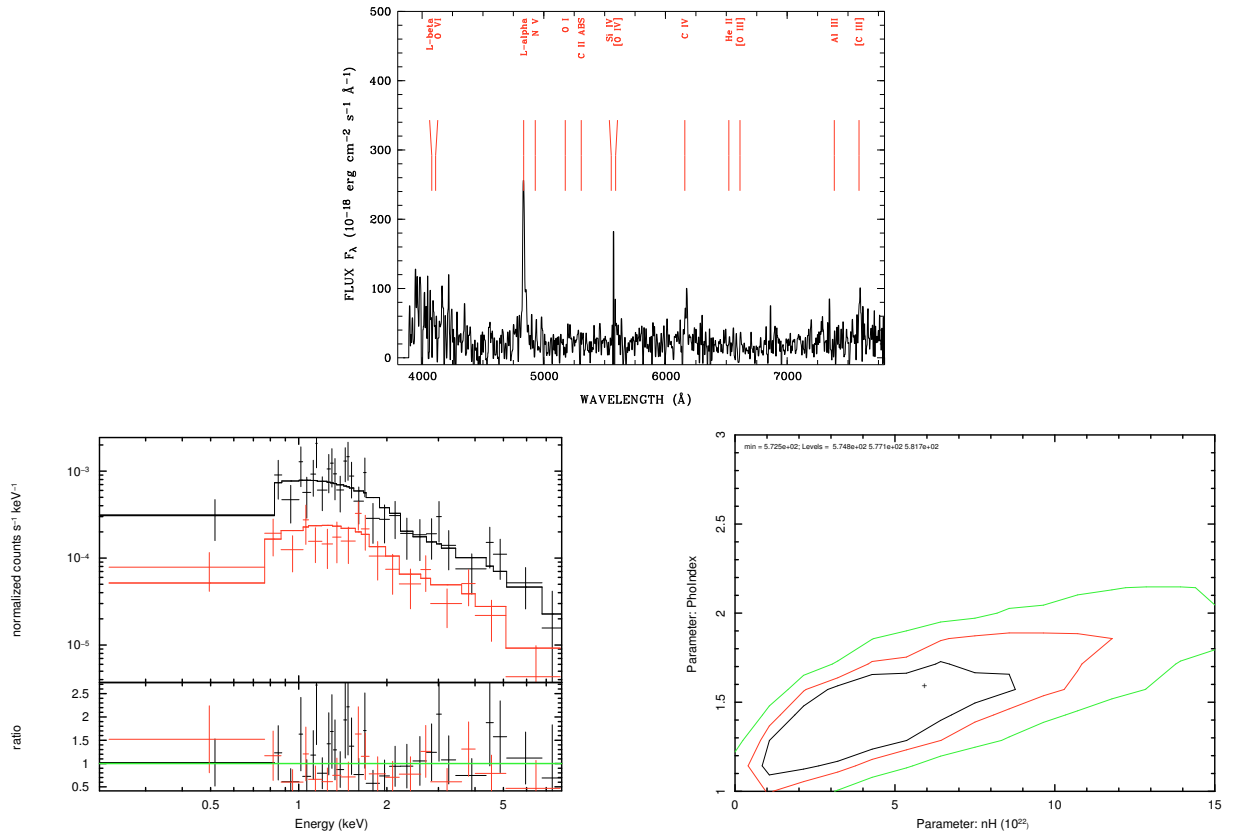
object X00851_154, z = 2.976, free X-ray spectrum fit
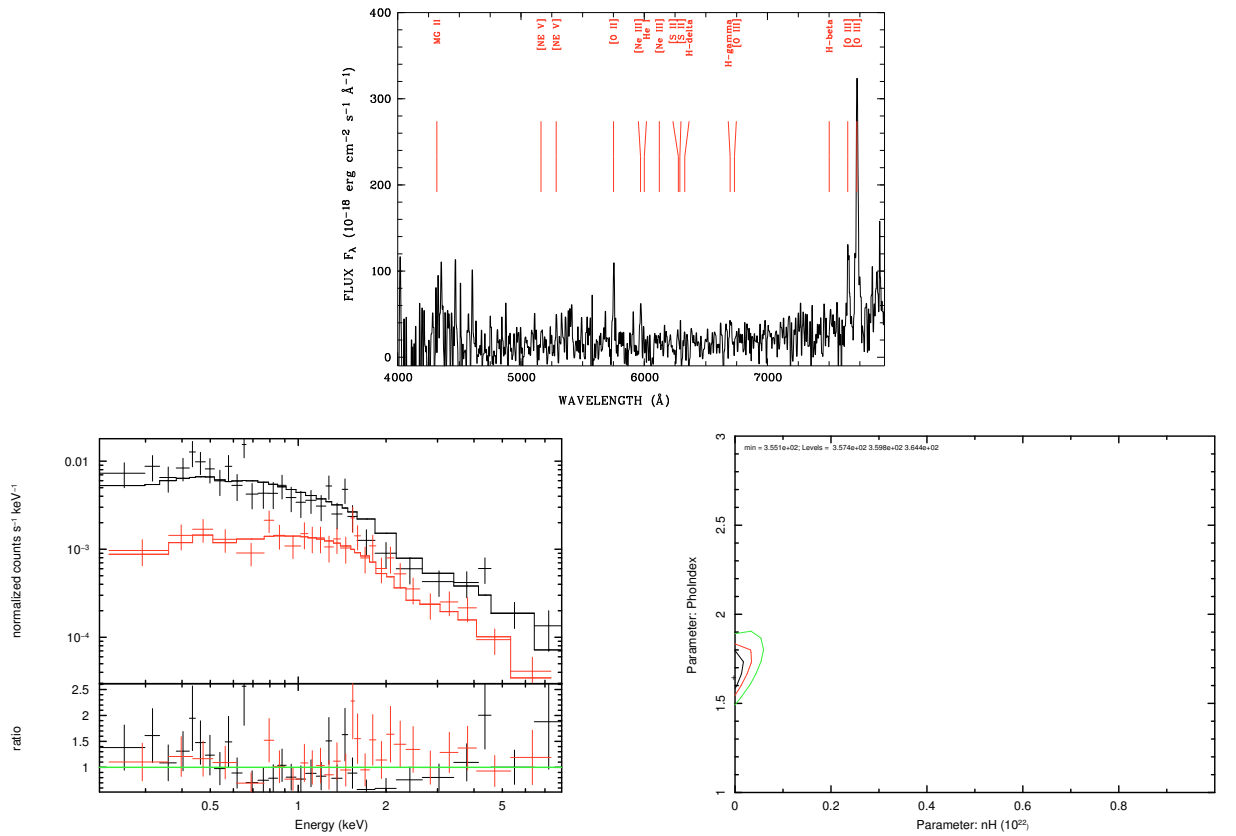
object X01135_126, z = 0.543, free X-ray spectrum fit
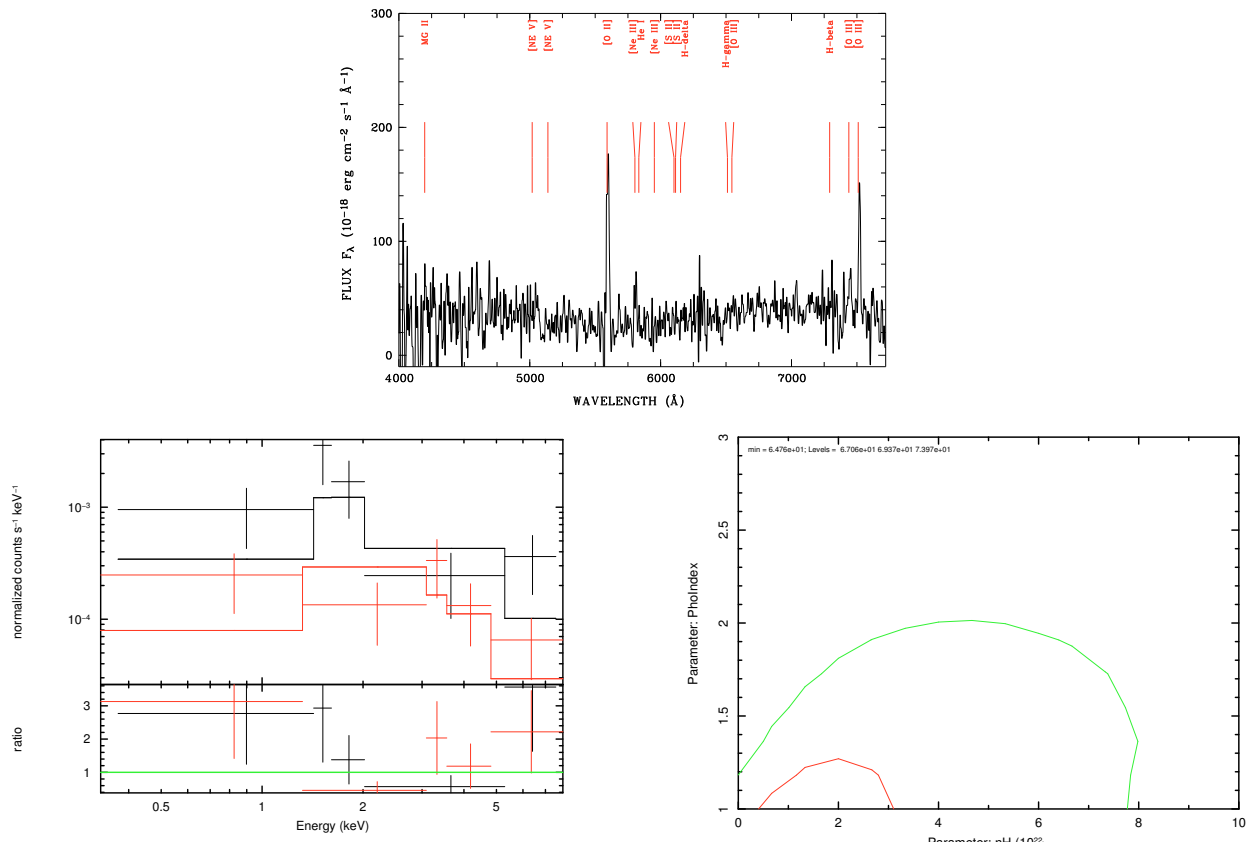
object X03246_092, z = 0.500, frozen $\Gamma = 2.0$ X-ray spectrum fit (0.3-8 keV)
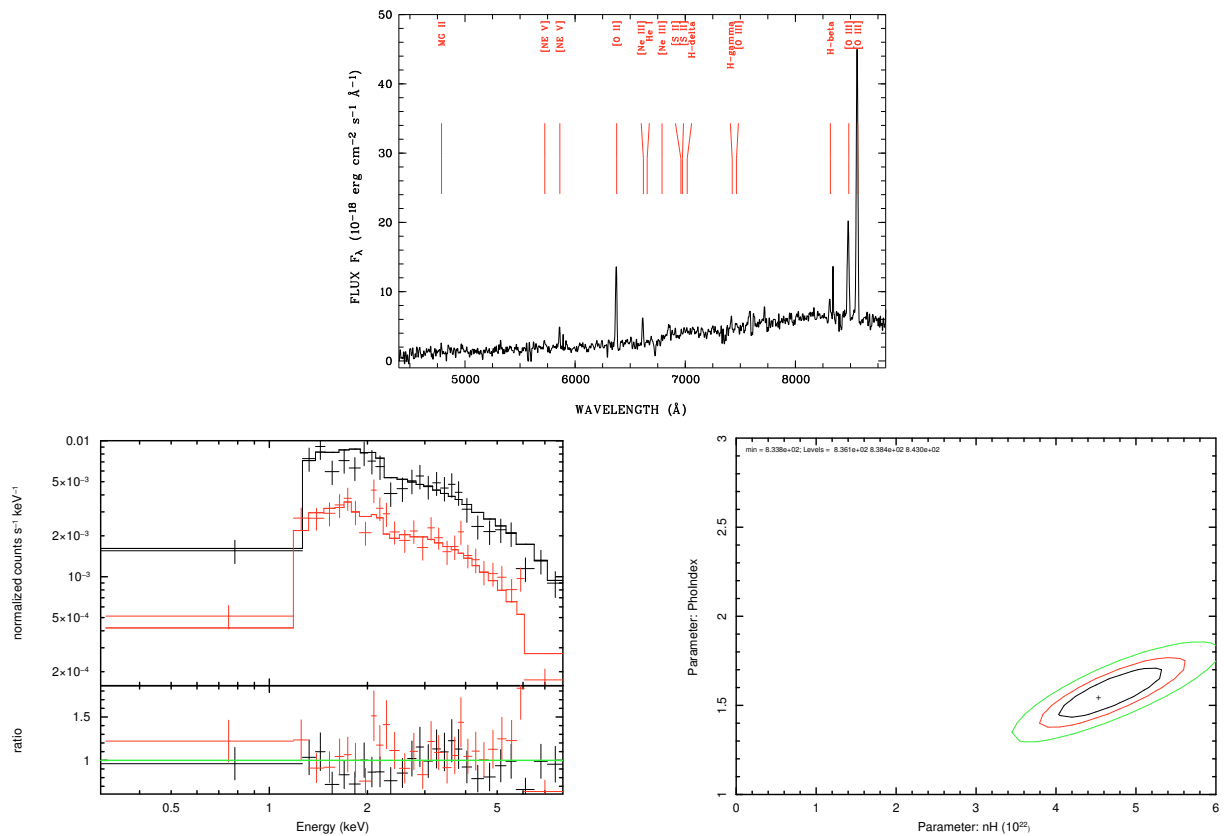
object phl5200-001, z = 0.711, free X-ray spectrum fit

object sds1b-014, z = 0.962, free X-ray spectrum fit

(optical spectrum taken from Akiyama et al. 2007)

Bibliography

ACTON, L.W. (1965). Contribution of Characteristic X-rays to the Radiation of Solar Flares. *Nature*, **207**, 737+. 19

AKIYAMA, M., UEDA, Y., OHTA, K., TAKAHASHI, T. & YAMADA, T. (2003). Optical Identification of the ASCA Medium Sensitivity Survey in the Northern Sky: Nature of Hard X-Ray-Selected Luminous Active Galactic Nuclei. *ApJS*, **148**, 275–315. 25

AKIYAMA ET AL. (2007). Subaru/XMM-Newton Deep Survey (SXDS). *in preparation*. 205

AKYLAS, A., GEORGANTOPOULOS, I., GEORGAKAKIS, A., KITSIONAS, S. & HATZIMINAOGLOU, E. (2006). XMM-Newton and Chandra measurements of the AGN intrinsic absorption: dependence on luminosity and redshift. *A&A*, **459**, 693–701. 65, 80, 86

ALEXANDER, D.M., BAUER, F.E., BRANDT, W.N., HORNSCHEMEIER, A.E., VIGNALI, C., GARMIRE, G.P., SCHNEIDER, D.P., CHARTAS, G. & GALLAGHER, S.C. (2003). The Chandra Deep Field North Survey. XIV. X-Ray-Detected Obscured AGNs and Starburst Galaxies in the Bright Submillimeter Source Population. *AJ*, **125**, 383–397. 33, 107

ANTONUCCI, R. (1993). Unified models for active galactic nuclei and quasars. *ARA&A*, **31**, 473–521. 22

ARETXAGA, I., JOGUET, B., KUNTH, D., MELNICK, J. & TERLEVICH, R.J. (1999). Seyfert 1 Mutation of the Classical Seyfert 2 Nucleus NGC 7582. *ApJL*, **519**, L123–L126. 25

ARNAUD, K.A. (1996). XSPEC: The First Ten Years. In G.H. Jacoby & J. Barnes, eds., *Astronomical Data Analysis Software and Systems V*, vol. 101 of *Astronomical Society of the Pacific Conference Series*, 17+. 54, 73

ASCHENBACH, B. (1985). X-ray telescopes. *Reports of Progress in Physics*, **48**, 579–629. 10

ASCHENBACH, B. & BRINKMANN, W. (1975). A model of the X-ray structure of the Crab Nebula. *A&A*, **41**, 147–151. 18

AVNI, Y. & TANANBAUM, H. (1986). X-ray properties of optically selected QSOs. *ApJ*, **305**, 83–99. 60

BAHCALL, J.N., KIRHAKOS, S., SAXE, D.H. & SCHNEIDER, D.P. (1997). Hubble Space Telescope Images of a Sample of 20 Nearby Luminous Quasars. *ApJ*, **479**, 642+. 21

BARCONS, X., CARRERA, F.J., WATSON, M.G., MCMAHON, R.G., ASCHENBACH, B., FREY-berg, M.J., PAGE, K., PAGE, M.J., ROBERTS, T.P., TURNER, M.J.L., BARRET, D., BRUNNER, H., CEBALLOS, M.T., DELLA CECA, R., GUILLOUT, P., HASINGER, G., MACCACARO, T., MATEOS, S., MOTCH, C., NEGUERUELA, I., OSBORNE, J.P., PÉREZ-FOURNON, I., SCHWOPE, A., SEVERGNINI, P., SZOKOLY, G.P., WEBB, N.A., WHEATLEY, P.J. & WORRALL, D.M. (2002). The XMM-Newton serendipitous survey . II. First results from the AXIS high galactic latitude medium sensitivity survey. *A&A*, **382**, 522–536. 67, 68

BARCONS, X., CARRERA, F.J., CEBALLOS, M.T., PAGE, M.J., BUSSONS-GORDO, J., COR-RAL, A., EBRERO, J., MATEOS, S., TEDDS, J.A., WATSON, M.G., BIRKINSHAW, M., BOLLER, T., BORISOV, N., BREMER, M., BROMAGE, G.E., BRUNNER, H., CACCIANIGA, A., CRAWFORD, C.S., CROPPER, M.S., DELLA CECA, R., DERRY, P., FABIAN, A.C., GUILLOUT, P., HASHIMOTO, Y., HASINGER, G., HASSALL, B.J.M., LAMER, G., LOARING, N.S., MACCACARO, T., MASON, K.O., MCMAHON, R.G., MIRIONI, L., MITTAZ, J.P.D., MOTCH, C., NEGUERUELA, I., OSBORNE, J.P., PANESSA, F., PEREZ-FOURNON, I., PYE, J.P., ROBERTS, T.P., ROSEN, S., SCHARTEL, N., SCHURCH, N., SCHWOPE, A., SEV-ERGNINI, P., SHARP, R., STEWART, G.C., SZOKOLY, G., ULLAN, A., WARD, M.J., WAR-WICK, R.S., WHEATLEY, P.J., WEBB, N.A., WORRALL, D., YUAN, W. & ZIAEEPOUR, H. (2007). The XMM-Newton Serendipitous Survey V. Optical identification of the XMM-Newton Medium sensitivity Survey (XMS). *ArXiv e-prints*, **710**. 24, 67, 68

BARGER, A.J., COWIE, L.L., BRANDT, W.N., CAPAK, P., GARMIRE, G.P., HORNSCHEMEIER, A.E., STEFFEN, A.T. & WEHNER, E.H. (2002). X-Ray, Optical, and Infrared Imaging and Spectral Properties of the 1 Ms Chandra Deep Field North Sources. *AJ*, **124**, 1839–1885. 88

BARGER, A.J., COWIE, L.L., CAPAK, P., ALEXANDER, D.M., BAUER, F.E., FERNANDEZ, E., BRANDT, W.N., GARMIRE, G.P. & HORNSCHEMEIER, A.E. (2003). Optical and Infrared Properties of the 2 Ms Chandra Deep Field North X-Ray Sources. *AJ*, **126**, 632–665. 13, 85

BASSANI, L., DADINA, M., MAIOLINO, R., SALVATI, M., RISALITI, G., DELLA CECA, R., MATT, G. & ZAMORANI, G. (1999). A Three-dimensional Diagnostic Diagram for Seyfert 2 Galaxies: Probing X-Ray Absorption and Compton Thickness. *ApJS*, **121**, 473–482. 65, 81, 82, 87

BLANDFORD, R.D., NETZER, H., WOLTJER, L., COURVOISIER, T.J.L. & MAYOR, M. (1990). *Active Galactic Nuclei*. Saas-Fee Advanced Course 20. Lecture Notes 1990. Swiss Society for Astrophysics and Astronomy, XII, 280 pp. 97 figs.. Springer-Verlag Berlin Heidelberg New York. 20

BOWYER, S., BYRAM, E., CHUBB, T. & FRIEDMAN, H. (1964a). Lunar Occultation of X-ray Emission from the Crab Nebula. *Science*, **146**, 912–917. 8

BOWYER, S., BYRAM, E.T., CHUBB, T.A. & FRIEDMAN, H. (1964b). X-Ray Sources in the Galaxy. *Nature*, **201**, 1307+. 16

BRADT, H.V.D., OHASHI, T. & POUNDS, K.A. (1992). X-ray astronomy missions. *ARA&A*, **30**, 391–427. 8

BRANDT, W.N. & HASINGER, G. (2005). Deep Extragalactic X-Ray Surveys. *ARA&A*, **43**, 827–859. 12, 28, 37, 63, 64, 82

BRUSA, M., COMASTRI, A., MIGNOLI, M., FIORE, F., CILIEGI, P., VIGNALI, C., SEVERGNINI, P., COCCHIA, F., LA FRANCA, F., MATT, G., PEROLA, G.C., MAIOLINO, R., BALDI, A. & MOLENDI, S. (2003). The HELLAS2XMM survey. III. Multiwavelength observations of hard X-ray selected sources in the PKS 0312-77 field. *A&A*, **409**, 65–78. 25

BURBIDGE, G. & BURBIDGE, E. (1967). *Quasi-stellar objects*. San Francisco, W.H. Freeman. 19

BURNIGHT, T. (1949). Soft X-Radiation in the Upper Atmosphere. *Physical Review*, **176**, 165. 8

CACCIANIGA, A., SEVERGNINI, P., BRAITO, V., DELLA CECA, R., MACCACARO, T., WOLTER, A., BARCONS, X., CARRERA, F.J., LEHMANN, I., PAGE, M.J., SAXTON, R. & WEBB, N.A. (2004). The XMM-Newton HBS28 sample: Studying the obscuration in hard X-ray selected AGNs. *A&A*, **416**, 901–915. 25, 50, 62, 63

CAMERON, A.G. (1959). Neutron Star Models. *ApJ*, **130**, 884+. 16

CARRERA, F.J., EBRERO, J., MATEOS, S., CEBALLOS, M.T., CORRAL, A., BARCONS, X., PAGE, M.J., ROSEN, S.R., WATSON, M.G., TEDDS, J.A., DELLA CECA, R., MACCACARO, T., BRUNNER, H., FREYBERG, M., LAMER, G., BAUER, F.E. & UEDA, Y. (2007). The XMM-Newton serendipitous survey. III. The AXIS X-ray source counts and angular clustering. *A&A*, **469**, 27–46. 67, 68

CASH, W. (1979). Parameter estimation in astronomy through application of the likelihood ratio. *ApJ*, **228**, 939–947. 39, 74

CHARLES, P. & SEWARD, F. (1995). *Exploring the X-ray Universe*. Cambridge University Press. 7, 9, 17, 18, 28

CILIEGI, P., ZAMORANI, G., HASINGER, G., LEHMANN, I., SZOKOLY, G. & WILSON, G. (2003). A deep VLA survey at 6 cm in the Lockman Hole. *A&A*, **398**, 901–918. 46

COHEN, R.D., PUETTER, R.C., RUDY, R.J., AKE, T.B. & FOLTZ, C.B. (1986). Variability of Markarian 1018 - Seyfert 1.9 to Seyfert 1. *ApJ*, **311**, 135–141. 25

COMASTRI, A. (2004). Compton-Thick AGN: The Dark Side of the X-Ray Background. In A.J. Barger, ed., *Supermassive Black Holes in the Distant Universe*, vol. 308 of *Astrophysics and Space Science Library*, 245+. 13, 14, 66, 81

COMASTRI, A., SETTI, G., ZAMORANI, G. & HASINGER, G. (1995). The contribution of AGNs to the X-ray background. *A&A*, **296**, 1+. 13

COMASTRI, A., FIORE, F., VIGNALI, C., MATT, G., PEROLA, G.C. & LA FRANCA, F. (2001). The BeppoSAX High Energy Large Area Survey (HELLAS) - III. Testing synthesis models for the X-ray background. *MNRAS*, **327**, 781–787. 12, 25

COMASTRI, A., MIGNOLI, M., CILIEGI, P., SEVERGNINI, P., MAIOLINO, R., BRUSA, M., FIORE, F., BALDI, A., MOLENDI, S., MORGANTI, R., VIGNALI, C., LA FRANCA, F., MATT, G. & PEROLA, G.C. (2002). The HELLAS2XMM Survey. II. Multiwavelength Observations of P3: An X-Ray-bright, Optically Inactive Galaxy. *ApJ*, **571**, 771–778. 28, 63

CORRAL ET AL. (2007). Stacking of X-ray spectra. *in preparation*. 78

CZERNY, B., NIKOŁAJUK, M., RÓŻAŃSKA, A., DUMONT, A.M., LOSKA, Z. & ZYCKI, P.T. (2003). Universal spectral shape of high accretion rate AGN. *A&A*, **412**, 317–329. 28, 30

DELLA CECA, R., MACCACARO, T., CACCIANIGA, A., SEVERGNINI, P., BRAITO, V., BARCONS, X., CARRERA, F.J., WATSON, M.G., TEDDS, J.A., BRUNNER, H., LEHMANN, I., PAGE, M.J., LAMER, G. & SCHWOPE, A. (2004). Exploring the X-ray sky with the XMM-Newton bright serendipitous survey. *A&A*, **428**, 383–399. 50, 67

DERMER, C.D., SCHLICKEISER, R. & MASTICHIADIS, A. (1992). High-energy gamma radiation from extragalactic radio sources. *A&A*, **256**, L27–L30. 18

DWELLY, T. & PAGE, M.J. (2006). The distribution of absorption in AGN detected in the XMM-Newton observations of the CDFS. *MNRAS*, **372**, 1755–1775. 65, 86

ELITZUR, M. (2006). Unification Issues and the AGN Torus. *ArXiv Astrophysics e-prints*. 26, 27, 89

ELITZUR, M. & SHLOSMAN, I. (2006). The AGN-obscuring Torus: The End of the "Doughnut" Paradigm? *ApJL*, **648**, L101–L104. 27

ELITZUR, M., NENKOVA, M. & IVEZIĆ, Z. (2004). IR emission from AGNs. In S. Aalto, S. Huttemeister & A. Pedlar, eds., *The Neutral ISM in Starburst Galaxies*, vol. 320 of *Astronomical Society of the Pacific Conference Series*, 242+. 24, 26, 27

FABIAN, A.C. (1999). X-ray studies of black holes in AGN. In B. Aschenbach & M.J. Freyberg, eds., *Highlights in X-ray Astronomy*, 127+. 29

FABIAN, A.C. & IWASAWA, K. (1999). The mass density in black holes inferred from the X-ray background. *MNRAS*, **303**, L34–L36. 13

FELTEN, J.E. & MORRISON, P. (1966). Omnidirectional Inverse Compton and Synchrotron Radiation from Cosmic Distributions of Fast Electrons and Thermal Photons. *ApJ*, **146**, 686+. 11

FRIEDMAN, H. (1960). Recent experiments from rockets and satellites. *AJ*, **65**, 264+. 8

FRIEDMAN, H., LICHTMAN, S. & BYRAM, E. (1951). Photon Counter Measurements of Solar X-rays and Extreme Ultraviolet Light. *Physical Review*, **83**, 1025–1030. 8

GABRIEL, C., DENBY, M., FYFE, D.J., HOAR, J., IBARRA, A., OJERO, E., OSBORNE, J., SAXTON, R.D., LAMMERS, U. & VACANTI, G. (2004). The XMM-Newton SAS - Distributed Development and Maintenance of a Large Science Analysis System: A Critical Analysis. In

F. Ochsenbein, M.G. Allen & D. Egret, eds., *Astronomical Data Analysis Software and Systems (ADASS) XIII*, vol. 314 of *Astronomical Society of the Pacific Conference Series*, 759+. 38, 73

GEORGE, I.M. & FABIAN, A.C. (1991). X-ray reflection from cold matter in active galactic nuclei and X-ray binaries. *MNRAS*, **249**, 352–367. 31

GERTHSEN, C., KNESER, H. & VOGEL, H. (1986). *Physik*. Springer-Verlag Berlin Heidelberg New York Tokyo, 15. Auflage. 5, 6

GIACCONI, R. & GURSKY, H. (1965). Observation of X-Ray Sources Outside the Solar System. *Space Science Reviews*, **4**, 151–175. 8, 10, 12

GIACCONI, R., GURSKY, H., PAOLINI, F.R. & ROSSI, B.B. (1962). Evidence for x Rays From Sources Outside the Solar System. *Physical Review Letters*, **9**, 439–443. xv, xvii, 8, 9, 11

GIACCONI, R., BECHTOLD, J., BRANDUARDI, G., FORMAN, W., HENRY, J.P., JONES, C., KELLOGG, E., VAN DER LAAN, H., LILLER, W., MARSHALL, H., MURRAY, S.S., PYE, J., SCHREIER, E., SARGENT, W.L.W., SEWARD, F. & TANANBAUM, H. (1979). A high-sensitivity X-ray survey using the Einstein Observatory and the discrete source contribution to the extragalactic X-ray background. *ApJL*, **234**, L1–L7. 10, 11

GILLI, R., COMASTRI, A. & HASINGER, G. (2007). The synthesis of the cosmic X-ray background in the Chandra and XMM-Newton era. *A&A*, **463**, 79–96. 65

GREEN, P.J., SCHARTEL, N., ANDERSON, S.F., HEWETT, P.C., FOLTZ, C.B., BRINKMANN, W., FINK, H., TRUEMPER, J. & MARGON, B. (1995). The Soft X-Ray Properties of a Large Optical QSO Sample: ROSAT Observations of the Large Bright Quasar Survey. *ApJ*, **450**, 51+. 60

GREEN, P.J., SILVERMAN, J.D., CAMERON, R.A., KIM, D.W., WILKES, B.J., BARKHOUSE, W.A., LACLUYZÉ, A., MORRIS, D., MOSSMAN, A., GHOSH, H., GRIMES, J.P., JANNUZI, B.T., TANANBAUM, H., ALDCROFT, T.L., BALDWIN, J.A., CHAFFEE, F.H., DEY, A., DOSAJ, A., EVANS, N.R., FAN, X., FOLTZ, C., GAETZ, T., HOOPER, E.J., KASHYAP, V.L., MATHUR, S., MCGARRY, M.B., ROMERO-COLMENERO, E., SMITH, M.G., SMITH, P.S., SMITH, R.C., TORRES, G., VIKHLININ, A. & WIK, D.R. (2004). The Chandra Multi-wavelength Project: Optical Follow-up of Serendipitous Chandra Sources. *ApJS*, **150**, 43–71. 36

GREENSTEIN, J.L. & MATTHEWS, T.A. (1963). Red-Shift of the Unusual Radio Source 3C48. *Nature*, **197**, 1041+. 19

GREULICH, W. (1998). *Lexikon der Physik*. Spektrum, Akad. Verl., Heidelberg. 9

GRUBER, D.E., MATTESON, J.L., PETERSON, L.E. & JUNG, G.V. (1999). The Spectrum of Diffuse Cosmic Hard X-Rays Measured with HEAO 1. *ApJ*, **520**, 124–129. 9, 10

GRUPPIONI, C., ZAMORANI, G., DE RUITER, H.R., PARMA, P., MIGNOLI, M. & LARI, C. (1997). Radio observations of the Marano Field and the faint radio galaxy population. *MNRAS*, **286**, 470–482. 35, 36, 63, 109

GURSKY, H., GIACCONI, R., PAOLINI, F. & ROSSI, B. (1963). Further Evidence for the Existence of Galactic x Rays. *Phys. Rev. Lett.*, **11**, 530–535. 8

HAARDT, F. & MARASCHI, L. (1993). X-ray spectra from two-phase accretion disks. *ApJ*, **413**, 507–517. 28

HAMBLY, N.C., MACGILLIVRAY, H.T., READ, M.A., TRITTON, S.B., THOMSON, E.B., KELLY, B.D., MORGAN, D.H., SMITH, R.E., DRIVER, S.P., WILLIAMSON, J., PARKER, Q.A., HAWKINS, M.R.S., WILLIAMS, P.M. & LAWRENCE, A. (2001). The SuperCOSMOS Sky Survey - I. Introduction and description. *MNRAS*, **326**, 1279–1294. 68, 69

HAO, L., STRAUSS, M.A., TREMONTI, C.A., SCHLEGEL, D.J., HECKMAN, T.M., KAUFF-MANN, G., BLANTON, M.R., FAN, X., GUNN, J.E., HALL, P.B., IVEZIĆ, Ž., KNAPP, G.R., KROLIK, J.H., LUPTON, R.H., RICHARDS, G.T., SCHNEIDER, D.P., STRATEVA, I.V., ZA-KAMSKA, N.L., BRINKMANN, J., BRUNNER, R.J. & SZOKOLY, G.P. (2005). Active Galactic Nuclei in the Sloan Digital Sky Survey. I. Sample Selection. *AJ*, **129**, 1783–1794. 21, 68

HASINGER, G., BURG, R., GIACCONI, R., SCHMIDT, M., TRUMPER, J. & ZAMORANI, G. (1998). The ROSAT Deep Survey. I. X-ray sources in the Lockman Field. *A&A*, **329**, 482–494. 11, 13, 33, 36

HASINGER, G., ALTIERI, B., ARNAUD, M., BARCONS, X., BERGERON, J., BRUNNER, H., DAD-INA, M., DENNERL, K., FERRANDO, P., FINOGUENOV, A., GRIFFITHS, R.E., HASHIMOTO, Y., JANSEN, F.A., LUMB, D.H., MASON, K.O., MATEOS, S., MCMAHON, R.G., MIYAJI, T., PAERELS, F., PAGE, M.J., PTAK, A.F., SASSEEN, T.P., SCHARTEL, N., SZOKOLY, G.P., TRÜMPER, J., TURNER, M., WARWICK, R.S. & WATSON, M.G. (2001). XMM-Newton observation of the Lockman Hole. I. The X-ray data. *A&A*, **365**, L45–L50. 13, 33, 48

HASINGER, G., MIYAJI, T. & SCHMIDT, M. (2005). Luminosity-dependent evolution of soft X-ray selected AGN. New Chandra and XMM-Newton surveys. *A&A*, **441**, 417–434. 14

HECKMAN, T.M. (1980). An optical and radio survey of the nuclei of bright galaxies - Activity in normal galactic nuclei. *A&A*, **87**, 152–164. 20

HENRY, R.C. (1999). Diffuse Background Radiation. *ApJL*, **516**, L49–L52. 11, 12

HESS, V.F. (1912). Durchdringende Strahlung bei sieben Freiballonfahrten. *Physikalische Zeitschrift*, **13**, 1084–1091. 7, 11

HO, L.C., FILIPPENKO, A.V. & SARGENT, W.L.W. (1993). A Reevaluation of the Excitation Mechanism of LINERs. *ApJ*, **417**, 63+. 20

HORNE, K. (1986). An optimal extraction algorithm for CCD spectroscopy. *PASP*, **98**, 609–617. 45

HORST, H., SMETTE, A., GANDHI, P. & DUSCHL, W.J. (2006). The small dispersion of the mid IR - hard X-ray correlation in active galactic nuclei. *A&A*, **457**, L17–L20. 25

ISOBE, T., FEIGELSON, E.D., AKRITAS, M.G. & BABU, G.J. (1990). Linear regression in astronomy. *ApJ*, **364**, 104–113. 60

IWASAWA, K. & TANIGUCHI, Y. (1993). The X-ray Baldwin effect. *ApJL*, **413**, L15–L18. 31

IWASAWA, K., MATT, G., FABIAN, A.C., BIANCHI, S., BRANDT, W.N., GUAINAZZI, M., MURAYAMA, T. & TANIGUCHI, Y. (2001). Nuclear obscuration in the high-ionization Seyfert 2 galaxy Tol 0109-383. *MNRAS*, **326**, 119–125. 81

JAFFE, W., MEISENHEIMER, K., RÖTTGERING, H.J.A., LEINERT, C., RICHICHI, A., CHESNEAU, O., FRAIX-BURNET, D., GLAZENBORG-KLUTTIG, A., GRANATO, G.L., GRASER, U., HEIJLIGERS, B., KÖHLER, R., MALBET, F., MILEY, G.K., PARESCE, F., PEL, J.W., PERRIN, G., PRZYGODDA, F., SCHOELLER, M., SOL, H., WATERS, L.B.F.M., WEIGELT, G., WOILLEZ, J. & DE ZEEUW, P.T. (2004). The central dusty torus in the active nucleus of NGC 1068. *Nature*, **429**, 47–49. 25

KASPI, S., SMITH, P.S., NETZER, H., MAOZ, D., JANNUZI, B.T. & GIVEON, U. (2000). Reverberation Measurements for 17 Quasars and the Size-Mass-Luminosity Relations in Active Galactic Nuclei. *ApJ*, **533**, 631–649. 24

KELLERMANN, K.I., SRAMEK, R., SCHMIDT, M., SHAFFER, D.B. & GREEN, R. (1989). VLA observations of objects in the Palomar Bright Quasar Survey. *AJ*, **98**, 1195–1207. 20

KEMBHAVI, A. & NARLIKAR, J. (2000). Book Review: Quasars and active galactic nuclei : an introduction / Cambridge U Press, 1999. *Physics Today*, **53**, 60+. 20

KENNICUTT, R.C., JR. (1992). The integrated spectra of nearby galaxies - General properties and emission-line spectra. *ApJ*, **388**, 310–327. 47

KHACHIKIAN, E.Y. & WEEDMAN, D.W. (1974). An atlas of Seyfert galaxies. *ApJ*, **192**, 581–589. 21

KLEINMANN, S.G., HAMILTON, D., KEEL, W.C., WYNN-WILLIAMS, C.G., EALES, S.A., BECKLIN, E.E. & KUNTZ, K.D. (1988). The properties and environment of the giant, infrared-luminous galaxy IRAS 09104 + 4109. *ApJ*, **328**, 161–169. 21

KOMOSSA, S., SCHULZ, H. & GREINER, J. (1998). ROSAT HRI discovery of luminous extended X-ray emission in NGC 6240. *A&A*, **334**, 110–116. 63

KROLIK, J.H. & BEGELMAN, M.C. (1988). Molecular tori in Seyfert galaxies - Feeding the monster and hiding it. *ApJ*, **329**, 702–711. 26

KRUMPE, M., LAMER, G., SCHWOPE, A.D., CORRAL, A., CARRERA, F.J., BARCONS, X., PAGE, M., MATEOS, S., TEDDS, J.A. & WATSON, M.G. (2007a). X-ray absorption in distant type II QSOs. *submitted to A&A*. 66

KRUMPE, M., LAMER, G., SCHWOPE, A.D. & HUSEMANN, B. (2007b). RBS1423 - a new QSO with relativistic reflection from an ionised disk. *A&A*, **470**, 497–503. 32

KRUMPE, M., LAMER, G., SCHWOPE, A.D., WAGNER, S., ZAMORANI, G., MIGNOLI, M., STAUBERT, R., WISOTZKI, L. & HASINGER, G. (2007c). The XMM-Newton survey in the Marano field. I. The X-ray data and optical follow-up. *A&A*, **466**, 41–61. 24, 36, 37, 68, 73

LA FRANCA, F., FIORE, F., COMASTRI, A., PEROLA, G.C., SACCHI, N., BRUSA, M., COC-CHIA, F., FERUGLIO, C., MATT, G., VIGNALI, C., CARANGELO, N., CILIEGI, P., LAMAS-TRA, A., MAIOLINO, R., MIGNOLI, M., MOLENDI, S. & PUCCETTI, S. (2005). The HEL-LAS2XMM Survey. VII. The Hard X-Ray Luminosity Function of AGNs up to z = 4: More Absorbed AGNs at Low Luminosities and High Redshifts. *ApJ*, **635**, 864–879. 65, 80, 87

LAMER, G., BRUNNER, H. & STAUBERT, R. (1997). Properties of optically and X-ray selected quasars. *A&A*, **327**, 467–478. 60

LAMER, G., UTTLEY, P. & MCHARDY, I.M. (2003). An absorption event in the X-ray light curve of NGC 3227. *MNRAS*, **342**, L41–L45. 25, 89

LAMPTON, M., MARGON, B. & BOWYER, S. (1976). Parameter estimation in X-ray astronomy. *ApJ*, **208**, 177–190. 55

LAOR, A. (1991). Line profiles from a disk around a rotating black hole. *ApJ*, **376**, 90–94. 31

LEHMANN, I., HASINGER, G., SCHMIDT, M., GIACCONI, R., TRÜMPER, J., ZAMORANI, G., GUNN, J.E., POZZETTI, L., SCHNEIDER, D.P., STANKE, T., SZOKOLY, G., THOMPSON, D. & WILSON, G. (2001). The ROSAT Deep Survey. VI. X-ray sources and Optical identifications of the Ultra Deep Survey. *A&A*, **371**, 833–857. 11, 33

LENK, R. & GELLERT, W. (1989). *Physik - Band 2/Ma-Z*. VEB F.A. Brockhaus Verlag Leipzig, DDR. 2

LUTZ, D., MAIOLINO, R., SPOON, H.W.W. & MOORWOOD, A.F.M. (2004). The relation between AGN hard X-ray emission and mid-infrared continuum from ISO spectra: Scatter and unification aspects. *A&A*, **418**, 465–473. 25

LYNDEN-BELL, D. (1969). Galactic Nuclei as Collapsed Old Quasars. *Nature*, **223**, 690+. 20

MAINIERI, V., BERGERON, J., HASINGER, G., LEHMANN, I., ROSATI, P., SCHMIDT, M., SZOKOLY, G. & DELLA CECA, R. (2002). XMM-Newton observation of the Lockman Hole. II. Spectral analysis. *A&A*, **393**, 425–438. 24, 50, 54, 55, 56, 57, 59, 66, 72, 74, 80, 81, 87, 88, 107

MAIOLINO, R., SALVATI, M., BASSANI, L., DADINA, M., DELLA CECA, R., MATT, G., RISAL-ITI, G. & ZAMORANI, G. (1998). Heavy obscuration in X-ray weak AGNs. *A&A*, **338**, 781–794. 65, 81

MARANO, B., ZAMORANI, G. & ZITELLI, V. (1988). A new sample of quasars to B = 22.0. *MNRAS*, **232**, 111–129. 35, 36, 48, 109

MARSHALL, F.E., BOLDT, E.A., HOLT, S.S., MILLER, R.B., MUSHOTZKY, R.F., ROSE, L.A., ROTHSCHILD, R.E. & SERLEMITSOS, P.J. (1980). The diffuse X-ray background spectrum from 3 to 50 keV. *ApJ*, **235**, 4–10. 9, 11

MARTÍNEZ-SANSIGRE, A., RAWLINGS, S., BONFIELD, D.G., MATEOS, S., SIMPSON, C., WAT-SON, M., ALMAINI, O., FOUCAUD, S., SEKIGUCHI, K. & UEDA, Y. (2007). Evidence for a large fraction of Compton-thick quasars at high redshift. *MNRAS*, **379**, L6–L10. 14, 66

MASON, R.E., GEBALLE, T.R., PACKHAM, C., LEVENSON, N.A., ELITZUR, M., FISHER, R.S. & PERLMAN, E. (2006). Spatially Resolved Mid-Infrared Spectroscopy of NGC 1068: The Nature and Distribution of the Nuclear Material. *ApJ*, **640**, 612–624. 25

MATEOS, S., BARCONS, X., CARRERA, F.J., CEBALLOS, M.T., HASINGER, G., LEHMANN, I., FABIAN, A.C. & STREBLYANSKA, A. (2005). XMM-Newton observations of the Lockman Hole IV: spectra of the brightest AGN. *A&A*, **444**, 79–99. 54, 66, 74, 87

MATHER, J.C., CHENG, E.S., EPLEE, R.E., JR., ISAACMAN, R.B., MEYER, S.S., SHAFER, R.A., WEISS, R., WRIGHT, E.L., BENNETT, C.L., BOGGESS, N.W., DWEK, E., GULKIS, S., HAUSER, M.G., JANSSEN, M., KELSALL, T., LUBIN, P.M., MOSELEY, S.H., JR., MURDOCK, T.L., SILVERBERG, R.F., SMOOT, G.F. & WILKINSON, D.T. (1990). A preliminary measurement of the cosmic microwave background spectrum by the Cosmic Background Explorer (COBE) satellite. *ApJL*, **354**, L37–L40. 11

MCHARDY, I.M., JONES, L.R., MERRIFIELD, M.R., MASON, K.O., NEWSAM, A.M., ABRAHAM, R.G., DALTON, G.B., CARRERA, F., SMITH, P.J., ROWAN-ROBINSON, M., WEGNER, G.A., PONMAN, T.J., LEHTO, H.J., BRANDUARDI-RAYMONT, G., LUPPINO, G.A., EFSTATHIOU, G., ALLAN, D.J. & QUENBY, J.J. (1998). The origin of the cosmic soft X-ray background - Optical identification of an extremely deep ROSAT survey. *MNRAS*, **295**, 641+. 11, 12

MCLEOD, K.K. & RIEKE, G.H. (1995). Luminous Quasars in Luminous Early-Type Host Galaxies. *ApJL*, **454**, L77+. 21

MCLURE, R.J., KUKULA, M.J., DUNLOP, J.S., BAUM, S.A., O'DEA, C.P. & HUGHES, D.H. (1999). A comparative HST imaging study of the host galaxies of radio-quiet quasars, radio-loud quasars and radio galaxies - I. *MNRAS*, **308**, 377–404. 21

MIGNOLI, M. & ZAMORANI, C. (1998). A Multi-Colour Deep CCD Survey in the Marano Field: The Final Catalogue. In S. D'Odorico, A. Fontana & E. Giallongo, eds., *The Young Universe: Galaxy Formation and Evolution at Intermediate and High Redshift*, vol. 146 of *Astronomical Society of the Pacific Conference Series*, 80+. 36

NETZER, H. & LAOR, A. (1993). Dust in the narrow-line region of active galactic nuclei. *ApJL*, **404**, L51–L54. 27

NETZER, H. & PETERSON, B.M. (1997). Reverberation Mapping and the Physics of Active Galactic Nuclei. In D. Maoz, A. Sternberg & E.M. Leibowitz, eds., *Astronomical Time Series*, vol. 218 of *Astrophysics and Space Science Library*, 85+. 24

NORMAN, C., HASINGER, G., GIACCONI, R., GILLI, R., KEWLEY, L., NONINO, M., ROSATI, P., SZOKOLY, G., TOZZI, P., WANG, J., ZHENG, W., ZIRM, A., BERGERON, J., GILMOZZI, R., GROGIN, N., KOEKEMOER, A. & SCHREIER, E. (2002). A Classic Type 2 QSO. *ApJ*, **571**, 218–225. 66, 87

OKE, J.B. & GUNN, J.E. (1974). The Distance of BL Lacertae. *ApJL*, **189**, L5+. 21

OKE, J.B. & GUNN, J.E. (1983). Secondary standard stars for absolute spectrophotometry. *ApJ*, **266**, 713–717. 108

OSBORNE, J. (2001). . *SSC-LUX-TN-0059 (issue3), http:--xmmssc-www.star.le.ac.uk/pubdocs/SSC-LUX-TN-0059_3.ps.gz*. 38

OSTERBROCK, D.E. (1981). Seyfert galaxies with weak broad H alpha emission lines. *ApJ*, **249**, 462–470. 21

PAGE, M.J., DAVIS, S.W. & SALVI, N.J. (2003). The origin of the Fe K features in Markarian 205 and Markarian 509. *MNRAS*, **343**, 1241–1247. 73

PANESSA, F. & BASSANI, L. (2002). Unabsorbed Seyfert 2 galaxies. *A&A*, **394**, 435–442. 25

PENZIAS, A.A. & WILSON, R.W. (1965). A Measurement of Excess Antenna Temperature at 4080 Mc/s. *ApJ*, **142**, 419–421. 11

PEROLA, G.C., PUCCETTI, S., FIORE, F., SACCHI, N., BRUSA, M., COCCHIA, F., BALDI, A., CARANGELO, N., CILIEGI, P., COMASTRI, A., LA FRANCA, F., MAIOLINO, R., MATT, G., MIGNOLI, M., MOLENDI, S. & VIGNALI, C. (2004). The HELLAS2XMM survey. VI. X-ray absorption in the 1df AGN sample through a spectral analysis. *A&A*, **421**, 491–501. 25

PETERSON, B.M. & WANDEL, A. (2000). Evidence for Supermassive Black Holes in Active Galactic Nuclei from Emission-Line Reverberation. *ApJL*, **540**, L13–L16. 24

POUNDS, K. & REEVES, J. (2002). What can we learn from EPIC X-ray spectra of Seyfert 1 galaxies? *ArXiv Astrophysics e-prints*. 29

PTAK, A., ZAKAMSKA, N.L., STRAUSS, M.A., KROLIK, J.H., HECKMAN, T.M., SCHNEIDER, D.P. & BRINKMANN, J. (2006). Type II Quasars from the Sloan Digital Sky Survey. IV. Chandra and XMM-Newton Observations Reveal Heavily Absorbed Sources. *ApJ*, **637**, 147–156. 66, 80, 87

REEVES, J.N. & TURNER, M.J.L. (2000). X-ray spectra of a large sample of quasars with ASCA. *MNRAS*, **316**, 234–248. 28

REYNOLDS, C.S. & NOWAK, M.A. (2003). Fluorescent iron lines as a probe of astrophysical black hole systems. *Phys. Rep.*, **377**, 389–466. 29, 31

RISALITI, G., GILLI, R., MAIOLINO, R. & SALVATI, M. (2000). The hard X-ray emission of luminous infrared galaxies. *A&A*, **357**, 13–23. 65, 81, 87

RISALITI, G., ELVIS, M. & NICASTRO, F. (2002). Ubiquitous Variability of X-Ray-absorbing Column Densities in Seyfert 2 Galaxies. *ApJ*, **571**, 234–246. 25, 27

RISALITI, G., ELVIS, M., FABBIANO, G., BALDI, A., ZEZAS, A. & SALVATI, M. (2007). Occultation Measurement of the Size of the X-Ray-emitting Region in the Active Galactic Nucleus of NGC 1365. *ApJL*, **659**, L111–L114. 25, 89

ROSATI, P., DELLA CECA, R., NORMAN, C. & GIACCONI, R. (1998). The ROSAT Deep Cluster Survey: The X-Ray Luminosity Function Out to $z = 0.8$. *ApJL*, **492**, L21+. 40

ROSS, R.R. & FABIAN, A.C. (2005). A comprehensive range of X-ray ionized-reflection models. *MNRAS*, **358**, 211–216. 29, 31, 32

RYBICKI, G. & LIGHTMAN, A. (2004). *Radiative Processes in Astrophysics*. Wiley-VCH Verlag GmbH & Co. KGaA, Weinheim. 18, 28

SALPETER, E.E. (1964). Accretion of Interstellar Matter by Massive Objects. *ApJ*, **140**, 796–800. 20

SANDAGE, A., OSMER, P., GIACCONI, R., GORENSTEIN, P., GURSKY, H., WATERS, J., BRADT, H., GARMIRE, G., SREEKANTAN, B.V., ODA, M., OSAWA, K. & JUGAKU, J. (1966). On the optical identification of SCO X-1. *ApJ*, **146**, 316+. 8

SARAJEDINI, V.L., GREEN, R.F., GRIFFITHS, R.E. & RATNATUNGA, K. (1999). Compact Nuclei in Galaxies at Moderate Redshift. II. Their Nature and Implications for the Active Galactic Nucleus Luminosity Function. *ApJ*, **514**, 746–764. 21

SARAZIN, C.L. (1997). X-ray Emission from Elliptical Galaxies. In M. Arnaboldi, G.S. Da Costa & P. Saha, eds., *The Nature of Elliptical Galaxies; 2nd Stromlo Symposium*, vol. 116 of *Astronomical Society of the Pacific Conference Series*, 375+. 63

SCHMIDT, M. (1963). 3C 273 : A Star-Like Object with Large Red-Shift. *Nature*, **197**, 1040+. 19

SCHMIDT, M. & GREEN, R.F. (1983). Quasar evolution derived from the Palomar bright quasar survey and other complete quasar surveys. *ApJ*, **269**, 352–374. 21

SCHWARTZ, D.A. (1980). Irregularities in the X-ray background. *Phys. Scr*, **21**, 644–649. 11

SETTI, G. & WOLTJER, L. (1989). Active Galactic Nuclei and the spectrum of the X-ray background. *A&A*, **224**, L21–L23. 13

SEVERGNINI, P., CACCIANIGA, A., BRAITO, V., DELLA CECA, R., MACCACARO, T., WOLTER, A., SEKIGUCHI, K., SASAKI, T., YOSHIDA, M., AKIYAMA, M., WATSON, M.G., BARCONS, X., CARRERA, F.J., PIETSCH, W. & WEBB, N.A. (2003). XMM-Newton observations reveal AGN in apparently normal galaxies. *A&A*, **406**, 483–492. 63

SEYFERT, C.K. (1943). Nuclear Emission in Spiral Nebulae. *ApJ*, **97**, 28+. 20

SIEGBAHN, K. (1968). *Alpha, Beta and Gamma Ray Spectroscopy, Vol. 1*. North-Holland Publishing Company, Amsterdam, 1st edition. 3

SILVERMAN, J.D., GREEN, P.J., BARKHOUSE, W.A., KIM, D.W., ALDCROFT, T.L., CAMERON, R.A., WILKES, B.J., MOSSMAN, A., GHOSH, H., TANANBAUM, H., SMITH, M.G., SMITH, R.C., SMITH, P.S., FOLTZ, C., WIK, D. & JANNUZI, B.T. (2005). Hard X-Ray-emitting Active Galactic Nuclei Selected by the Chandra Multiwavelength Project. *ApJ*, **618**, 123–138. 63

SMITH, H.J. & HOFFLEIT, D. (1961). Photographic History and Suggested Nature of the Radio Source 3C 48. *PASP*, **73**, 292+. 19

STEFFEN, A.T., STRATEVA, I., BRANDT, W.N., ALEXANDER, D.M., KOEKEMOER, A.M., LEHMER, B.D., SCHNEIDER, D.P. & VIGNALI, C. (2006). The X-Ray-to-Optical Properties of Optically Selected Active Galaxies over Wide Luminosity and Redshift Ranges. *AJ*, **131**, 2826–2842. 60, 61

STEIDEL, C.C., HUNT, M.P., SHAPLEY, A.E., ADELBERGER, K.L., PETTINI, M., DICKINSON, M. & GIAVALISCO, M. (2002). The Population of Faint Optically Selected Active Galactic Nuclei at z ~ 3. *ApJ*, **576**, 653–659. 21

STERN, B.E., POUTANEN, J., SVENSSON, R., SIKORA, M. & BEGELMAN, M.C. (1995). On the Geometry of the X-Ray–Emitting Region in Seyfert Galaxies. *ApJL*, **449**, L13+. 29

SUGANUMA, M., YOSHII, Y., KOBAYASHI, Y., MINEZAKI, T., ENYA, K., TOMITA, H., AOKI, T., KOSHIDA, S. & PETERSON, B.A. (2006). Reverberation Measurements of the Inner Radius of the Dust Torus in Nearby Seyfert 1 Galaxies. *ApJ*, **639**, 46–63. 27

SUTHERLAND, W. & SAUNDERS, W. (1992). On the likelihood ratio for source identification. *MNRAS*, **259**, 413–420. 46

SZOKOLY, G.P., BERGERON, J., HASINGER, G., LEHMANN, I., KEWLEY, L., MAINIERI, V., NONINO, M., ROSATI, P., GIACCONI, R., GILLI, R., GILMOZZI, R., NORMAN, C., RO-MANIELLO, M., SCHREIER, E., TOZZI, P., WANG, J.X., ZHENG, W. & ZIRM, A. (2004). The Chandra Deep Field-South: Optical Spectroscopy. I. *ApJS*, **155**, 271–349. 24, 53, 54, 57, 62, 65, 66, 72, 80, 85, 87, 88, 107

TANANBAUM, H., AVNI, Y., BRANDUARDI, G., ELVIS, M., FABBIANO, G., FEIGELSON, E., GIACCONI, R., HENRY, J.P., PYE, J.P., SOLTAN, A. & ZAMORANI, G. (1979). X-ray studies of quasars with the Einstein Observatory. *ApJL*, **234**, L9–L13. 11

TEDDS ET AL. (2007). XMM-Newton-2dF wide angle survey. *in preparation*. 24, 67, 68

TEPLITZ, H.I., COLLINS, N.R., GARDNER, J.P., HILL, R.S., HEAP, S.R., LINDLER, D.J., RHODES, J. & WOODGATE, B.E. (2003). Emission-Line Galaxies in the Space Telescope Imaging Spectrograph Parallel Survey. I. Observations and Data Analysis. *ApJS*, **146**, 209–248. 109

TOZZI, P., GILLI, R., MAINIERI, V., NORMAN, C., RISALITI, G., ROSATI, P., BERGERON, J., BORGANI, S., GIACCONI, R., HASINGER, G., NONINO, M., STREBLYANSKA, A., SZOKOLY, G., WANG, J.X. & ZHENG, W. (2006). X-ray spectral properties of active galactic nuclei in the Chandra Deep Field South. *A&A*, **451**, 457–474. 25, 65, 74, 75, 86

TRAN, H.D., OSTERBROCK, D.E. & MARTEL, A. (1992). Extreme spectral variations of the Seyfert galaxy Markarian 993. *AJ*, **104**, 2072–2077. 25

TRIPP, T.M., BECHTOLD, J. & GREEN, R.F. (1994). Spectral energy distributions of the brightest Palomar-Green quasars at intermediate redshifts. *ApJ*, **433**, 533–552. 28

TURNER, T.J. & POUNDS, K.A. (1989). The EXOSAT spectral survey of AGN. *MNRAS*, **240**, 833–880. 11

URRY, C.M. & PADOVANI, P. (1995). Unified Schemes for Radio-Loud Active Galactic Nuclei. *PASP*, **107**, 803+. 19, 22, 23

VANDEN BERK, D.E., RICHARDS, G.T., BAUER, A., STRAUSS, M.A., SCHNEIDER, D.P., HECKMAN, T.M., YORK, D.G., HALL, P.B., FAN, X., KNAPP, G.R., ANDERSON, S.F., ANNIS, J., BAHCALL, N.A., BERNARDI, M., BRIGGS, J.W., BRINKMANN, J., BRUNNER, R., BURLES, S., CAREY, L., CASTANDER, F.J., CONNOLLY, A.J., CROCKER, J.H., CSABAI, I., DOI, M., FINKBEINER, D., FRIEDMAN, S., FRIEMAN, J.A., FUKUGITA, M., GUNN, J.E., HENNESSY, G.S., IVEZIĆ, Ž., KENT, S., KUNSZT, P.Z., LAMB, D.Q., LEGER, R.F., LONG, D.C., LOVEDAY, J., LUPTON, R.H., MEIKSIN, A., MERELLI, A., MUNN, J.A., NEWBERG, H.J., NEWCOMB, M., NICHOL, R.C., OWEN, R., PIER, J.R., POPE, A., ROCKOSI, C.M., SCHLEGEL, D.J., SIEGMUND, W.A., SMEE, S., SNIR, Y., STOUGHTON, C., STUBBS, C., SUBBARAO, M., SZALAY, A.S., SZOKOLY, G.P., TREMONTI, C., UOMOTO, A., WADDELL, P., YANNY, B. & ZHENG, W. (2001). Composite Quasar Spectra from the Sloan Digital Sky Survey. *AJ*, **122**, 549–564. 108

VÉRON-CETTY, M.P. & VÉRON, P. (2000). The emission line spectrum of active galactic nuclei and the unifying scheme. *A&A Rev.*, **10**, 81–133. 20, 21

VOGES, W., BOLLER, T., ENGLHAUSER, J., FREYBERG, M. & SUPPER, R. (2001). The ROSAT X-ray Database from All-Sky Survey and Pointed Observations. In R.J. Brunner, S.G. Djorgovski & A.S. Szalay, eds., *Virtual Observatories of the Future*, vol. 225 of *Astronomical Society of the Pacific Conference Series*, 234+. 10

WALTER, R. & FINK, H.H. (1993). The Ultraviolet to Soft X-Ray Bump of SEYFERT-1 Type Active Galactic Nuclei. *A&A*, **274**, 105+. 28

WARDZIŃSKI, G. & ZDZIARSKI, A.A. (2000). Thermal synchrotron radiation and its Comptonization in compact X-ray sources. *MNRAS*, **314**, 183–198. 28

WATSON, M.G., AUGUÈRES, J.L., BALLET, J., BARCONS, X., BARRET, D., BOER, M., BOLLER, T., BROMAGE, G.E., BRUNNER, H., CARRERA, F.J., CROPPER, M.S., DENBY, M., EHLE, M., ELVIS, M., FABIAN, A.C., FREYBERG, M.J., GUILLOUT, P., HAMEURY, J.M., HASINGER, G., HINSHAW, D.A., MACCACARO, T., MASON, K.O., MCMAHON, R.G., MICHEL, L., MIRIONI, L., MITTAZ, J.P., MOTCH, C., OLIVE, J.F., OSBORNE, J.P., PAGE, C.G., PAKULL, M., PERRY, B.H., PIERRE, M., PIETSCH, W., PYE, J.P., READ, A.M., ROBERTS, T.P., ROSEN, S.R., SAUVAGEOT, J.L., SCHWOPE, A.D., SEKIGUCHI, K., STEWART, G.C., STEWART, I., VALTCHANOV, I., WARD, M.J., WARWICK, R.S., WEST, R.G., WHITE, N.E. & WORRALL, D.M. (2001). The XMM-Newton Serendipitous Survey. I. The role of XMM-Newton Survey Science Centre. *A&A*, **365**, L51–L59. 67

WEEDMAN, D.W. (1977). Seyfert galaxies. *ARA&A*, **15**, 69–95. 21

WHITE, R.E., III & DAVIS, D.S. (1998). X-Ray Properties of a Complete Sample of Elliptical Galaxies: Implications for Dark Matter Halos. In D. Zaritsky, ed., *Galactic Halos*, vol. 136 of *Astronomical Society of the Pacific Conference Series*, 299+. 63

WOLTER, A., GIOIA, I.M., HENRY, J.P. & MULLIS, C.R. (2005). Unobscured QSO 2: a new class of objects? *A&A*, **444**, 165–174. 25

WORSLEY, M.A., FABIAN, A.C., BAUER, F.E., ALEXANDER, D.M., HASINGER, G., MATEOS, S., BRUNNER, H., BRANDT, W.N. & SCHNEIDER, D.P. (2005). The unresolved hard X-ray background: the missing source population implied by the Chandra and XMM-Newton deep fields. *MNRAS*, **357**, 1281–1287. 14, 33, 90

ZAKAMSKA, N.L., STRAUSS, M.A., KROLIK, J.H., COLLINGE, M.J., HALL, P.B., HAO, L., HECKMAN, T.M., IVEZIĆ, Ž., RICHARDS, G.T., SCHLEGEL, D.J., SCHNEIDER, D.P., STRATEVA, I., VANDEN BERK, D.E., ANDERSON, S.F. & BRINKMANN, J. (2003). Candidate Type II Quasars from the Sloan Digital Sky Survey. I. Selection and Optical Properties of a Sample at $0.3 < z < 0.83$. *AJ*, **126**, 2125–2144. 21, 24

ZAMORANI, G., MIGNOLI, M., HASINGER, G., BURG, R., GIACCONI, R., SCHMIDT, M., TRÜMPER, J., CILIEGI, P., GRUPPIONI, C. & MARANO, B. (1999). The ROSAT deep survey. V. X-ray sources and optical identifications in the Marano field. *A&A*, **346**, 731–752. 35, 36, 41, 48, 51, 52, 109, 111, 112, 113

ZITELLI, V., MIGNOLI, M., ZAMORANI, G., MARANO, B. & BOYLE, B.J. (1992). A spectroscopically complete sample of quasars with B_J not greater than 22.0. *MNRAS*, **256**, 349–367. 35, 36, 48, 51, 52, 109, 112

ZOMBECK, M.V. (1990). *Handbook of space astronomy and astrophysics*. Cambridge: University Press, 1990, 2nd ed. 57, 72

Acknowledgments

I would like to express my thanks to my supervisors, PD Dr. habil Axel D. Schwope and Prof. Dr. Matthias Steinmetz, who introduced me to the wonderful subject of high energy astrophysics and guided me all the time through my Ph.D. work. As my supervisors they always gave me useful instructions and integrated me to international collaborations.

I would especially like to thank Dr. Georg Lamer who always had time for my problems and questions and answered them with great patience. He assisted me with specific computer and coding issues. In particular, I would like to thank him for inspiring discussions and his valuable advices.

My special thanks go to Justus Vogel, Jan Kohnert, Marcel "Marci" Kappel, Nicolas Lodieu, Mareike Godolt, Stefan Schmeja, Anne-Katharina Jappsen, Robert Schwarz, Andreas Staude, and Ada Nebot for providing a pleasant working ambience.

I would like to thank the staff at the Astrophysical Institute of Potsdam (AIP), especially the computing personnel Mario Dionies, Dr. Karl-Heinz Böning and Andre Saar for their assistance.

In addition, I thank my Italian colleagues Marco Mignoli and Giovanni Zamorani for providing unpublished optical imaging for the Marano field.

Many thanks go also to Robert A. Piontek. On an incredibly short timescale he sacrificially corrected this thesis for all the small typos that occur when a German writes an English thesis.

Beyond all others I would like to thank my family. My deepest personal thanks go to my parents, Bernd and Christel Krumpe, who always gave me full support in all my decisions:

Liebe Mutti, lieber Vati,
ich danke Euch, dass Ihr mich in allen meinen Entscheidungen immer unterstützt habt und mir mit Rat und Tat stets zur Seite standet. Ohne diese Hilfe und Eure Motivation wäre der Schritt von einem 13jährigen, der davon träumt Astrophysiker zu werden, bis zu dieser Arbeit nicht möglich gewesen. Vielen Dank auch für Eure aufopferungsbereite finanzielle Unterstützung während meines Studiums, vor allem in der Zeit in Santa Cruz. Ohne Euch hätte mein Studienabschluss sicherlich nicht so zügig erfolgen können und wäre die Studentenzeit nicht so schön gewesen. Ich bin mir bewusst, welchen Verdienst Ihr an dieser Arbeit habt und möchte mich vom ganzen Herzen bei Euch bedanken. Ihr seid wunderbare Eltern!
In Liebe Eurer Mirko

Last but not least, I thank Susanne Schmeltzer for listening at every time of day or night and for motivating me at the right moments. Thank you for reading, correcting, and helping me to finish my Ph.D. thesis.

Publications

KRUMPE, M., LAMER, G., SCHWOPE, A.D., CORRAL, A., CARRERA, F.J., BARCONS, X., PAGE, M., MATEOS, S., TEDDS, J. & WATSON, M. (2007). X-ray absorption in distant type II QSOs. *submitted to A&A*.

GARCET, O., GANDHI, P., GOSSET, E., SPRIMONT, P.G., SURDEJ, J., BORKOWSKI, V., TAJER, M., PACAUD, F., PIERRE, M., CHIAPPETTI, L., MACCAGNI, D., PAGE, M.J., CARRERA, F.J., TEDDS, J.A., MATEOS, S., KRUMPE, M., CONTINI, T., CORRAL, A., EBRERO, J., GAVIGNAUD, I., SCHWOPE, A.D., LE FÈVRE, O., POLLETTA, M., ROSEN, S., LONSDALE, C., WATSON, M., BORCZYK, W. & VAISANEN, P. (2007). The XMM large scale structure survey: optical versus X-ray classifications of active galactic nuclei and the unified scheme. *A&A*, 474, 473-489.

KRUMPE, M., LAMER, G., SCHWOPE, A.D & HUSEMANN, B. (2007). RBS1423 - a new QSO with relativistic reflection from an ionised disk. *A&A*, 470, 497-503.

STAUDE, A., SCHWOPE, A.D., SCHWARZ, R., VOGEL, J., KRUMPE, M. & NEBOT GOMEZ-MORAN, A. (2007). The changing accretion states of the intermediate polar MU Cam. *submitted to A&A*.

KRUMPE, M., LAMER, G., SCHWOPE, A.D., WAGNER, S., ZAMORANI, G., MIGNOLI, M., STAUBERT, R., WISOTZKI, L. & HASINGER, G. (2007). The XMM-Newton Survey in the Marano Field I. The X-ray data and optical follow-up. *A&A*, 466, 41-61.

KRUMPE, M., COFFEY, D., EGGER, G., VILARDELL, F., LEFEVER, K., LIERMANN, A., HOFFMANN, A.I.D., STEIPER, J., CHERIX, M., ALBRECHT, S., RUSSO, P., STRODL, T., WAHLIN, R., DEROO, P., PARMAR, A., LUND, N. & HASINGER, G. (2005). X-RED: a satellite mission concept to detect early universe gamma ray bursts *Proceedings of the SPIE*, Volume 5898, 419-432.

STAUDE, A., SCHWOPE, A.D., KRUMPE, M., HAMBARYAN, V. & SCHWARZ, R. (2003). 1RXSJ062518.2+733433: A bright, soft intermediate polar. *A&A*, 406, 253-258.

CURRICULUM VITAE
Mirko Krumpe

Address: Kirschallee 5
City, Country: 16359 Biesenthal, Germany
Telephone number: +49 (0)331 7499 328
Cell phone number: +49 (0)177 4613 504
E-mail: mkrumpe@aip.de

PERSONAL DATA

Date of birth	May 17, 1977
Place of birth	Bernau, Germany
Gender	Male
Marital status	Single
Nationality	German

RESEARCH FOCUS

- X-ray surveys and multi-wavelength follow-up
- Active galactic nuclei (AGN)
- Immediate vicinity of super-massive back holes
- Seyfert I/II galaxies
- X-ray bright optically normal galaxies
- Gamma-ray bursts

SKILLS

- Analysing XMM-Newton X-ray data with SAS and XSPEC
- Reduction and analysis of optical data and spectra
- Familiarity with Linux, Windows, Office, Latex
- Proficiency in software development in MIDAS, IDL, C, Perl, Fortran, TurboPascal, Basic,Testpoint, HTML
- Languages: English: fluent writing and speaking, German: native

Education

since October 2004	Ph.D. student on "X-ray and optical properties of X-ray luminous AGN" at the Astrophysical Institute Potsdam, Germany (supervised by A.D. Schwope & M. Steinmetz)
Oct. 2003 – Sept. 2004	Research assistant at the Astrophysical Institute Potsdam
Oct. 1997 – Sept. 2003	Studies in physics at the University of Potsdam, Germany and Technical University of Berlin, Germany
	Specialisation in astrophysics and attitude control of satellites

Awards

Sept. 2001 – July 2002	Scholarship of the University of Potsdam for studies at the University of California, Santa Cruz, USA
	Fulbright "Travel Grant Only" scholarship

Affiliated appointments

since January 2003	Secretary of the editorial office of Astronomical Notes

Teaching Experience

April 2005 – Sept. 2005	Seminar on classical mechanics for first and second year students
Jan. 2000 – Aug. 2001	Tutor for theoretical and experimental physics for first and second year students

Interests

- Ballroom and Latin tournament dancing
- Space flight and space technology
- Sailing, scuba diving, surfing

Selbstständigkeitserklärung

Hiermit versichere ich, dass ich die vorliegende Arbeit selbstständig verfasst und keine anderen als die im Literaturverzeichnis angegebenen Quellen und Hilfsmittel benutzt habe. Die Arbeit wurde an keiner weiteren Universität eingereicht.

Mirko Krumpe